12-20-2009

Study of Magnetization Switching for MRAM Based Memory Technologies

Huy Pham
University of New Orleans

Study of Magnetization Switching for MRAM Based Memory Technologies

A Dissertation

Submitted to the Graduate Faculty of the
University of New Orleans
in partial fulfillment of the
requirements for the degree of

Doctor of Philosophy
in
Engineering and Applied Science
Physics

by

Huy Pham

B.S. Hanoi University of Science, Vietnam, 2001
M.S. University of New Orleans, USA, 2005

December, 2009

Acknowledgments

I am greatly thankful to my advisor, Prof. Leonard Spinu who taught me with a wealth of knowledge in study and gave me a lot of helpful suggestions in life. This dissertation could not have been done without his priceless guidance.

I would like to thank my supervisory committee members for their valuable and insightful suggestions and guidance for this work and for various courses these last years as well: Prof. Leonard Spinu, the committee chair, Prof. Leszek Malkinski, and Prof. Ashok Puri from Department of Physics, Prof. Dimitrios Charalampidis from Department of Engineering, and Prof. Scott L. Whittenburg, Vice Chancellor for Research and Dean of the Graduate School at University of New Orleans.

I am deeply grateful to my colleagues: Dr. Dorin Cimpoesu, Dr. Ioan Dumitru, Dr. Juliano Denardin, and Dr. Cosmin Radu for their support and valuable opinions. A lot of results in this dissertation were contributed by their hard work.

I want to express my deepest gratitude for the continuous support from the Advanced Materials Research Institute (AMRI) at University of New Orleans that offered me a graduate research assistant position for all the duration of my studies. I also would like to thank all of my colleagues at AMRI for their assistances.

Table of Contents

List of Figures

List of Tables

Abstract

Understanding magnetization reversal is very important in designing high density and high data transfer rate recording media. This research has been motivated by interest in developing new nonvolatile data storage solutions as magnetic random access memories - MRAMs. This dissertation is intended to provide a theoretical analysis of static and dynamic magnetization switching of magnetic systems within the framework of critical curve (CC). Based on the time scale involved, a quasi-static or dynamic CC approach is used.

The static magnetization switching can be elegantly described using the concept of critical curves. The critical curves of simple uncoupled films used in MRAM are discussed. We propose a new sensitive method for CC determination of 2D magnetic systems. This method is validated experimentally by measuring experimental critical curves of a series of Co/SiO_2 multilayers systems.

The dynamics switching is studied using the Landau-Lifshitz-Gilbert (LLG) equation of motion. The switching diagram so-called dynamic critical curve of Stoner-like particles subject to short magnetic field pulses is presented, giving useful information for optimizing field pulse parameters in order to make ultrafast and stable switching possible.

For the first time, the dynamic critical curves (dCCs) for synthetic antiferromagnet (SAF) structures are introduced in this work. Comparing with CC, which are currently used for studying the switching in toggle MRAM, dCCs show the consistent switching and bring more useful information on the speed of magnetization reversal. Based on dCCs, better understanding of the switching diagram of toggle MRAM following toggle writing scheme can be achieved.

The dynamic switching triggered by spin torque transfer in spin-torque MRAM cell has been also derived in this dissertation. We have studied the magnetization's dynamics properties as a function of applied current pulse amplitude, shape, and also as a function of the Gilbert damping constant. The great important result has been obtained is that, the boundary between switching/non-switching regions is not smooth but having a seashell spiral fringes.

The influence of thermal fluctuation on the switching behavior is also discussed in this work.

Keywords: magnetization switching, critical curve, SAF, MRAM, toggle MRAM, STT-MRAM, Landau-Lifshitz-Gilbert equation, spin torque transfer.

Introduction

Magnetization dynamics is one of the central issues in the physics of mesoscopic magnetic systems [1, 2] and its understanding is important not only for its evident fundamental interest but also due to the big impact on the information technology, more specifically on magnetic information storage. Magnetic recording is rapidly approaching the nanometer scale as storage densities are projected to increase to a terabit per square inch. High volume of data requires higher data transfer rates. These present new challenges and opportunities in nanometer scale materials engineering and in inderstanding the magnetic properties of nanometer scale magnetic materials. Among the critical issues is the manner and speed which the magnetization direction can be reversed from one stable configuration to another. Also, for the magnetic random access memories (MRAMs) [3] unlike present forms of nonvolatile memories, they must have switching rates and rewrite-ability properties surpassing those of conventional RAMS. This can be achieved only first by understanding and then by controlling the magnetization dynamics of very confined magnetic elements.

The magnetization dynamics at different timescales is governed by different physical dynamic mechanisms. Firstly, on the nanosecond range (0.1 ns to 100 ns) the dipolar interactions, external fields and spin–lattice interactions are the major driving forces. The magnetization reversal occurs through a process called precessional motion,

which is the primary source of magnetization rotation that is gradually opposed by damping [4, 5]. This regime is described theoretically by the phenomenological magnetization's equation of motion Landau-Lifshitz-Gilbert (LLG) and is able to describe the precessional reversal mechanism. In this regime, the weakly damped precession of spins induces the so-called ringing of magnetization, which can persist up to several nanoseconds. Recently, it was shown that it is possible to suppress the ringing, and so reduce the switching time through a ballistic switching process, by matching the field-pulse parameters to the frequency and the phase of the magnetic excitation [4]. For shorter time scales of the order of picoseconds (1-100 ps) the electron excitations cannot be ignored and electron-phonon, phonon-phonon, and spin-lattice interactions start to be important. In this case the LLG formalism gradually becomes invalid as quantum effects appear. Here a new mechanism of magnetization reversal is possible, induced by an angular momentum transfer from a magnetically polarized electron current [6-9]. Finally, for very short time scales (1fs-1ps), electron–electron and spin-orbit interactions dominate. Magnetic structures can be excited by optical probes that are shorter than fundamental timescales such as spin-lattice relation times and precession times. This regime became accessible only recently when novel pulsed magneto-optical lasers were developed capable of studying the spin dynamics at femtosecond resolution [10, 11].

This thesis is intended to provide a theoretical analysis of magnetization dynamics in nanometer scale magnetic structures in the first regime among those mentioned above. In spite of continuous efforts on studying this dynamics, there are several fundamental physics issues which remain poorly understood including the effect of dipolar

interactions, the spin-torque transfer effects, the role of thermal fluctuations, and the basic mechanism of damping of magnetization motion. Specifically, in this work the study of magnetization dynamics will be performed using the formalism of the critical curve. The critical curve is a very important concept for both, theoretical study of switching mechanism in magnetic system and device applications, as MRAM. The critical curve was first discussed by Slonczewski [12] and then developed further by André Thiaville in 1997 [13]. However, the name of "critical curve" basically comes from the Stoner-Wohlfarth model, which was early introduced by Stoner and Wohlfarth to describe the simplest case of the uniaxial, single domain particles in 1947 [14]. Based on the remarkable properties of the critical curve, the hysteresis and the corresponding transverse susceptibility curves can be constructed, providing a lot of useful information of magnetic materials. It is clear, therefore, that the critical curve is the key to the understanding of the static behavior of magnetic materials. There are several techniques developed so far to measure the critical curve. In the first part of this work the quasi-static case will be considered where a new method for measuring the static critical curve using the reversible susceptibility measurements is proposed. This method will be theoretically presented and experimentally validated in the case of a nanostructured magnetic system consisting of multilayers of Co/SiO_2.

In the case of faster magnetization switching, a dynamic critical curve approach is used. The switching properties are discussed in the case of interacting single domain particles subject to an external field pulse. The theoretical description of precessional motion is obtained using the phenomenological Landau - Lifshitz - Gilbert (LLG)

equation that includes the pulse magnetic excitation, the exchange and dipolar interaction fields. The weakly damped precessions of spin induce small fluctuation of magnetization, or in other words, ringing of magnetization, for a time of nanoseconds. The ringing of magnetization is strongly dependent on field pulse parameters (as shape, rising and falling times) and a precise control of ultra fast magnetization can be obtained. The main goal is to determine the parameters of field pulse for which a fast and stable switching can be achieved. The influences of interaction between particles and the spatial placement of the particles on switching behavior are discussed. Our results and analysis suggest that in dealing with the problem of improving the density of data storage in MRAM, the dipolar interaction between neighboring magnetic elements is one of important aspects that needs to be considered carefully.

Recently, there are several novel approaches that eliminate the half-select disturb phenomenon present in conventional MRAM [15-18]. Among them, "magnetization toggling" and "spin torque transfer" switching are the most promising, introducing new advanced generations of MRAM, as "toggle-MRAM" and "Spin transfer torque MRAM", respectively. This study is also motivated by the considerable interest in investigating the dynamic switching properties of magnetization in these new advanced types of MRAM. In toggle MRAM, proposed by Savtchenko [15], the free layer in a MRAM cell consists of two weakly anti-parallel coupled ferromagnetic layers instead of a single layer as used in conventional MRAM. Therefore, the free layer in a toggle cell is a synthetic antiferromagnet (SAF) trilayer stack. The theory of simple uncoupled films of critical curve (CC) does not work in the case of coupled films, and an equivalent

approach was developed [19-21]. Subsequently, CCs of SAF have been extensively studied due their technological important for toggle-MRAM [22-29]. However, the CCs of SAF are restricted only to a quasistatic regime, where the magnetization dynamics and precessional effects are neglected. As demanding for a high throughput and very short access time, the magnetization is forced by pulsed magnetic fields to switch at nanosecond and sub-nanosecond time scales for which the static CC approach is not anymore adequate. In this dissertation, a dynamic generalization of critical curves for coupled thin films is presented, analyzing the magnetization switching of SAF elements subjected to pulsed magnetic fields. The boundary between switching/non-switching regions represents the natural generalization of static CC, namely the dynamic CC (dCC). Our original contribution to the study of dCCs gives better understanding of the toggle dynamic switching mechanism in Toggle MRAM.

The other advanced generalization of MRAM based on "spin transfer torque" switching approach, so-called spin transfer torque MRAM (STT-MRAM), also attracted an increased interest [16-18]. The concept of spin angular momentum transfer torque was proposed in 1996 by Slonczewski [8] and Berger [6]. In the presence of an electric current, a torque may act on the magnetization of a thin ferromagnetic layer, arising primarily from the transmission and reflection of incoming electrons. The spin-torque offers a new way to control the writing process in high density MRAM because a spin-polarized current can switch the magnetization of a ferromagnetic layer more efficiently than a current-induced magnetic field. An essential problem in the development of a device based on the spin-torque transfer is the evaluation of the minimum switching

current that ensures a reliable magnetization reversal at high operating frequencies. In this work we present how the current sweep rate, damping constant, initial position, waiting time, and also thermal fluctuation affect the switching, the reliability, and the writing speed of spin-torque devices. The main goal is to determine the optimum parameters of current pulse to achieve a fast and stable switching.

In this thesis, these two recent developments of MRAM mentioned above will be studied by comprehensive micromagnetic simulations. To be more specific, we shall now outline the organization of the dissertation below:

Chapter 1, *Overview of Magnetism,* gives an overview of the background information required for a full understanding of the remainder of the thesis. The background information includes a short presentation of the free energy of magnetic systems, Stoner-Wohlfarth and Néel-Brown models and LLG/stochastic equations of motion.

Chapter 2, *Static Critical Curve,* begins with a brief description of the importance of the critical curve in magnetization switching processes in general and in MRAM technology in particular. Based on the remarkable properties of the critical curve, the hysteresis and the corresponding transverse susceptibility curves are also determined and discussed. The final point of this chapter is concerned about our new sensitive method based on susceptibility measurements for the critical curve determination of two-dimension (2D) magnetic systems.

Chapter 3, *Magnetization Dynamics in Interacting Magnetic Systems,* presents the dynamic switching properties of an isolated MRAM cell, subject to short magnetic field

pulses, obtained by numerical investigations of the Landau-Lifshitz-Gilbert equation. The switching properties are discussed as a function of the external field pulse strength and direction, pulse length and the pulse shape. We advanced the work of M. Bauer and his co-authors [4] that was developed for non-interacting systems, and we have studied the dynamic magnetization behavior of a MRAM cell taking into account the dipolar interaction with neighboring cells.

Chapter 4, *Spin Transfer Switching,* presents our original contribution to the problem of dynamic magnetization switching triggered by spin angular momentum transfer in a pulsed current of a spin-valve-type trilayer structure, and its dependence on thermal effects. The magnetization switching under coexistence of the spin-transfer torque and the torque by a pulsed magnetic field is also discussed in this chapter. Our model is based on the LLG equation and the stochastic LLG equation with a spin-transfer torque term included.

Chapter 5, *Static and Dynamic Critical Curves of a Synthetic Antiferromagnet,* begins with a brief description of a synthetic antiferromagnet (SAF) and its technological applications. The static critical curve of SAF and its remarkable properties in understanding the magnetization switching mechanism in Toggle-MRAM are presented. Then, we discuss our original contribution to the study of a dynamic generalization of critical curves for SAF structures, analyzing the magnetization switching of SAF elements subject to pulsed magnetic fields. In order to determine dynamic critical curves (dCCs) dependence on field pulse's parameters, we have studied the switching properties as a function of pulse's shape and length, damping, and magnetostatic coupling. Based on

the dCCs, we further investigate the dynamic toggle switching in toggle MRAM and its dependence on thermal effects.

Finally, conclusions are drawn in the last chapter.

Each of the last four chapters ends with a *summary* that briefly presents the essential information such way that one can faster focus its attention on a specific section.

The dissertation ends with a *list of author's publications* and a short *Vita*. The list of publications includes also several papers published during the last year pertinent to an experimental work that the author carried out in the framework of a collaborative work between Prof. Spinu's research group and Prof. Zhiqiang Mao's group from Tulane Universitiy. This works is not directly related to the theoretical work presented in this thesis and is concerned with the study of the newly discovered family of unconventional superconductors containing layers of iron arsenide, the iron oxypnictides.

Chapter 1

Overview of Magnetism

Magnetism is certainly one of the cornerstones of what we today call *the information technology era*. Following the huge development of electronic devices such as the personal computer, this era has been strongly driven by the growing demand to increase the density and the speed of writing and retrieving data in memory devices. Today, the demand for information storage is enormous and expected to increase even further. High density of data requires higher data transfer rates. These present new challenges in understanding of the magnetization behavior from both static and dynamic points of views. The understanding of the magnetization reversal is extremely important not only for its evident fundamental interest but also due to the big impact on the information technology.

This chapter will present the most important contributions to the free magnetic energy, and the overview of some basic theoretical models describing the static and dynamic behavior of magnetization. The Stoner-Wohlfarth model regarding the static switching behavior of an assembly of single domain ferromagnetic particles, the Néel-Brown model for the system of superparamagnetic particles, as well as the LLG equation of motion describing the magnetization dynamics will be given in detail.

1.1 Magnetic free energy

The following section is intended to facilitate the understanding of the concept of the energy of magnetic systems. As we all know the problem of investigating the static equilibrium of a system is always related to the problem of minimizing the total free energy of the system. For instance, in Stoner- Wohlfarth model (SW) [14] by finding the total magnetic energy minima, it is possible to predict the magnetization rotation and switching behavior of the particle under the influence of an applied field. Another straightforward example is that the existence of well-known domain structure in ferromagnetic materials can be explained by the result of minimization of the total free energy. In general, in order to observe the behavior of a magnetic system, it is of important to fully understand the contribution of each energy term in the total free energy of the system. In the following, we shall present the most important energy terms.

1.1.1 Magnetocrystalline anisotropy

In a magnetic crystal, the disposition of the magnetic moments reflects the symmetry of the lattice. Interactions of the magnetic moments between themselves or with the lattice are thus affected by the symmetry of the crystal and give rise to anisotropic energy contributions, summarized under the term of magnetocrystalline anisotropy [30]. Therefore, there are directions in space lattice along which it is easier to magnetize a given crystal than in other directions. These directions are called easy directions. Let us now consider the simplest case of the uniaxial magnetic anisotropy, and suppose that the uniaxial anisotropy axis, or easy axis, is parallel to the c-axis of the crystal. The anisotropy energy is invariant with respect to rotations around the anisotropy

axis, and depends only on the relative orientation of magnetization vector $\mathbf{M}$ with respect to the axis. As $\mathbf{M}$ rotates away from *c*-axis, the anisotropy energy initially increases with θ, the angle between the *c*-axis and the magnetization vector, then reaches a maximum value at $\theta = 90^0$, and decreases to its original value at $\theta = 180^0$. In other words, the minimum of anisotropy energy occurs when the magnetization points in either the + or – direction along the *c*-axis. We can express this energy density as follows:

$$W_K = K_0 + K_1 \sin^2\theta + K_2 \sin^4\theta + ... \tag{1.1}$$

The coefficients $K_n \ (n = 0,\ 1,\ 2....)$ are called anisotropy constants, having the dimension of energy per unit volume. The higher-order terms above K_2 are negligible since they are very small. The K_0 term is a constant; therefore, it also can be disregarded. For small deviations of the magnetization vector from the equilibrium position, the anisotropy density can be approximated, to second order in θ, as

$$W_K \cong K_1\theta^2 \cong 2K_1 - 2K_1\cos\theta = 2K_1 - \mathbf{M}.\mathbf{H}_K \tag{1.2}$$

Where $H_K = \dfrac{2K_1}{M_s}$, with M_s is the magnitude of the magnetization vector $\mathbf{M}$. H_K is called the anisotropy field, giving a natural measure of the strength of the anisotropy effect and of the torque necessary to take the magnetization away from the easy axis. For cubic crystals, the anisotropy energy can be expressed in terms of the direction cosines $(\alpha_1,\ \alpha_2,\ \alpha_3)$ of the magnetization vector with respect to the three cube edges

$$W_K = K_1(\alpha_1^2\alpha_2^2 + \alpha_2^2\alpha_3^2 + \alpha_3^2\alpha_1^2) + K_2\alpha_1^2\alpha_2^2\alpha_3^2 \tag{1.3}$$

1.1.2 Magnetostriction and stress anisotropy

Magnetostriction is the phenomenon whereby the shape and volume of a magnetic specimen change during the process of magnetization. The reason for this behavior is that the crystal lattice inside each domain is spontaneously deformed in the direction of domain magnetization and its strain axis rotates with the rotation of the domain magnetization, thus resulting in a deformation of the specimen as a whole [30]. The magnetoelastic energy density for isotropic magnetostriction is given by:

$$W_\sigma = \frac{3}{2}\lambda_s \sigma \sin^2 \theta_s \tag{1.4}$$

where θ_s is the angle between the magnetization and the stress direction, λ_s is the appropriate magnetostriction constant, σ is a uniaxial stress applied along the certain direction.

1.1.3 Shape anisotropy

The origin of shape anisotropy is magnetostatic energy. The magnetization curve of a material depends not only on its magnetic susceptibility, but also on the shape of the specimen. When a specimen of finite size is magnetized by an external magnetic field, the free poles, which appear on its ends, will produce a magnetic field directed opposite to the magnetization [30]. This field is called the demagnetizing field, and is given by:

$$\mathbf{H}_d = -N\mathbf{M} \tag{1.5}$$

where N is called the demagnetizing factor, which depends only on the shape of the specimen. For a single domain particle, the magnetostatic energy is related to the magnetization components and it can be expressed exactly only if the particle has an

ellipsoidal shape. If we take the principal axes *a*, *b*, and *c* of the ellipsoid as Cartesian axes, the magnetostatic energy density takes the form

$$W_D = \frac{1}{2}(N_a M_x^2 + N_b M_y^2 + N_c M_z^2) \tag{1.6}$$

where N_a, N_b and N_c are the demagnetizing factors pertaining to the three principal axes, and satisfy the equation $N_a + N_b + N_c = 4\pi$ (in cgs units system).

It is well known that the longer the principal axis, the lower the corresponding demagnetizing factor and the lower the energy when $\mathbf{M}$ points along that direction.

1.1.4 Zeeman energy

Zeeman energy is simply the energy of the interaction between the magnetization vector and the external applied field, given as:

$$W_H = -\mathbf{M}.\mathbf{H} \tag{1.7}$$

1.1.5 Exchange energy

The exchange interaction was first introduced by Heisenberg in 1928 to interpret the origin of the enormously large molecular fields acting in ferromagnetic materials. This interaction is due to a quantum mechanical effect. The energy of exchange interaction is given by:

$$W_E = -2\sum_{ij} J_{ij}\mathbf{S_i}\mathbf{S_j} \tag{1.8}$$

where $\mathbf{S_i}$, $\mathbf{S_j}$ are spins. The term J_{ij}, which has no corresponding concept in classical physics, is called the exchange integral. Here $J_{ij} > 0$ brings two spins parallel to each other (ferromagnetism) whereas $J_{ij} < 0$ brings two spins anti-parallel to each other (antiferromagnetism).

1.2 Stoner-Wohlfarth model

Based on the understanding of energy terms defined previously, we are able to study the magnetization process of magnetic systems through various models. It is well known that a magnetic body, in general consists of many domains, or in other words has a multi-domain structure. Thus, the magnetic system is divided into uniformly magnetized regions (domains) separated by domain walls in order to minimize its total free energy. However, due to the energy cost of the domain walls formation, the balance with the magnetostatic energy limits the subdivision in domains to a certain optimum domain size. As a matter of fact, there is a corresponding lower limit in the crystal size, below which a single-domain structure does exist, since the energy increase due to the formation of domain walls in this case is higher than the energy decrease obtained by dividing the single domain into smaller domains [31].

The magnetization behavior of an assembly of single domain ferromagnetic particles has been one of the central issues in the physics of magnetism. Many different models have been taken, in which, Stonne-Wohlfarth (SW) model is one of the simplest and successful approaches. In 1948, starting from the assumption that it is possible to identify all magnetic particles which reverse their magnetization by coherent rotation, Stoner and Wohlfarth came up with a model to describe such a system [14]. The basic idea of their model, or coherent rotation model, is that a single magnetization vector is sufficient to describe the state of the whole system. This reduces the number of degree of freedom to one. The approach is somehow idealized and should not be expected to give accurate prediction of the behavior of real systems. One can apply this model for a

monodomain particle in which the exchange interaction will be able to keep the elementary spins parallel with respect to each other so that the whole system can be considered uniform as a big single magnetization vector (see Fig. 1.1). One additional notable exception of SW model is that the temperature of the system is not taken into account or, in other words, it can be considered equal to zero. This can be reasonable when the sizes of all ferromagnetic particles are still large enough so that the thermal energy is negligibly small, compared to the anisotropy energy $E = KV$. In this case the magnetic relaxation (superparamagnetism) phenomena can be disregarded. Also, the SW model does not take into account the interaction between particles.

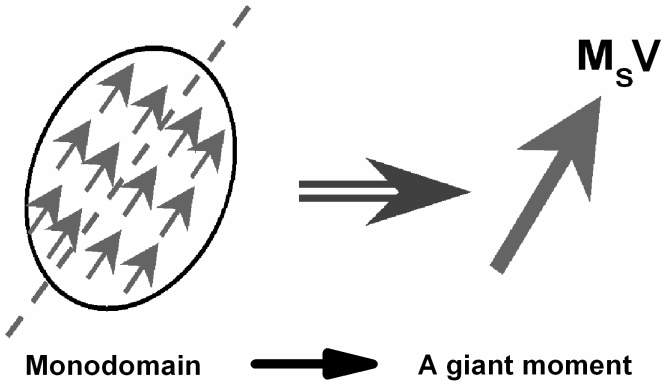

Figure 1.1. Considering an assembly of small magnetic particles as a big single moment.

1.2.1 The free energy function

Let us now firstly consider the free energy of a single-domain SW particle. The free energy of the uniaxial particle per unit volume is composed of two terms, the magnetocrystalline anisotropy energy and the energy of interaction with the external field, described as follows:

$$W(\theta, \mathbf{H}) = K_1 \sin^2 \theta - M_s H \cos(\theta - \theta_K) \tag{1.9}$$

where K_1 is the first anisotropy constant, $\mathbf{H}$ the external field, θ and θ_K the angles made by normalized vectors $\mathbf{m} = \dfrac{\mathbf{M}}{M_S}$ and $\mathbf{h} = \dfrac{\mathbf{H}}{H_K}$ (see Fig. 1.2). It would be convenient to write (1.9) in dimensionless form, by introducing the dimensionless quantity:

$$g_l = \frac{W}{2K_1} \tag{1.10}$$

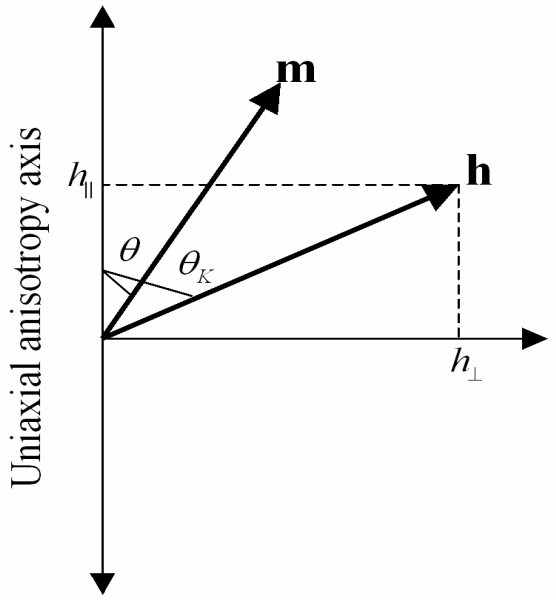

Figure 1.2. Relation between uniaxial anisotropy axis, magnetization unit vector $\mathbf{m}$, and external field, $\mathbf{h}$.

With this notation (1.9) becomes: $g_l(\theta, \mathbf{h}) = \dfrac{1}{2}\sin^2 \theta - h\cos(\theta - \theta_K)$ (1.11)

Instead of using the variables (h, θ_K) in (1.11) one can use the field components perpendicular and parallel to the easy axis ($h_{\perp} = h\sin\theta_K$; $h_{\|} = h\cos\theta_K$) obtaining:

$$g_l(\theta, \mathbf{h}) = \frac{1}{2}\sin^2 \theta - h_{\perp} \sin\theta - h_{\|} \cos\theta \tag{1.12}$$

1.2.2 Astroid curve

Now we would be able to observe the change of the energy function when we move around in the control plane represented by the plane of coordinates $h_{\perp}$ and $h_{\parallel}$. By taking the first and second derivative of the energy function as described in (1.12) and by imposing the condition $\frac{\partial g_l}{\partial \theta} = 0;\ \frac{\partial g_l^2}{\partial \theta^2} = 0$ one can obtain two equations:

$$h_{\perp} = \sin^3 \theta;\ h_{\parallel} = -\cos^3 \theta \tag{1.13}$$

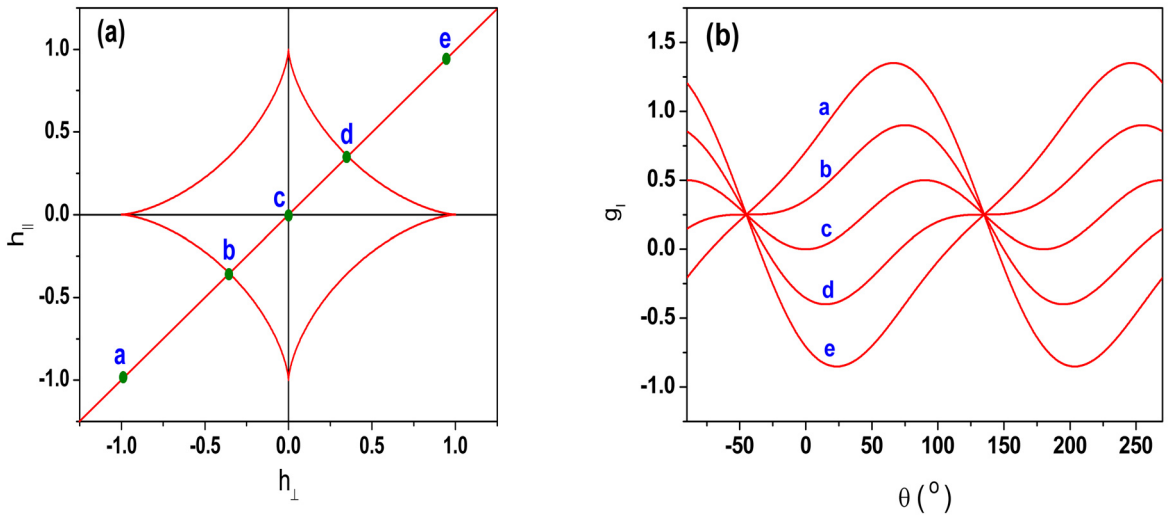

Figure 1.3. (a) Control plane of coordinates $h_{\parallel}$ and $h_{\perp}$. The astroid curve defined by (1.13). (b) Examples of the dependence of the system energy g_l in (1.12) on θ at different points in control space are shown.

The curve generated by (1.13) when θ varies in the interval $(0,\ 2\pi)$ as shown in Fig. 1.3(a) is the critical curve or astroid curve [32]. The figure 1.3(b) shows the energy obtained from (1.12) as a function of θ at different values of the applied field corresponding to the points pointed out in Fig. 1.3(a).

The astroid curve has remarkable properties. The orientations of **m** for a given field **h** can be determined by drawing the tangents to the astroid passing through the point **h** of the control plane (see Fig. 1.4). Each tangent may identify either a stable or an unstable state. The stable orientation provides an energy minimum, and it can be selected using the two conditions:

$$\frac{\partial g_l}{\partial \theta} = 0; \quad \text{and} \quad \frac{\partial g_l^2}{\partial \theta^2} > 0 \tag{1.14}$$

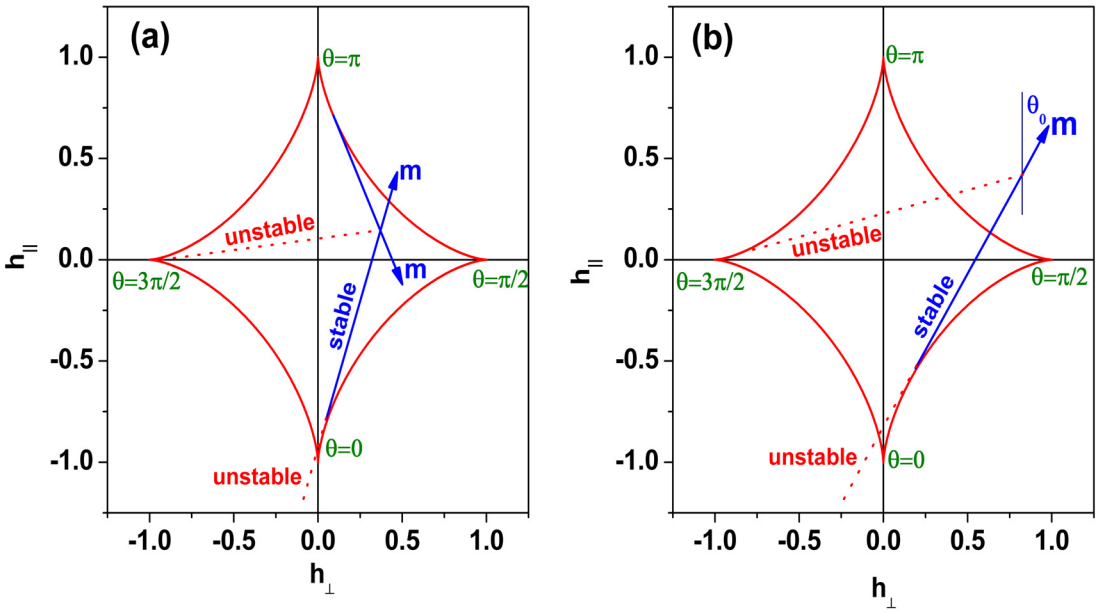

Figure 1.4. Graphical construction defining the possible **m** orientations associated with a given applied field: (a) Inside the astroid. (b) Outside the astroid. The straight half-lines marked as "stable" ("unstable") are sets of local energy minima (maxima) characterized by the same **m** orientation. θ values show how the angle parameter of (1.13) varies along the astroid.

As a result, we can easily realize that there is only one stable solution when the point is located outside the astroid, whereas there are two stable tangents that can be drawn when the point is inside the astroid.

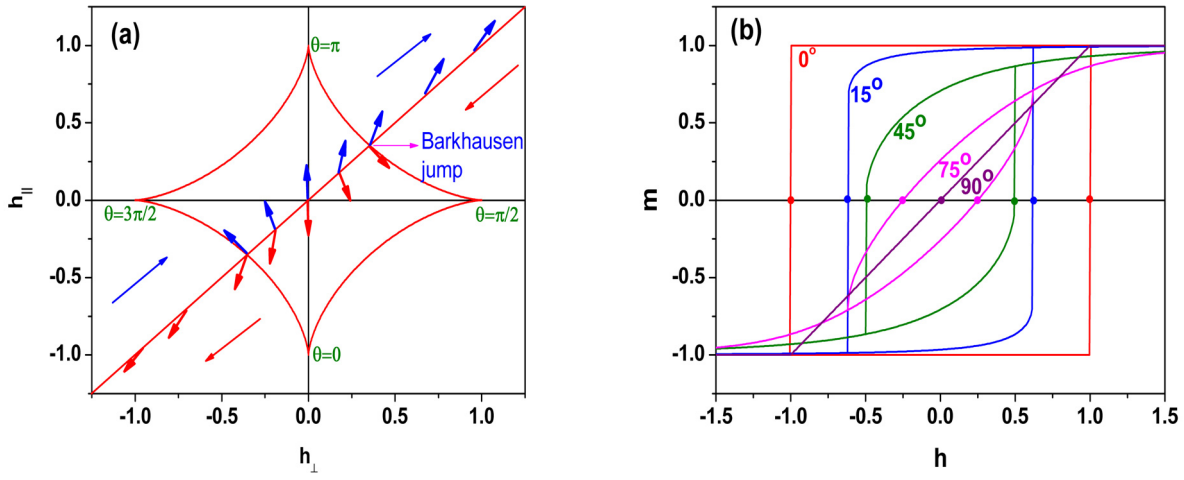

Figure 1.5. (a) Magnetization process under alternating field. Black arrows represent the **m** orientation in the state occupied by the system, white arrows in the other state available to the system. (b) Hysteresis loops for different values of θ_K .

1.2.3 Hysteresis

The typical properties of the astroid curve discussed above are the basis for the analysis of the phenomena taking place when the field is slowly varied over time. The magnetization process under alternating field, where **h** oscillates between opposite values along a fixed direction, is shown in Fig. 1.5(a). The field representative point moves back and forth in control space along a fixed straight line. The **m** orientation at each point is obtained by the tangent construction discussed in the preceding subsection. Inside the astroid, two orientations are possible, and the one actually realized depends on the past history. If the field oscillation were all contained inside the astroid, the magnetization would reversibly oscillate around the orientation initially occupied. If the field can cross over the astroid boundary, a magnetization reversal (Barkhausen jump) takes place, thus the hysteresis loop will be generated (see Fig. 1.5(b)).

1.2.4 Reversible transverse susceptibility

In the previous section we showed the importance of the astroid, or in general of the switching critical curve. There are several methods [33, 34] for determining experimentally the critical curve of magnetic materials and the reversible transverse susceptibility (RTS) is one of them [35]. In the next chapter we will discuss this method in some detail and the crucial role of RTS in studying the magnetization process. Therefore, it is worth mentioning here how to obtain the RTS based on the SW model.

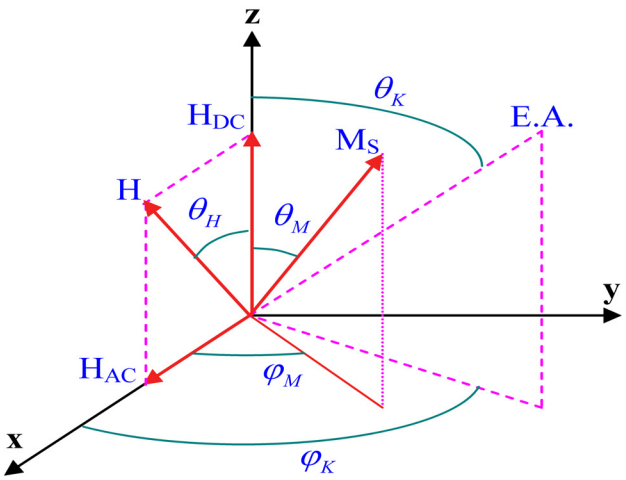

Figure 1.6. The vector diagram corresponding to a uniaxial magnetic particle subjected to a magnetization process in perpendicular fields.

The reversible transverse susceptibility (RTS), χ_T, is actually a component of the reversible susceptibility (RS) tensor [36]. In order to define this tensor; one considers a magnetic field $\mathbf{H}$ applied along to *z*-direction of a ferromagnetic specimen. For a change $\Delta\mathbf{H}$ of the field, the RS tensor, χ_{ik}, is defined as $\Delta M_i = \chi_{ik}\Delta H_k$, for $\Delta H_k \to 0$, provided only reversible changes contribute to the change in magnetization $\Delta\mathbf{M}$. From the above

results that one has two components for RTS measured in two perpendicular directions with respect to the applied field, and given by:

$$\chi_{T_1} = \left(dM_x / dH_x \right)_{H_z=0}, \; H_y = 0 \tag{1.15}$$

$$\chi_{T_2} = \left(dM_y / dH_y \right)_{H_y=0}, \; H_x = 0 \tag{1.16}$$

We will briefly outline the derivation of the χ_T expression in the case of a uniaxial single-domain SW particle with the first anisotropy constant K_1, and the saturation magnetization M_S. Based on the spherical coordinate system as shown in Fig. 1.6, the free energy density of the magnetic system, $W = W_K + W_H$, considered in the dimensionless form of $h = HM_S / 2K_1$ is

$$\begin{aligned} W = & -K_1 \left(\sin\theta_K \cos\varphi_K \sin\theta_M \cos\theta_M + \sin\theta_K \sin\varphi_K \sin\theta_M \sin\theta_M + \cos\theta_K \cos\theta_M \right)^2 \\ & - 2hK_1 (\sin\theta_H \sin\theta_M \cos\varphi_M + \cos\theta_H \cos\theta_M) \end{aligned} \tag{1.17}$$

The angle θ_M and φ_M will be determined from two conditions of minimizing the free energy $\left(\frac{\partial W}{\partial \theta_M} = 0, \text{ and } \frac{\partial W}{\partial \varphi_M} = 0 \right)$ as follows:

$$\begin{aligned} & \sin^2\theta_K \sin 2\theta_M \cos^2(\varphi_K - \varphi_M) + \sin 2\theta_K \cos 2\theta_M \cos(\varphi_K - \varphi_M) \\ & - \cos^2\theta_K \sin 2\theta_M - 2h\left(\cos\theta_H \sin\theta_H - \sin\theta_H \cos\theta_M \cos\varphi_M \right) = 0 \end{aligned} \tag{1.18}$$

$$\begin{aligned} & \sin\theta_M \sin\theta_M \left(\sin\theta_K \sin(\varphi_K - \varphi_M) \right. \\ & \left. \left[\sin\theta_K \sin\theta_M \cos(\varphi_K - \varphi_M) + \cos\theta_K \cos\theta_M \right] - h \sin\theta_M \sin\varphi_M \right) = 0 \end{aligned} \tag{1.19}$$

In the limit $\theta_H \to 0$, the equation (1.19) can be rewritten as

$$\varphi_M = \varphi_K + n\pi \tag{1.20}$$

where n is an integer. In most cases $n = 0$, but there are some cases in which $n = 1$ give the energy minimum. In the limit $\theta_H \to 0$, and using either of the condition $n = 0$ or $n = 1$, the equation (1.18) reduces to:

$$\sin 2(\theta_M - \theta_K) + 2h \sin \theta_M = 0 \tag{1.21}$$

or

$$\sin 2(\theta_M + \theta_K) + 2h \sin \theta_M = 0 \tag{1.22}$$

From the figure 1.6, we have:

$$H_x = H \sin \theta_H,\ H_z = H \cos \theta_H,\ M_x = M_s \sin \theta_M \cos \varphi_M$$

Hence,

$$\frac{\chi_T}{\chi_0} = \frac{3}{2} \underset{\theta_H \to 0}{Lim} \frac{d(\sin \theta_M \cos \varphi_M)}{d(h \sin \theta_H)} \tag{1.23}$$

where $\chi_0 = M_s^2 / 3K_1$. By differentiating (1.18) and (1.19) with respect to θ_H, and using (1.20) in the case of $n = 0$ one can obtain the final expression for χ_T as follows

$$\frac{\chi_T}{\chi_0} = \frac{3}{2}\left[\cos^2 \varphi_K \frac{\cos^2 \theta_M}{h \cos \theta_M + \cos 2(\theta_M - \theta_K)} + \sin^2 \varphi_K \frac{\sin(\theta_K - \theta_M)}{h \sin \theta_K} \right] \tag{1.24}$$

This expression of TS of SW particles in (1.24) was first obtained by Aharoni [36]. A complete analysis of TS curve in the case of quartic crystalline anisotropy will be given in the next chapter.

1.3 Néel and Brown models

When the system of small single domain particles is concerned, the thermal effect needs to be taken into account since in this case the thermal energy of the system is comparable to the magnetic anisotropy energy barrier of single domain particles. Specifically, as mentioned before the anisotropy energy of a uniaxial single domain

particle is given by $E = KV\sin^2\theta$ where K is the anisotropy constant and θ the angle between the magnetization vector and the easy axis. Thus, the energy barrier, separating easy directions is $E_B = KV$, proportional to the volume V. Therefore by decreasing particle size the anisotropy energy decreases, and for a size lower than a certain value, it may become comparable to or even lower than the thermal energy kT. This implies that, the energy barrier for magnetization reversal may be overcome, and then the magnetic moment of the particle can thermally fluctuate from one easy direction to the other, even in the absence of the applied field, like a single spin in a paramagnetic material. The magnetic behavior of an assembly of such small particles is called superparamagnetism [31]. In the case of dealing with a system of magnetic nanoparticles concerning the occurrence of superparamagnetism, the SW model failed to describe such a system. The thermal fluctuation of the magnetic moments of a single-domain particle and its decay toward thermal equilibrium was then introduced by Néel [37] and further developed by Brown [38]. The main difference between these two authors is the pre-exponential factor in their formulas. This pre-factor depends on several parameters such as damping, temperature and exchange interaction. For simplicity, the pre-factor is assumed to be constant, and this assumption became well known as the Néel-Brown model. This model is widely used in magnetism, particular in order to describe the temperature and time-dependence of the magnetization. However, in this work it will not be discussed in detail but briefly. The model stated that the timescale for magnetization reversal τ, in a single particle with uniaxial anisotropy, depends on the anisotropy energy barrier ΔE and the temperature T, and can be expressed by the equation

$$\tau = \tau_0 \exp(\Delta E / kT) \tag{1.25}$$

The pre-exponential factor τ_0 as mentioned above depends on various parameters but typically is in the timescale $10^{-9} s$ and plays a crucial role in determining the resulting time frame for superparamagnetic relaxation and hence the blocking behavior observed by a particular technique.

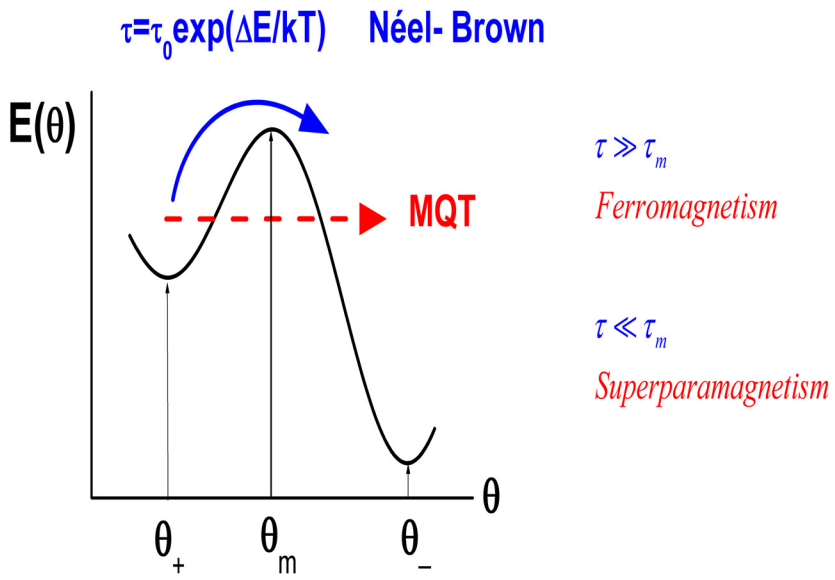

Figure 1.7. Illustrating the barrier energy and Néel-Brown model.

From (1.25), one can see that for the fine magnetic particles the actual magnetic behavior depends on the measuring time τ_m of the specific experimental technique with respect to the relaxation time τ associated with the overcoming of the energy barriers. If $\tau_m > \tau$, the relaxation appears to be so fast that the magnetic moment can easily overcome the energy barriers and the assembly of particles behaves like a paramagnetic system (superparamagnetic state). On the contrary, if $\tau_m < \tau$, and the probability of overcoming

the energy barrier is negligible, the relaxation appears so slow that the assembly of particles will be in blocked state (ferromagnetic state) (see Fig. 1.7).

The blocking temperature T_B, separating the two states, is defined as the temperature at which measuring time becomes equal to relaxation time, i.e.

$$\tau_m = \tau = \tau_0 \exp(\Delta E / kT) \qquad (1.\ 26)$$

Therefore the blocking temperature is not uniquely defined but it related to the time scale of the experimental technique.

In this work, we only investigate theoretically the magnetization dynamics under thermal relaxation. Thus, the magnetization dynamics we will mainly focus on is related with the time necessary for a system to reverse the magnetization. This aspect could not be achieved in the framework of SW model, but only by using a time dependent equation of motion of magnetization. This will be the object of the following sections.

1.4 Landau – Lifshitz – Gilbert equation of motion

The behavior of the magnetization of a single domain ferromagnetic particle has been the subject of many studies. As mentioned in the preceding section, the SW model can describe the system of single domain particles, provided that the coherent rotation condition is satisfied, and the magnetic relaxation (superparamagnetism) phenomena and the interparticle interactions can be neglected. The SW model, however, says nothing about two other important aspects: how the system will approach equilibrium and how the magnetization will react to a time-varying applied field. In order to discuss these points, Landau and Lifshitz in their 1935 paper [39] proposed an equation of motion for

magnetization in a homogeneously magnetized body. This equation is useful not only to describe the equilibrium position but also the dynamics of the moment reaching that position. Gilbert then modified it in 1955 to overcome the unphysical solution for large damping parameters [40]. Because the so-called Landau – Lifshitz – Gilbert (LLG) is a nonlinear differential equation, analytical solutions can be found only in special cases.

1.4.1 The gyromagnetic equation

Let us firstly consider the LLG equation in the absence of the damping term. It is well known that the magnetic moment of an electron is related to spin momentum by:

$$\mathbf{M} = \gamma \mathbf{S} \tag{1.27}$$

where γ is the gyromagnetic ratio for an electron spin, given by

$$\gamma = \frac{-ge}{2mc} \tag{1.28}$$

Here, e is the electron charge, m the electron mass, c the velocity of light, and g the Landé splitting factor. It is worth pointing out that since the charge of an electron is negative, γ is a positive constant. However, Landau and Lifshitz used a negative γ and consequently so did many researchers [41].

The equation (1.27) is valid in both classical and quantum mechanics. The torque exerted on a magnetic moment $\mathbf{M}$ by a magnetic field $\mathbf{H}$ is

$$\mathbf{T} = \mathbf{M} \times \mathbf{H} \tag{1.29}$$

Equations (1.27) and (1.29) give an equation of motion for the magnetic moment of an electron spin

$$\frac{d\mathbf{M}}{dt} = \gamma \mathbf{M} \times \mathbf{H} \tag{1.30}$$

The simple gyromagnetic equation (1.30), simply describes an instantaneous precessional motion of the magnetization vector, as sketched in Fig. 1.8. This is the most basic equation describing the dynamic behavior of the magnetization of a single domain ferromagnetic particle.

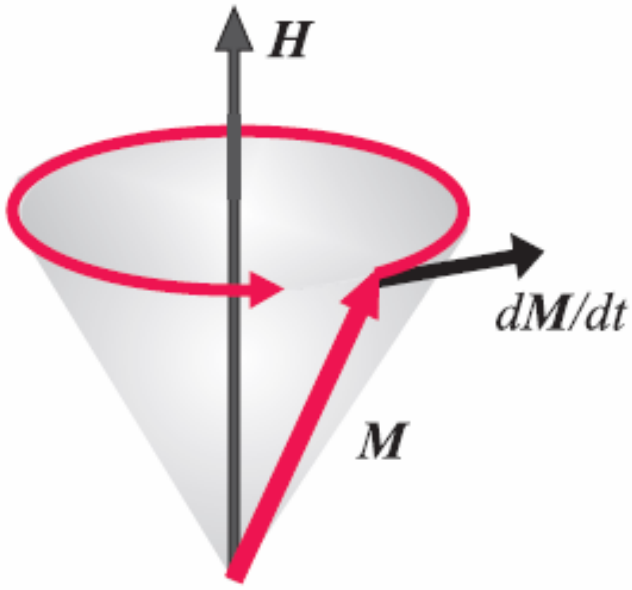

Figure 1.8. Precessional motion of magnetization.

The applicability of (1.30) is not limited to the torque exerted by an external magnetic field. Any torque on a magnetic moment $\mathbf{M}$ can be written in the form of (1.30) if we define an "effective" magnetic field:

$$\mathbf{H} = -\frac{\partial E(\mathbf{M})}{\partial \mathbf{M}} \tag{1.31}$$

where $E(\mathbf{M})$ is the potential energy of the system with respect to the work done by rotating the moment against whatever forces are present. Experimental and theoretical

studies of the properties of ferromagnets have led to identification of five different domain energy terms

$$E = \left(W_H + W_D + W_E + W_K + W_\sigma\right) * V \tag{1.32}$$

where V is the volume and W_H is the external field energy density, W_D is the demagnetization energy density, W_E is the exchange energy density, W_K is the anisotropy energy density, and W_σ is the magnetoelastic energy density. The corresponding effective fields are

$$\mathbf{H}_{Total} = \mathbf{H}_H + \mathbf{H}_D + \mathbf{H}_E + \mathbf{H}_K + \mathbf{H}_\sigma \tag{1.33}$$

The first two terms are magnetic fields. The last three are effective fields that have quantum mechanical origins.

1.4.2 The Landau-Lifshitz equation

The equation (1.30) represents uniform undamped precession of the vector $\mathbf{M}$ about the axis of the field $\mathbf{H}$. The observable behavior, however, of the magnetization of a single domain ferromagnetic particle, is that of alignment of $\mathbf{M}$ with $\mathbf{H}$ in time. This alignment is due to the collisions between precessing electrons which take place within particle. It is apparent, therefore, that the field does not directly cause alignment; rather it causes a precession of $\mathbf{M}$ about the axis of the field, which along with collision will produce alignment. With the aim of including this fact in the mathematical analysis, Landau and Lifshitz introduced a second term into the gyromagnetic equation (1.30), the tendency of which is to align $\mathbf{M}$ with $\mathbf{H}$. In their 1935 paper [39], they proposed an equation for the dynamic behavior of $\mathbf{M}$, which included a term proportional to

$$(\mathbf{M}\times\mathbf{H})\times\mathbf{M}=\mathbf{H}(\mathbf{M}.\mathbf{M})-(\mathbf{H}.\mathbf{M})\mathbf{M} \tag{1.34}$$

The Landau-Lifshitz equation in the original form is:

$$\dot{\mathbf{M}}=-\gamma\left[\mathbf{H}\times\mathbf{M}+\lambda\left(\mathbf{H}-\frac{(\mathbf{H}.\mathbf{M})\mathbf{M}}{M_s^2}\right)\right] \tag{1.35}$$

where λ is a constant of the same dimensions as M_s and limited by the condition that $\lambda \ll M_s$. Using (1.34), the Landau-Lifshitz equation is more commonly written in the following form:

$$\dot{\mathbf{M}}=\gamma\mathbf{M}\times\mathbf{H}-\frac{\gamma\lambda}{M_s^2}\mathbf{M}\times\mathbf{H}\times\mathbf{M} \tag{1.36}$$

This equation now represents damped precessional motion, wherein alignment ultimately takes place between the two vectors, $\mathbf{M}$ and $\mathbf{H}$.

1.4.3 Gilbert damping term, Gilbert equation

The Landau-Lifshitz phenomenological damping term could be used when the damping was small, but encountered problems for large damping. In 1955, Gilbert proposed an equation describing the dynamic behavior of $\mathbf{M}$ which incorporated the collision damping incurred by the precessional motion, in an effective damping field term [40]. He assumed that the damping field is

$$\mathbf{H}_{damping}=-\eta\dot{\mathbf{M}} \tag{1.37}$$

where η is a damping constant with units such that $\eta\gamma M_s$ is dimensionless. Including this damping field in the simple gyromagnetic equation, we have

$$\dot{\mathbf{M}}=\gamma\mathbf{M}\times\left(\mathbf{H}-\eta\dot{\mathbf{M}}\right) \tag{1.38}$$

This is Gilbert's equation, and graphically visualized in Fig. 1.9.

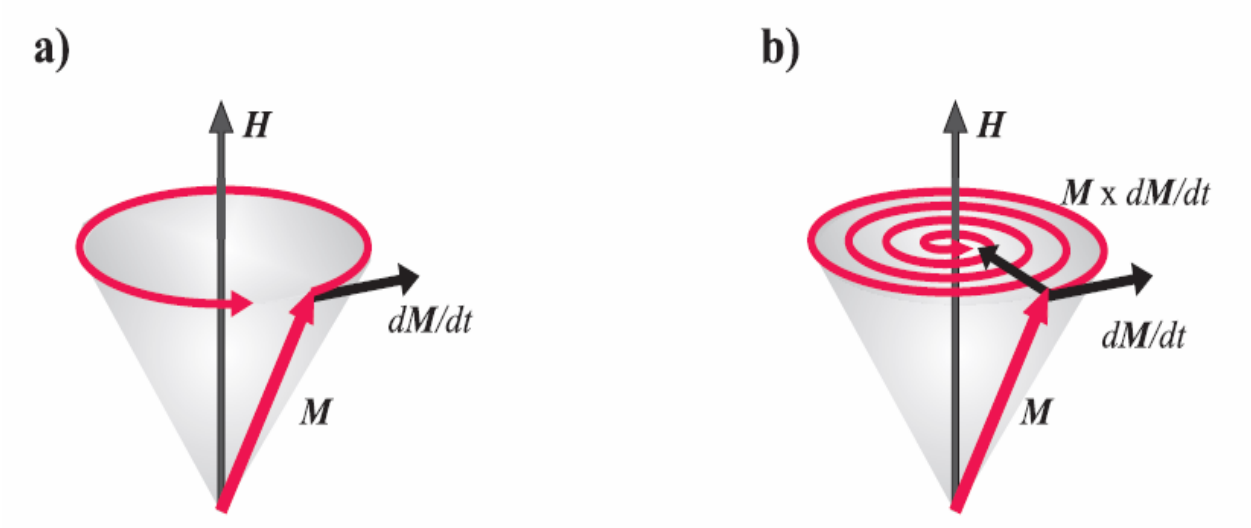

Figure 1.9. Magnetization torque without damping and with damping term

It is of interest to compare (1.38) with the Landau-Lifshitz equation (1.36). To do that, we will bring two equations to the same form and then compare their coefficients. The equation (1.38) can be rewritten as

$$\frac{\partial \mathbf{M}}{\partial t} = \gamma \mathbf{M} \times \mathbf{H} - \frac{\alpha}{M_s} \mathbf{M} \times \frac{\partial \mathbf{M}}{\partial t} \tag{1.39}$$

where $\alpha = \eta \gamma M_s$, and M_s is the magnitude of vector $\mathbf{M}$.

By substituting the equality $\mathbf{M} \times \mathbf{H} = \gamma^{-1} \left[\partial \mathbf{M} / \partial t + \left(\gamma \lambda / M_s^2 \right) \mathbf{M} \times \mathbf{H} \times \mathbf{M} \right]$ into the right-hand term in (1.36) and simplifying, the equation (1.36) can be rewritten as:

$$\frac{\partial \mathbf{M}}{\partial t} = \gamma^* \mathbf{M} \times \mathbf{H} - \frac{\alpha}{M_s} \mathbf{M} \times \frac{\partial \mathbf{M}}{\partial t} \tag{1.40}$$

where

$$\gamma^* = \gamma (1 + \alpha^2) \tag{1.41}$$

We observe that the damping terms in (1.39) and (1.40) are identical, the only difference between the two equations being that as the dimensionless damping parameter

α increases in the Landau-Lishitz form, the gyromagnetic ratio γ^* and, hence, the rate of precession of spin also increases. The difference between the two equations is small and ignorable when $\alpha^2 \ll 1$. The connection between these two equations also can be understood in graphical manner, which was performed by Mallison in 1987 [42].

It is convenient to rewrite the Gilbert equation (1.39) in the form of using the negative value of γ as mentioned above in (1.28)

$$\frac{\partial \mathbf{M}}{\partial t} = -|\gamma|\,\mathbf{M}\times\mathbf{H} + \frac{\alpha}{M_s}\mathbf{M}\times\frac{\partial \mathbf{M}}{\partial t} \tag{1.42}$$

This equation may be visualized easily upon the surface of a sphere or radius equal to $|\mathbf{M}|$. Applying the cross-product right-hand rule, the vector diagram can be shown in Fig. 1.10(a). From the figure 1.10(a), we have

$$tg\beta = \frac{\alpha\left|\dot{\mathbf{M}}\right|}{\left|\dot{\mathbf{M}}\right|} = \alpha \tag{1.43}$$

hence, $\cos\beta = \dfrac{1}{\sqrt{1+\alpha^2}}$, $\sin\beta = \dfrac{\alpha}{\sqrt{1+\alpha^2}}$

and $$\left|\frac{\partial \mathbf{M}}{\partial t}\right| = \left|\gamma\left(\mathbf{M}\times\mathbf{H}\right)\cos\beta\right| = \left|\frac{1}{\sqrt{1+\alpha^2}}\gamma\left(\mathbf{M}\times\mathbf{H}\right)\right| \tag{1.44}$$

Besides we have: $$\frac{\partial \mathbf{M}}{\partial t} = \left|\frac{\partial \mathbf{M}}{\partial t}\right|\cos\beta.\hat{u}_\varphi - \left|\frac{\partial \mathbf{M}}{\partial t}\right|\sin\beta.\hat{u}_\theta \tag{1.45}$$

Using (1.44), (1.45) becomes

$$\frac{\partial \mathbf{M}}{\partial t} = -\frac{1}{1+\alpha^2}|\gamma|\left(\mathbf{M}\times\mathbf{H}\right) - \frac{\alpha}{1+\alpha^2}|\gamma|\frac{\mathbf{M}}{M_s}\times\left(\mathbf{M}\times\mathbf{H}\right) \tag{1.46}$$

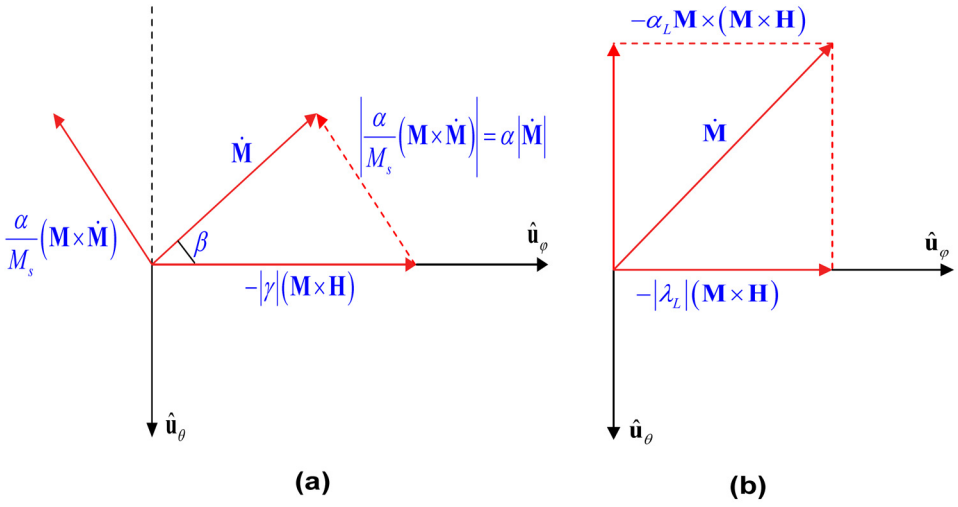

Figure 1.10. Graphical representation of the Landau-Liftshitz and Gilbert equations. (a) Vector diagram of Gilbert's equation (1.42). (b) Vector diagram of Landau-Liftshitz's equation (1.47).

Now if we put $|\gamma_L| = \dfrac{|\gamma|}{1+\alpha^2}$ and $\alpha_L = \alpha|\gamma_L|$ we can bring the equation (1.46) to the form of Landau-Liftshitz equation

$$\frac{\partial \mathbf{M}}{\partial t} = -|\gamma_L|(\mathbf{M}\times\mathbf{H}) - \frac{\alpha_L}{M_S}\left[\mathbf{M}\times(\mathbf{M}\times\mathbf{H})\right] \tag{1.47}$$

with the vector diagram shown in Fig. 1.10(b).

1.4.4 Numerical integration of LLG equation

The first studies of magnetization switching using the LLG equation were performed by Kikuchi [43]. An analytical solution was found for the magnetization switching of an isolated, isotropic, single domain sphere. In 1958, anisotropy was included in this calculation [44]. However, detailed solutions of the LLG equation require extensive numerical integration and have been feasible only since the mid-1990s due to the increase in computing power.

We shall now express the LLG equation in spherical polar coordinates $(r,\ \varphi,\ \theta)$, reducing Gilbert's equation to two differential equations, one in each of the angular variables φ and θ, which can be fully solved by computer. Starting from Gilbert equation (1.42) and using (1.41) or (1.46), the equation (1.42) can be rewritten as the form of Landau-Lifshitz equation, described as follows:

$$\frac{1+\alpha^2}{\gamma}\frac{\partial \mathbf{M}}{\partial t} = -\mathbf{M}\times\mathbf{H} - \frac{\alpha}{M_s}\left[\mathbf{M}\times\left(\mathbf{M}\times\mathbf{H}\right)\right] \tag{1.48}$$

Divided both sides this equation by M_s^2 to give

$$\frac{1+\alpha^2}{\gamma}\frac{1}{M_s}\frac{\partial}{\partial t}\left(\frac{\mathbf{M}}{M_s}\right) = -\left(\frac{\mathbf{M}}{M_s}\times\frac{\mathbf{H}}{M_s}\right) - \alpha\left[\frac{\mathbf{M}}{M_s}\times\left(\frac{\mathbf{M}}{M_s}\times\frac{\mathbf{H}}{M_s}\right)\right] \tag{1.49}$$

By writing $\tau = \frac{\gamma}{1+\alpha^2}M_s t$, $\mathbf{m} = \frac{\mathbf{M}}{M_s}$, and $\mathbf{h} = \frac{\mathbf{H}}{M_s}$, we can write the equation (1.49) in reduced (dimensionless) variables form as follows:

$$\frac{\partial \mathbf{m}}{\partial \tau} = -\mathbf{m}\times\mathbf{h} - \alpha\left[\mathbf{m}\times\left(\mathbf{m}\times\mathbf{h}\right)\right] \tag{1.50}$$

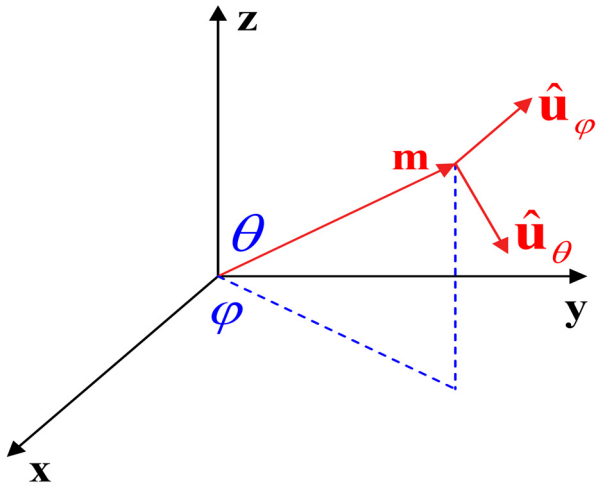

Figure 1.11. Magnetization vector $\mathbf{m}$ in spherical coordinates.

It is worth reminding that the reduced magnetic field **h** is the total effective field of the system. The *x*, *y*, *z* components of (1.50) can then be written

$$\begin{aligned}
\frac{\partial m_x}{\partial \tau} &= -\left(m_y h_z - m_z h_y\right) - \alpha\left[m_x\left(m_x h_x + m_y h_y + m_z h_z\right) - h_x\right] \\
\frac{\partial m_y}{\partial \tau} &= -\left(m_z h_x - m_x h_z\right) - \alpha\left[m_y\left(m_x h_x + m_y h_y + m_z h_z\right) - h_y\right] \\
\frac{\partial m_z}{\partial \tau} &= -\left(m_x h_y - m_y h_x\right) - \alpha\left[m_z\left(m_x h_x + m_y h_y + m_z h_z\right) - h_z\right]
\end{aligned} \tag{1.51}$$

Now it is convenient to express m_x , m_y, and m_z in terms of spherical coordinates $\left(\mathbf{m} = \left(\cos\varphi\sin\theta,\ \sin\varphi\sin\theta,\ \cos\theta\right)\right)$ as shown in Fig. 1.11. When these substitutions are made and the following equations are thus obtained

$$\frac{\partial \theta}{\partial \tau} = \mathbf{h}.\hat{u}_\varphi + \alpha\mathbf{h}.\hat{u}_\theta = h_\varphi + \alpha h_\theta \tag{1.52a}$$

$$\frac{\partial \varphi}{\partial \tau} = \frac{-\mathbf{h}.\hat{u}_\theta + \alpha\mathbf{h}.\hat{u}_\varphi}{\sin\theta} = \frac{-h_\theta + \alpha h_\varphi}{\sin\theta} \tag{1.52b}$$

where $\left(\hat{u}_\varphi = -\sin\varphi\hat{i} + \cos\varphi\hat{j},\ \hat{u}_\theta = \cos\theta\cos\varphi\hat{i} + \cos\theta\sin\varphi\hat{j} - \sin\theta\hat{k}\right)$.

The numerical simulations can be performed by integrating the two equations (1.52a) and (1.52b) using standard self-optimizing, embedded Runge-Kutta algorithm (see Appendix A for details).

1.5 Langevin dynamics – Stochastic LLG equation

Study of thermally activated processes in magnetic systems is currently an extremely important research topic not only from the fundamental point of view but also due to the miniaturization of magnetic devices such as heads and sensors, increasing

density of magnetic storage and development of novel magnetic technologies like MRAM. In all the cases the decreasing size of magnetic elements makes thermally activated processes extremely important because the activation barrier decreases with the volume of a magnetic unit whose magnetization should be reversed, thus setting fundamental limits on the smallest size of reliable magnetic devices.

The most straightforward way to study the system dynamics taking into account thermal fluctuations is by the solution of the corresponding stochastic (Langevin) equations. In this framework, the LLG equation becomes a stochastic differential equation which can be studied by using two approaches: Fokker-Planck equation [45] and Langevin dynamics [38]. The former allows one to study the transient evolution of the probability density function of magnetization, while the latter allows one to integrate directly the stochastic LLG equation to determine the realizations of the magnetization stochastic process. In the case of nonuniformly magnetized particles, the only applicable method is the Langevin approach which has indeed been widely used in micromagnetics, whereas the solution of the Fokker-Planck equation becomes unfeasible since one has to deal with a probability density defined on a space with very high dimensionality. On the other hand, the direct integration of the stochastic LLG equation is complicated by the fact that the random field appears as “multiplicative noise”, which leads to the so-called Ito-Stratonovich dilemama [45], [46]. The Forkker-Planck equation method is extremely lengthy to use, in practice, since it involves many mathematical manipulations, especially for rotation in three dimensions, Thus, in the framework of this dissertation, the stochastic Langevin-type, Landau-Lifshitz-Gilber equation will be discuss in detail.

1.5.1 Stochastic Landau-Lifshitz-Gilbert equation

Brown in 1963 [38] extended the LLG equation of motion to describe not the average but the specific behavior of the magnetization of an individual single domain ferromagnetic particle. He based his work on Langevin's approach to the theory of Brownian motion, which starts from the equation of motion of a Brownian particle in a fluid. In order to describe the magnetization behavior of an individual particle, the random fluctuations outlined by Langevin will be included. This can be achieved by augmenting the effective field with a Gaussian white noise random field, possessing statistical properties [47]. The resulting equation will called the stochastic Landau-Lifshitz-Gilbert equation, and reads

$$\frac{1+\alpha^2}{\gamma}\frac{\partial \mathbf{M}}{\partial t} = -\mathbf{M}\times\left(\mathbf{H}+\mathbf{H}_{fl}(t)\right) - \frac{\alpha}{M_s}\left[\mathbf{M}\times\left(\mathbf{M}\times\left(\mathbf{H}+\mathbf{H}_{fl}(t)\right)\right)\right] \tag{1.53}$$

This equation is obtained by augmenting a fluctuating or stochastic field term $\mathbf{H}_{fl}(t)$ to the effective field in the LLG equation (1.48). A fluctuating part $\mathbf{H}_{fl}(t)$ is characteristic of a Gaussian stochastic process with the following statistical properties:

$$< \mathbf{H}_{fl,i}(t) >= 0, \quad < \mathbf{H}_{fl,i}(t)\mathbf{H}_{fl,j}(t') >= 2D\delta_{ij}\delta(t-t') \tag{1.54}$$

where i and j are Cartesian indices, the constant D measures the strength of the thermal fluctuations, and $<>$ denotes an average taken over different realizations of the fluctuating field. The value of the constant D in thermodynamic equilibrium, related to the diffusion constant in the Fokker-Plank equation [48] can be derived from the fluctuation-dissipation theorem, leading to $D = \frac{\alpha k_B T}{M_S V \gamma}$, where V is the volume of the

nanoparticle. The Dirac δ expresses that above certain temperature the autocorrelation time of $\mathbf{H}_{fl}(t)$ is much shorter than the rotational-response time of the system ("white" noise), while the Kronecker δ expresses that the different component of $\mathbf{H}_{fl}(t)$ are assumed to be uncorrelated. It is customarily assumed that the fluctuating fields acting on different magnetic moments are independent.

For numerical integration purpose, it is now worthy rewriting (1.53) and (1.54) in dimensionless form by using $\tau = \frac{\gamma}{1+\alpha^2} M_s t$, $\mathbf{m} = \frac{\mathbf{M}}{M_s}$, $\mathbf{h} = \frac{\mathbf{H}}{M_s}$, and $\mathbf{h}_{fl} = \frac{\mathbf{H}_{fl}}{M_S}$, leading to

$$\frac{\partial \mathbf{m}}{\partial \tau} = -\mathbf{m} \times \left(\mathbf{h} + \mathbf{h}_{fl}(\tau)\right) - \alpha \left[\mathbf{m} \times \left(\mathbf{m} \times \left(\mathbf{h} + h_{fl}(\tau)\right)\right)\right] \tag{1.55}$$

and

$$< \mathbf{h}_{fl,i}(\tau) >= 0, \quad < \mathbf{h}_{fl,i}(\tau)\mathbf{h}_{fl,j}(\tau') >= \frac{2D}{M_S^2} \frac{\gamma M_S}{1+\alpha^2} \delta_{ij}\delta(\tau - \tau') \tag{1.56}$$

Put $D = \frac{\alpha k_B T}{M_S V \gamma}$ into (1.56), we have

$$< \mathbf{h}_{fl,i}(\tau)\mathbf{h}_{fl,j}(\tau') >= \frac{2\alpha k_B T}{(1+\alpha^2) M_S^2 V} \delta_{ij}\delta(\tau - \tau') \tag{1.57}$$

Apparently, for a given D, Eq. (1.55) fully determines the dynamical problem under consideration. Nevertheless, due to the vectors products of $\mathbf{m}$ and $\mathbf{h}_{fl}(\tau)$ occurring in this equation, the fluctuating field $\mathbf{h}_{fl}(\tau)$ enters in a multiplicative way. This gives rise to some formal problems, because for white multiplicative noise, any Langevin equation must be supplemented by an interpretation rule to properly define it. Two dominant interpretations, which lead to either the Itô or the Stratonovich stochastic calculus, are usually considered, yielding different dynamical properties of the systems [45], [46].

The choice of specific interpretations of the stochastic LLG equation imposes the use of specific numerical schemes for its integration. For instance, if one considers Eq. (1.55) in the sense of Stratonovich, one has to choose a numerical scheme that in the limit of time step $\Delta t \to 0$ converges to the Stratonovich solution. Analogously, in the sense of Itô, one has to choose specific numerical schemes converging to the Itô solution for $\Delta t \to 0$.

The Euler scheme and the simple implicit methods obviously converge to the Itô solution, the Heun and Milstein schemes can converge to the Stratonovich integral [49] and the Runge-Kutta schemes can converge to anything (including the cases in between) depending on the coefficients used there [50]. Most authors and commercial micromagnetic packages use the Heun and Runge-Kutta schemes or methods based on midpoint rule converging to the Stratonovich solution, simply because they are far more stable than the Euler method. The sections below will give more detail about the Heun scheme and other methods based on midpoint rule.

1.5.2 Heun scheme

Concerning the choice of the numerical integration scheme, one must keep in mind that the noise terms in Eq. (1.55) are multiplicative. Together with difficulties at the level of definition, the occurrence of multiplicative white noise in a Langevin equation entails some technical problem as well. Depending on the original deterministic scheme chosen, its naive stochastic translation might converge to an Itô solution, to a Stratovich solution, or to none of them [48].

Let us now consider the general systems of Langevin equations

$$\frac{dy_i}{dt} = A_i(y,t) + \sum_k B_{ik}(y,t) L_k(t), \tag{1.58}$$

where $\mathbf{y} = (y_1, .. y_n)$ (the variables of the system), and the "Lagenvin" sources $L_k(t)$ are (independent) Gaussian stochastic processes satisfying

$$\langle L_k(t) \rangle = 0, \quad \langle L_k(t) L_l(t') \rangle = 2D\delta_{kl}\delta(t-t') \tag{1.59}$$

The stochastic generalization of the deterministic Heun scheme is given as follow:

$$y_i(t+\Delta t) = y_i(t) + \frac{1}{2}\left[A_i(\tilde{\mathbf{y}}, t+\Delta t) + A_i(\mathbf{y},t)\right]\Delta t + \frac{1}{2}\left[B_{ik}(\tilde{\mathbf{y}}, t+\Delta t) + B_{ik}(\mathbf{y},t)\right]\Delta W_k, \tag{1.60}$$

where Δt is the discretization time interval, $\mathbf{y} = \mathbf{y}(t)$, the $\tilde{y}_i$ are Euler-type supporting values:

$$\tilde{y}_i = y_i(t) + A_i(\mathbf{y},t)\Delta t + \sum_k B_{ik}(\mathbf{y},t)\Delta W_k \tag{1.61}$$

and the $\Delta W_k = \int_t^{t+\Delta t} ds L_k(s)$ are Gaussian random numbers, the first two moments of which are

$$\langle \Delta W_k \rangle = 0, \quad \langle \Delta W_k \Delta W_l \rangle = (2D\Delta t)\delta_{kl} \tag{1.62}$$

By substituting $\tilde{y}_i$ from (1.61) into (1.60), we have

$$y_i(t+\Delta t) = \frac{1}{2}\left(\tilde{y}_i + y_i(t)\right) + \frac{1}{2} A_i\left(\tilde{\mathbf{y}}, t+\Delta t\right)\Delta t + \frac{1}{2}\sum_k B_{ik}\left(\tilde{\mathbf{y}}, t+\Delta t\right)\Delta W_k \tag{1.63}$$

The stochastic Heun scheme (1.60) converges in quadratic mean to the solution of the general system of stochastic differential equations (1.58) when interpreted in the sense of Stratonovich [50]. On the other hand, if one uses the Euler-type Eq. (1.61) as the numerical integration scheme [by identifying $y_i(t+\Delta t) = \tilde{y}_i$], the constructed trajectory converges to the Itô solution of the same system of equations (1.58) [50].

The integration of the stochastic LLG equation is performed by starting from a given initial configuration, and updating recursively the state of the system, $\mathbf{m}(t) \to \mathbf{m}(t+\Delta t)$, by means of the set of finite-difference equations (1.60). This generates stochastic trajectories from which, when required, averages are directly computed. The Gaussian random numbers required to simulate the ΔW_k occurring in (1.60) are constructed from uniformly distribution functions.

1.5.3 Midpoint numerical technique

The (implicit) midpoint numerical technique is another approach in dealing with the stochastic LLG equation. The midpoint method is unconditionally stable, consistent with the Stratonovich calculus, preserves the fundamental properties of LLG dynamics and has been widely used in many micromagnectics packages [51-53]. We now proceed to derive the full numerical investigations of LLG equations by applying the mid-point rule technique. Let us start our discussion by writing the stochastic LLG equation (1.55) in terms of spherical coordinates as shown in Eqs. (1.52a) and (1.52b), leading to

$$\frac{\partial \theta}{\partial \tau} = \left(\mathbf{h} + \mathbf{h}_{fl}\right).\hat{u}_{\varphi} + \alpha\left(\mathbf{h} + \mathbf{h}_{fl}\right).\hat{u}_{\theta} = h_{\varphi} + h_{fl,\varphi} + \alpha\left(h_{\theta} + h_{fl,\theta}\right) \tag{1.64a}$$

$$\frac{\partial \varphi}{\partial \tau} = \frac{-\left(\mathbf{h} + \mathbf{h}_{fl}\right).\hat{u}_{\theta} + \alpha\left(\mathbf{h} + \mathbf{h}_{fl}\right).\hat{u}_{\varphi}}{\sin\theta} = \frac{-\left(h_{\theta} + h_{fl,\theta}\right) + \alpha\left(h_{\varphi} + h_{fl,\varphi}\right)}{\sin\theta} \tag{1.64b}$$

The second-order accurate midpoint rule simply states that:

$$\left(\frac{d\mathbf{M}}{dt}\right)^{(i+1/2)} = \frac{\mathbf{M}^{(i+1)} - \mathbf{M}^{(i)}}{\Delta t} + O\left(\Delta t^2\right), \tag{1.65}$$

$$\mathbf{M}^{(i+1/2)} = \frac{\mathbf{M}^{(i+1)} + \mathbf{M}^{(i)}}{2} + O\left(\Delta t^2\right) \tag{1.66}$$

where subscripts (i) denote quantities computed at time instants t_i of the temporal uniform mesh $t_1,\ t_2,\ t_3 \ldots$ with $\Delta t = t_{i+1} - t_i$. Accordingly, superscripts $(i+1/2)$ denotes quantities computed at mesh mid point $t_{(i+1/2)} = t_i + \Delta t/2$. In addition, we use the notation $O\left(\Delta t^2\right)$ to denote the terms of the second order of smallness with respect to Δt. Let us now apply the midpoint scheme and neglecting $O\left(\Delta t^2\right)$ to the two equations for spherical components of $\mathbf{M}^{(i+1)}$ in (1.64a) and (1.64b), leading to

$$\theta^{(n+1)} - \theta^n - \Delta t\left[\alpha\left(h_\theta + h_{fl,\theta}\right) + \left(h_\varphi + h_{fl,\varphi}\right)\right] = 0 \tag{1.67}$$

$$\varphi^{(n+1)} - \varphi^n - \frac{\Delta t}{\sin\dfrac{\theta^{(n+1)} + \theta^n}{2}}\left[-\left(h_\theta + h_{fl,\theta}\right) + \alpha\left(h_\varphi + h_{fl,\varphi}\right)\right] = 0 \tag{1.68}$$

where $h_\theta = h_\theta\left(\dfrac{\theta^{(n+1)} + \theta^n}{2}, \dfrac{\varphi^{(n+1)} + \varphi^n}{2}, t^n + \dfrac{\Delta t}{2}\right)$, and $h_\varphi = h_\varphi\left(\dfrac{\theta^{(n+1)} + \theta^n}{2}, \dfrac{\varphi^{(n+1)} + \varphi^n}{2}, t^n + \dfrac{\Delta t}{2}\right)$.

As far as the solutions of the time-stepping Eqs. (1.67) and (1.68) are concerned, they can be obtained by using Newton-Raphson (NR) algorithm for the equations $\mathbf{F}_1\left(\theta^{(n+1)}\right) = 0$, and $\mathbf{F}_2\left(\varphi^{(n+1)}\right) = 0$ where

$$\mathbf{F}_1 = \theta^{(n+1)} - \theta^n - \Delta t\left[\alpha\left(h_\theta + h_{fl,\theta}\right) + \left(h_\varphi + h_{fl,\varphi}\right)\right] = 0, \tag{1.69}$$

and

$$\mathbf{F}_2 = \varphi^{(n+1)} - \varphi^n - \frac{\Delta t}{\sin\dfrac{\theta^{(n+1)} + \theta^n}{2}}\left[-\left(h_\theta + h_{fl,\theta}\right) + \alpha\left(h_\varphi + h_{fl,\varphi}\right)\right] = 0 \tag{1.70}$$

To this end, we must derive the Jacobian matrix of these equations J_F of the vector function $\mathbf{F}$ at each iteration step.

Up to this point, the midpoint method presented above is applied to the stochastic LLG equation concerning the thermal effects of the system consisting of non-interacting magnetic moments. In fact, the use of the midpoint rule to devise the numerical schemes that preserve invariants (e.g., magnetization, energy, angular momentum, etc.) of dynamical systems has been extensively explored in the area of micromagnetic simulations [52, 53]. To start discussion of using midpoint scheme in full 3D micromagnetics dynamical problem, let us assume that the magnetic body has been subdivided in N cells or finite elements. We shall denote the magnetization vector associated with the *k*-th cell by $\mathbf{m}_k(t) \in R^3$, and the collection of all vectors $\mathbf{m}_k(t)$ by the vector $\underline{\mathbf{m}} = \begin{pmatrix} \mathbf{m}_1 \\ . \\ . \\ . \\ \mathbf{m}_N \end{pmatrix}$.

Analogous notation are used for the effective field $\mathbf{h}$ and the magnetization angles θ and φ. The midpoint rule in (1.65) and (1.66) is applied to all N elements, as consequence, we have to solve a systems of 2N nonlinear equations in the 2N unknown $\underline{\theta}^{(n+1)}$, and $\underline{\varphi}^{(n+1)}$. To find solution of this system of equations, the Newton-Raphson (NR) algorithm is still applied for the equations $F_1^n\left(\underline{\theta}^{(n+1)}\right) = 0$ and $F_2^n\left(\underline{\varphi}^{(n+1)}\right) = 0$. The main difficulty in applying NR method is that the Jacobian J_F^n is a full matrix, due to the long-range character of magnetostatic interactions between elements. The inversion of the matrices J_F^n at each NR iteration would lead to an exceedingly high computational cost.

1.6 LLG micromagnetic dynamics

The analysis of magnetization dynamics in nanoscale ferromagnetic bodies is a very important issue from both scientific and technological points of views. A ferromagnetic body is a complex nonlinear system which may exhibit a very rich variety of dynamical behaviors including bifurcations, metastability, nonlinear resonances, quasi-periodic dynamics and spatio-temporal chaos [53]. Magnetization dynamics and relaxation, on the other hand, is one of the fundamental problems in modern magnetic storage technologies. The general method to study magnetization dynamics is to solve the LLG equation by suitable numerical methods. As we have mentioned so far in the previous section, the well-known midpoint rule time-stepping has been successfully used for accurate micromagnetic simulations. In the following, we will discuss the full numerical technique for solving LLG dynamics in micromagnetic systems.

Let us start the discussion by subdividing the magnetic body into a collection of rectangular prism with edges parallel to the coordinate axes. The edges lengths are $d_x,\ d_y,\ d_z$. In this framework, it is convenient to identify each cell by three indices i, j, k. The magnetization $\mathbf{m}_{i,j,k}$ is assumed to be uniform within the generic (i,j,k) cell. With this notation, the effective field in the generic (i,j,k) cell, which consists of the exchange, anisotropy, demagnetizing, external applied and thermal fluctuating fields, can be expressed as:

$$\mathbf{h}_{i,j,k} = \mathbf{h}_{ex;i,j,k} + \mathbf{h}_{m;i,j,k} + \mathbf{h}_{an;i,j,k} + \mathbf{h}_{applied;i,j,k} + \mathbf{h}_{fl;i,j,k} \tag{1.71}$$

where $\mathbf{h}_{ex};i,j,k$ is the exchange field, $\mathbf{h}_{m;i,j,k}$ is the magnetostatic field, and $\mathbf{h}_{an;i,j,k}$ is the anisotropy field.

The exchange field $\mathbf{h}_{ex;i,j,k}$ can be computed by means of a 7-point laplacian discretization, which is second order accurate in space. In the generic "internal" cell (i,j,k), it can be expressed as follows:

$$\mathbf{h}_{ex;i,j,k} = \frac{2A}{M_S^2}\left[\frac{\mathbf{m}_{i+1,j,k}+\mathbf{m}_{i-1,j,k}}{d_x^2}+\frac{\mathbf{m}_{i,j+1,k}+\mathbf{m}_{i,j-1,k}}{d_y^2}+\frac{\mathbf{m}_{i,j,k+1}+\mathbf{m}_{i,j,k-1}}{d_z^2}\right.$$

$$\left.-\left(\frac{2}{d_x^2}+\frac{2}{d_y^2}+\frac{2}{d_z^2}\right)\mathbf{m}_{i,j,k}\right] \tag{1.72}$$

A similar expression holds for the boundary cells, where the Neumann boundary condition $\frac{\partial \mathbf{m}}{\partial \mathbf{n}} = 0$ with $\mathbf{n}$ the outward normal to the boundary of the magnetic body, taken into account. The magnetosatic field $\mathbf{h}_{m;i,j,k}$, which is simply a discrete convolution of the demagnetizing tensor and the magnetization, can be expressed as:

$$\mathbf{h}_{m;i,j,k} = \sum_{i'}\sum_{j'}\sum_{k'} N(i',j',k')\mathbf{m}_{i-i',j-j',k-k'} \tag{1.73}$$

where $N(i',j',k')$ is the demagnetizing tensor which describes the contribution of the magnetization $\mathbf{m}_{i-i',j-j',k-k'}$ in the source cell specified by indices $i-i', j-j', k-k'$ and can be expressed analytically. The discrete convolution (1.73) is computed by means of 3D Discrete Fast Fourier Transform (DFFT). The DFT of convolution is applicable to non-periodic, i.e., isolated structures by using zero-padding technique [54].

As far as the anisotropy is concerned, we assume that the anisotropy field is

$$\mathbf{h}_{an;i,j,k} = \frac{2K_1}{M_S^2}(\mathbf{m}_{i,j,k}.\mathbf{e}_{an})\mathbf{e}_{an} \tag{1.74}$$

where $\mathbf{e}_{an}$ is the easy axis unit-vector.

The midpoint rule time discretization technique, which is discussed in section 1.5.3, then will be applied to the numerical integration of dynamic LLG equations. It is of important to keep in mind that the most time-consuming procedure in micromagnetic simulations is the calculation of the demagnetizing field, which is proportional to the square of the number of the cells in the computing region.

Chapter 2

Static Critical Curve

The problem of determining the orientation of a magnetic moment subject to an applied field in the presence of uniaxial anisotropy energy was firstly investigated theoretically by Stoner and Wohlfarth, in two dimensions (2D) as mentioned previously. Despite the simplicity of the SW model, the problem of magnetization by coherent rotation in the case of arbitrary anisotropy energy cannot in general be solved analytically. In 1956, Slonczewski proposed a geometrical solution, which became known as the astroid method [12]. The name comes from the critical curve for the simplest case of the model – the uniaxial case, when the shape and the surface energy are neglected and the magnetocrystalline anisotropy is considered to be uniaxial. The derivation of Slonczewski applies in fact to any anisotropy function in 2D case. André Thiaville later in his 1998 paper performed further development of this method and made it applicable in 3D case [13].

The critical curve, therefore, plays an important role in investigating static magnetic behavior of magnetic materials that are part of new data storage devices. Moreover, the critical curve is essential in the operation of newer magnetic memories such as magnetic random access memory (MRAM), which is an emerging memory

technology and, if successful, will be the most popular memory in the future and the first in a number of magnetoelectric, or ‘spintronic”, devices in wide use [3].

This chapter is divided into three main parts. The first part presents briefly the working principles of MRAM and how the critical curve plays a significant role in MRAM technology. The astroid and the influence of the second anisotropy constant on the shape of the critical curve are given later in the second part. In the third part, a new experimental method to determine the critical curve is proposed.

2.1 The role of critical curve in MRAM

With the widespread development of portable digital electronic and wireless communication devices, the increasing demand for solid-state memories continues unabated. Among new memory devices in progress, a new technology, magnetoresistive random access memory (MRAM) based on magnetic tunnel junction (MTJ) effect has the potential to be competitive and to become “the most amazing memory device” in the future [3, 55]. The key attributions of MRAM technology are “nonvolatility” combined with the high-speed operation and effectively unlimited read-write endurance.

In traditional MRAM, each magnetic element or memory cell uses a magnetic tunnel junction (MTJ) device, which is composed of a fixed magnetic layer, a thin dielectric tunnel barrier, and a free magnetic layer. The MTJ element has a low resistance when the magnetic moment of the free layer is parallel to the fixed layer and a high resistance when the free layer moment is oriented anti-parallel to the fixed layer moment.

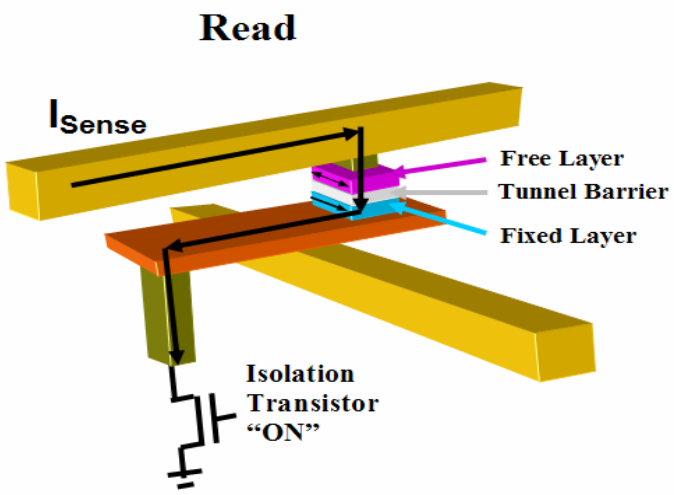

Figure 2.1. MRAM read operation [55].

The corresponding logic state (*'0'* or *'1'*) of the memory is hence defined by its resistance state (low or high), monitored by a small current as shown in Fig. 2.1.

The elements are arranged on a square grid. Data are then written by passing currents through electrical tracks positioned above and below the elements, called the word lines and bit lines (or digit lines) (see Fig. 2.2).

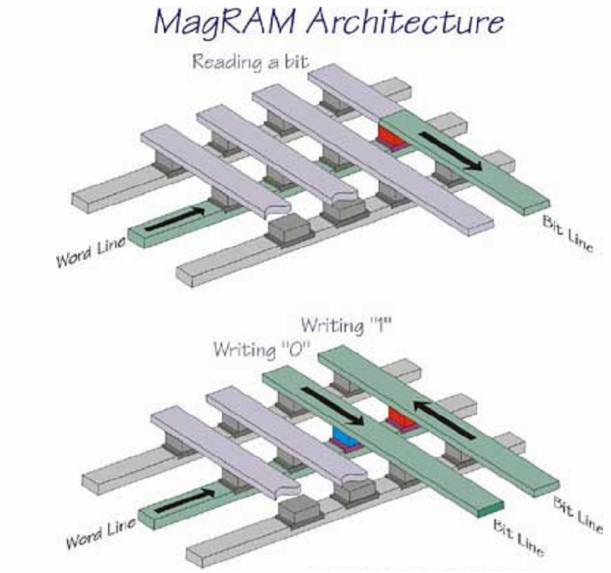

Figure 2.2. MRAM writing operation [55].

A current following along a planar track generates a magnetic field in the plane of the track, perpendicular to the direction of flow of current. Unfortunately, this field is generated along the entire length of the conductor, and so a subtle trick is employed to write data selectively to one specific magnetic element in the memory array. The trick bases on the fact that the strength of the magnetic field required to reverse the magnetization of the free layer in an element (and hence write a new data) is a function of the direction in which that field is applied. The relationship between the strength of the field required writing the magnetization and the direction of the field is given by the Stoner-Wohlfarth model. The significant point of this model is that when the total applied field made up from an *x*-component (bit line component), H_x, and a *y*-component (word line component), H_y, falls inside of the SW astroid, then no switching of magnetization observed, corresponding to no data writing occurred; if, on the other hand, the $\left(H_x, H_y\right)$ combination falls outside of the SW astroid, then the switching behavior of magnetization will occur, corresponding to the data writing observed. The figure 2.3 shows the important regions for MRAM operation in which application of either H_x or H_y by itself will not result in writing, while a simultaneous application of the two will result in writing. Here is the ability to select a single element from an array; all of the elements underneath the bit line ("half-select") will experience H_x and all of the elements underneath the word line ("half-select") will experience H_y, but only the single element at the intersection of the word and bit lines ("full-select") will experience both H_x and H_y, and so it is to only this element that data will be written [3, 56].

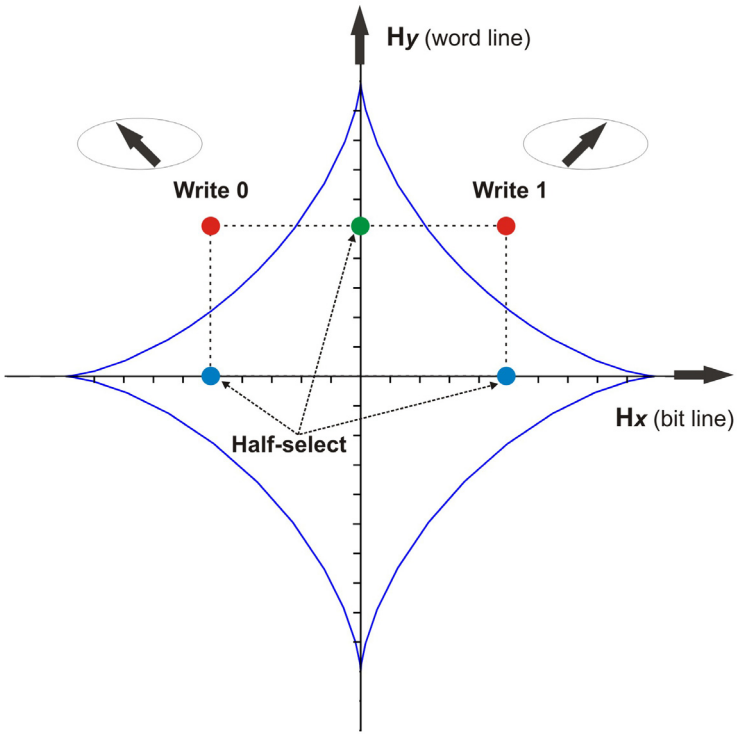

Figure 2.3. Ideal critical curve plot describing the switching of the free layer in MRAM cells. Combinations of H_x and H_y that line within the astroid do not cause switching, while those that lie outside of the astroid do [56].

The astroid shown in Fig. 2.3 is ideal, as in SW model. The real shape and size of the astroid are dependent upon the shape, size, and other properties of the MTJ.

Based on all analysis above, it is obvious that the critical curve plays an essential role in MRAM writing operation. Therefore, it is of important to understand the magnetization SW reversal not only for its evident fundamental interest but also due to the big impact on the MRAM technology.

2.2 Complex critical curve with quartic crystalline anisotropy

Up to this point we have discussed about the ideal case of critical curves related to K_1 (uniaxial anisotropy) as described in the section 1.2.2 and its application in MRAM

writing operation above. The role of the second anisotropy constant K_2 has been totally disregarded. Indeed, K_2 greatly exceeds K_1 for certain situations, such as for Co, a common magnetic material. Moreover, when the direction of magnetization rotates away from the easy axis, the contribution from the second anisotropy energy becomes important [57]. The complicated behavior corresponding to the complex forms of critical curves, as sketched in Fig. 2.4, is found when the second anisotropy energy is considered. Clearly, as one can see from the figure 2.4, comparing to the astroid, the critical curves have more vertices, as well as extra cusps.

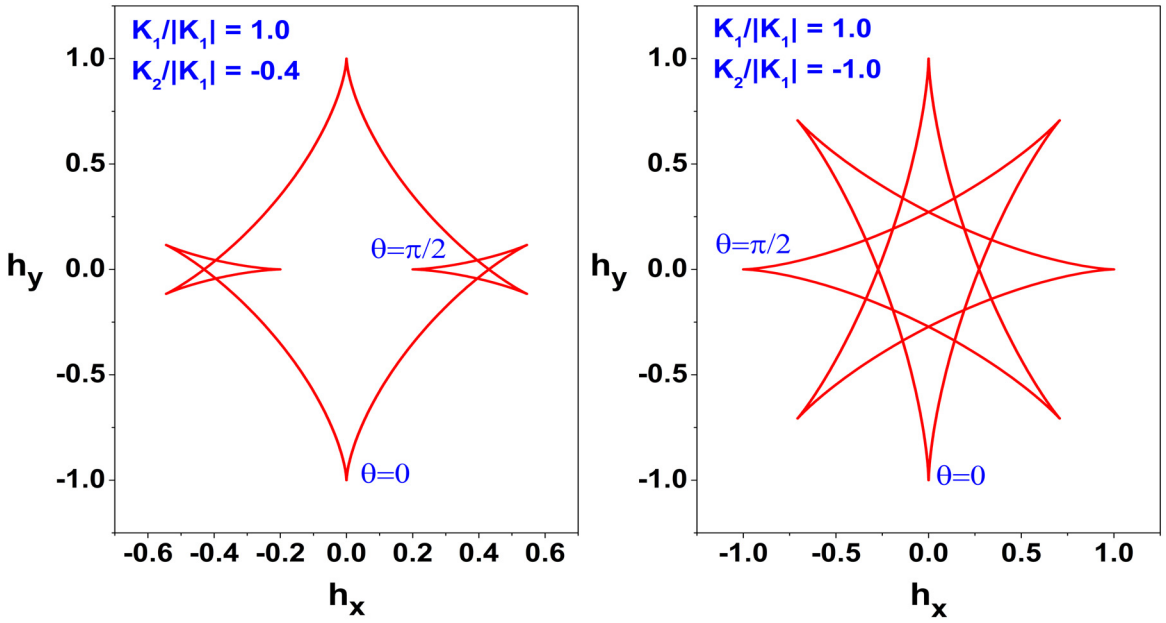

Figure 2.4. Illustration of some complicated critical curves.

As mentioned in the preceding chapter, by drawing all possible tangents to the simple astroid curve, one can obtain the hysteresis loop describing the behavior of magnetic materials, but this is not a general method. The problem was face is due to the fact that disadvantage of obscuring the drawings of many half stable tangents in the case

of complex critical curves. Thus, that method no longer can be applied in this situation. An alternative general method of using critical curves was presented by Thiaville [13], by simply orienting the critical curve, as described below. First, we will express again the free energy density function in a slightly different way with respect to the one in the SW model:

$$W(\mathbf{h}) = E(\mathbf{m}) - 2\mathbf{h}.\mathbf{m} \tag{2.1}$$

The vector $\mathbf{m}$ is normalized to the saturation magnetization M_s ($\mathbf{m} = \mathbf{M}/M_s$), $E(\mathbf{m})$, in general, is the anisotropy energy density divided by its constant K_1, and $\mathbf{h}$ is the reduced applied field defined as $\mathbf{h} = \mathbf{H}/H_K$, where $H_K = 2K_1/M_s$ is the anisotropy field. In unitarity condition, $\mathbf{m}$ is implemented by writing $\mathbf{m} = (\sin\theta,\ \cos\theta)$. Thus, $\frac{d\mathbf{m}}{d\theta} = \mathbf{e} = (\cos\theta,\ -\sin\theta)$ are the orthogonal vectors. The extremum condition of the energy function in (2.1) and its second derivative respectively are:

$$E' - 2\mathbf{h}.\mathbf{e} = 0 \tag{2.2}$$

$$\frac{d^2W}{d\theta^2} = E'' + 2\mathbf{h}.\mathbf{m} \tag{2.3}$$

Denoting the critical field by $\mathbf{h}_0$, one finds immediately from (2.2) and (2.3) that

$$\mathbf{h}_0 = (E'\mathbf{e} - E''\mathbf{m})/2 \tag{2.4}$$

Deriving the equation (2.4) with respect to θ, one finds

$$\frac{d\mathbf{h_0}}{d\theta} = -\frac{1}{2}\frac{d}{d\theta}(E + E'')\mathbf{m} \tag{2.5}$$

Now, Thiaville's theory stated that the critical curve is oriented in such a way that $\mathbf{h}_0$ always moves in the direction of vector $\mathbf{m}$. The orientation will reverse at the points where $(E+E'')$ has an extremum, positions which are the cusps of the critical curve. The orientation of the tangents, if taken to follow that of the critical curve, defines directly the stable half tangents. The tangents for which point H (the extremity of the vector $\mathbf{h}$ drawn from the origin) is on the stable half then define the stable solutions. If H is on the unstable part of a tangent this solution is unstable too and it corresponds to a local energetic maximum. Furthermore, for a stable solution the magnetic moment $\mathbf{m}$ points towards H whereas it points in the opposite direction in the unstable cases.

We shall now be ready to study the magnetization process of magnetic materials in the case of quartic crystalline anisotropy, as shown in detail below. This work was first performed by Ching-Ray Chang in 1990 [57].

The magnetic free energy per unit volume can be written as the sum of the energy due to crystalline anisotropy, shape anisotropy, and Zeeman energy as follows:

$$W = W_K + W_D + W_H \tag{2.6}$$

The shape anisotropy energy can be combined with the crystal anisotropy energy ($W_K = K_1^0 \sin^2\theta + K_2 \sin^4\theta$, with θ the angle between the magnetization and uniaxial anisotropy axis – *c*-axis (see Fig. 2.5)), by replacing the anisotropy constant $K_1 = K_1^0 + \frac{1}{2}\left(N_\perp - N_\parallel\right)M_s^2$ where $N_\perp$ is the demagnetization factor perpendicular to the easy axis and $N_\parallel$ is the demagnetization factor parallel to the easy axis.

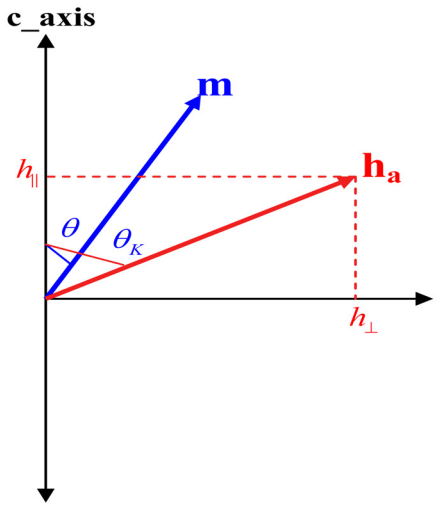

Figure 2.5. Vector diagram corresponding to a uniaxial anisotropy magnetic particle subjected to an external field.

Table 2.1. The values of K_1 and K_2 are used for eight different regions in Figs. 2.6, 2.7, and 2.8.

Region	Range	K_1	K_2
I	$0 \le 4K_2 \le K_1$	1.0	0.2
II	$0 \le K_1 \le 4K_2$	1.0	1.0
III	$K_1 \le -6K_2 \le 0$	-1.0	0.1
IV	$K_1 \ge -6K_2 \ge 0$	1.0	-0.1
V	$-6K_2 \le K_1 \le -2K_2 \le 0$	-1.0	0.4
VI	$-6K_2 \ge K_1 \ge -2K_2 \ge 0$	1.0	-0.4
VII	$-2K_2 \le K_1 \le 0$	-1.0	1.0
VIII	$-2K_2 \ge K_1 \ge 0$	1.0	-1.0

Putting $k_2 = \dfrac{K_2}{K_1}$ and following the same way as we did in section 1.2.1, we may rewrite (2.6) in the dimensionless form:

$$W = \frac{1}{2}\sin^2\theta + \frac{1}{2}k_2\sin^4\theta - \frac{h_{\perp}K_1}{|K_1|}\sin\theta - \frac{h_{\parallel}K_1}{|K_1|}\cos\theta \qquad (2.7)$$

Therefore, the equation for critical curve is given by:

$$h_{\perp} = 6k_2 \sin^5\theta + (1-4k_2)\sin^3\theta \tag{2.8a}$$

$$h_{\parallel} = 6k_2 \cos^5\theta + (-1-6k_2)\cos^3\theta \tag{2.8b}$$

and the equation for obtaining the cusp points by:

$$\left(\frac{15}{2}\sin(4\theta) - 3\sin(2\theta)\right)k_2 - 3\sin(2\theta) = 0 \tag{2.9}$$

The modified critical curves of different ranges obtained by (2.8a) and (2.8b), corresponding to eight different regions generated by the values of K_1 and K_2 in the table 2.1, are shown in Fig. 2.6. The critical curve orientation given by the arrows in Fig. 2.6 indicates the stable half tangents that corespond to the stable equilibrium orientations of the magnetization vector. The change in the shape of the critical curve and especially the occurrence of the extra cusps is of crucial importance in determination of a qualitative change in the switching behavior of the system. The direction of the applied field will cross the critical curve at points that correspond to field values at which the magnetization reversals (Barkhausen jumps) occur. In order to find new stable orientation of magnetization after jump, one has to follow the Thiaville's theory, traveling along the critical curve in the sense given by its orientation up to a point where the stable half tangent passes through the jump point. The figure 2.7 represents the different hysteresis loops in each of the eight regions, which are characterized by different orientations $\theta_K = 0^0,\ 30^0,\ 60^0$, and 90^0 between the applied field and the easy axis. The corresponding transverse susceptibility curves, which are derived from Eq. (1.24), for the decreasing field are shown in Fig. 2.8.

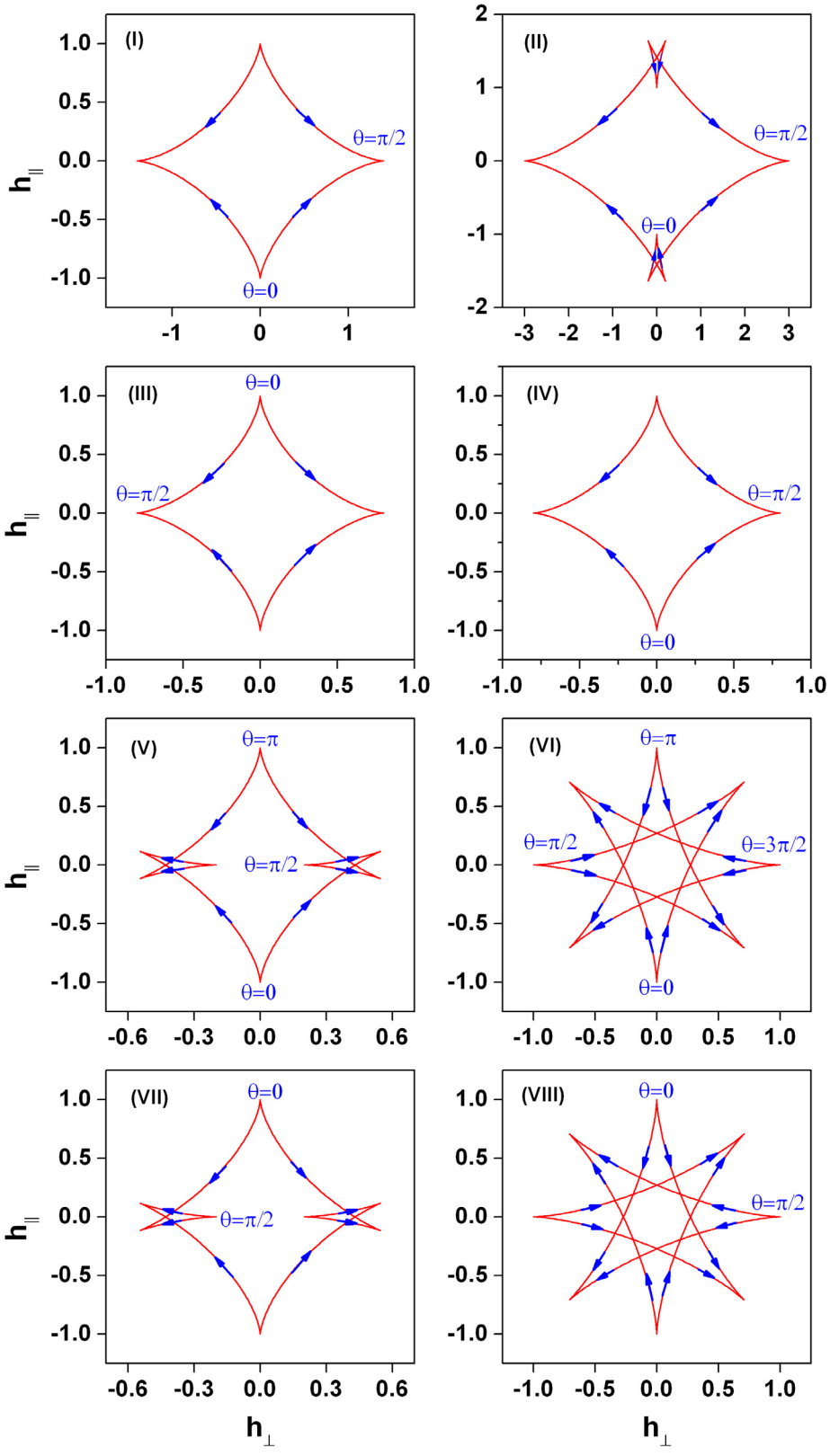

Figure 2.6. The complex critical curves in eight regions corresponding to table 2.1.

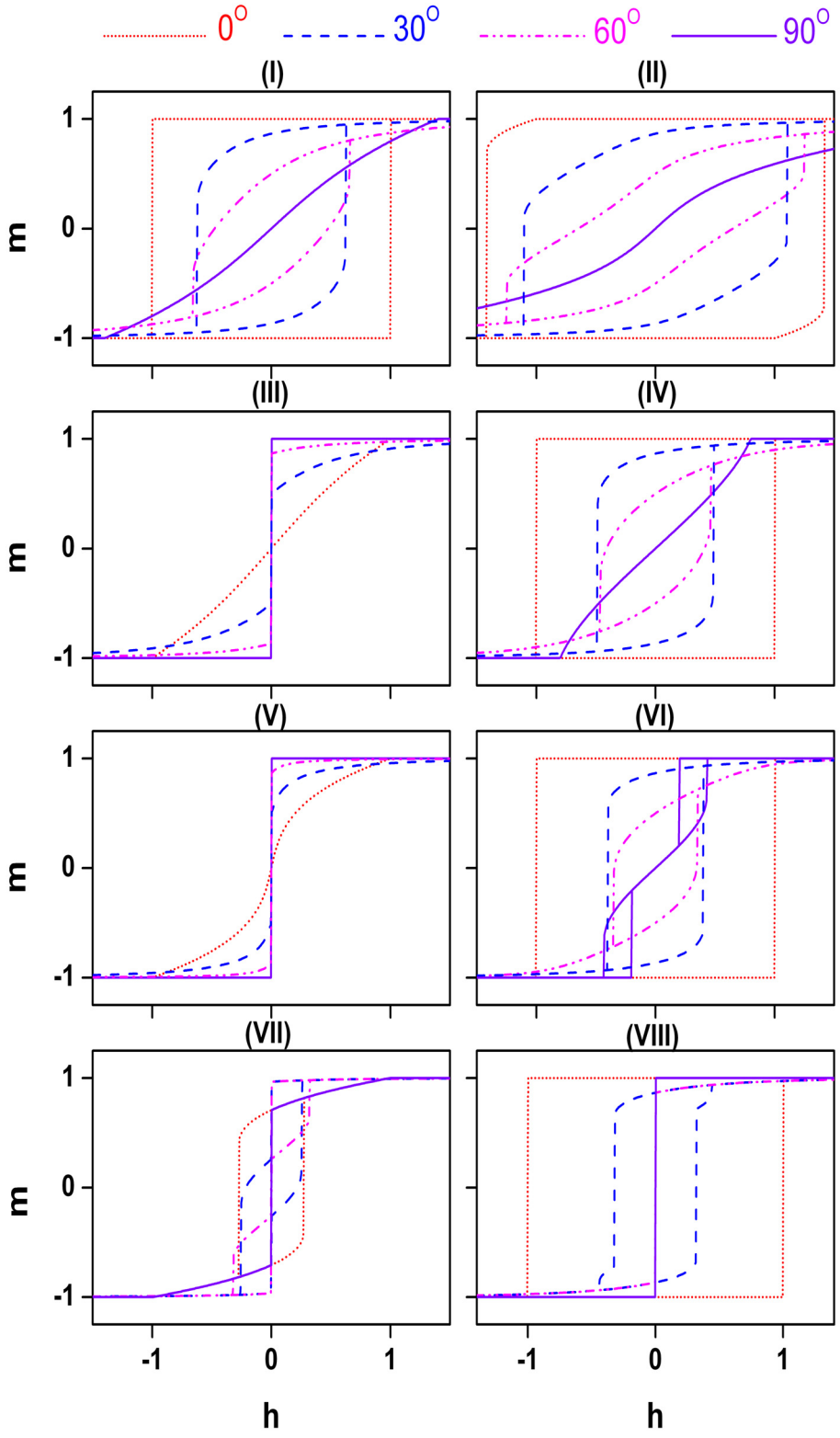

Figure 2.7. Hysteresis loops in eight regions corresponding to table 2.1, for four orientations of the applied field.

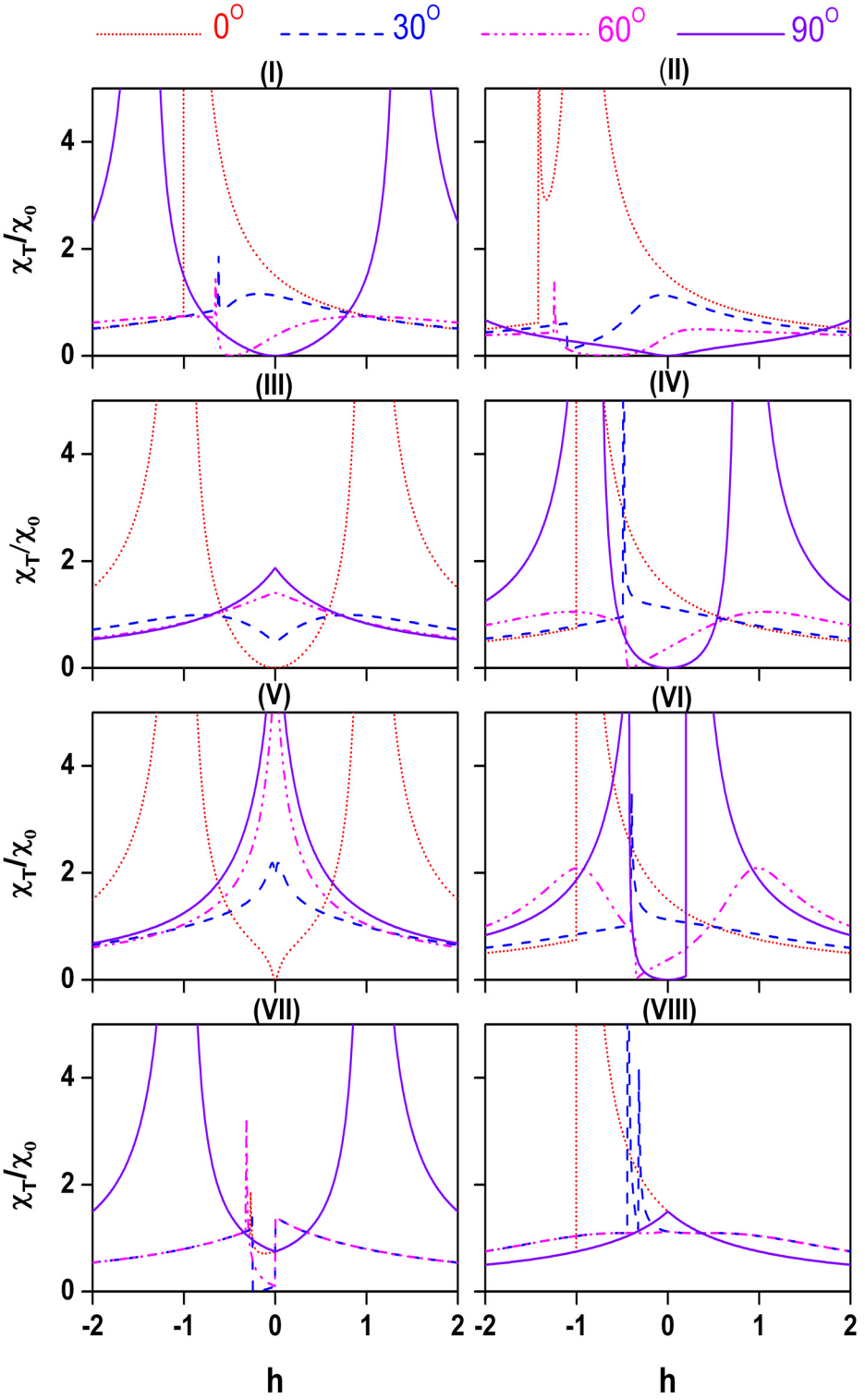

Figure 2.8. Transverse susceptibility curves in the case of decreasing field, in eight regions corresponding to table 2.1, for four orientations of the applied field.

As it can be seen in Fig. 2.8, the TS curve shape is changed dramatically with the variation of the value of k_2 for both negative and positive of K_1. The appearance of supplementary peaks in the TS curves in certain cases is associated with the existence of additional Barkhausen jumps in the corresponding hysteresis loops.

Below we will discuss in detail how the different shapes of the critical curves (Fig. 2.6) affect the corresponding hysteresis loops (Fig. 2.7) and TS curves (Fig. 2.8) for each region.

A. Region I

Because the value of K_1 is positive and significantly greater than K_2, the hysteresis loops are similar to those obtained by SW model. The only contribution from K_2, basically, is a contraction of the astroid along $h_\perp$.

B. Region II

The astroid is modified with the appearance of some extra cusps along the easy axis. A suitable tangent can still be constructed, however, similar to region I. The only change here is that the extra cusps make the hysteresis loops round out their sharp corners. Thus, there is no square hysteresis loop, even for the easy axis direction.

C. Region III

Since the value of K_1 is negative, the *c*-axis becomes the hard axis whereas the plane perpendicular to *c*-axis through the origin is an easy plane. When the absolute value of the applied field is infinitesimally small, the moment vector can freely move in the easy plane along the direction which can reduce the Zeeman energy. Thus, the

discontinuities in the magnetization can be observed at $h=0$, and there is no hysteresis (see Fig. 2.9).

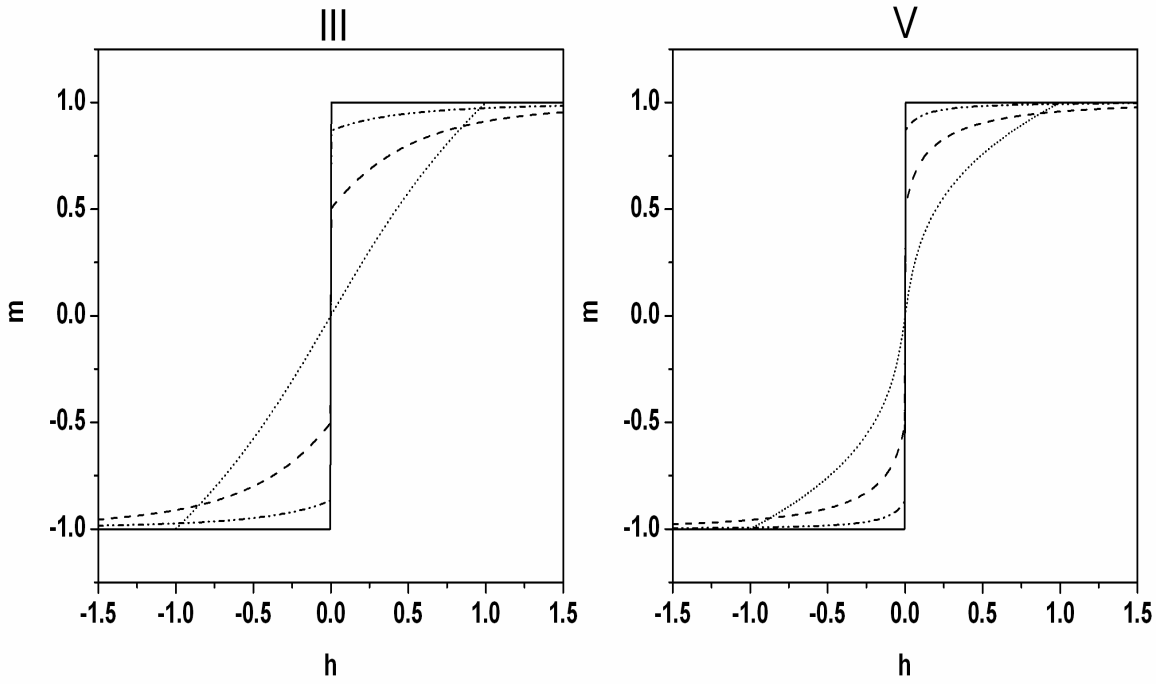

Figure 2.9. The behavior of magnetization in region III and V. Discontinuities in the magnetization occur at $h=0$.

D. Region IV

One can easily see that the behavior of magnetization in region IV is similar to region I. The only small change is the compression in the hard direction of the astroid.

E. Region V

The same arguments in region III can be applied in this region. The only difference between these two regions is the modified astroid (see Fig. 2.9).

F. Region VI

Although the shape of the astroid curve in this region is exactly the same as the curve from region V, the angle θ differs in the two regions. When the applied field is not

crossing the extra cusps, the hysteresis loop is similar to the SW results. For a field crossing the extra cusps as in the case $\theta_K = 90^0$, the complicated hysteresis loop related to the additional Barkhausen jump will be obtained as shown on the top in Fig. 2.10. On the bottom of this figure are the corresponding TS curves with supplementary peaks.

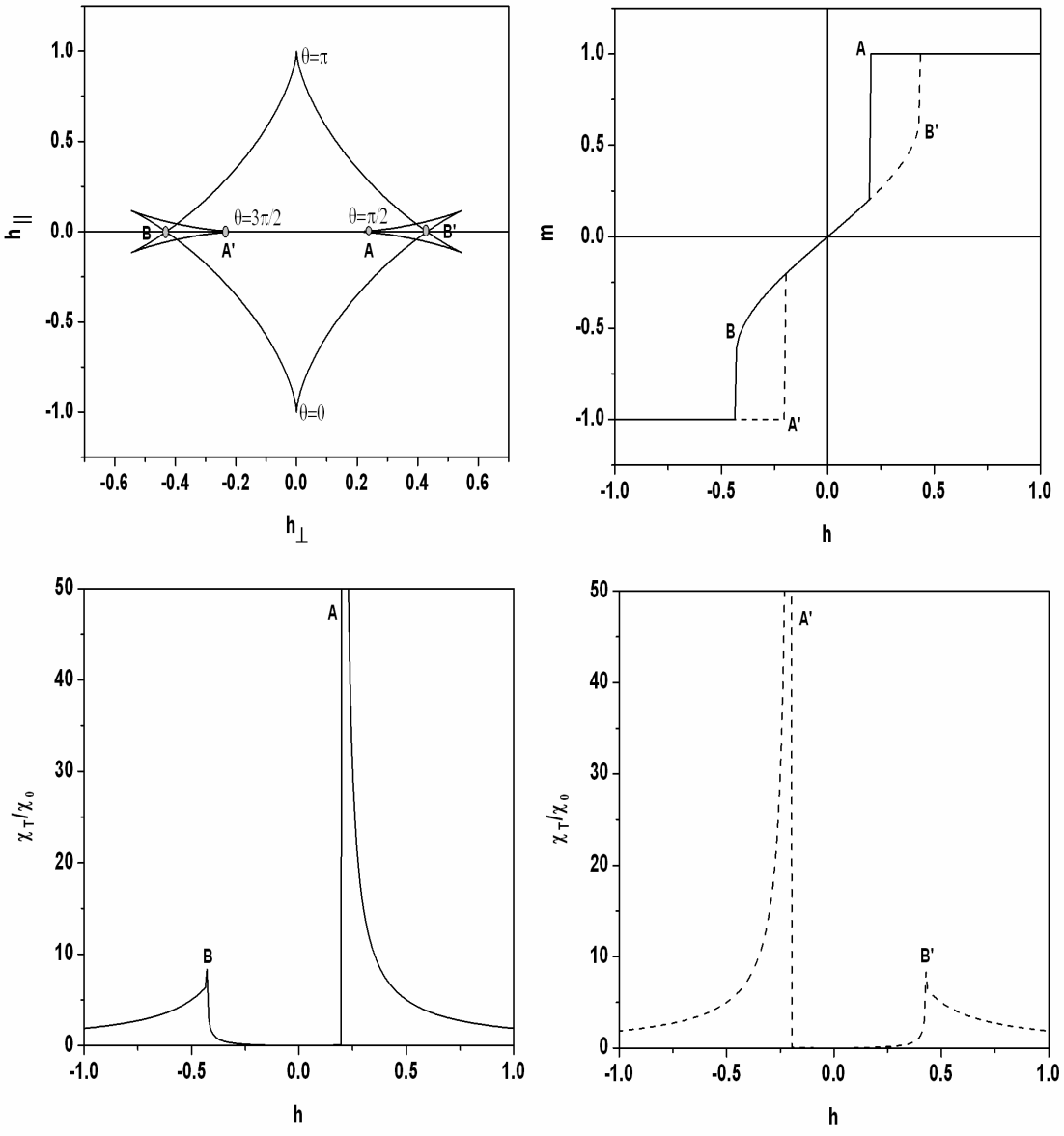

Figure 2.10. The astroid, hysteresis loops on the top, and the corresponding TS curves on the bottom with the solid line for decreasing field and the dash line for increasing field, in region VI for the applied field angle of 90^0 crossing the extra cusps.

G. *Region VII*

Because of the large positive value of K_2, instead of creating an easy plane as in region III and V, a new easy cone surface is formed along a certain angle with respect to the easy axis, θ_c. Taking derivative of the anisotropy energy with respect to θ and putting it equal to zero, one can find out $\theta_c = \frac{1}{\sin\left(\sqrt{-K_1/2K_2}\right)}$. When h is infinitesimally small, instead of rotating 180^0 like in the case of the easy plane, the magnetization rotates to a certain angle to minimize the Zeeman energy on the easy cone surface. A jump of magnetization; therefore, will occur at $h = 0$. For the same deviation of angle from the easy cone axis but with the smaller applied field angle with respect to the *c*-axis, the projection of magnetization along the applied field always jump less (see Fig. 2.11).

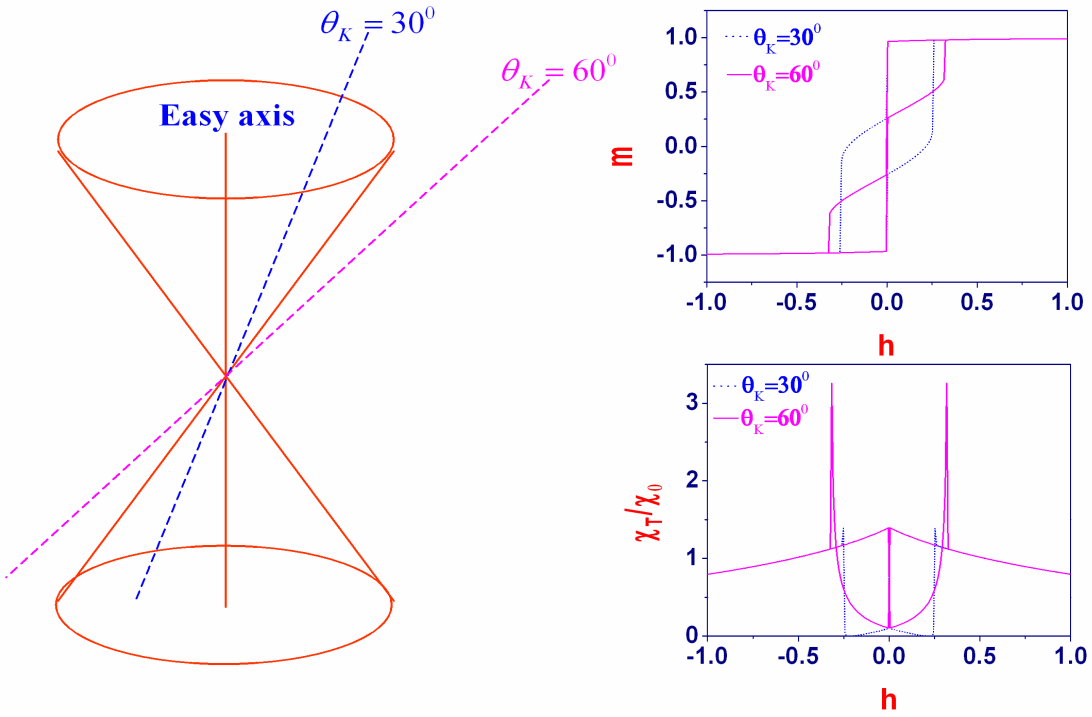

Figure 2.11. Right: the easy cone surface; Left: the hysteresis loops and the corresponding TS curves, at two different applied field angles 30^0 and 60^0 in region VII.

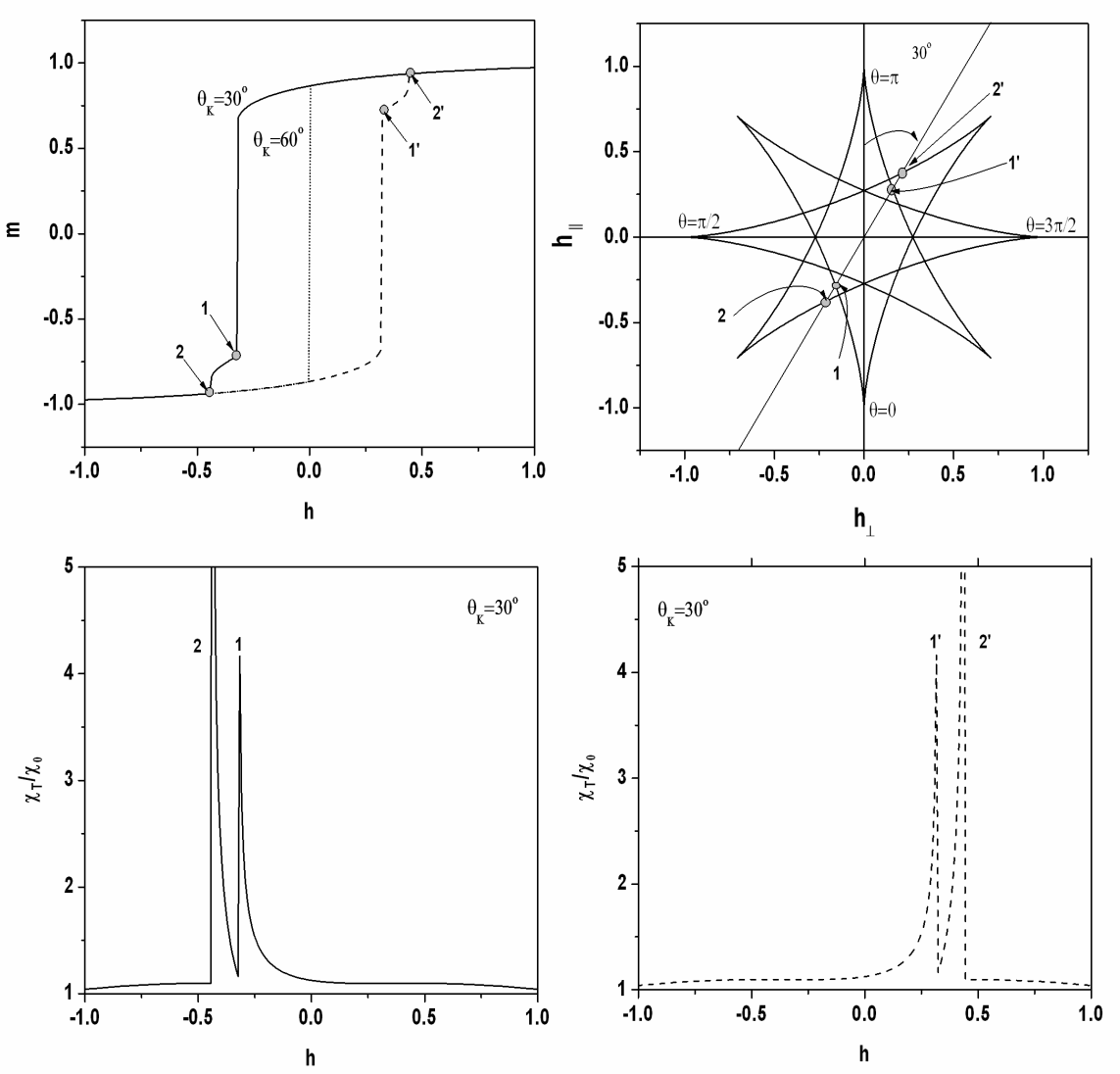

Figure 2.12. The calculated hysteresis loops, astroid and χ_T curves in region VIII.

H. Region VIII

Once again, the shape of the astroid curve in this region is the same as region VII, but the behavior of magnetization is totally different in the two regions. Instead of forming the easy cone symmetry, a new hard cone exists at an oblique direction. The applied field angles 30^0 and 60^0 have the same magnetization as for positive applied field; but there is no hysteresis for the field angle of 60^0. The additional Barkhausen

jumps in the field angle of 30^0 are the direct consequence of the second anisotropy constant. The panel of Fig. 2.12 presents in detail this case, showing in addition to the hysteresis loop and the critical curve are the corresponding transverse susceptibility χ_T curves. Note the points where the Barkhausen jumps occur in all the curves [58].

2.3 The measurement of the critical curve via reversible transverse susceptibility experiments

From the previous section, we understand that the critical curve is a very important tool to study the static switching behavior of magnetic materials. So, a question comes up, how we can measure the critical curve? Since the critical curve is the locus of points for which the magnetization reversal occurs, any experimental method able to probe the discontinuous and irreversible changes in magnetization orientation can be employed to determine this map of switching fields. So far there are several methods developed. One of these methods, that we should firstly notice, is the one using magnetoresistance (MR) measurements recently proposed by S. Parkin and his co-workers in their papers for the study of magnetic tunneling junctions (MTJs) [33]. Based on the measurement of MR hysteresis loop, the switching field was defined as the magnetic field at which the resistance curve had maximum slope. Thus, by recording two such points in field space $\left(h_x,\ h_y\right)$ for each loop, one can plot these points in 2D field space to obtain the critical curve. Obviously, this method would not be able to apply for all kinds of samples, such as for insulators. Another method that is worth being mentioned here is the one using micro-SQUID technique [34]. Basically, this method is only useful for the detailed study

of the magnetization reversal of single nanometer-sized particles. In this section, we introduce a new method, much simpler for determining critical curve for 2D magnetic systems from reversible susceptibility experiments. This method recently mentioned in our paper [35], is sensitive and it can be applied to magnetic systems with any type of anisotropy.

2.3.1 Model

The original TS formula was firstly proposed by Aharoni [36] as pointed out in section 1.2.4. Recently, it was shown that this traditional expression for TS was in fact the zero-frequency limit of the ferromagnetic resonance (FMR) [59]. The importance of this statement brings a new approach, which allows one to find general TS for virtually any magnetic system if an expression for the magnetic free energy density, W is known. In addition, the Ref. 59 proposed the general TS formula that takes into account the dynamics of magnetization – or in other words taking into account the dependence of TS on the excitation frequency of the ac field. For TS experiments, two magnetic fields are applied, a dc field, $\mathbf{H}_{dc}$ and small perturbing ac field, $\mathbf{H}_{ac}$, oriented perpendicularly to the dc field, and the magnetization variation along the ac field direction, and therefore transverse to $\mathbf{H}_{dc}$ is measured. If the dc field is applied along the *z*-axis and the ac field along the *x*-axis of a Cartesian reference system, the transverse susceptibility will be measured along the *x*-axis.

For the limiting case when the frequency of the ac field approaching zero, the reversible TS is given by:

$$\chi_T = \chi_{xx} = \frac{M_s^2}{W_{\theta\theta}W_{\varphi\varphi} - W_{\theta\varphi}^2}\left(\sin^2\theta_M \sin^2\varphi_M W_{\theta\theta} + \frac{\sin 2\theta_M \sin 2\varphi_M}{2} W_{\theta\varphi} + \cos^2\theta_M \cos^2\varphi_M W_{\varphi\varphi}\right) \tag{2.10}$$

where θ_M and φ_M are the equilibrium polar and azimuthal angles of magnetization vector $\mathbf{M}$ and $W_{\theta\theta}$, $W_{\varphi\varphi}$, and $W_{\theta\varphi}$ are second derivatives of the free energy density at the equilibrium position (θ_M, φ_M) at which W has a minimum. The denominator of χ_{xx}, $D(\theta_M, \varphi_M) = W_{\theta\theta}W_{\varphi\varphi} - W_{\theta\varphi}^2$, is actually the curvature of the free energy surface $W(\theta, \varphi)$ at the equilibrium position (θ_M, φ_M). Obviously, one can realize why the TS can be used for switching fields probing. The switching points of a system described by the free energy $W(\theta, \varphi)$ satisfy the equation $D(\theta, \varphi) = 0$ and would be found from the singular points of susceptibility χ_{xx}.

For thin film samples, by performing TS experiments with the dc field applied at various orientations in the sample's plane, it would be able to track the angular variation of the switching fields and therefore able to determine the critical curve. Experimentally, however, this is so difficult to perform since it requires one to physically rotate the sample located inside a sensing coil with small diameter. The demand of rotating sample with precision turned out to be very complicated. We propose herein an alternative method, easier to apply experimentally, that is, instead of rotating sample, rotating the dc field in the plane of the sample while keeping the sample fixed inside the sensing coil. In this case the susceptibility χ_{xx} no longer presents the TS but a combination of both

transverse and longitudinal susceptibilities, however still preserving the same singularity characterizing the switching fields.

To better understand this approach we consider a uniaxial magnetic system as in the case of the SW model. Now using the geometry and notations of Fig. 2.13, the free energy density is given by

$$W = -K_1(\hat{u}_K.\mathbf{M})^2 - \mathbf{M}.\mathbf{H}_{dc} \tag{2.11}$$

Thus, from (2.10) and using notations mentioned in the subsection 1.2.1 describing the TS in chapter 1, one easily obtains:

$$\chi_{xx} = \frac{3}{2}\chi_0 \frac{\cos^2\theta_M}{\cos 2(\theta_M - \theta_K) + h\cos(\theta_M - \theta_H)} \tag{2.12}$$

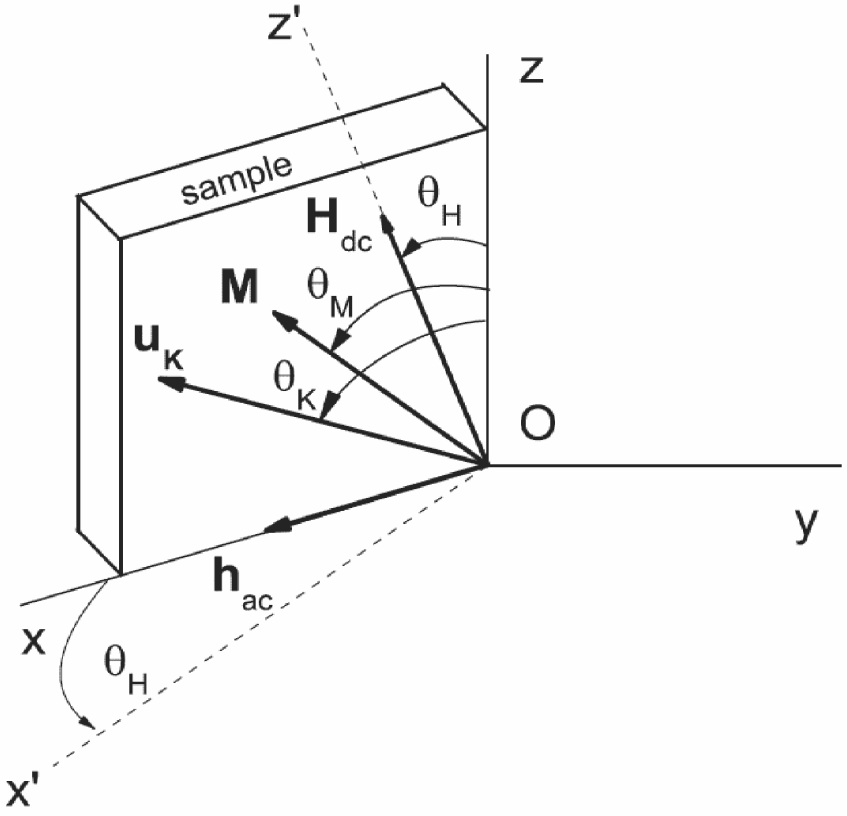

Figure 2.13. A thin film sample with coordinate system.

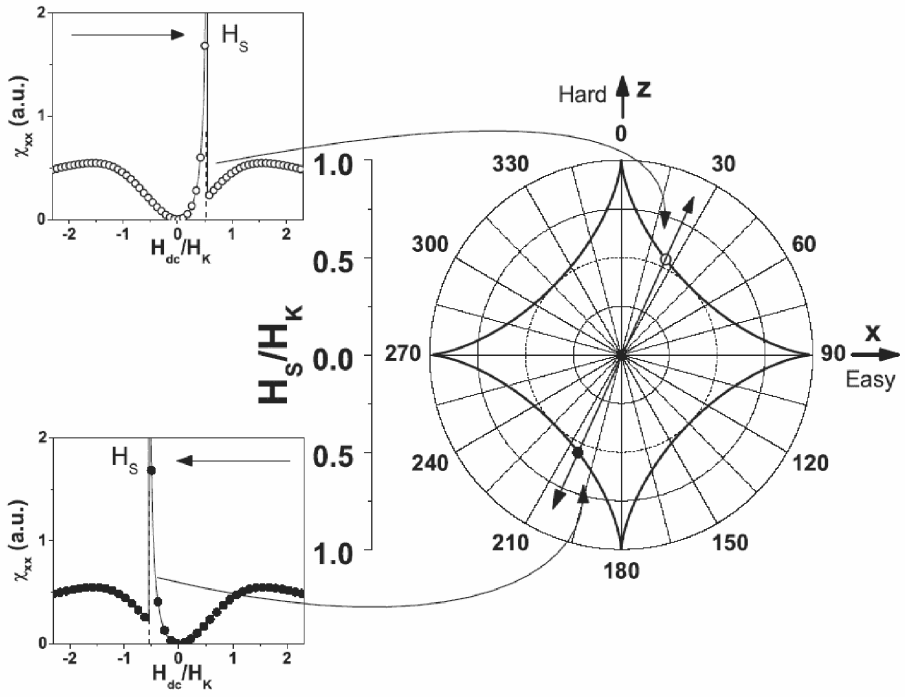

Figure 2.14. The right panel is the theoretical curve (astroid) as can be determined from susceptibility measurements for an ideal single-domain particle with uniaxial anisotropy. Whereas, the left shows susceptibility signal χ_{xx} detected along the *Ox* axis, for increasing (top) and decreasing (bottom) field sweeping in the geometry of Fig. 2.13 for $\theta_H = 25^0$ and $\theta_K = 90^0$.

By determining the singularities of the TS curve obtained from (2.12) at different angles of dc field, θ_H, in the sample's plane, the critical curve can be achieved as shown in Fig. 2.14 (plotted in polar coordinates).

2.3.2 Experimental results

The above-presented technique was employed to determine the critical curves of different samples of $\left[Co\left(t_{Co}\right)/SiO_2(1nm)\right]\times 10$ multi-layers grown by DC (*Co*) and RF (SiO_2) sputtering on *Si* substrates held at room temperature as described in Ref. 60. A 10 nm buffer layer of SiO_2 was deposited on the *Si* substrate before the sequential deposition

of *Co* and SiO_2 layers [60]. Several samples can be obtained by varying the nominal thickness of *Co* and SiO_2 layers. The samples considered in this work are three metallic samples with *Co* nominal thickness t_{Co} of 1 nm (sample 90A), 1.5 nm (sample 90B) and 2nm (sample 90C). The samples then were cut into 5 mm × 5 mm pieces, with one edge parallel to the easy axis of the ferromagnetic layers. These samples were provided by Dr. Juliano Denardin from Unicamp University, Campinas, Brazil.

To measure the susceptibility we used a very sensitive method based on a tunnel-diode oscillator (TDO) technique [61]. The sample was placed in the sensing coil with both ac and dc fields lying in the sample plane (see Fig. 2.15).

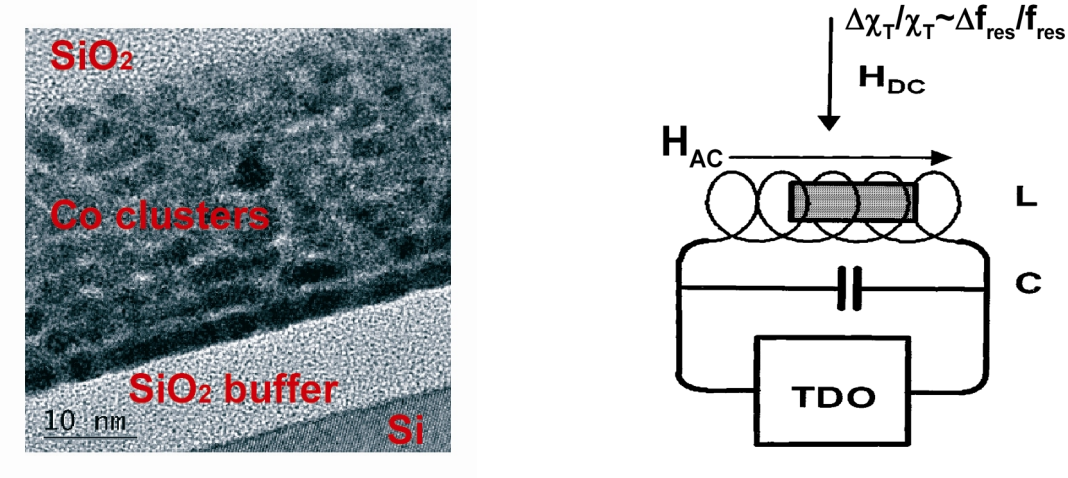

Figure 2.15. Right: Schematic of the transverse susceptibility experiment. Left: TEM image of Co/SiO_2 multilayer sample.

The dc magnetic field was generated by an electromagnet placed on a revolving stage with a protractor for measurement of the field direction. In the experiment, the measured quantity is the shift in resonant frequency as the static field is varied. The frequency shift arises from a change in coil inductance *L*, related to the change in

transverse susceptibility of the sample via the formula $\Delta\chi_T / \chi_T \sim \Delta f_{res} / f_{res}$. The reversible susceptibility signal then was recorded for different orientations of the dc field with respect to the sensing coil direction. Starting from $\theta_H = 0^0$ to $\theta_H = 360^0$ with the angle step 5^0, the signals recorded for the sample 90A are presented in Fig. 2.16, which is the equivalent of Fig. 2.14 for the experimental data.

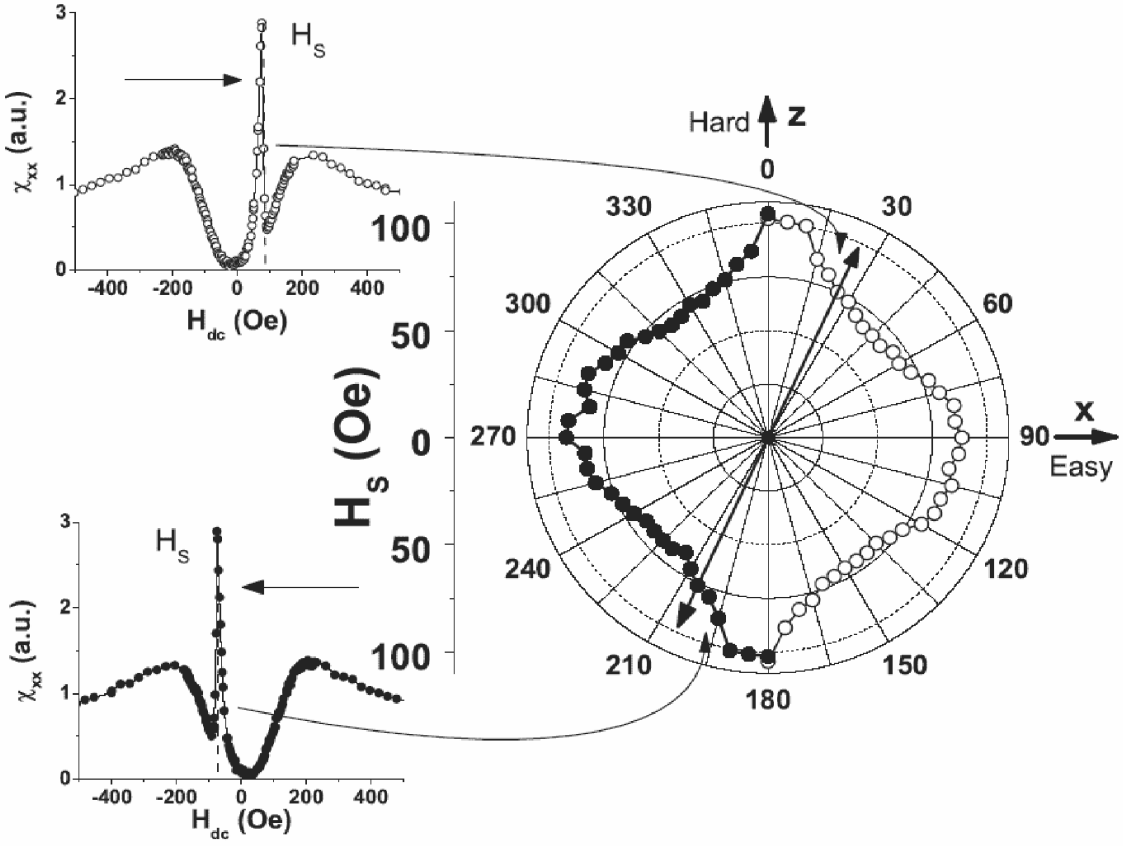

Figure 2.16. Right: Experimental switching critical curve as determined from susceptibility measurements for sample 90A. Left: Experimental susceptibility signal χ_{xx} for increasing (top) and decreasing (bottom) field sweeping at $\theta_H = 25^0$.

One observes that while preserving some of the expected characteristics, the experimental curve deviates from the theoretical astroid. In order to quantify the

difference between the experimental critical curves and the astroid, one can use five parameters: the coordinates of the center of the curve, the dimensions of the curve along its natural axes, and the angle at which these axes were tilted from field axes (*Ox* and *Oz*). It can be observed that for sample 90A the critical curve is well centered, which is evidence for the absence of unidirectional (exchange) anisotropy [58] or Néel coupling [62] in the studied magnetic system. In addition, the symmetry axes almost coincide with the field axes (a small inclination of about 5° of the symmetry axes with respect to the field axes can be noticed), the easy axis being oriented along the *Ox* direction. This is determined by the initial positioning of the sample in the sensing coil, which was oriented with the deposition direction along the *Oz* axis. In other words, the easy axis of the film is perpendicular to the deposition direction, a fact consistent with the results obtained using other measurement techniques and determined by the deposition system's geometry. A 5° misalignment in the initial sample position is responsible for the slightly critical curve tilting.

The dimensions of the critical curve along the hard and easy axes are 103 and 90 Oe, respectively. One observes that the aspect ratio of the experimental critical curve (defined as the ratio between the maximum length of the critical curve along the easy axis to that along the hard axis) is about 0.87, which is smaller than the unit astroid aspect ratio as predicted by Stoner–Wohlfarth model [14]. The reduced critical curve aspect ratio was already observed for 2D magnetic systems and was connected to the existence of the edge domains or noncoherent rotation switching modes.

A more dramatic change in the critical curve aspect ratio was observed for samples 90B and 90C, whose curves are displayed in Fig. 2.17. Thus, the aspect ratio for sample 90B is 0.55 while for sample 90C it is 0.39, with lengths of the critical curves along the hard axis of about the same value.

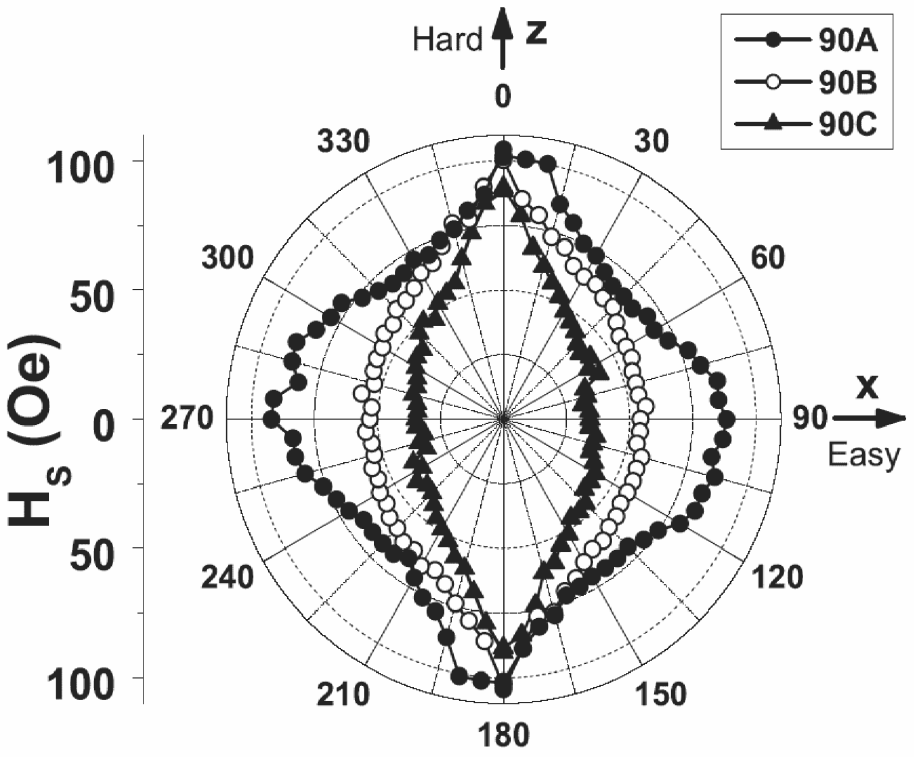

Figure 2.17. Experimental switching critical curves as determined from susceptibility measurements for samples 90A, 90B, and 90C.

The critical curve shape is sensitive to domain formation and switching modes [63]. Hence, incoherent switching modes, as the fanning [63] appearing in the "chain-of-spheres" model [64] determine a truncated astroid along the easy axis. In our case, the observed shrinkage of the critical curves along the easy axis as the Co layers' thickness increases is consistent with the observation that for larger thicknesses, the influence of the domain wall motions in the dynamics of magnetization is more important [33].

2.4 Summary

Magnetization switching behavior is one of the key issues of magnetic materials that are part of new data storage devices. For two-dimensional (2D) devices used in magnetic random access memories (MRAM), the magnetization dynamics is determined by the 2D magnetization switching properties as the MRAM cells require that the magnetic field be applied in two dimensions in the plane of the device. Therefore, it is important to study the response of such magnetic systems to fields applied along different directions with respect to easy and hard axes. Moreover, study of 2D magnetic switching enables us to determine the critical curve, which constitutes the fingerprint of the switching behavior and provides information about micromagnetic and structural properties of magnetic systems. The critical curve depends on magnetic system anisotropy and its shape can become more complex if taking into the second anisotropy constant. There is a lot of interest in determining the critical curve and several methods were proposed. As the critical curve is the locus of points for which the magnetization reversal occurs, any experimental method able to probe the discontinuous and irreversible changes in magnetization orientation can be employed to determine this polar map of the switching fields. Our novel method presented in this chapter, based on reversible susceptibility's singularities detection, is one of the most sensitive methods for determining the critical curve for 2D magnetic systems. The method, which is demonstrated both theoretically and experimentally on Co/SiO_2 multilayers, can be generally applied to magnetic systems with any type of anisotropy.

Chapter 3

Magnetization Dynamics in Interacting Magnetic Systems

So far, we have just concerned about the switching behavior of magnetization in the applied field in the quasistatic regime, where the magnetization dynamics and precessional effects are neglected. The static switching behavior of Stoner-like magnetic particles was discussed in the frame of the SW model using remarkable properties of the static critical curve. In this chapter the magnetization dynamics of magnetic particles in a data storage medium such as magnetic random access memory (MRAM) cells is addressed in detail.

It is well known that the study of magnetization reversal is very important in designing high density and high data transfer rate recording media. This determined the seeking of new strategies for magnetization reversal. Thus, recently it was observed that for Stoner-like magnetic particles without interactions the switching field and switching time could be decreased by using short magnetic field pulses [1, 2, 4]. Since in real magnetic systems the effect of interaction cannot be avoided, in this study we present an analysis of magnetization reversal in interacting SW particles.

This chapter will be divided into two main parts. In the first part, we concentrate on the magnetization dynamics of isolated single domain magnetic particles with homogeneous magnetization in pulsed applied magnetic fields. The dynamic behavior of

magnetization in the case of interacting magnetic systems is revealed in the second part. In both parts, the useful models for the switching process can be described theoretically by the phenomenological magnetization's equation of motion Landau-Lifshitz-Gilbert.

3.1 Magnetization behavior of isolated single domain ellipsoidal particles

Magnetization dynamics is one of the central issues in the physics of magnetic systems. An understanding of the switching behavior in small magnetic particles is of crucial importance in the development of memory devices. The purpose of this section is to specifically examine the reversal process, calculated for single domain ellipsoidal particles, under a variety of different effective field configurations. The present results apply to the switching properties of individual MRAM cells.

3.1.1 Model

As pointed out in the chapter 1, the motion of the magnetization under the influence of an effective magnetic field could be described by the Gilbert form of the Landau-Lifschitz equation

$$\frac{\partial \mathbf{M}}{\partial t} = -\gamma \mathbf{M} \times \mathbf{H}_{eff} + \alpha \frac{\mathbf{M}}{M_S} \times \frac{\partial \mathbf{M}}{\partial t} \tag{3.1}$$

The first term on the right-hand side of LLG equation is the precession term and the second one is the damping term. We now shall apply the model for all calculations below for ellipsoidally shaped permalloy particle with demagnetization factors $N_x / 4\pi = 0.008$, $N_y / 4\pi = 0.012$, $N_z / 4\pi = 0.980$, gyromagnetic factor $\gamma = 0.0176$ $\mathrm{Oe}^{-1} ns^{-1}$, damping parameter $\alpha = 0.008$ and the saturation magnetization $4\pi M_S = 10.8kG$, as mentioned in

Ref. 4. Only shape and uniaxial in-plane anisotropies are considered. For all anisotropies the x axis corresponds to the easy axis of magnetization.

The effective field $\mathbf{H}_{eff}$ can be written as the sum of all fields acting on the magnetic moment, is given as follows:

$$\mathbf{H}_{eff} = \mathbf{H}_{pulse} + \mathbf{H}_{shape} + \mathbf{H}_{ani} \tag{3.2}$$

with $\mathbf{H}_{pulse}$ is the external applied pulsed field, $\mathbf{H}_{ani}$ the uniaxial in-plane anisotropy field, and $\mathbf{H}_{shape}$ the shape anisotropy. The results are obtained by numerical integration of (3.1) using a standard, self-optimizing, embedded Runge-Kutta algorithm.

3.1.2 Time evolution of the magnetization in pulsed magnetic fields

In this sub-section, the precessions of the magnetization under application of different short magnetic field pulses are discussed. The pulse is characterized by the triplets of numbers "rise time/pulse length/fall time." (see Fig. 3.1)

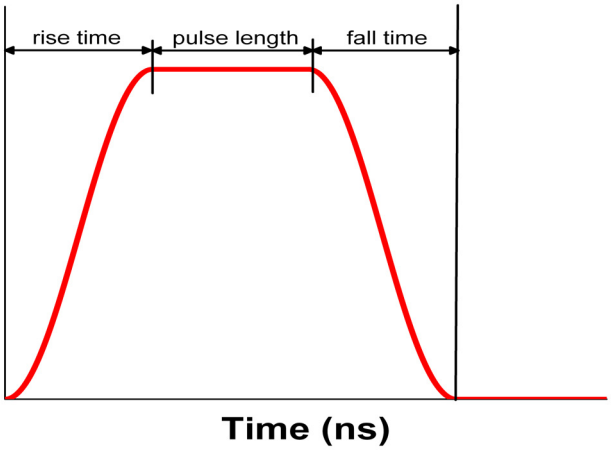

Figure 3.1. Scheme of the magnetic field pulse to explain the parameters pulse rise time/pulse length/pulse fall time. All values are given in units of nanoseconds. Rise and fall times have a sinusoidal shape.

In Fig. 3.2, the switching behavior of magnetization in the influence of the pulsed field 0.0/10/0.0 ns of 50 Oe is given by two graphical representations. One way to characterize the dynamics of the precessional switching is to plot the time-dependence of three components of magnetization vector separately as shown on the bottom of the figure.

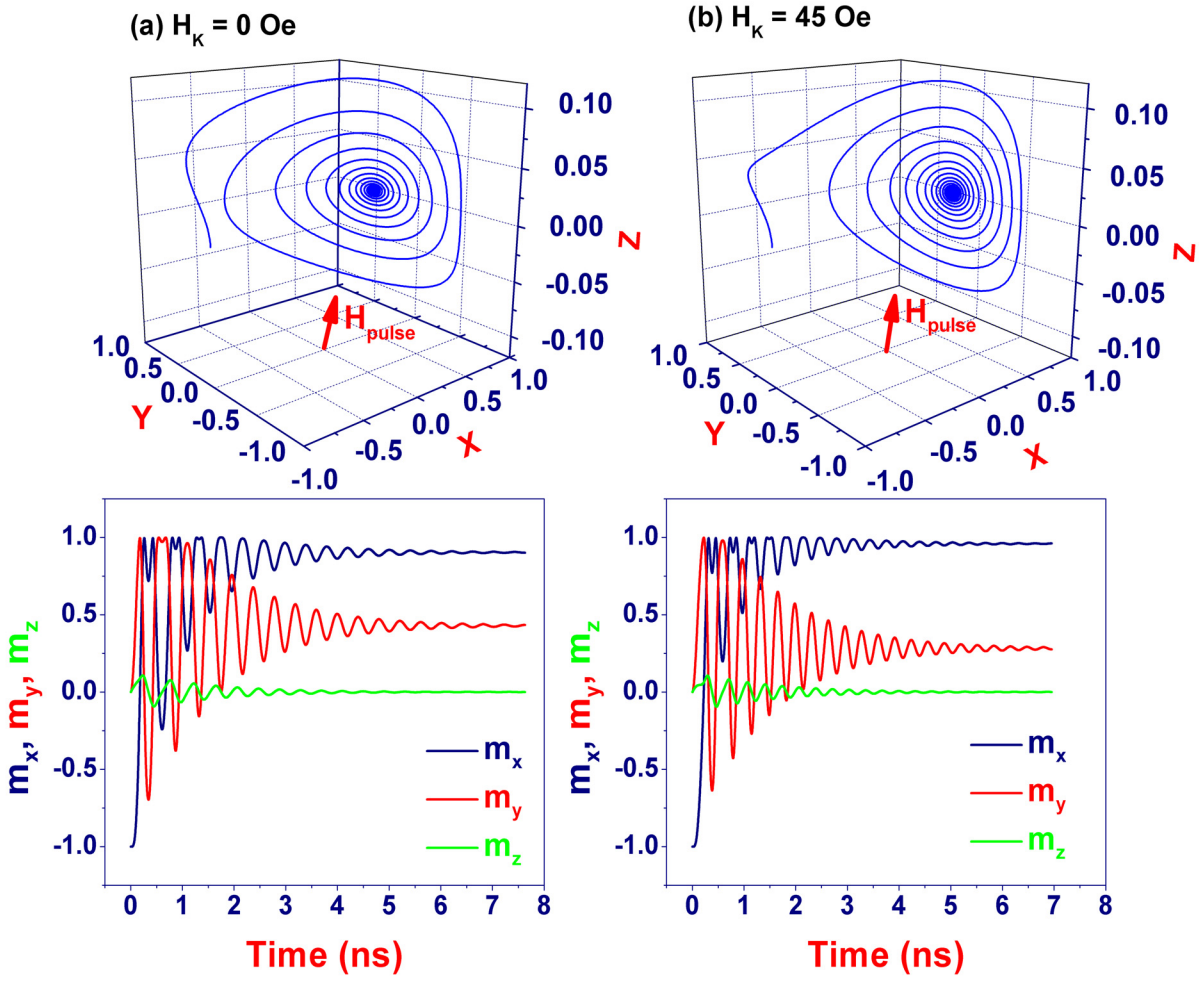

Figure 3.2. Different representations of the precessional switching of an ellipsoidally shaped particle with the demagnetization factors $N_x / 4\pi = 0.008$, $N_y / 4\pi = 0.012$, and $N_z / 4\pi = 0.980$, i.e, the x-axis is the easy magnetization axis. A field pulse 0.0/10/0.0 ns of 50 Oe is applied. Time evolution of the magnetization vector is displayed: (a) In the case without anisotropy. (b) In the case with anisotropy $H_K = 45\ Oe$.

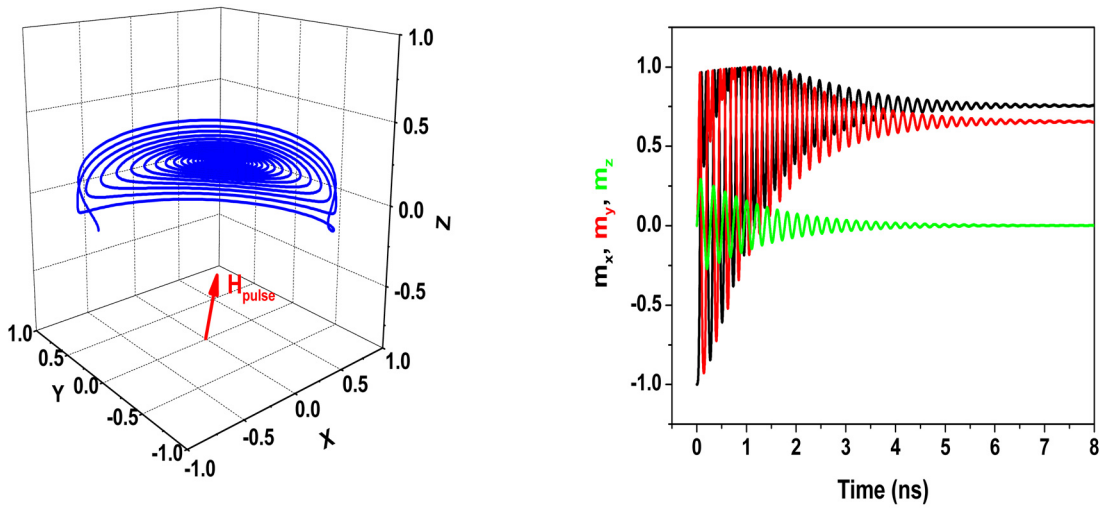

Figure 3.3. Time evolution of magnetization in a field pulse 0/10/0 ns of 300 Oe.

The other way is to plot the time variation of the whole magnetization vector as shown on the top of the figure. The time evolution is observed for the first 8 ns. The pulse is applied at an angle 135^0 in the *xy* plane, in which the magnetization initially points to the left in the *–x* direction. The damped precession of magnetization during the application of the magnetic field pulse in the case without/with anisotropy is shown in Fig. 3.2(a)/Fig. 3.2(b), respectively. After 8 ns, in both cases, all components of magnetization vector are stable; therefore, one can conclude that the pulse length, 10 ns, is long enough and basically the pulse can be considered as the static field in this case. However, the final position of magnetization turned out to be not aligned along the applied field but deviated along a direction making a certain angle with respect to the applied field direction. This can be explained that the applied field is not strong enough to counteract the effect of demagnetizing and anisotropy fields. So, instead of damped precession around the applied field, the magnetization gradually approaches the effective

field entirely due to the sum of the applied field, the demagnetization field, and an additional anisotropy field for the case of uniaxial anisotropy. When the magnitude of the pulsed field is increased, the pulsed field will play a primary role in contribution to the effective field and lead to a damped precession about the applied field direction as shown in Fig. 3.3. It is also worth noting here that the magnetization trajectory is located almost in the plane $z = 0$ because of in-plane components of the shape anisotropy.

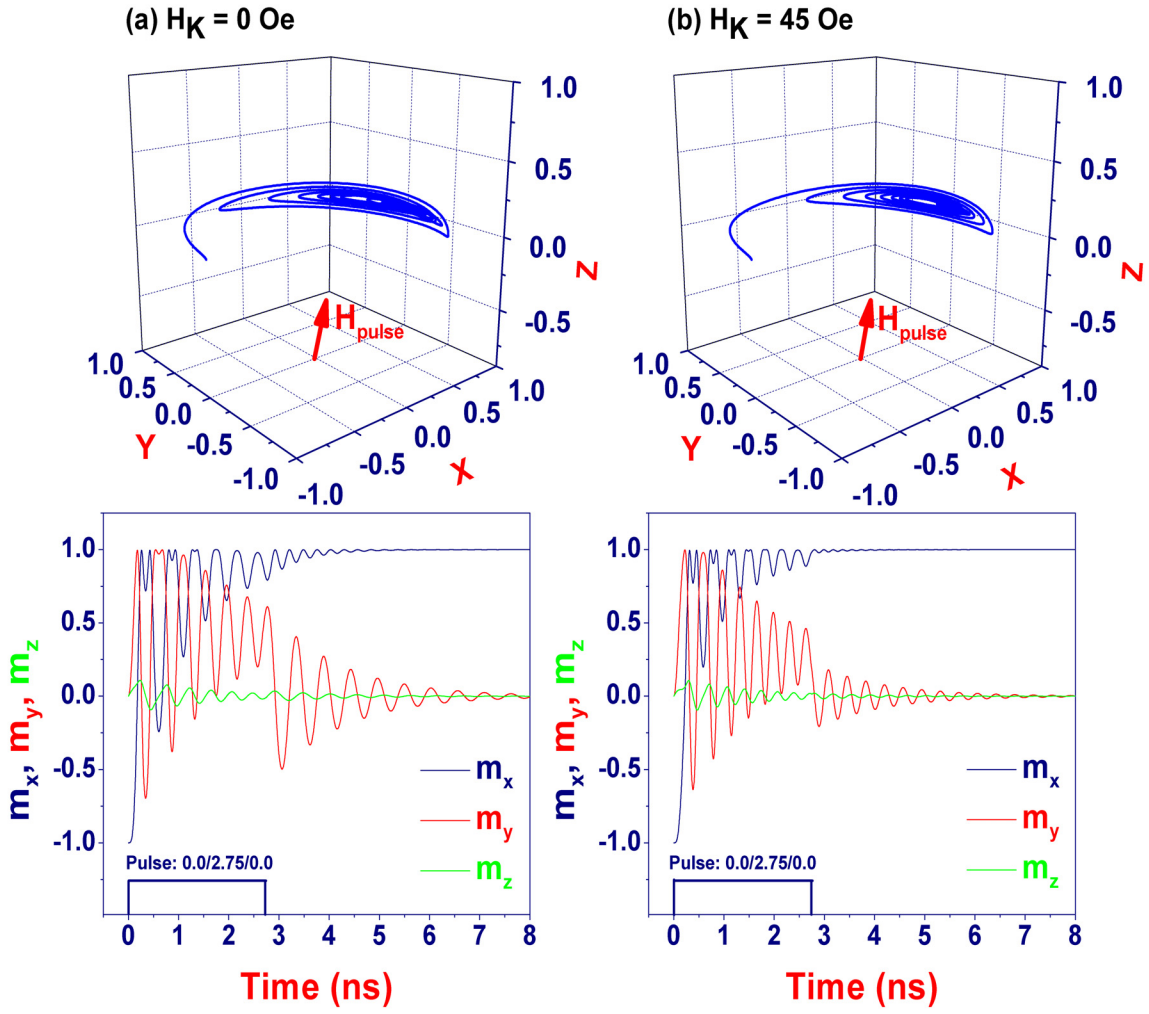

Figure 3.4. Time evolution of the magnetization vector under a field pulse 0.0/2.75/0.0 ns of 50 Oe is displayed: (a) In the case without anisotropy. (b) In the case with anisotropy $H_K = 45$ *Oe*.

In Fig. 3.4, the relaxation of the magnetization leads to the final easy magnetization direction when the pulse was terminated at 2.75 ns. In both cases, with or without uniaxial anisotropy, the reversal and ringing of magnetization were observed. The magnetization was reversed from the negative *x* direction to the positive *x* direction. It is also worth noting the discontinuous change of magnetization trajectory at the time of termination of the field pulse.

3.1.3 Switching diagram of the magnetization in pulsed magnetic fields

In the previous section, the magnetization trajectory was calculated, and one can realize that magnetic field pulses can be used to initiate magnetization reversal. The main goal now is to determine a parameter regime for the magnetic field pulse where fast and stable switching can be achieved. In order to do this, we will use the switching diagram proposed in Ref. 4, in which the final configuration state of the magnetization vector is displayed as a function of the pulse strength and direction. Prior to the field pulse applied, the magnetization lies along the negative *x* direction in *xOy* plane. If the magnetization is reversed to the positive *x* direction, the corresponding gray-tone scale is chosen to represent the switching time (white-gray: for fast switching, black: for slow switching). If the magnetization is not reversed, the pure white color is used instead. For the following results, the shape anisotropy is taken into account, no further anisotropy is considered.

In Fig. 3.5, switching diagrams of magnetization vector at different pulse lengths of 2.75 ns (top), 1.4 ns (middle), and 0.25 ns (bottom) are shown. For the pulse length of 2.75 ns, it is evident that reversal takes place for most of the parameters, where the field direction has a component along to the positive x direction.

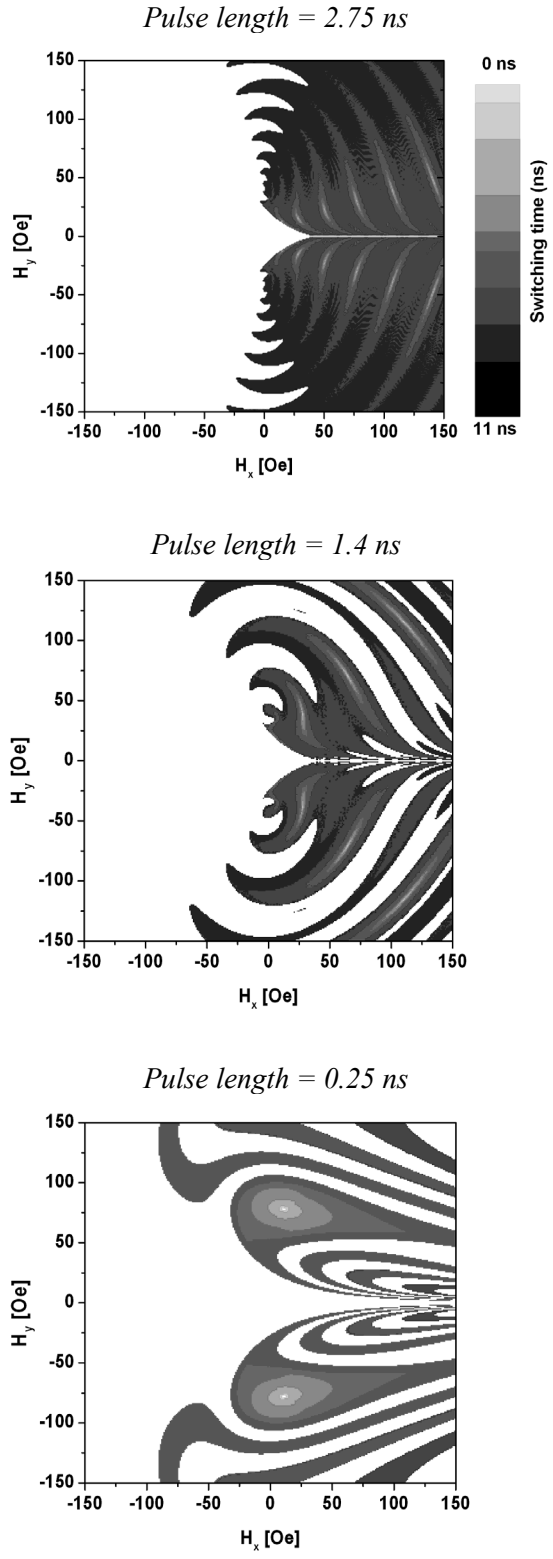

Figure 3.5. Switching diagrams for different rectangular pulse lengths of 2.75 ns (top), 1.4 ns (middle), and 0.25 ns (bottom). The gray scale represents the switching time. If the magnetization does not switch, light white color is used instead.

Therefore, the separation boundary between switching and non-switching regions is very well defined. If the field is aligned near the $\pm y$ directions, switching and non-switching areas alternate with increasing field strength.

When the pulse length is shorter, one can see that the regions in the left part of diagram (the negative *x*-direction), at which switching can occur, are greatly enlarged whereas, in the right part of the diagram, parameter sets, for which switching and non-switching occurs, alternate successively.

The figures 3.7a-d show the time evolution of the magnetization components for several points as pointed in Fig. 3.6 describing switching diagram of magnetization in the short pulse of 0/0.25/0 ns. As expected from switching diagram, for points (a) and (b), magnetization is reversed, whereas for points (c) and (d), non-switching behavior is observed. The most remarkable situation is observed in Fig 3.7(a), in which the point is located in the white-gray region indicating short switching time. Full magnetization reversal is achieved in only few nanoseconds without significant ringing after the field pulse has been turned off. This is due to the fact that the pulse is terminated closely at the point where the magnetization on its trajectory crosses the easy direction of the shape anisotropy. Thus, after the termination of the pulse, the magnetization is lined up with the shape anisotropy field.

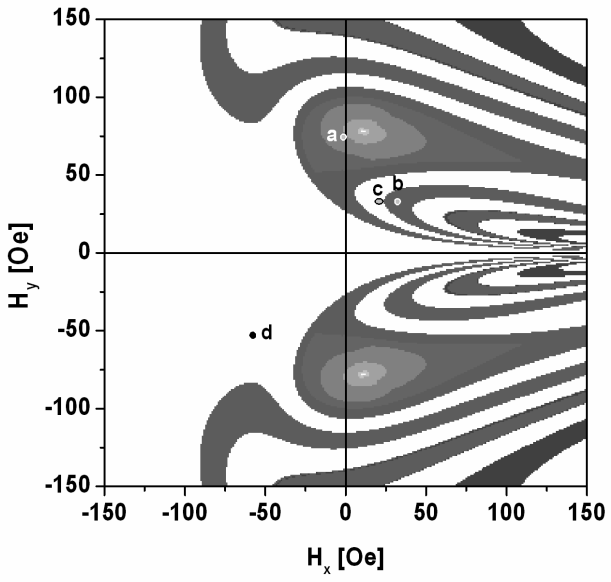

Figure 3.6. Switching diagram of the magnetization vector under the application of a 0/0.25/0-ns field pulse.

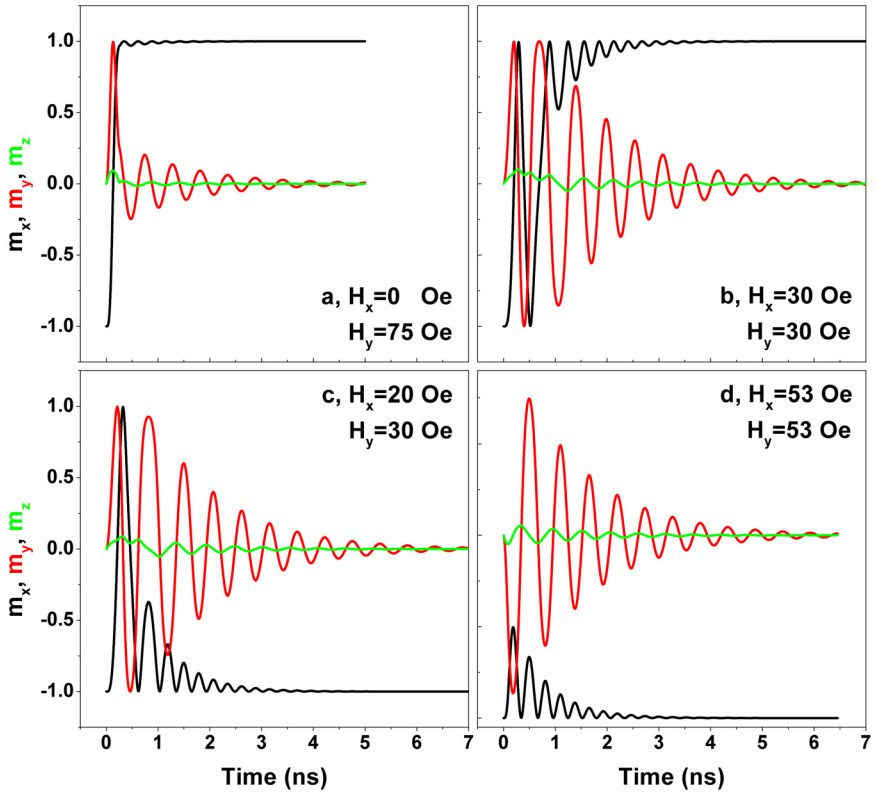

Figure 3.7. Time evolution of the magnetization components m_x, m_y, and m_z for the four parameter sets labeled (a)-(d) in Fig. 3.6.

3.2 Magnetization reversal in interacting magnetic systems

In the study of magnetization reversal of magnetic particles from the previous section, the interaction between magnetic particles was ignored. However, as the density of magnetic recording media becomes higher, the problem of dipolar interactions between neighboring magnetic elements becomes more acute so that it should be taken into account. In the case of interacting particles the dynamics of magnetization becomes fairly complicated. The general treatment of such a problem is very difficult; therefore, instead of dealing with many-particles problem, simpler systems as two coupled moments are usually considered, but which still can provide useful information on the dynamics of interacting magnetic systems.

We now consider two coupled ellipsoidal particles as before with magnetic moments $\mathbf{m}_1$ and $\mathbf{m}_2$, in different initial configurations as shown in Fig. 3.8 in which the separation between magnetic dipoles (D) is given in unit of the length of the principal axes of ellipsoidal particles.

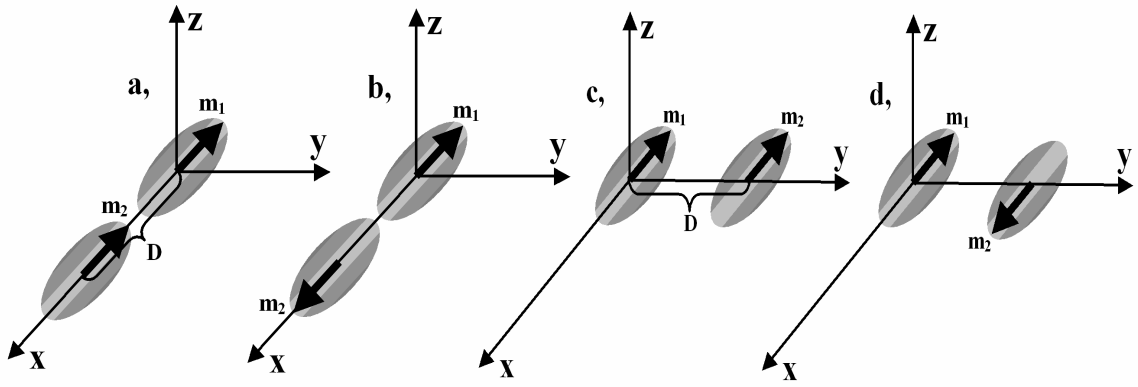

Figure 3.8. Initial configurations of the system consisting of two particles $\mathbf{m}_1$ and $\mathbf{m}_2$.

In all configurations above (a-d), besides the external pulsed field, the moment $\mathbf{m}_1$ (located at the origin) will be subjected to the additional dipolar field created from the moment $\mathbf{m}_2$. Thus, a new term, $\mathbf{H}_{dip}$, which is the dipolar field due to neighboring moments [65, 66], needs to be added to the effective field in Eq. 3.2 (see Appendix B).

In order to observe the complicated reversal process of the magnetization vector $\mathbf{m}_1$ and $\mathbf{m}_2$, besides the switching diagram mentioned in the preceding section, we shall use another useful geometrical representation, so-called the phase portrait proposed in Ref. 67. The phase portrait is to present the final state of the magnetization as a function of its initial configuration. Recently, such a geometrical representation was displayed in the stereographic plane of coordinates $W_1 = \frac{m_x}{1+m_z}$ and $W_2 = \frac{m_y}{1+m_z}$, where m_x, m_y, m_z are the Cartesian components of magnetization vector [67]. To show the usefulness of the phase portrait representation, we shall first consider the simplest case - when the separation between moment $\mathbf{m}_1$ and moment $\mathbf{m}_2$ is large enough, so that the dipolar interaction can be neglected, or in other words, we are going back to the situation of an isolated single domain particle discussed in the previous section. The phase portrait diagram of the moment $\mathbf{m}_1$ in this case as shown in Fig. 3.9(c) is numerically computed as in Ref. 40 by integrating the LLG equation in the absence of any external applied field for all orientations possible of the moment $\mathbf{m}_1$. The position on the diagram gives the initial configuration of the magnetization vector whilst the color gives the information on its final orientation after relaxation process (ringing) finishes, i.e., black for $\mathbf{m}_1$ along the

negative *x*, and white for along the positive *x*. One observes that the phase portrait presents a central part in which the black and white regions are intertwined. The central part is surrounded by an annular area, in which the black and white regions are well separated. A reliable switching is obtained only using these two regions located in this annular area, i.e. if the field is switched off when the magnetization is located inside one of these regions it will be easy to control in which final position the magnetization will be.

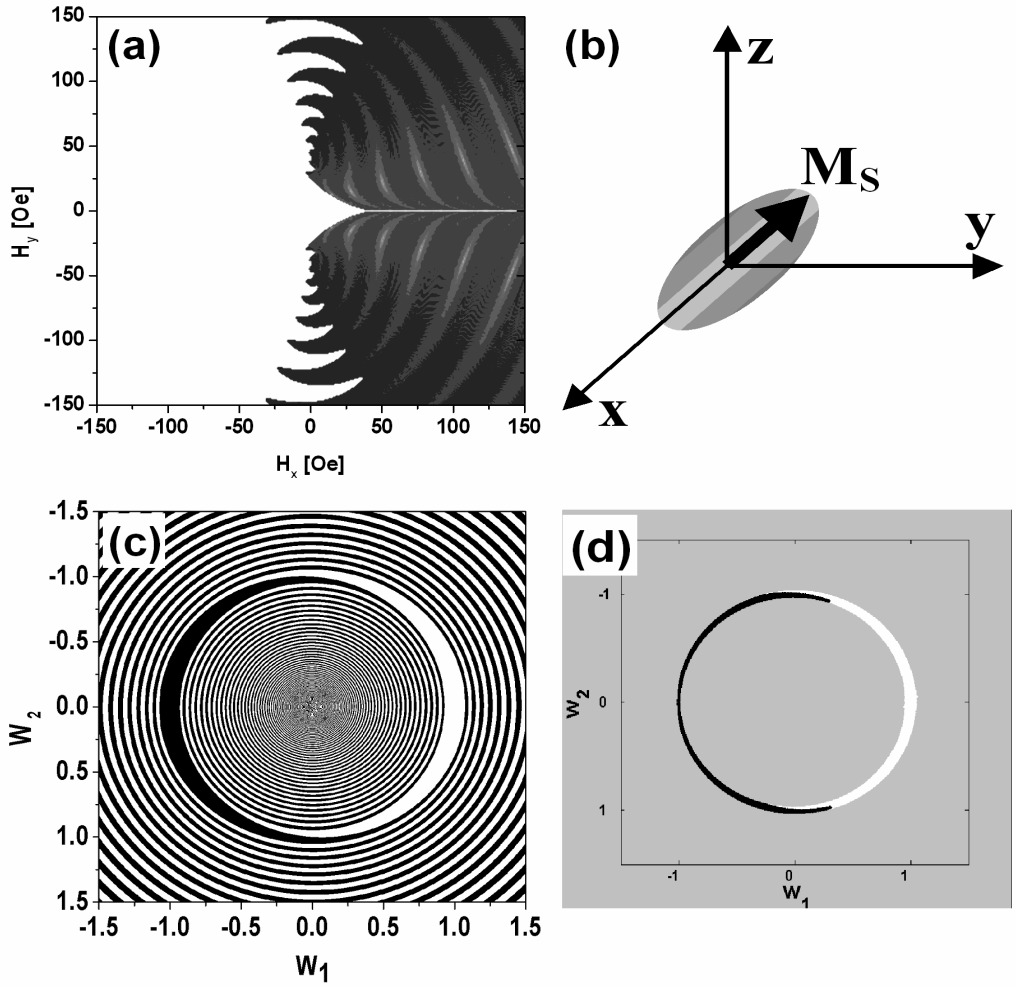

Figure 3.9. Different representations of the switching behavior of an isolated ellipsoidal particle: (a) Switching diagram represented in the field plane (H_x, H_y) subjected to a pulsed field of 0/2.75/0 ns; (c) Phase portrait in the stereographic plane for the same particle in the absence of the magnetic field, computed as in Ref. 67. (d) Phase portrait of the same particle represented only for the initial orientations of the magnetization "excited" by the field pulses from (a).

In the switching diagram from Fig. 3.9(a) a situation is shown in which the black and white regions are fairly well separated and consequently the precessional switching can be easily controlled. In the phase portrait diagram, that of Fig. 3.9(c), this would correspond to a situation in which the initial positions of the magnetization, after the pulse is switched off, are confined in the black/white annular region.

In order to verify this postulate, after each pulse shown in Fig. 3.9(a) ends, we calculated the components of magnetization $\left(m_x, m_y, m_z\right)$ and we represented them in the stereographic plane of coordinates $\left(W_1, W_2\right)$ with a color depending on their final state. In other words, from diagram shown in Fig. 3.9(c) we selected only the points corresponding to orientations of magnetization "excited" by the pulses applied in the switching diagram from Fig. 3.9(a). The resultant diagram is presented in Fig. 3.9(d) where one observes that, indeed, as it was previously postulated, the points are confined in the annular regions [68].

We are now ready to go back to the case of two coupled dipoles. The similar phase portrait diagram for the dipole located in the origin, which will be only subjected to the dipolar field (and not in the zero field as in Fig. 3.9(c)), can be constructed. The switching diagram for the dipole is built considering as initial configuration all its possible orientations, while dipole $\mathbf{m}_2$ is initially oriented parallel to the negative *x*-axis direction. Using a similar approach as for the isolated particle, the LLG equation is solved and the final orientation of $\mathbf{m}_1$ is determined and represented in the $\left(W_1, W_2\right)$ plane. The obtained results are displayed in Fig. 3.10 for the initial configurations (with D=6) as

shown on the top of the figure 3.10 corresponding to configurations (a) and (c) in the figure 3.8. One observes a dramatic change in the diagram, where the annular regions, from the case of isolated dipole, become asymmetric and colored in a single color, black or white, for cases 3.10(a) and 3.10(b), respectively. This is a direct consequence of the different character of the dipolar field sensed by dipole located in the origin, magnetizing for the diagram 3.10(a) or demagnetizing in the case of diagram 3.10(b). One expects that these new characteristics of the dynamics of couple particles revealed by the phase portrait representations given in Fig. 3.10 to be reflected in the switching diagrams.

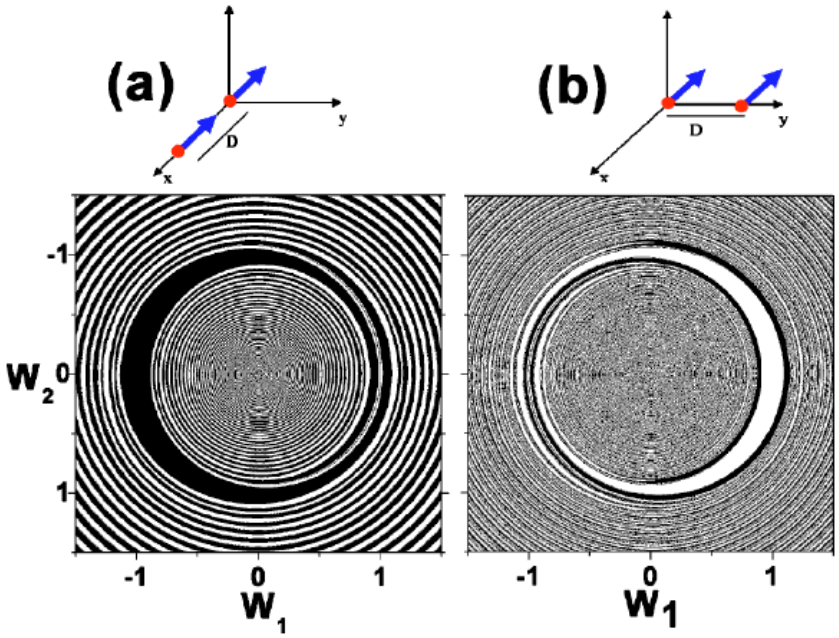

Figure 3.10. The phase portrait for the particle located at origin in interaction with a neighbor particle situated at the distance D=6. The reciprocal orientation of the magnetization vectors for interacting particles is represented above each diagram.

Now, for the same initial configuration displayed on top of Fig. 3.10(a) the switching diagrams for both dipoles $\mathbf{m}_1$ and $\mathbf{m}_2$ are displayed in Figs. 3.11(a) and 3.11(b), respectively.

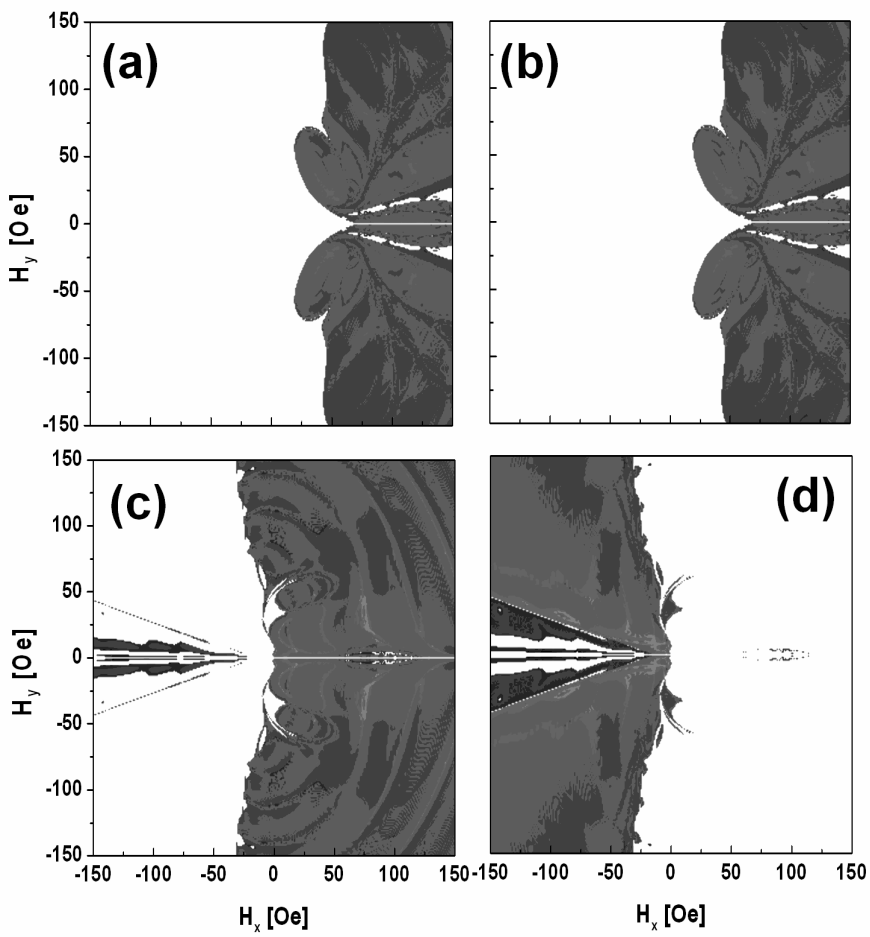

Figure 3.11. Switching diagrams for two interacting particles: (a) The switching diagrams of the particle that receives the pulsed magnetic field of 0/2.75/0 ns and (b) of the particle situated at the distance D=6, and oriented as in Fig. 3.10(a). (c) The switching diagrams of the particle that receives the pulsed magnetic field of 0/2.75/0 ns and (d) of the particle situated at the distance D=6, and oriented as in Fig. 3.10(b).

The diagrams are determined following a similar approach as in the case of isolated ellipsoidal particle and for the same pulse parameters, i.e. 0/2.75/0 ns. As a general remark, one observes that for this specific initial reciprocal orientation of $\mathbf{m}_1$ and $\mathbf{m}_2$, both dipoles present a similar switching diagram as a direct consequence of the strong magnetizing character of dipolar field. In other words, even if only dipole $\mathbf{m}_1$ is subject to the magnetic pulse, both spins will switch together toward the same final state.

This kind situation is undesirable in the case of MRAM elements, where the magnetic pulse is supposed to address a specific magnetic element while all the others preserve their magnetic state.

In the case of coupled dipoles with initial configuration characterized by a bond angle of $90°$ the switching diagrams are displayed in Figs. 3.11(c) and 3.11(d) for dipoles $\mathbf{m}_1$ and $\mathbf{m}_2$. For this particular separation between dipoles, one observes that the switching diagrams for dipoles $\mathbf{m}_1$ and $\mathbf{m}_2$ are complementary, i.e. a white region on the left diagram corresponds to a black region on right diagram and vice-versa. Thus, due to the demagnetizing type interaction field, the final dipoles configuration will be anti-parallel.

Some other results for different configurations as shown in Fig. 3.8 at various separations D=5 (top), 6 (middle), and 7 (bottom) are given in Figs. 3.12–3.15. On the left panel of those figures are the switching diagrams of the moment $\mathbf{m}_1$, and on the right of the moment $\mathbf{m}_2$. As observing all switching diagrams on the bottom of Figs. 3.12-3.15, it is obvious to see that when the separation between two moments is larger, the dipolar field becomes smaller, so that the switching diagram of the moment $\mathbf{m}_1$ gradually approaches the one of an isolated particle discussed previously, whereas the moment $\mathbf{m}_2$ is gradually hardly affected.

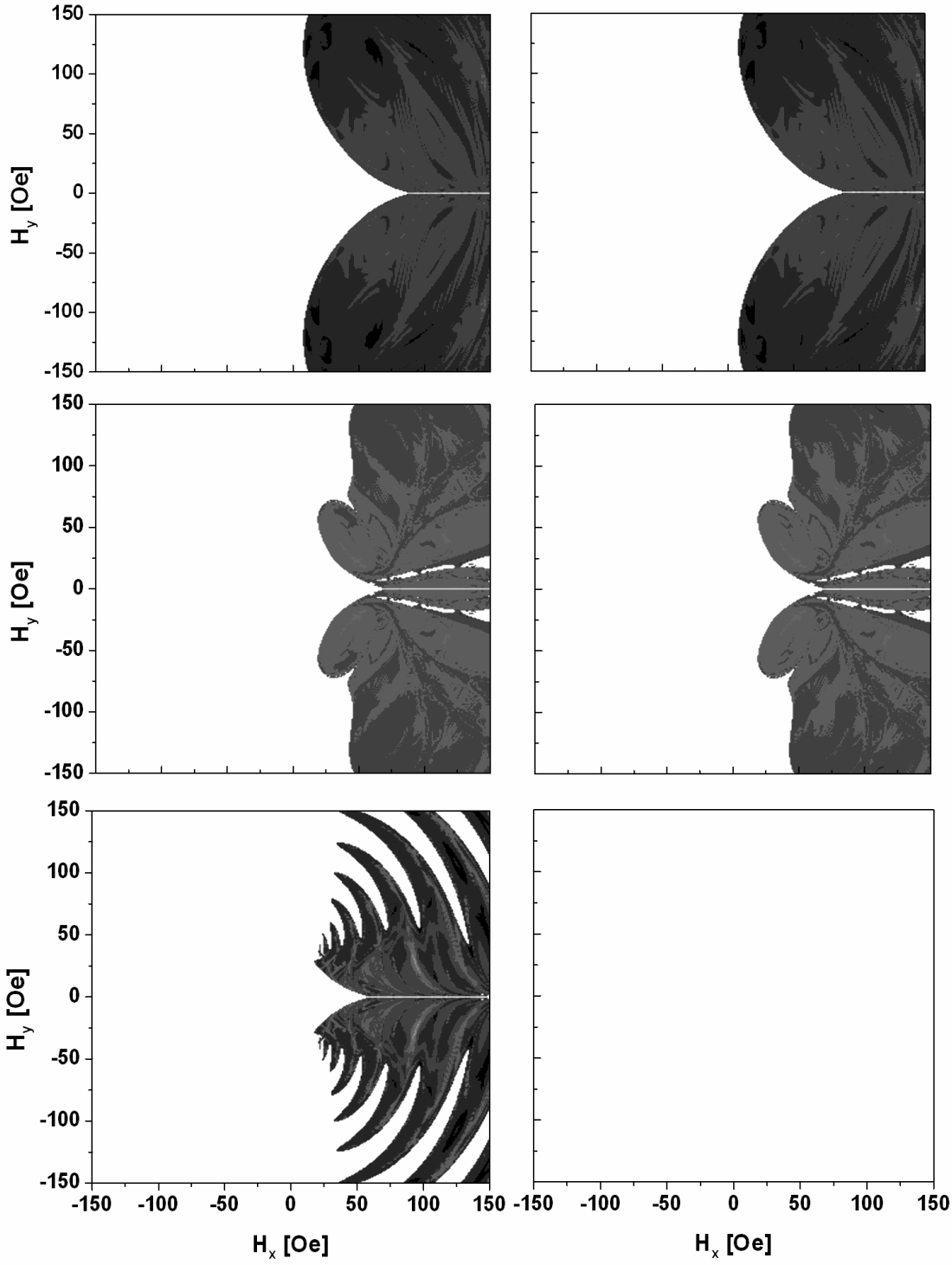

Figure 3.12. Switching diagrams for two interacting particles corresponding to the configuration of Fig. 3.8a. On the left are the switching diagrams for the moment $\mathbf{m}_1$ that receives the pulsed magnetic field of 0/2.75/0 ns, and on the right for the moment $\mathbf{m}_2$ located at different separation with respect to $\mathbf{m}_1$, D=5 (on top), D=6 (middle), and D=7 (at bottom).

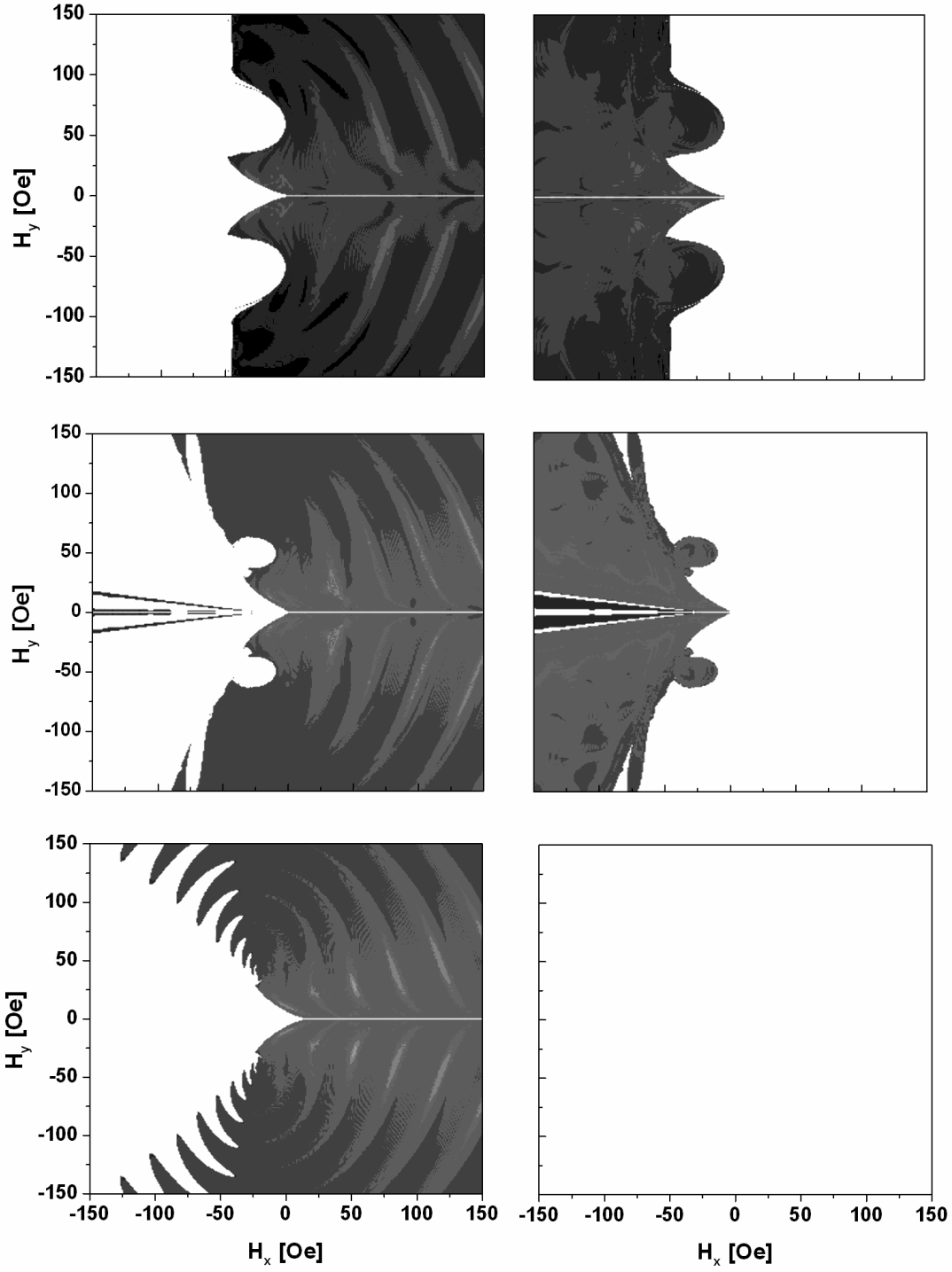

Figure 3.13. Switching diagrams for two interacting particles corresponding to the configuration of Fig. 3.8b. On the left are the switching diagrams for the moment $\mathbf{m}_1$ that receives the pulsed magnetic field of 0/2.75/0 ns, and on the right for the moment $\mathbf{m}_2$ located at different separation with respect to $\mathbf{m}_1$, D=5 (on top), D=6 (middle), and D=7 (at bottom).

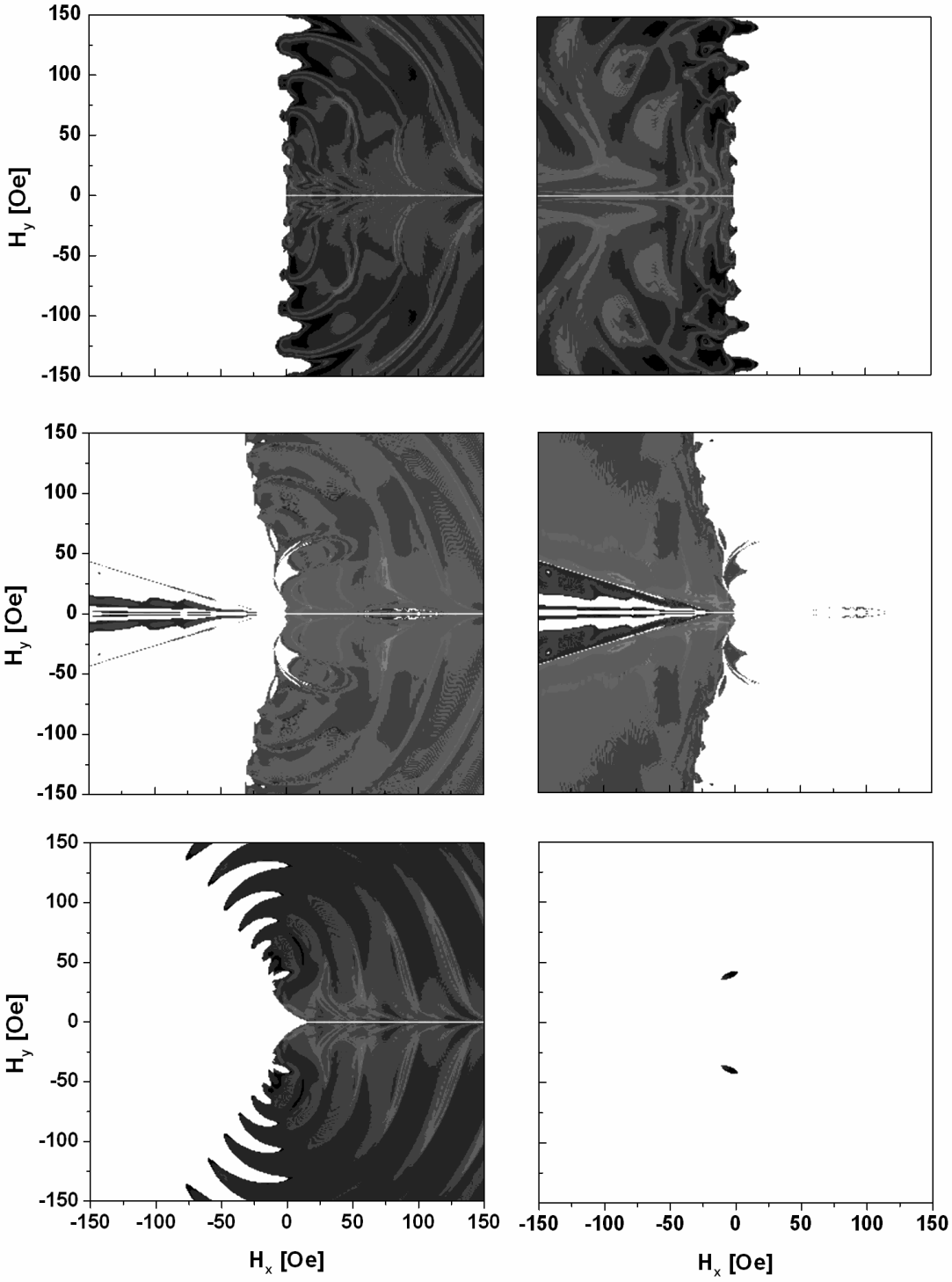

Figure 3.14. Switching diagrams for two interacting particles corresponding to the configuration of Fig. 3.8c. On the left are the switching diagrams for the moment $\mathbf{m}_1$ that receives the pulsed magnetic field of 0/2.75/0 ns, and on the right for the moment $\mathbf{m}_2$ located at different separation with respect to $\mathbf{m}_1$, D=5 (on top), D=6 (middle), and D=7 (at bottom).

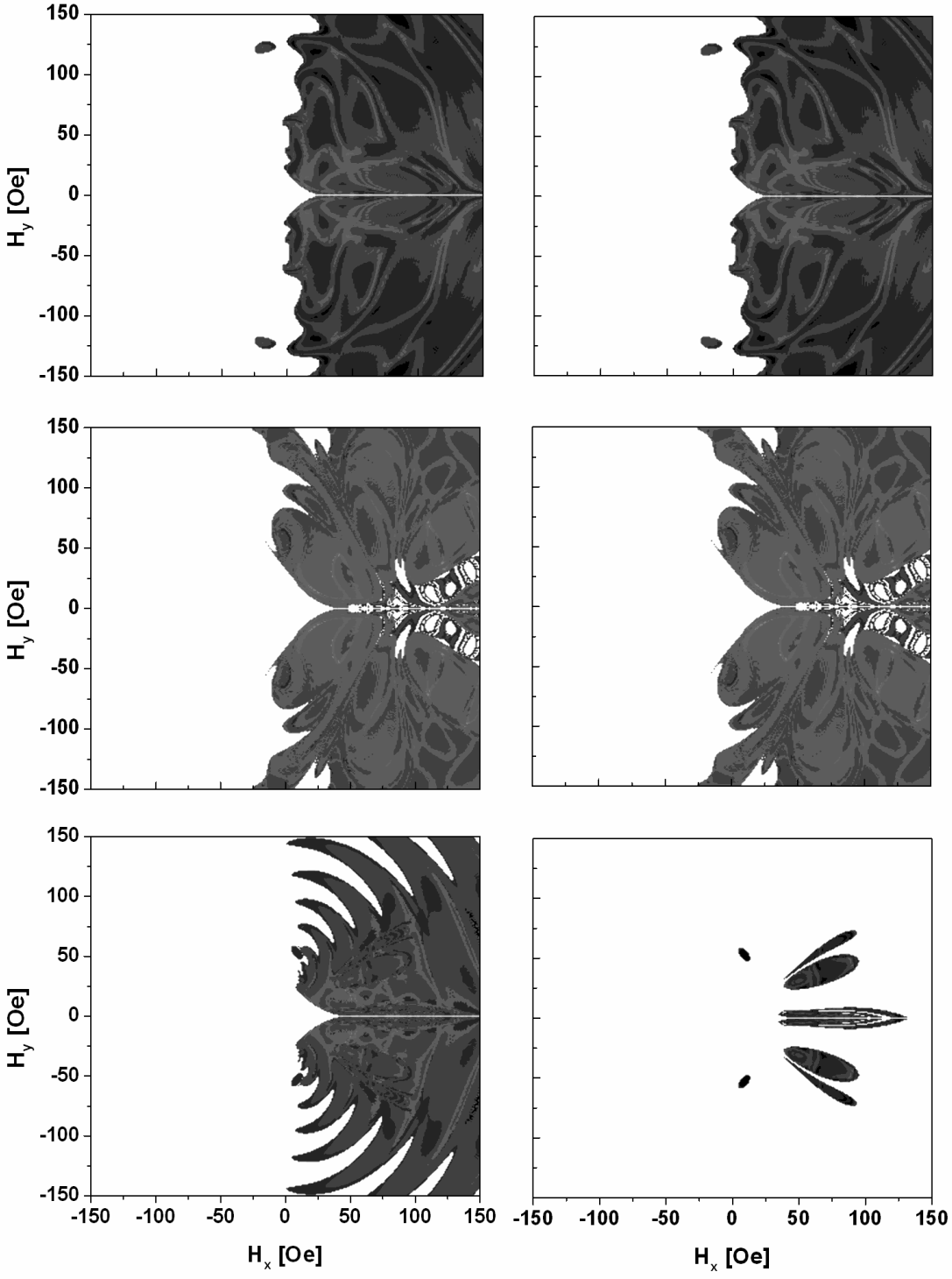

Figure 3.15. Switching diagrams for two interacting particles corresponding to the configuration of Fig. 3.8d. On the left are the switching diagrams for the moment $\mathbf{m}_1$ that receives the pulsed magnetic field of 0/2.75/0 ns, and on the right for the moment $\mathbf{m}_2$ located at different separation with respect to $\mathbf{m}_1$, D=5 (on top), D=6 (middle), and D=7 (at bottom).

From all analysis above we can learn that the final configuration of coupled dipoles is strongly dependent on reciprocal orientation of the spins (bond angle) and interparticle separation. Consequently, in dealing with the issue of improving the density of data storage medium, one needs to carefully pay attention on the dipolar interaction between neighboring magnetic elements.

3.3 Summary

Results of the dynamics switching properties of Stoner-like particles, subject to short magnetic field pulses, obtained by numerical investigations based on the Landau-Lifshitz-Gilbert equation are presented. The switching properties are discussed as a function of the external field pulse strength and direction, pulse length and the pulse shape. The ultrafast switching can be achieved by choosing the right field pulse parameters. It is possible to optimize pulse parameters in order to provide switching over a wide range of applied field directions.

The effects of the dipolar coupling between particles on precessional switching are also analyzed in this chapter. It is found that due to the demagnetizing type interaction field, the dynamics of the coupled system is strongly dependent of the interparticle distance and their bond angle.

Chapter 4

Spin Transfer Switching

The concept of spin angular momentum transfer torque recently proposed by Slonczewski [8] and Berger [6] in 1996 attracted considerable interest. In the presence of an electric current, a torque may act on the magnetization of a thin ferromagnetic layer, arising primarily from the transmission and reflection of incoming electrons. The spin-torque offers a new way to control the writing process in high density magnetic random access memory (MRAM) because a spin-polarized current can switch the magnetization of a ferromagnetic layer more efficiently than a current-induced magnetic field. One year later, Slonczewski proposed a spin-torque based magnetic memory [16], followed immediately by other ideas [18, 69]. Subsequently, it has been shown experimentally that spin transfer can indeed induce switching [70] or microwave oscillations of the magnetization [71], and in 2005 a non-volatile memory using a spin torque magnetization switching, so-called spin transfer torque MRAM (STT-RAM) was presented by Hosomi *et al.* [17] with a writing speed as high as 2 ns, and a write current as low as $200\ \mu\text{A}$. The technology using spin-torque effect is expected to increase the recording density of MRAM devices.

The aim of this chapter is twofold. First, we present briefly the concept of the spin transfer torque and discuss its role on the dynamic magnetization switching of the free

magnetic layer in a spin-valve-type trilayer structure. In order to determine the spin-torque current pulse parameters, where fast and stable switching can be achieved, we have studied the magnetization's dynamics properties as a function of applied current pulse amplitude and shape, waiting time, and initial orientation and also as a function of the Gilbert damping constant. We analyze also how the thermal fluctuations affect the switching behavior. Second, we have studied the magnetization switching under coexistence of the spin-transfer torque and the torque by a pulsed magnetic field. The main goal is to determine the parameters of field pulse for the fast and stable switching under spin-torque effects can be achieved.

4.1 Spin transfer torques

Spin transfer torques (STT) have been intensively explored during the last 20 years. In the middle of the 80s, theoretical and experimental studies on current induced domain wall (DW) motion in ferromagnetic films [72, 73], showed that an electrical current sent through ferromagnetic films or wires containing DW, interacts with the walls and, if the current density is high enough, can cause DW motion. In 1989 Slonczewski calculated STT for the case of current traversing on ferromagnetic/non-magnetic tunnel barrier/ferromagnetic MTJ [74]. It turned out to be impractical to apply torques across MTJs, and the following theoretical works [6, 8] by Berger and Slonczewski predicted much more efficient spin transfer in metallic multilayers, such as ferromagnetic /non-magnetic metal/ferromagnetic (F/N/F) structures. These papers triggered further theoretical as well experimental research [70, 75, 76] on STT.

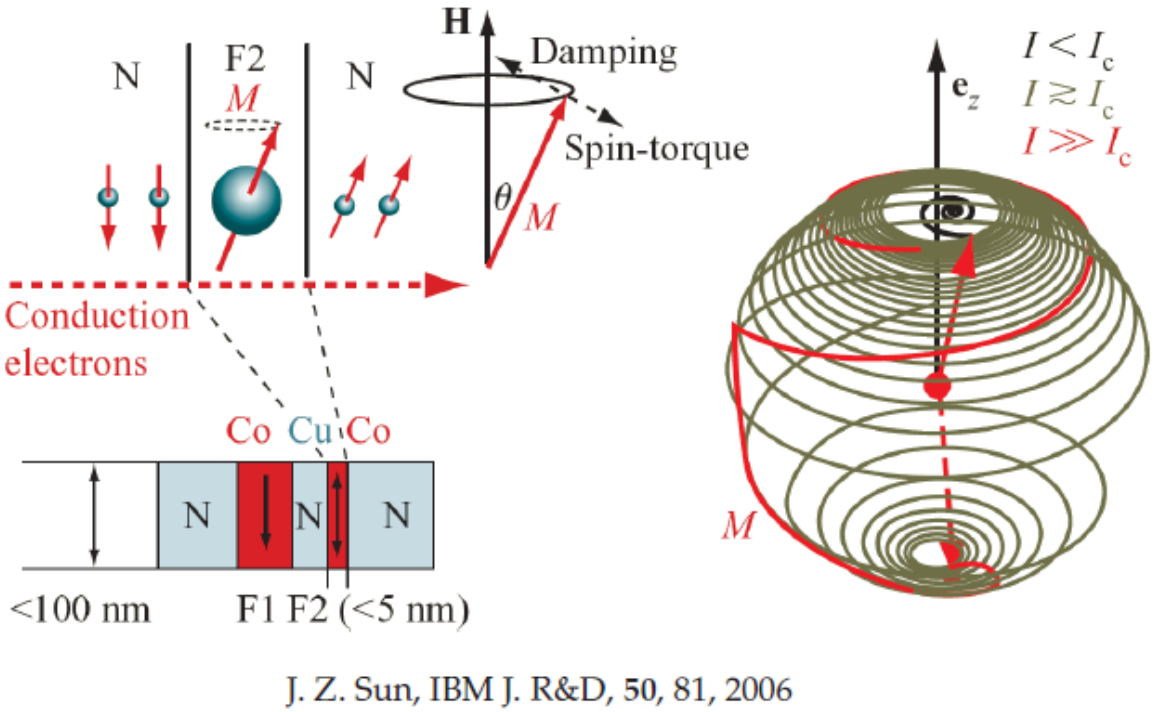

J. Z. Sun, IBM J. R&D, 50, 81, 2006

Figure 4.1. Illustration of the STT in a F/N/F pillar (left). Magnetization switching trajectory in a free layer subject to STT (right), after [77].

Let us now present briefly their work and the remarkable idea of using STT for the writing process in MRAM memory cells. Consider a spin-valve-type trilayer F/N/F device containing a thick pinned/fixed magnetic layer and a thin free magnetic layer, separated by a nonmagnetic metal spacer as shown in Fig. 4.1 [77], where the electrons flow from the left to the right (negative current) traversing the two ferromagnetic layers. The pinned layer serves as a polarizer for the unpolarized electrons and, assuming that the thickness of the spacer N is smaller than the spin diffusion length in N, the conduction electrons are spin-polarized when entering the free layer. If the magnetic moment of the free layer is oriented at an angle to the moment of the fixed layer, the free layer will absorb the component of the incoming spin-polarized current transverse to the

layer's magnetic moment, as a result the free layer will feel a torque tending to rotate its moment toward the orientation of the incoming spins, as schematically illustrated in Fig. 4.1 (left). The spin torque vector will act on the magnetic moment of the free layer in the opposite direction from the magnetic damping torque vector, as shown in Fig. 4.1 by the black dashed arrows. Fig 4.1 (right) illustrates the magnetization switching trajectory in the free layer subject to STT. The magnetic moment can perform three types of precessional motion when subject to spin torque: when the current is below a certain threshold value the excited magnetic moment relaxes back to the easy axis; if the current is just above the threshold then the moment makes many precessional cycles before it reverses its direction; and finally, much higher current than the threshold value leads to a quick magnetization reversal.

The remarkable property of STT in F/N/F structures offering a new way controlling the magnetization reversal in MRAM memory cells which replaces the conventional method utilizing magnetic field. The transfer of the spin angular momentum between two magnetic layers by the current flowing perpendicular to plane can reverse the magnetization of one of the magnetic layers. As mentioned above the current becomes spin polarized after the electrons pass through the pinned layer. The spin-polarized electrons cross the nonmagnetic spacer and then, through conservation of angular momentum, place a torque on the free layer, which switches the orientation of the free layer's magnetization parallel to the pinned layer's magnetization. If a current of the opposite polarity is applied, the electrons pass first through the free layer and after crossing the nonmagnetic spacer, a torque is applied to the fixed layer. However, due to

its larger thickness, the fixed layer does not switch. Simultaneously, a fraction of the electrons will then reflect on the fixed layer and travel back across nonmagnetic spacer before interacting with the free layer. In this case the spin torque tends to align antiparallelly the magnetizations of the two layers. This interaction due to spin-transfer is qualitatively different from the Ruderman–Kittel–Kasuya–Yosida exchange observed in the absence of the current, and also is different from the interaction with the magnetic field created by the current. In the simplest case such structure has two stable magnetic configurations, with the magnetizations of the two layers aligned parallel or antiparallel. A spin-transfer transmission mode or a spin-transfer reflection mode can be used to write the information.

4.2 Dynamic and temperature effects in spin transfer switching

Analytical and numerical simulations have shown that the magnetization reversal becomes very complicated when the spin-torque effect is taken into account, both in a macrospin model [75, 77-79] and in a non-uniform magnetization model [80-83]. Because the spin-torque can increase or decrease the magnetic energy, stable precessional states can exist, and thus the magnetization will never converge to a final stable direction. Moreover, there are situations in a hysteresis loop when the magnetization increases with decreasing magnetic field. Thus, the analysis of thermal fluctuations in these systems is complicated because the self-oscillatory regions may exits in addition to stationary equilibrium states, and thermal fluctuations can induce switching between them. Since spin-transfer torque can pump a magnetic energy into the magnetic system, and thus the equilibrium temperature of the magnetic system is ill defined, in Ref. 84 an effective

temperature and effective activation energy are introduced, based on a stationary solution of the Fokker-Planck equation. The numerical integration of stochastic Landau-Lifsitz equation is used to support this theory. Using Fokker-Plank rate calculation, Apalkov *et al.* [84] show that the spin-torque effect increases the Arhenius factor in the switching rate, not by lowering the energy barrier, but by raising the effective spin temperature.

In Refs. [85-89] it is shown experimentally that the sub-ns pulse durations leading to successful switching events are discrete durations reflecting the precessional nature of magnetization dynamics and the topological peculiarities in the set of possible magnetization trajectories. Flat plateaus alternating with rounded steps in the switching diagrams are explained taking into account the statistics of the possible initial states due to thermal fluctuations. The model developed in Ref. 88 assumes that the nonzero temperature results in a probabilistic distribution of the initial direction of the free layer's magnetization, already present when the current pulse is switched on, but that the temperature has no additional effect during the pulse application (i.e., during reversal).

An essential problem in the development of a device based on the spin-torque transfer is the evaluation of the minimum switching current that ensures a reliable magnetization reversal at high operating frequencies. Switching diagrams represented as current versus pulse duration plots [85] are very useful in finding optimum conditions for an error-free switching. In previous studies the influence of parameters as pulse amplitude, polarity and duration [85], or bias hard axis fields [87] on switching diagrams were considered. With increasing demand for fast and low power nonvolatile memory devices the influence of other variables on the switching diagrams must be considered. In

this section we present how the current sweep rate, damping constant, initial position, waiting time, and also the thermal fluctuations affect the switching, the reliability, and the writing speed of spin-torque devices.

4.2.1 Model

In the absence of thermal fluctuations the dynamic behavior of the free layer's magnetization $\mathbf{M} = M_s \mathbf{m}$ ($M_s = |\mathbf{M}|$ being the saturation magnetization and assumed to be constant in magnitude) is described by LLG equation (1.42) with the spin-transfer term included [6, 8],

$$\frac{d\mathbf{M}}{dt} = -\gamma \mathbf{M} \times \mathbf{H}_{\text{eff}} + \frac{\alpha}{M_s} \mathbf{M} \times \frac{d\mathbf{M}}{dt} + \gamma \frac{a_J}{M_s} \mathbf{M} \times \left(\mathbf{M} \times \mathbf{m}_p \right), \tag{4.1}$$

where $\gamma = 0.0176$ Oe$^{-1}ns^{-1}$ is the gyromagnetic ratio, α the Gilbert damping constant, $\mathbf{H}_{\text{eff}}$ is the deterministic effective field which incorporates the applied field and the effects of different contributions to the free energy, the unit vector $\mathbf{m}_p$ gives the direction of the spin polarization (direction of the fixed layer's magnetization), and the parameter a_J, which represents the strength of spin-transfer torque, is proportional to the current density J_e as follows: $a_J = \hbar J_e / 2|e| M_s d$, where e is the electron charge, d is the thickness of the free layer, $\hbar$ is the reduced Planck constant. The parameter a_J has the dimension of a magnetic field, and is positive when the electrons flow from the free into the fixed layer, stabilizing the anti-parallel configuration. The applied current is perpendicular to the sample's plane, and it is assumed to carry a spin polarization parallel to the pinned layer's magnetization. We assume that the parameter a_J is independent of the orientation of free

layer, namely the spin-transfer torque is proportional to the sine of the angle between $\mathbf{m}_p$ and $\mathbf{m}$ (i.e. the so-called sine approximation). The damping parameter is treated as a constant, even though there are theoretical and experimental evidences that α can be affected with various factors such as the magnetization's orientation [90, 91] and temperature [92]. We also note that the validity of the Gilbert damping term in the presence of spin-torque is being debated in literature [93]. In our simulations the effective field consists only of demagnetizing field, no further anisotropy being considered. The magnetic field created by the applied current, the magnetostatic and exchange coupling fields between the two layers are neglected.

Equation (4.1) can be equivalently written as:

$$\frac{1+\alpha^2}{\gamma}\frac{d\mathbf{M}}{dt} = -\mathbf{M}\times\left(\mathbf{H}_{\text{eff}} + \alpha\, a_J\, \mathbf{m}_p\right) - \frac{\alpha}{M_s}\mathbf{M}\times\left[\mathbf{M}\times\left(\mathbf{H}_{\text{eff}} - \frac{a_J}{\alpha}\mathbf{m}_p\right)\right] \tag{4.2}$$

where the first term on the right-hand side describes the gyromagnetic precession (conserving the energy), and the second term describes damping (dissipating energy and making the system to relax to a local energy minimum).

From Eq. (4.2) we observe that the spin-torque is fundamentally different from the effective field and from damping, having both effects: it is a source of precessional motion as a magnetic field, and also can serve as damping/antidamping source (see Fig. 4.2). Due to this dual function of the spin torque the magnetization reversal becomes a very complicated issue even for a single domain (macrospin) model.

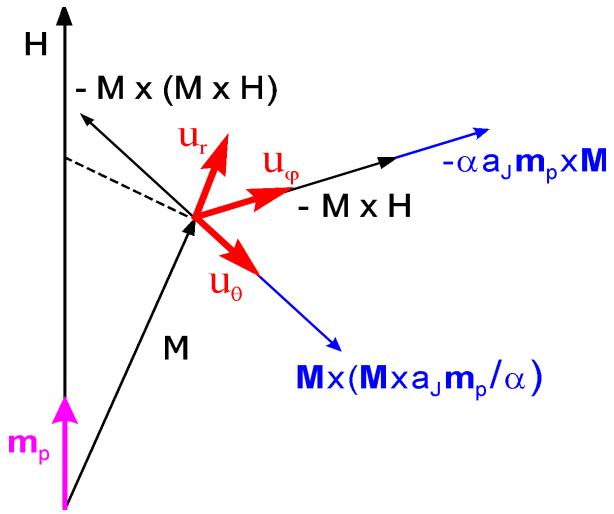

Figure 4.2. Vector diagram of LLG's equation (4.2) with the spin torque term added.

In the presence of thermal agitation it is supposed that the damping α describes in LLG equation only the statistical (ensemble) average of rapidly fluctuating random forces, and a stochastic thermal field $\mathbf{H}_{th}$ should be added to the deterministic effective field $\mathbf{H}_{eff}$ in Eqs (4.1) and (4.2).

The stochastic field is assumed to be a Gaussian random process with a white spectrum [38],

$$\begin{aligned}
&\left\langle H_{th,i}(t)\right\rangle = 0,\\
&\left\langle H_{th,i}(t)H_{th,j}(t')\right\rangle = 2D\delta_{ij}\delta(t-t'),\\
&D = \frac{\alpha k_B T}{\gamma M_S V},
\end{aligned}$$

where $\langle\ \rangle$ means the statistical average over different realizations of the fluctuating field, k_B is Boltzmann's constant, i and j are Cartesian indices, the Kronecker δ_{ij} expresses that the different components of $\mathbf{H}_{th}$ are uncorrelated, an the Dirac δ expresses that

$H_{th,i}(t)$ and $H_{th,j}(t')$ are correlated only for time intervals $t-t'$ much shorter than the time required for an appreciable change in $\mathbf{M}$. The constant D as discussed in the section 1.5 gives the strength of the thermal fluctuations, and it is determined from statistical-mechanical considerations.

We assume that solely the free layer is affected by thermal fluctuations, while $\mathbf{m}_p$ does not change its direction. Also it is assumed that thermal fluctuations do not affect the spin torque term a_J, because the spin torque comes from the conduction electrons, whose transport properties are less affected by thermal fluctuations since the Fermi level is much higher than thermal energy. Besides, the fluctuating field is assumed independent of the spin torque. No temperature dependence of the anisotropy constant and saturation magnetization is taken.

The stochastic field changes the deterministic motion of the magnetization into a random walk. The stochastic LLG equation is numerically integrated using an implicit midpoint time-integration technique [51]. The magnetic properties follow from an average over many numerical realizations of the dynamic process (discrete Brownian paths).

The free magnetic layer is assumed to be single domain, ellipsoid shaped, making the demagnetizing field uniform across the entire layer. The saturation magnetization $4\pi M_S = 12$ kG, as for ferromagnetic material Cobalt, was chosen. The ellipsoid's principal axes are taken along *x, y* and *z* axes, respectively (see Fig. 4.3): long-axis length $2a = 100$ nm (along *Ox* axis), short-axis length $2b = 75$ nm (along *Oy* axis), and thickness

$d = 2\,\text{nm}$, leading to demagnetizing factors $N_x/4\pi = 0.014$, $N_y/4\pi = 0.022$, and $N_z/4\pi = 0.964$, and accordingly to demagnetizing fields: $H_{D,x} = N_x M_s = 169.3$ Oe, $H_{D,y} = N_y M_s = 259.7$ Oe, $H_{D,z} = N_z M_s = 11.57$ kOe, and to in-plane uniaxial shape anisotropy field $H_{\text{sh}} = \left(N_y - N_x\right) M_s = 90.4$ Oe.

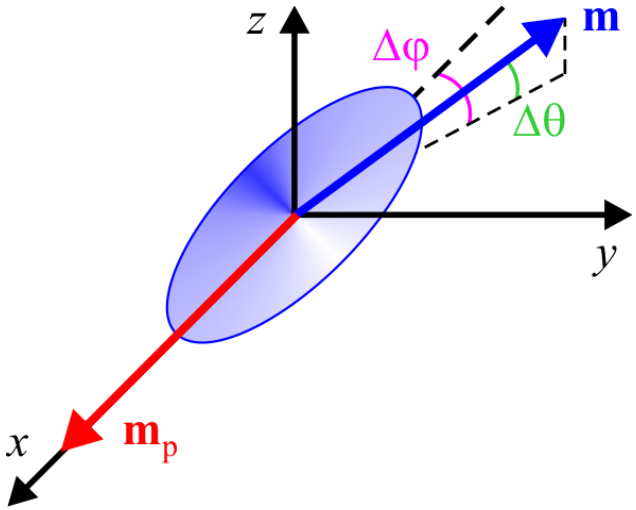

Figure 4.3. Schematic of the free layer, assumed to be ellipsoid shaped, and single domain. The ellipsoid's principal axes are along x, y, and z axes, with x and y in the plane of layer, and x along long axis. The axes' lengths are: $2a = 100$ nm, $2b = 75$ nm, and thickness $d = 2$ nm. The initial direction of the free layer's normalized magnetization $\mathbf{m}$ is described by the angles $\Delta\theta$ and $\Delta\varphi$. The pinned ferromagnetic layer's normalized magnetization $\mathbf{m}_p$ is held fixed at the direction of the free layer's long axis.

Hereby we assume that the free layer has two contributions to anisotropy: an easy plane and an easy axis that is directed in this plane. In this way, in the absence of any applied magnetic field or electric current, the $\mathbf{m}$'s equilibrium orientations are along $-x$ and $+x$ axis. By passing a current through spin-valve device one can switch $\mathbf{m}$ back and forth between these two stable states. A current $I = 1$ mA corresponds to a current density $J_e = I/\pi ab = 0.17\times 10^8$ A/cm^2 and to $a_J = 292.7$ Oe. The direction $\mathbf{m}_p$ of the fixed layer's

magnetization is taken along $+x$ direction, so that the free layer's easy axis is parallel to the spin polarization of the electric current. If initially the magnetic moments of fixed layer and free layer are aligned, there is no torque acting on the free layer. However, at finite temperature the thermal agitation assures that at no time this happens. In our simulations in the absence of thermal fluctuations, the initial direction of **m** is described by the angles $\Delta\theta$ and $\Delta\varphi$, as shown in Fig. 4.3.

Because an instantaneous change of the applied current from zero to any other value is not very realistic, sinusoidal time dependence for the current pulse rise and fall are assumed (see Fig. 4.4).

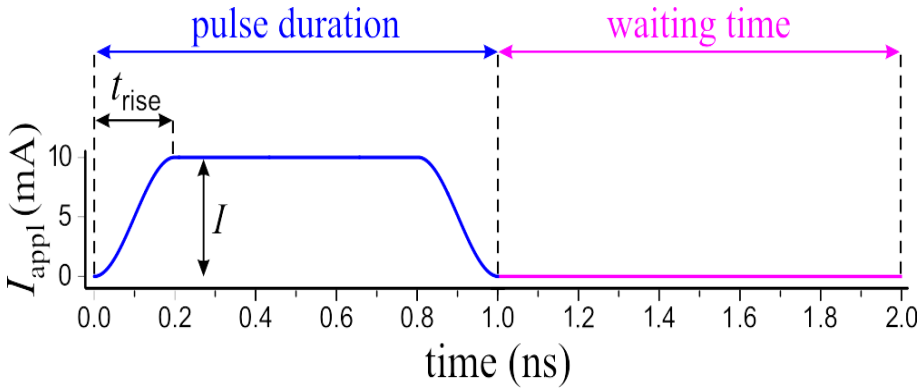

Figure 4.4. Time dependence of the applied current pulse. The sweep rate is defined as $\upsilon_I = I/t_{rise}$ and it is constant, so that the rise/fall time is function of pulse's amplitude. Unless otherwise specified, the final state of the magnetic moment is taken after a waiting time equal with the pulse duration.

The rise/fall time is a function of the pulse's amplitude so that the current sweep rate υ_I, defined as the ratio between the amplitude and pulse's rise/fall time, is constant. Pulse duration is defined as the interval between the moment when current begins to increase, and the moment when the current comes back to zero. At a given temperature the switching properties are discussed as a function of applied current pulse amplitude,

duration and shape. Unless otherwise specified, the final state of the magnetic moment is taken after a time equal with the pulse duration, following pulse's termination.

4.2.2 Dynamic effects

Let us assume that before applying the current pulse the free layer's magnetization $\mathbf{m}$ is slightly tilted away from the negative x direction, into xy plane, making a small angle $\Delta\varphi$ with $-x$ axis (see Fig. 4.3). As it is shown by dynamical equation (4.2), the first term on the right-hand side pulls the magnetization vector away from the xy plane in $+z$ direction, while the second term causes a movement into the direction of the $-x$ axis. The torque created by a negative current pulse (which stabilizes the parallel configuration) has an opposite effect: the precessional term pulls $\mathbf{m}$ in $-z$ direction, and the second term serves as an antidamping source, pushing $\mathbf{m}$ in the opposite direction as demagnetizing field does, away from $-x$ axis direction. The spin-torque term increases as the applied current increases. In some ranges of applied current amplitude and duration, $\mathbf{m}$ switches its orientation to become aligned with the spin polarization. As we see from this simple description, it is of paramount importance to take into account a current pulse with an increasing time, instead of a current applied infinitely abruptly (Heaviside step function). On the other hand, the magnetization reversal in a time dependent applied current is different from that in a constant current, making the magnetization dynamics quite complicated.

The damping α is not accurately known in a spin valve system, and recent studies [94-96] for ultrathin films show that α is enhanced when a nonmagnetic metal is

deposited on a ferromagnetic film. Consequently, first we have studied the damping dependence of the spin torque assisted switching. For convenience, in all figures presented throughout this chapter the absolute value of the applied current is used, while a negative current was used in simulations in order to switch **m** from antiparallel (AP) to parallel (P) configuration.

The AP-P switching maps in the absence of thermal fluctuations ($T = 0$ K), as a function of current pulse amplitude (from 0 to $I_{\max} = 10$ mA) and duration (from $t_{\min} = I_{\max}/\upsilon_I$ to $t_{\max} = 2$ ns), for a current sweep rate $\upsilon_I = 1\,\mathrm{mA/ps}$, and different values of damping constant α, are presented in Fig. 4.5(a). The minimum pulse duration $t_{\min}$ is imposed by the condition to have a "pure" sinusoidal pulse for the maximum amplitude $I_{\max}$. Initially the magnetization **m** of the free layer is in the film plane ($\Delta\theta = 0$), making an angle $\Delta\varphi = 10^{-3}$ degree with the direction of the pinned layer. The state of the magnetic moment is taken after a time equal with the pulse duration, following the pulse's termination. From Fig. 4.5(a) we can see that the boundary which delimits the switching and non-switching regions is not only a smooth hyperbola, it also has superimposed discrete features with a seashell spiral pattern or onion-like structure. In the seashell patterns the switching and non-switching areas alternate with increasing current pulse amplitude and duration. When the pulse's length is too short, a significant ringing of the magnetization still exists during the current pulse and the final state is determined by the position of the magnetization at the end of the pulse. Consequently, the layered structure predominates for short current pulses.

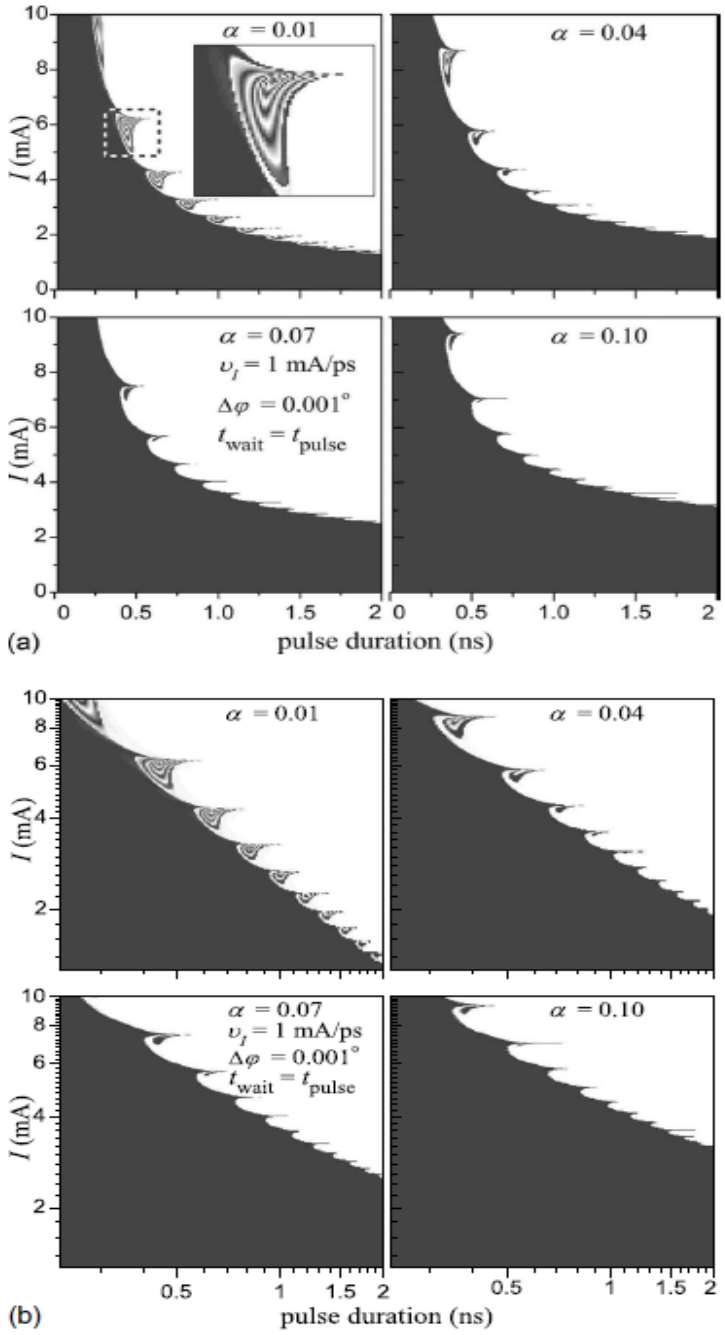

Figure 4.5. (a) AP-P switching diagrams at $T = 0\,\mathrm{K}$, as a function of current pulse amplitude and duration, for a current sweep rate $\upsilon_I = 1\,\mathrm{mA/ps}$, and different values of damping constant α. Initially the magnetization of the free layer is in the film plane ($\Delta\theta = 0$), making an angle $\Delta\varphi = 10^{-3}$ deg with the direction of the fixed layer. Black areas represent $m_x = -1$ (where m_x is the **m**'s projection on the x axis), white areas represent $m_x = 1$, and the intermediate values of m_x are represented with shades of gray. The state of the magnetic moment is taken after a time equal with the pulse duration, following the pulse's termination. The inset (top left) shows a zooming into a portion of the border between stable switching and non-switching zones. (b) same as (a) but on a log-log scale.

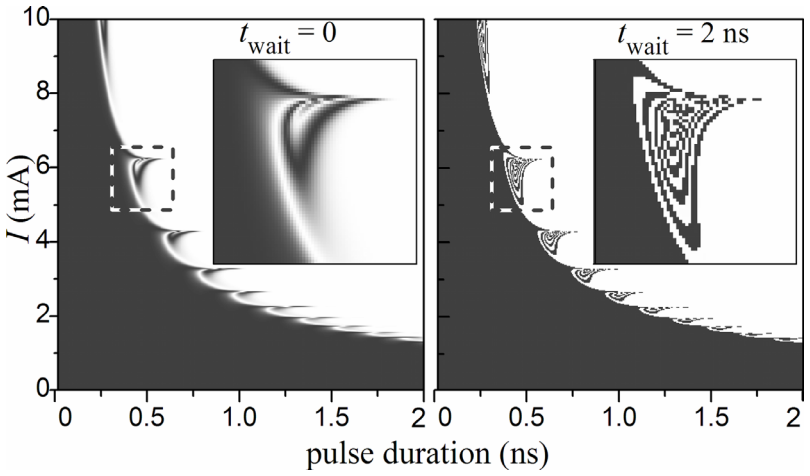

Figure 4.6. AP-P switching diagrams at $T = 0$ K for a current sweep rate $\upsilon_I = 1\,\text{mA/psec}$, damping constant $\alpha = 0.01$, the state of the magnetic moment being taken after a waiting time $t_{\text{wait}} = 0$ (left) and $t_{\text{wait}} = 2$ ns (right), respectively, after pulses' termination.

An increase in α diminishes the layered structure of the switching diagrams, giving rise to a clearer separation between the non-switching/switching regions, but decreases the area of stable switching region, i.e., higher amplitude or longer pulse is needed to switch the magnetization. An increase in α increases the energy dissipation rate [see Eq. (4.2)] and in this way diminishes the ringing of the magnetization. The position of the seashell spiral patterns are changing with the increase in α, shifting toward higher values of the current amplitude.

On a log-log scale the border between switching and non-switching regions is almost a straight line, with seashell spiral patterns superimposed [see Fig. 4.5(b)]. An increase in α decreases the straight line's inclination and changes also its position, decreasing the extent of switching region. The straight line border illustrates that the switching requires a pulse duration that scales with the inverse of the current pulse

amplitude, recalling the result of Sun from Ref. 75. Further in this chapter the Gilbert damping is kept constant, and a value $\alpha = 0.01$ is used.

For $\alpha = 0.01$ the magnetization vector is still ringing after a waiting time equal with pulse duration, and consequently in corresponding diagram the magnetization is not only along $-x$ or $+x$ axis in the border region, but can take any other direction, shown in Fig. 4.5 with shades of gray. If some states of intermediate orientation are created by a given pulse, these states will relax to either parallel or antiparallel state, along easy axis, after a sufficient long time, as we can see in the right panel of Fig. 4.6, where the switching diagram is built using the magnetization's orientation after a waiting time $t_{\text{wait}} = 2$ ns, when the magnetization's ringing almost vanishes and **m** is either along $-x$ or along $+x$ axis. The seashell spiral pattern of the diagram persists even after a long time after the current pulse is cut-off, this being a signature of dynamical effects in spin torque switching. Also, it exists when the current is cut-off (see left panel in Fig. 4.6) and evolves in time into a more intricate structure (see right panel in Fig. 4.6).

Because no interaction has been taken between the pinned and free layers, the P-AP switching diagrams are similar, only the sign of m_x being reversed. All the results presented in this section are obtained when a current pulse is applied to a spin-valve in AP state.

Flat plateaus alternating with rounded steps in experimental switching diagrams were reported by Devolder *et al.* in Ref. 88 and they were explained by taking into account the statistics of the possible initial states due to thermal fluctuations. However,

our results show that a seashell spiral pattern can be obtained in the absence of thermal fluctuations, i.e., at $T = 0$ K, with no distribution of the initial states, only as an effect of the dynamics described by the LLG equation with a spin-transfer term included. The reported pulse durations in Ref. 88 are from 1 to 10 ns (full width at half maximum), with a rise time of 55 ps, a maximum current of 20 mA, and a 1 nm thick CoFe free layer, etched into 75×150 and 75×113 nm^2 elongated hexagons, respectively.

From Figs. 4.5 and 4.6 we can see that in the border region the final state is sensitive to the pulse duration and amplitude. But also the precession of the magnetization is very sensitive to these parameters, as we can see in Figs. 4.7 and 4.8. In the first case from Fig 4.7 one observes that the magnetic moment can cross the energy barrier, from -1 to $+1$, followed by a return to the initial state, while in the second and third cases the magnetic moment oscillates many times between -1 and $+1$, the magnetization finally relaxing to the reverse easy axis position $m_x = +1$.

We can observe not only an in-plane dynamics of the magnetic moment, but also a significant out-of-plane component (*z* direction) during the oscillation. However, we note that not all three axes are equal in Figs. 4.7 and 4.8, namely that z axis is from -0.4 to $+0.1$, while x and y axes are from -1 to $+1$. Thus, current pulses with the same amplitude but different duration have not only different switching outcomes, but also very different precession trajectories.

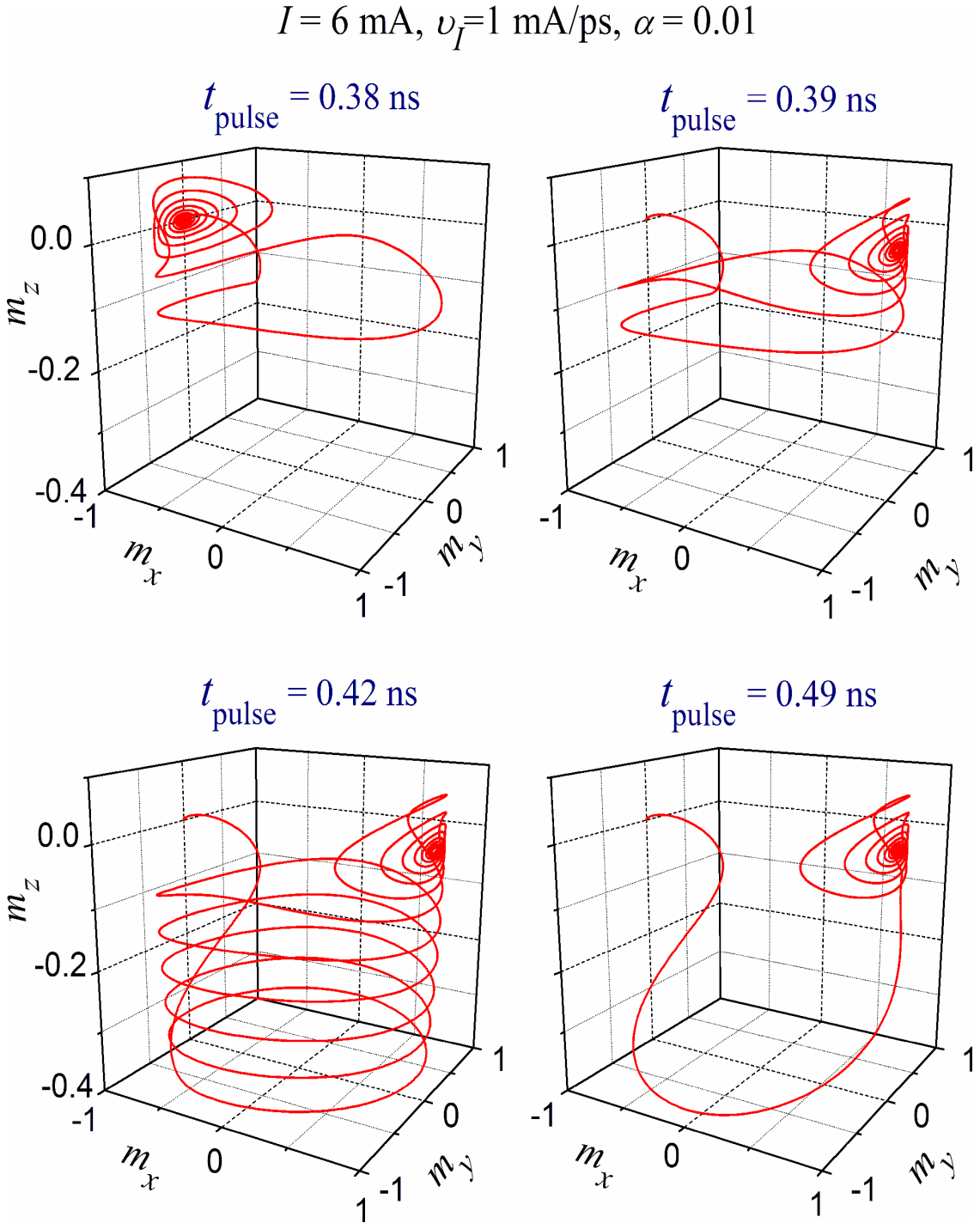

Figure 4.7. The precession of magnetization **m** under the influence of a spin current pulse with $I = 6$ mA, $\upsilon_I = 1$ mA/ps, and different values of the pulse duration: $t_{\text{pulse}} = 0.38, 0.39, 0.42,$ and 0.49 ns, for a damping $\alpha = 0.01$. Initially **m** is in the film plane, making an angle $\Delta\varphi = 10^{-3}$ degree with $\mathbf{m}_p$.

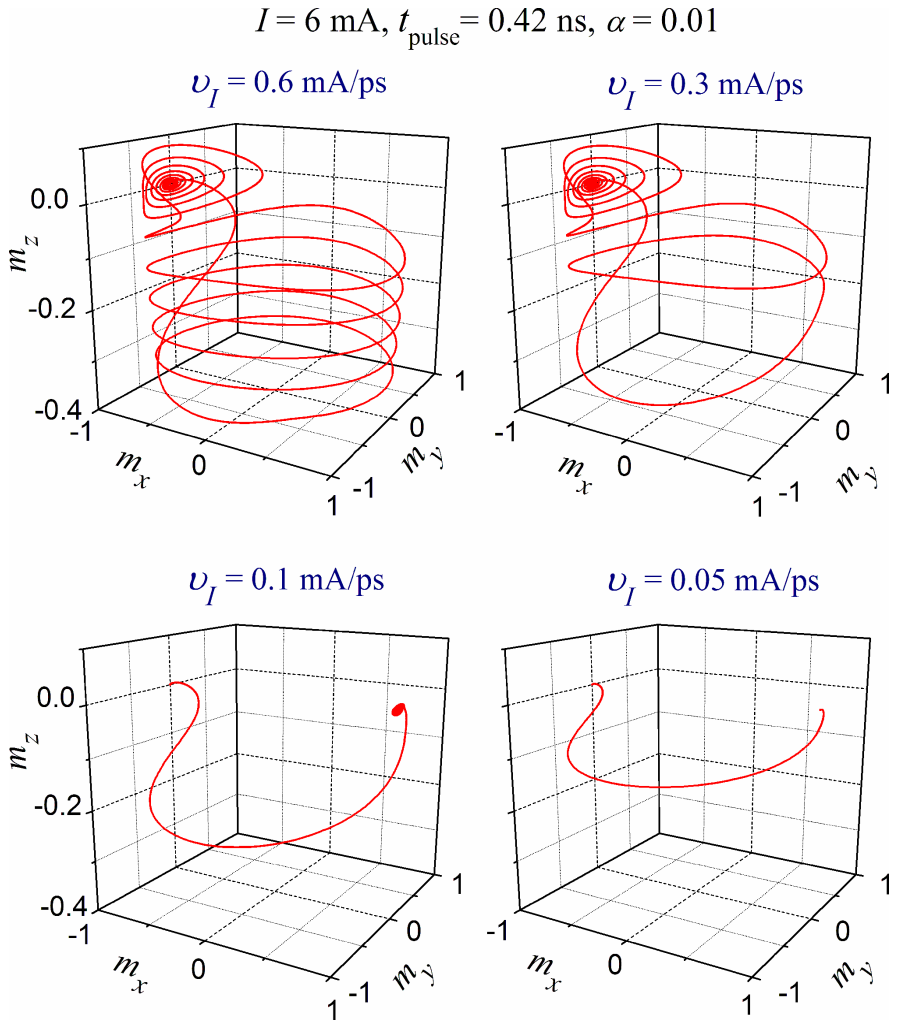

Figure 4.8. The precession of magnetization $\mathbf{m}$ under the influence of a spin current pulse with $I = 6\ \text{mA}$, $t_{\text{pulse}} = 0.42\ \text{ns}$, and different values of the current sweep rate: $\upsilon_I = 0.6, 0.3, 0.1, \text{and } 0.05\ \text{mA/ps}$, for a damping constant $\alpha = 0.01$. Initially $\mathbf{m}$ is in the film plane, making an angle $\Delta\varphi = 10^{-3}$ degree with $\mathbf{m}_p$.

Decreasing the pulse's sweep rate, namely increasing the pulse's rising time, the out-of-plane movement of the magnetization diminishes, and also the ringing diminishes (see Fig. 4.8). For a fast and reliable switching such ringing must be avoided, as the damping time can take several nanoseconds. The ringing may be diminished using a relatively slow rise time pulse (see Fig. 4.8, where in the last case a ballistic trajectory is obtained).

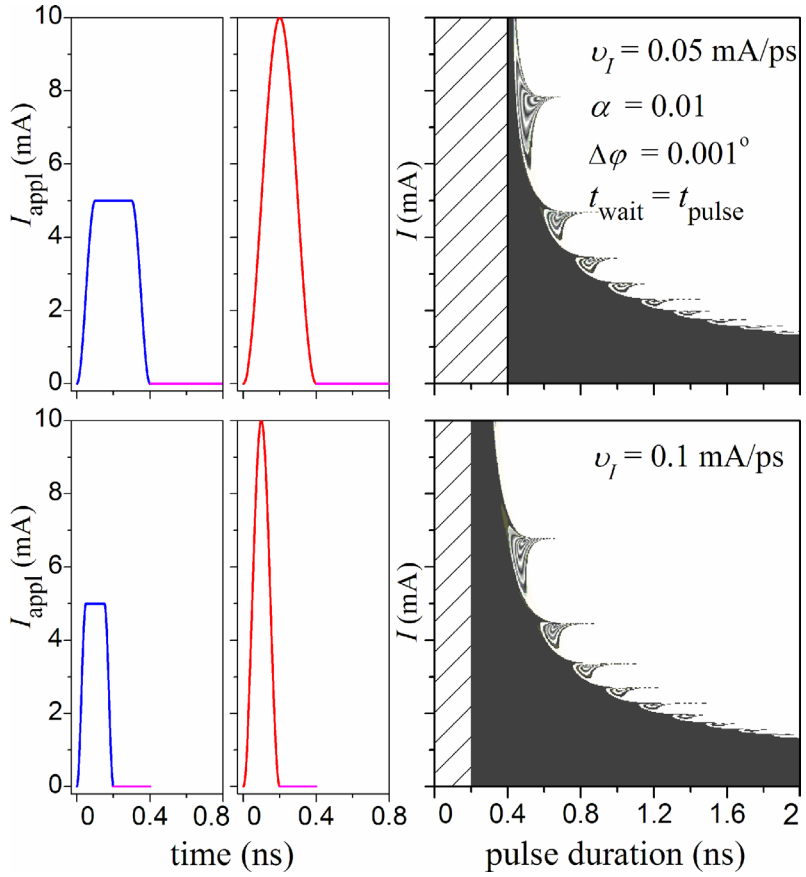

Figure 4.9. AP-P switching diagrams at $T = 0$ K for a current sweep rate $\upsilon_I = 0.05$ mA/ps (up right), and $\upsilon_I = 0.1$ mA/ps (down right), respectively, for a damping constant $\alpha = 0.01$. In the hatched zones no current pulses is applied. In the left panels the applied current pulses corresponding to minimum pulse duration $t_{min} = I_{max}/\upsilon_I$ for $I_{max} = 5$ mA and $I_{max} = 10$ mA, respectively, are presented. For $I_{max} = 10$ mA the pulse is "pure" sinusoidal.

However even diminishing sweep rate, the switching properties are dominated by the details of the magnetization's precession, and a layer-like structure of switching diagram has been obtained also for $\upsilon_I = 0.05$ mA/ps (see Fig. 4.9). Decreasing the sweep rate also diminishes the region of stable switching (white region in switching diagram).

In Ref. 88 the switching duration is defined as the instant time when the hard axis is overcome, i.e., when the condition $m_x = 0$ is fulfilled. However, from Figs. 4.7 and 4.8

we can see that the magnetization can undergoes many precessions between AP and P states, overcoming the hard axis several times, with different final states, depending on many factors, such as damping constant, current pulse's shape or duration. In all the results presented until now the initial direction of $\mathbf{m}$ was considered in the layer's plane, making an angle $\Delta\varphi = 10^{-3}$ degree with the direction $\mathbf{m}_p$ of the fixed layer. Increasing the offset angle $\Delta\varphi$, the switching region increases, and still there are fringes at the border between switching and non-switching areas (see Fig. 4.10). For the same value, a deviation $\Delta\theta$ out-of-plane has a bigger effect than the in-plane deviation $\Delta\varphi$ (see Figs. 4.10 and 4.11).

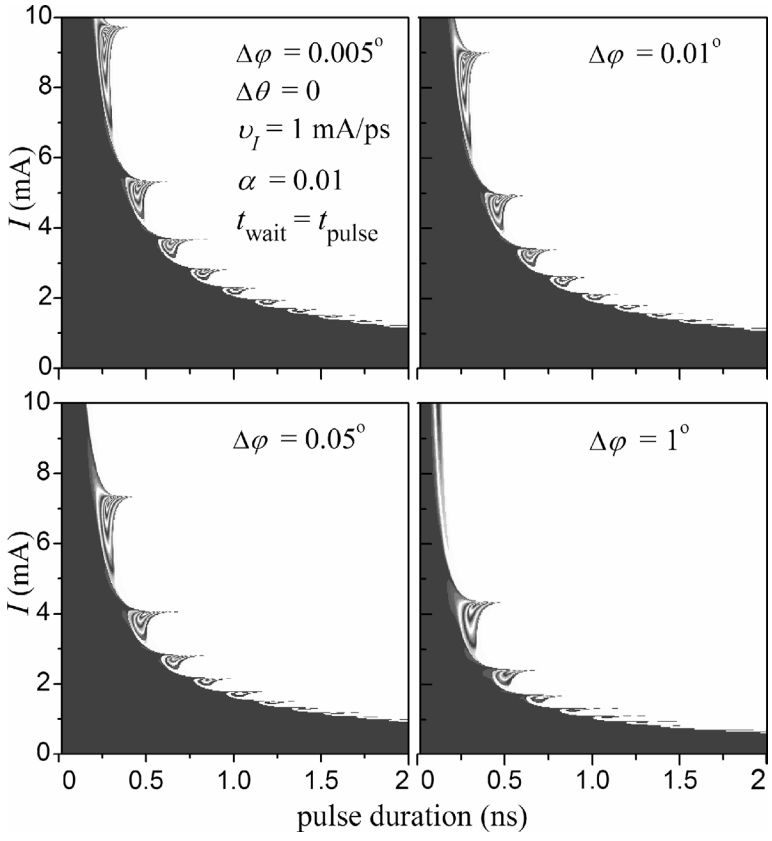

Figure 4.10. AP-P switching diagrams at $T = 0\,\mathrm{K}$ for a current sweep rate $\upsilon_I = 1\,\mathrm{mA/ps}$, a damping constant $\alpha = 0.01$, for different initial orientation $\Delta\varphi$ of magnetization $\mathbf{m}$ in the layer's plane.

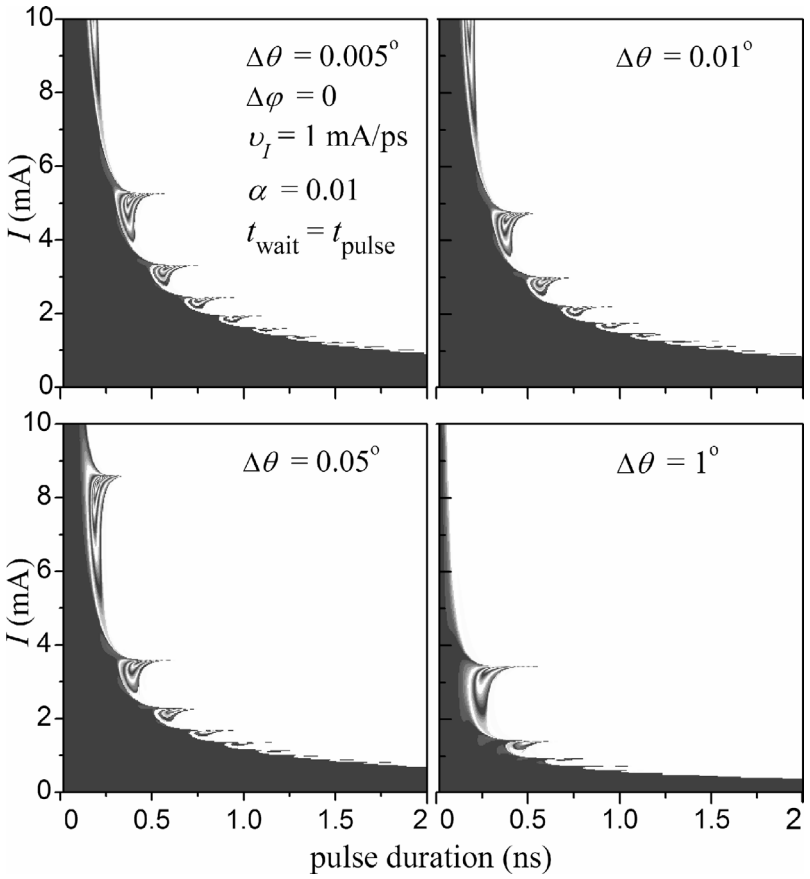

Figure 4.11. AP-P switching diagrams at $T = 0$ K for a current sweep rate $\upsilon_I = 1\,\mathrm{mA/ps}$, a damping constant $\alpha = 0.01$, for different out-of-plane initial orientation $\Delta\theta$ of magnetization $\mathbf{m}$.

4.2.3 Temperature effects

The effect of spin-transfer torque is significant for magnetic particles of small dimensions, typically few tens of nanometers. For such small dimensions thermal fluctuations, high-frequency magnetic noise due to the thermal fluctuations may pose a fundamental limitation to the device performance, significantly influencing the magnetization's dynamics and switching. The magnetic moments have thermally activated random oscillations close to the bottom of the energy minima. This type of oscillations can be induced over a finite energy barrier, as well.

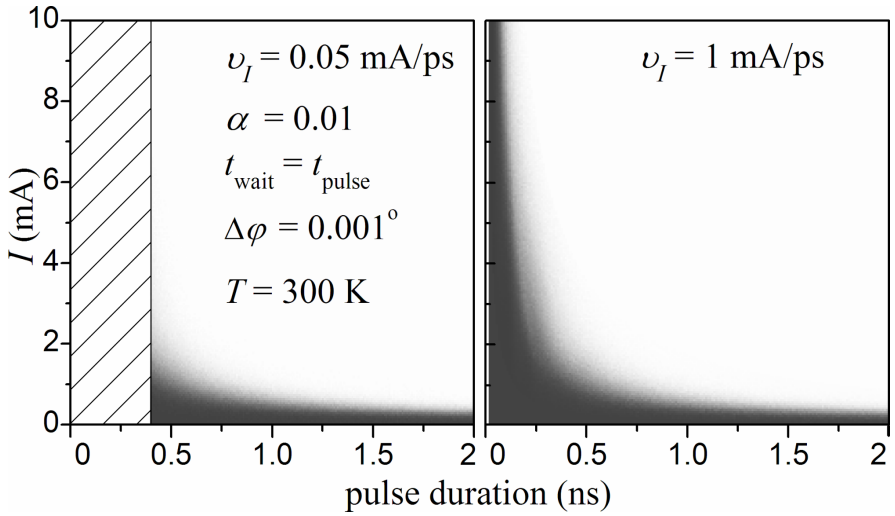

Figure 4.12. AP-P switching diagrams at $T = 300\ \mathrm{K}$ for a current sweep rate $\upsilon_I = 0.05\ \mathrm{mA/ps}$ (left), and $\upsilon_I = 1\ \mathrm{mA/ps}$ (right), respectively, for a damping constant $\alpha = 0.01$.

In the presence of thermal fluctuations identical pulses do or do not switch the magnetization, with a certain probability. The probability of switching is plotted in a gray coded diagram as a function of current pulse amplitude and duration in Fig. 4.12 for two values of the current sweep rate. Each simulated point from diagrams represents the statistic of 1024 repeatedly writing operations at certain pulse amplitude and duration. We can see that temperature increases the switching area, and that instead of a clear border between switching and non-switching areas we have a transition region where the final state is sensitive to thermal fluctuations [97].

4.3 Magnetization switching under a spin torque current and a magnetic field

One of the attractive topics related to the spin-transfer torque controlling the magnetization in data storage devices is the magnetization under coexistence of the spin-

transfer torque and the magnetic field. Early theoretical works [8, 75, 76] derived an analytical expression for the critical reversal current, which includes the effect of a rather small magnetic field, which is typically less than the coercive field. Later the critical current for a larger magnetic field was also obtained [83]. However, the precise nature of magnetization dynamics when a spin-polarized current and an external field are simultaneously present has not been well studied.

In the previous section we have presented the dynamic switching triggered by a spin-torque current without any external applied field. In this section we will continue discussing the switching properties for the case when spin torques and external field are simultaneously present. The switching is discussed as a function of the applied field strength and direction, and also as a function of the length of the current pulse [98].

4.3.1 Model

We will use the same configuration and all parameters as in the previous section, except adding an in-plane external applied field to the effective field $\mathbf{H}_{\text{eff}}$ in Eq. (4.1). Let us rewrite this equation in dimensionless form as:

$$\frac{d\mathbf{m}}{dt} = \alpha\,\mathbf{m}\times\frac{d\mathbf{m}}{dt} - \mathbf{m}\times(\mathbf{h}_{\text{eff}} - a_J\,\mathbf{m}\times\mathbf{m}_{\text{p}}), \tag{4.3}$$

where the free-layer magnetization $\mathbf{m}$, the spin torque parameter a_J, and the effective field $\mathbf{h}_{\text{eff}}$ are now normalized by the saturation magnetization M_s. Time is measured in units of $(\gamma M_s)^{-1}$. The electron current is sent along z direction across a metallic multilayer element with layers parallel to (x, y) plane. The unit vector $\mathbf{m}_{\text{p}}$ gives the

direction of the spin polarization (along x direction in our case) (see Fig 4.13). The fixed value $\alpha = 0.01$ was chosen. The effective field $\mathbf{h}_{\text{eff}}$ consists of applied field and demagnetizing field, no further anisotropy being considered.

For the current and field pulses, rise and fall sinusoidal time dependence is assumed, and to describe the pulse, the notation from section 3.1 is used: the pulse is characterized by the triplets of numbers "rise time/pulse length/fall time", with all values given in units of nanoseconds.

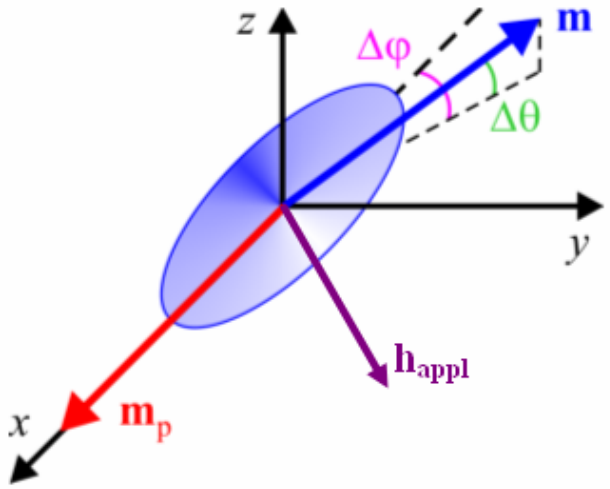

Figure 4.13. Schematic of the free layer, assumed to be ellipsoid shaped, and single domain. The ellipsoid's principal axes are along x, y, and z axes, with x and y in the plane of layer, and x along long axis. The axes' lengths are: $2a = 100$ nm, $2b = 75$ nm, and thickness $d = 2$ nm. The pinned ferromagnetic layer's normalized magnetization $\mathbf{m}_p$ is held fixed at the direction of the free layer's long axis. An external magnetic field is applied in (x, y) plane.

All calculations presented in the following are performed for a maximum value of the current pulse of 0.5 mA (i.e. $a_J = 1.22 \times 10^{-2}$). The results are obtained by numerical integration of Eq. (4.3) using a standard, self-optimizing, embedded Runge-Kutta algorithm.

4.3.2 Precession of the magnetization in a dc applied field and a pulsed current

In this section, the switching of the magnetization under application of a dc magnetic field and of a pulse of current is discussed. In order to characterize the precessional switching of magnetization subjected to a dc applied magnetic field with different strengths and orientations, taking into account also the effect of spin transfer torque, the switching diagram introduced in chapter 3 will be applied, in which the final value of the projection m_x of the magnetization vector is displayed as a function of the strength and direction of the applied field.

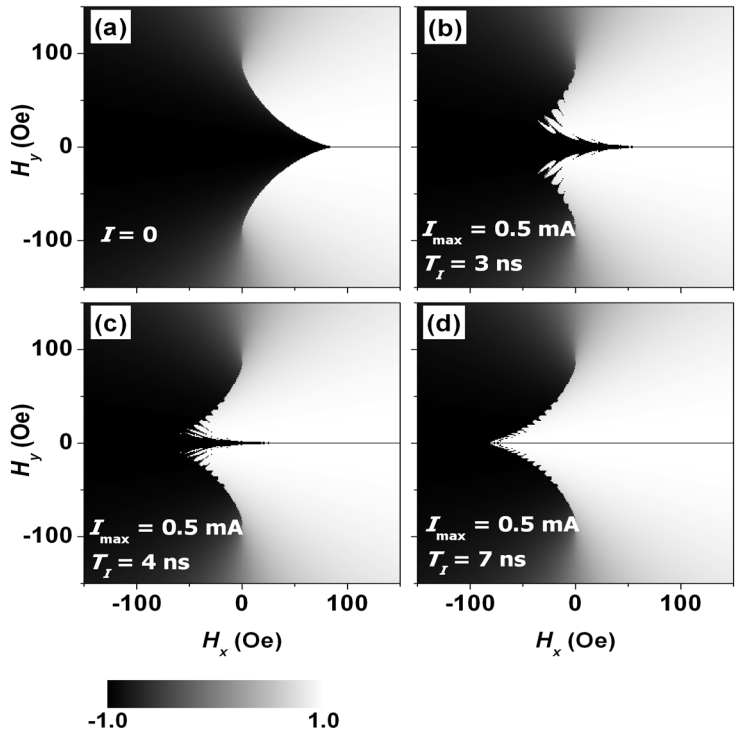

Figure 4.14. Switching diagram as a function of the applied dc field, for different values of the current pulse length $0.25 / T_I / 0.25$: (a) no current applied, (b) $T_I = 3\,\text{ns}$, (c) $T_I = 4\ \text{ns}$, (d) $T_I = 7\ \text{ns}$. The direction of the spin polarization (pinned layer) is along the negative x direction and the initial direction of magnetization is also along the negative x direction ($m_x = -1$). Black areas represent $m_x = -1$ (non-switching), white areas represent $m_x = 1$, and the intermediate values of m_x are represented with shades of gray. The maximum value of the current pulse is $0.5\ \text{mA}$.

In Fig. 4.14 different scenarios of the magnetization switching in the non-presence/presence of the spin-transfer torque, initiated by a dc magnetic field, are shown. Prior to the applied field, the magnetization lies along negative x direction and the color in grayscale from black to white on the diagram indicates the final state of m_x: black areas represent $m_x = -1$ (non-switching), white areas represent $m_x = 1$, and the intermediate values of m_x are represented with shades of gray. Fig. 4.14(a) represents the switching diagram in the case when no spin-transfer torque is included. One can observe that switching is induced only when the applied field has a component along the positive x direction, the separation boundary between black and white, corresponding to switched and non-switched regions, is very well defined, forming an astroid-like shape.

Dramatic changes are easily observed in the switching diagrams taking into account the spin-transfer torque term with different current pulse lengths (T_1) [see Figs. 4.14(b)-(d)]. The maximum value of the current pulse is 0.5 mA. Increasing the current pulse length, the white color region enlarge gradually to the left, gnawing the astroid-like region, and the switching can be induced also by a field with a negative component along the x direction. One observes that for the longest current pulse [see Fig. 4.14(d)] almost entire interior region of the astroid switches.

From Fig. 4.14 we can see that even if the supplementary current-induced torque is equivalent with a variable field, the global effect on the switching diagram is not a translation of the diagram, but a deformation on the x direction, with maximum deformation at $H_x = 0$.

4.3.3 Precession of the magnetization in a pulsed applied field and a pulsed current

In this section we describe the switching of the magnetization in a pulsed field and a pulsed current applied synchronously or asynchronously. Instead of the final state of m_x, now we map the switching time, defined as the time required for the magnetization to approach the equilibrium position along the positive x axis, until the torque acting on the magnetization becomes negligible (there is no significant ringing), after the cut-off of both pulses. In Figs. 4.15 and 4.16 the black areas represent no switching, and the gray level is scaled from dark gray for 6 nanoseconds (ns), to white for 13 ns.

We now apply a 0.25/0.0/0.25 pulse of field, and construct the switching diagrams of magnetization for different cases of the pulse length of the current pulse. The result is displayed in Fig. 4.15. The final state is determined by the position of the magnetization when the field pulse and the spin-transfer current pulse are terminated. The switching time is found in the range of few nanoseconds, which is the evolution time required for the magnetization approaching the equilibrium position along the positive x axis. Figs. 4.15(b)-(d) show that as the time length of current pulse increases, the regions of stable switching into the positive x direction are enlarged compared to the case of no spin-transfer torque current applied, as shown in Fig. 4.15 (a). It is clear that the longer the pulse duration of the spin-transfer current, the stronger effects of spin torque on switching diagram are observed. We come up to conclusion that the spin torque plays very important role in driving switching of the magnetization. Improved switching of an MRAM memory cell, therefore, could be achieved by simultaneously addressing the short pulse of field and pulse of current.

If in Fig. 4.15 the spin-polarized current pulse is starting at the same time with the pulse of field (synchronously), let us now investigate the influence of the starting time of the current pulse, which is denoted as t_1, on the magnetization reversal (see Fig. 4.16).

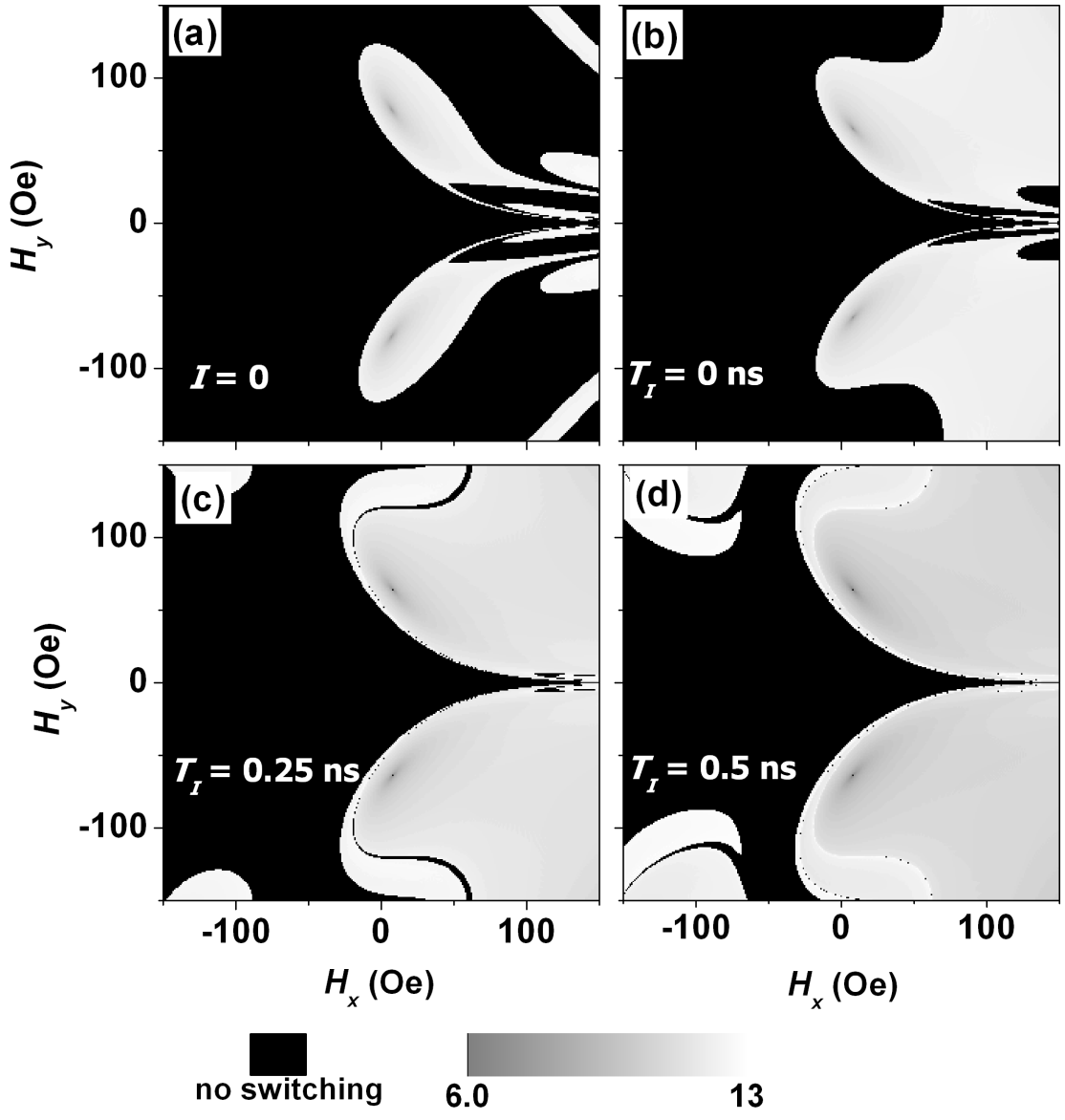

Figure 4.15. Time switching as a function of the maximum value of a pulse field with the length $0.25/0.0/0.25$, for different values of the current pulse length $0.25/T_I/0.25$: (a) no current applied, (b) $T_I = 0$ ns, (c) $T_I = 0.25$ ns, (d) $T_I = 0.5$ ns. Black areas represent no switching, and the gray level is scaled from dark gray for 6 ns, to white for 13 ns.

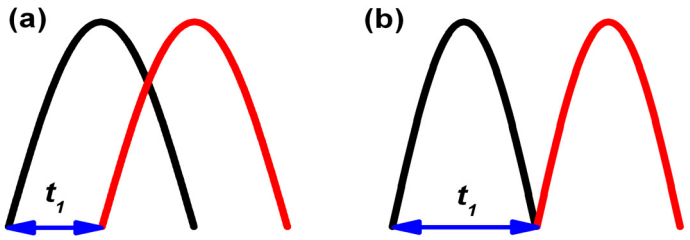

Figure 4.16. Schematic of the pulsed field and pulsed current applied asyncronously. The pulse of current starts at the moment t_1 : (a) when the pulse of field reaches its maximum value of the sinusoidal form. (b) when the pulse of field is finished.

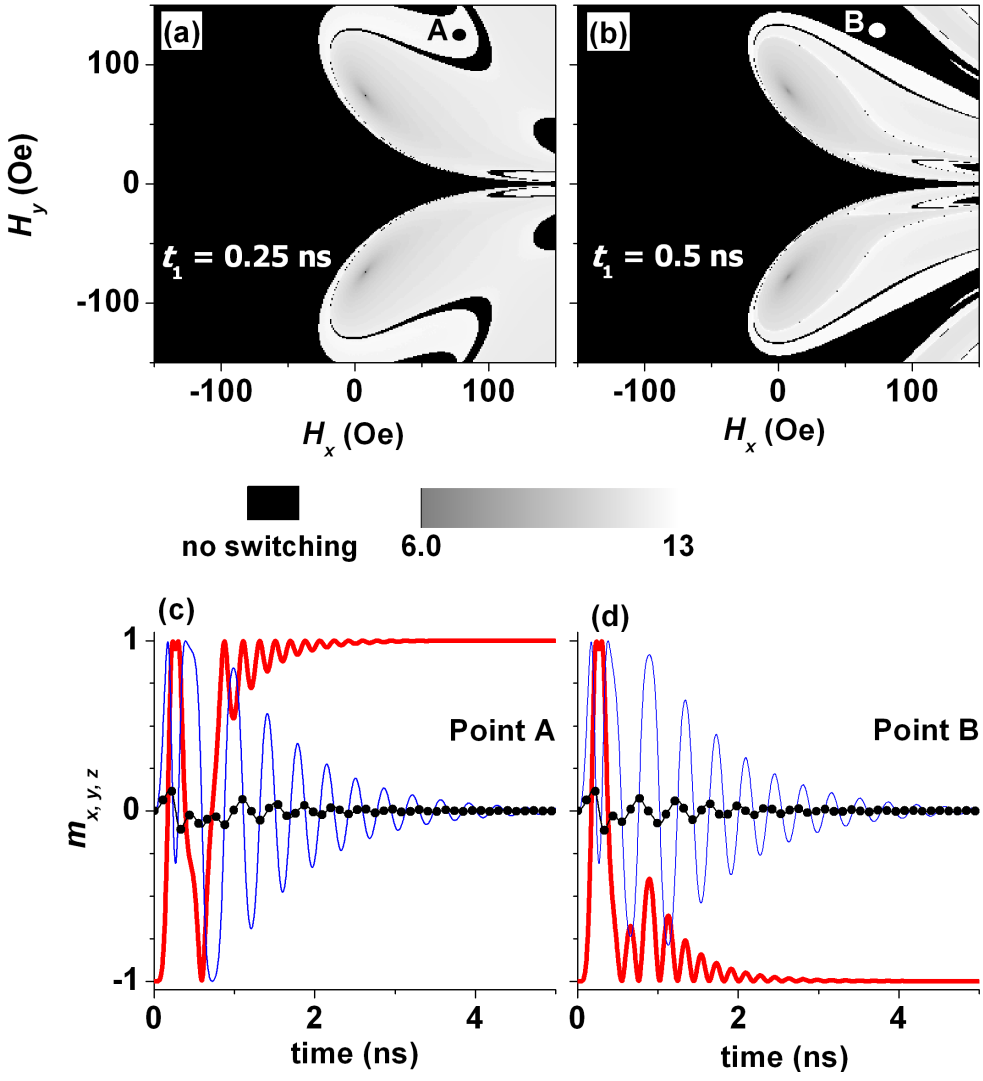

Figure 4.17. Time switching as a function of the maximum value of a pulse field with the length $0.25/0.0/0.25$, and for a current pulse with the length $0.25/0.0/0.25$ starting at the moment t_1: (a) $t_1 = 0.25$ ns, (b) $t_1 = 0.5$ ns (see Fig. 4.16). Black areas represent no switching, and the gray level is scaled from dark gray for 6 ns, to white for 13 ns. (c) and (d) time evolution of m_x (bold line), m_y (thin line), and m_z (symbols) at the positions A, and B indicated in the top diagrams.

In Fig. 4.17(a) the pulse of current starts when the pulse of field reaches its maximum value of the sinusoidal form. The white region (the switching region) is enlarged compared with the case of synchronous pulses [Fig. 4.15(b)]. In Fig. 4.17(b) the pulse of current starts when the pulse of field is finished, the switching region decreases again. Moreover, the pulse current delay is a critical parameter in the switching behavior, as it can be observed from the bottom panels of Fig. 4.17. Thus, points A and B with the same field pulse but different t_1 delays have different switching outcomes, with point B remaining in the initial state (no-switching) and point A switching.

4.4 Summary

The current-induced spin-transfer torque has recently been proposed as a convenient writing process in high density magnetic random access memories (MRAM), which replaces the conventional method utilizing magnetic field. A spin-polarized current can switch the magnetization of a ferromagnetic layer more efficiently than a current induced magnetic field. The novel technology utilizing the spin-transfer torque is expected to reduce the switching time of magnetization as well as to increase the recording density of MRAMs and the other data storage devices.

In this chapter we have explored the dynamic switching triggered by spin angular momentum transfer in a pulsed current of a spin-valve-type trilayer structure, which is currently used as a free layer in MRAM, and its dependence on thermal effects. The model is based on the LLG equation and the stochastic LLG equation with a spin-transfer torque term included. The calculated switching diagrams reveal the pulse parameters that

are suitable for ultrafast spin switching. We showed that the boundary, which delimits the nonswitching and ultrafast switching regions, develops into a ripple structure with switching and non-switching areas alternating with increasing current pulse amplitude and duration. The ripple structure still exists when the current is cut-off and evolves in time into a more intricate structure. Also, we have presented how the thermal fluctuations affect the switching behavior.

Furthermore, the dynamic behavior of magnetization under the competitive torques of a spin-polarized current and an external magnetic field has been derived. The switching process and the corresponding switching parameters are shown to depend significantly on the interplay between the torques due to spin transfer and external magnetic field. The switching properties of magnetization are strongly enhanced by the presence of the spin-transfer torque current. Magnetization reversal processes can become complex, but switching regions presented in switching diagram are enlarged. Our calculations are useful to develop an understanding of the current-induced magnetic switching.

Chapter 5

Static and Dynamic Critical Curves of a Synthetic Antiferromagnet

Stonner and Wohlfarth derived the critical curve theory for a uniaxial single domain undergoing rotational reversal. The theory as discussed in chapter 1 and 2 provides an essential framework for depicting the reversal behavior of thin films. Its application to magnetic thin films indicates several properties useful for memory and logic schemes.

As broader and deeper understanding is gained for single films, current interest has branched into multi-film structures. For instance, two films may be superposed in closely spaced parallel planes. The spacing is large enough to prevent atomic interaction but small enough to permit magnetostatic interaction. The strength of interaction depends on the thickness-to-diameter ratios and the magnetizations of the films. The magnetostatically coupled films exhibit static and dynamic behaviors significantly different from the individual films.

This chapter will focus on the study of synthetic antiferromagnet (SAF) - a sandwich of two ferromagnetic thin films antiferromagnetically coupled through a non-magnetic metallic spacer, usually Ru, Os, Re, Cr, Cu, Rh. Due to SAF shape anisotropy, reduced anisotropy field and its capacity for spin transfer [99], SAF has many technological applications as hard layer of exchange coupled composite media [100], soft

under-layer for perpendicular recording [101], pinned and free layers for toggle MRAM cells [15], hard disk reading heads, or magnetic sensors [102].

5.1 Synthetic antiferromagnet and its application in toggle MRAM

5.1.1 Synthetic antiferromagnet concepts

The synthetic antiferromagnet (SAF) structures are key elements in modern devices based on tunnel magnetoresistance (TMR) or giant magnetoresistance (GMR) effects as reading heads and magnetic random access memories (MRAMs). SAF consists of two ferromagnetic layers that are coupled through a nonmagnetic spacer whose thickness is tuned to provide an antiferromagnetic coupling (see Fig. 5.1). The performance of the devices using SAF structures relies heavily on their switching characteristics, which are governed by the individual reversal of the SAF.

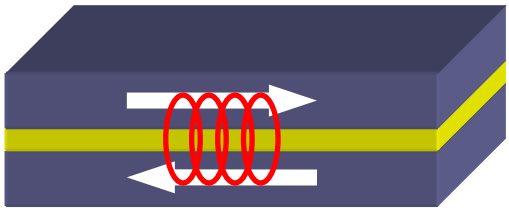

Figure 5.1. Schematic representation of the SAF showing the two ferromagnetic layers antiferromagnetically coupled through an interlayer of non-magnetic material.

The two ferromagnetic layers in a SAF type of structure are coupled together through a Ruderman-Kittel-Kasuya-Yosida (RKKY) interaction. This type of coupling was first proposed by Ruderman and Kittel and later extended by Kasuya and Yosida to give the theory now generally know as the RKKY interaction. We will briefly explain how this interaction works for SAF: the indirect exchange couples moments over relatively large distances; this is the dominant exchange interaction in metals because

there is little or no direct overlap between neighboring magnetic electrons. It therefore acts through an intermediary - which in metals are the conduction electrons (itinerant electrons). The interaction is characterized by a coupling coefficient, j, given by [103]:

$$j(R_l - R_{l'}) = 9\pi\left(\frac{j^2}{\varepsilon_F}\right)F(2k_F|R_l - R_{l'}|) \tag{5.1}$$

where k_F is the radius of the conduction electron Fermi surface, R_l and $R_{l'}$ are the lattice positions of the point moment, ε_F is the Fermi energy and $F(x) = \frac{x\cos x - \sin x}{x^4}$. The RKKY exchange coefficient, j, oscillates from positive to negative as the separation length changes and has the damped oscillatory nature shown in Fig. 5.2. Therefore, depending upon the separation between a pair of ions their magnetic coupling can be ferromagnetic or antiferromagnetic. A magnetic ion induces a spin polarization in the conduction electrons in its neighborhood. This spin polarization in the itinerant electrons is felt by the moments of other magnetic ions within range, leading to an indirect coupling.

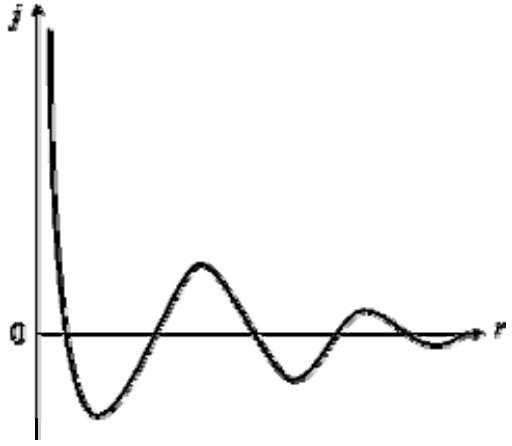

Figure 5.2. Variation of the indirect exchange coupling constant, j, of a free electron gas in the neighborhood of a point magnetic moment at the origin $r = 0$ [103].

In rare-earth metals, whose magnetic electrons in the *4f* shell are shielded by the *5s* and *5p* electrons, direct exchange is rather weak and insignificant and indirect exchange via the conduction electrons gives rise to magnetic order in these materials.

The SAF materials are designed in such a way that the coupling is antiferromagnetic. Although not so complicated as a structure, SAF is an important component of modern magnetic devices with a rather complicated magnetic behavior, as it will be shown in the next sections.

5.1.2 Toggle MRAM

By far until now the most important application of SAF is as a part of magnetic memory elements in MRAM and toggle MRAM [15], [26]. To illustrate the significance of SAF for this magnetic device we will dedicate the following sub-section to the MRAM and toggle MRAM designs and operations, focusing our attention on SAF role.

In "conventional" MRAM as described in section 2.1, information is stored by selective switching the magnetic moment direction of the single free layer of individual bits. The switching behavior is following Stonner-Wohlfarth reversal. As shown in Fig. 5.3 (b), for fields applied outside the astroid boundary only one state is stable, whereas at $T = 0$, for fields inside the astroid boundary both states are stable and no switching occurs between them. Switching is accomplished by simultaneously applying both bit-line and word-line fields (full-select) to the selected bit. Since this full-select field is outside the astroid boundary, the selected bit is stable only in the state to be written. At the same time, the other "half-selected" bits on the same bit line and word line do not switch because half-select field is inside the astroid boundary. This SW method of

switching has two major disadvantages. The first is that the margin between half select and full select is small. The second disadvantage is that for $T \neq 0$, there is a large drop in the activation energy for half-selected bits as shown in Fig 5.3 (c). This activation energy is the barrier preventing the bit from making a thermally activated switch into the other state. These two problems, half-select margin and activated errors, limit the usefulness of SW MRAM to small arrays and short lifetimes.

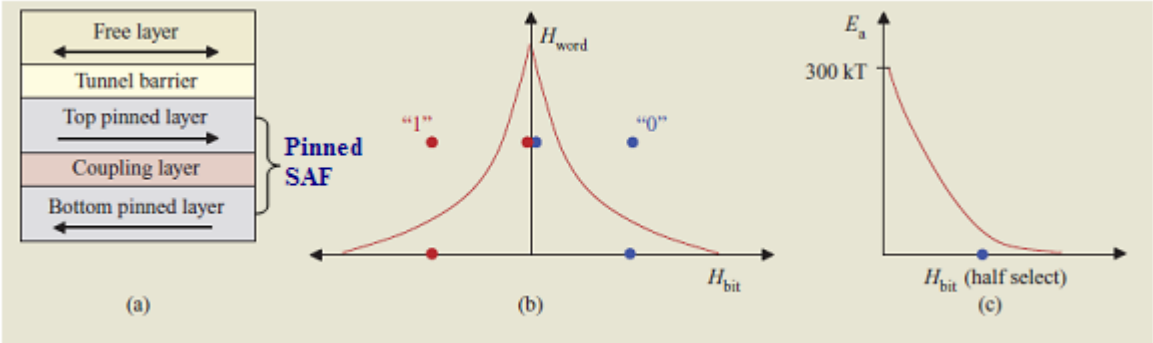

Figure 5.3. Illustrative switching by Stonner-Wohlfarth reversal MRAM. In traditional SW switching, use is made of a single free layer, as shown in the tunnel junction cross section (a), which switches when a field is applied across the critical switching curve, or "astroid" (b). When a field is applied along half-select direction, the activation energy decreases dramatically (c) [26].

In response to the write margin difficulties associated with the conventional MRAM, a more advanced, "toggle-mode" switching MRAM has been proposed by Leonid Savtchenko [15]. Savtchenko switching relies on the unique behavior of a SAF free layer. Fig. 5.4(a) illustrates the toggle-mode MTJ device structure. The structure is similar to that of the conventional MTJ except that the free layer consists of two weakly anti-parallel coupled ferromagnetic layers. Therefore, the free layer in a toggle cell is a synthetic antiferromagnet SAF trilayer stack. In addition, the long axis of the structure lies at 45° with respect to the World Line (WL) as opposed to being parallel to the WL, in the conventional MRAM.

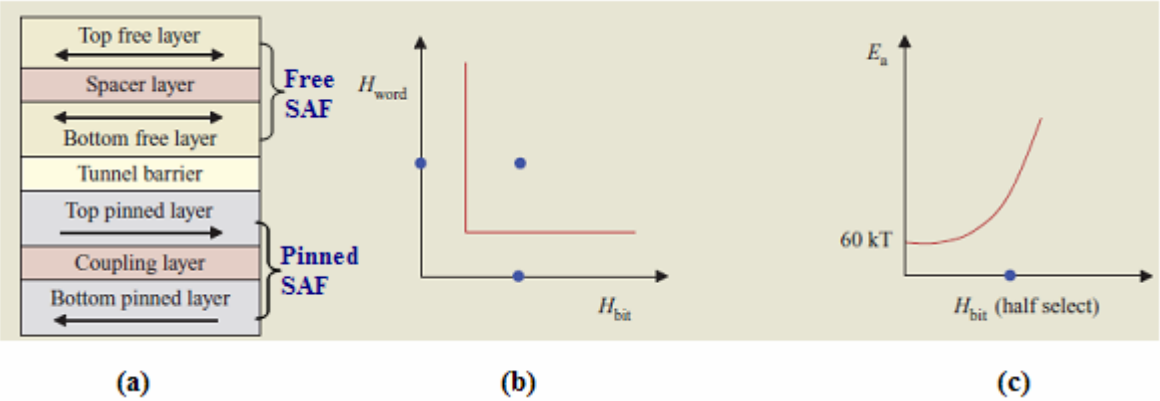

Figure 5.4. Illustrative switching by toggle MRAM. In toggle switching, use is made of two magnetic free layers (a), which switch when a rectangular excursion crosses the L-shaped critical switching curve (b). When a field is applied along half-select direction, the activation energy initially increases, making the bit more stable (c) [26].

The read operation is essentially unchanged, with the magnetic orientation of the lower free layer determining the effective resistance of the structure. In the writing process, magnetic fields from bit and word lines are applied in sequence (see Fig. 5.5).

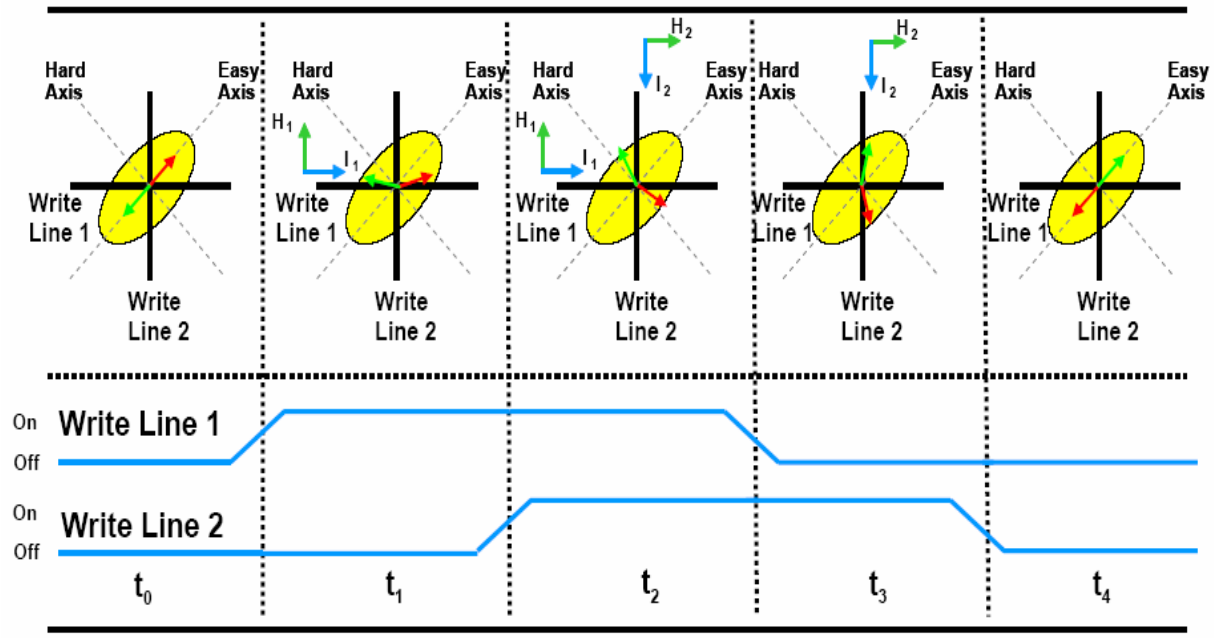

Figure 5.5. Schematic of the toggling operation of Savtchenko switching. Pulse are applied in a sequence designed to rotate the SAF 180^0 to the opposite resistance state [15].

Whereas the conventional MTJ is written directly into one state or the other depending on the polarity of the Bit Line (BL) current, the toggle-mode MTJ toggles its state when exposed to a similar WL and BL current pulse sequence. As illustrated in Fig. 5.5 the dipoles of the free layer rotate slightly in the direction of the applied field, and essentially follow the applied field as it rotates during the WL and BL current pulse sequence. At the end of the sequence, the free-layer dipoles have rotated 180° from the initial state, regardless of the initial state. The criterion for a successful toggle is that the applied field must trace a path in the applied field plane that encloses a particular point in the plane, referred to as the "spin-flop" point.

Unlike a conventional MTJ, a toggle-mode MTJ is largely insensitive to half-select disturbs, regardless of WL and BL field strength, since such disturbs do not trace a path that encloses the spin-flop point. Fig. 5.4(b) illustrates the dramatically changes the shape of the critical switching curve. Note that there are no disturbs all the way up to the highest fields, displaying the remarkable half-select robustness of this approach. In addition, as shown in Fig. 5.4(c) the activation energy under half-select actually increases, thus making the bit more rather than less thermally stable. This essentially eliminates the activated-error problem.

A final advantage of the toggle-mode MTJ is that only one BL write current direction must be supported, simplifying the design of the write circuits. Because of the toggle nature of the device, the device must be read at the start of the write cycle. The device is then toggled if its current state does not match that of the incoming write data. Although the read can be performed concurrently with preparations for the WL and BL

write pulse sequence, the required read represents a write-performance disadvantage compared with that of a conventional MTJ.

5.2 Static critical curve of SAF

From previous sections one can see that the performance of the devices using SAF structures relies heavily on their switching characteristics, which are governed by the individual reversal of the SAF. The magnetization behavior of individual SAF can be investigated by analytic/numerical method, applying Stoner-Wohlfarth model to each layer.

In this section the magnetization behavior including the switching of the magnetization configuration in the SAF based on analytical methods with the aid of numerical calculations will be presented. Critical conditions for toggle mode switching based on the critical field curves are also given.

5.2.1 Magnetization behavior of the SAF

We now investigate briefly how the magnetization of each layer of the SAF behaves as a function of in-plane magnetic field applying the SW model to each layer. This work was published in papers by Fujiwara and Wang [23-25].

The generalized SAF consists of two ferromagnetic layers 1 and 2 that have the thickness t_1 and t_2, magnetizations M_1 and M_2, and uniaxial anisotropy constants K_{u1} and K_{u2}, respectively. If we assume that the easy axes of the two layers are parallel to each other, then, the energy density per unit area w normalized by $2K_{u1}t_1$, can be expressed as:

$$w = \frac{1}{2}\left(\sin^2\theta_1 + kt\sin^2\theta_2\right) - \left[h_x\cos\theta_1 + h_y\sin\theta_1\right] - mt\left[h_x\cos\theta_2 + h_y\sin\theta_2\right] + h_J\cos(\theta_1 - \theta_2) \tag{5.1}$$

where $k = K_{u2}/K_{u1},\ m = M_2/M_1,\ t = t_2/t_1$. Two angles θ_1 and θ_2 denote the magnetization angle of the layer 1 and the layer 2 with respect to the easy axes, h_x and h_y the applied field normalized by $2K_{u1}t_1$ in the easy and hard axis directions, respectively, and h_J the antiferromagnetic coupling strength between the two layers.

In order to understand the response of the magnetizations to the applied vector-field in the (h_x, h_y) plane, it is convenient to find the trajectories of the field giving a constant θ_1 leaving θ_2 to be a variable and vice versa. The stability conditions are given by

$$w_1 = 0,\ w_2 = 0$$

and

$$w_{11} > 0,\ w_{22} > 0,\ \mathrm{w}_{11}w_{22} - w_{12}^2 > 0,$$

where w_1, w_2, w_{11}, w_{22}, and w_{12} are the first and second derivatives of w with respect to θ_1 and θ_2, respectively. The results are:

$$h_x = \frac{kt\cos\theta_1\sin 2\theta_2 - mt\cos\theta_2\sin 2\theta_1 + 2h_J\left(\cos\theta_1 + mt\cos\theta_2\right)\sin\left(\theta_1 - \theta_2\right)}{2mt\sin\left(\theta_1 - \theta_2\right)} \tag{5.2}$$

$$h_y = \frac{kt\sin\theta_1\sin 2\theta_2 - mt\sin\theta_2\sin 2\theta_1 + 2h_J\left(\sin\theta_1 + mt\sin\theta_2\right)\sin\left(\theta_1 - \theta_2\right)}{2mt\sin\left(\theta_1 - \theta_2\right)} \tag{5.3}$$

The constant angle contours for layer 1 or for layer 2 can be plotted using the solutions (5.2) and (5.3) by assuming either θ_1 or θ_2 to be a constant and the other a variable. When the parameters for the two layers are identical, that is, $m = k = 1$, the constant angle contours must be identical for both layers. The envelopes of the constant

angle contour map are the critical curves, which replaces the well-known astroid representing the critical curve for switching for the single layer. Figure 5.6 presents the critical curves of SAF with different values of thickness ratio t. It is seen that the envelopes consist of two parts: astroid-like part and heart-shaped part. Those "astroid" and "heart" parts may be disappeared in some cases with the change of the parameters. The outermost envelope is the critical curve for saturation, that means, outside of which the magnetization in layers 1 and 2 become parallel to each other, and the inner envelopes are the critical curves for switching.

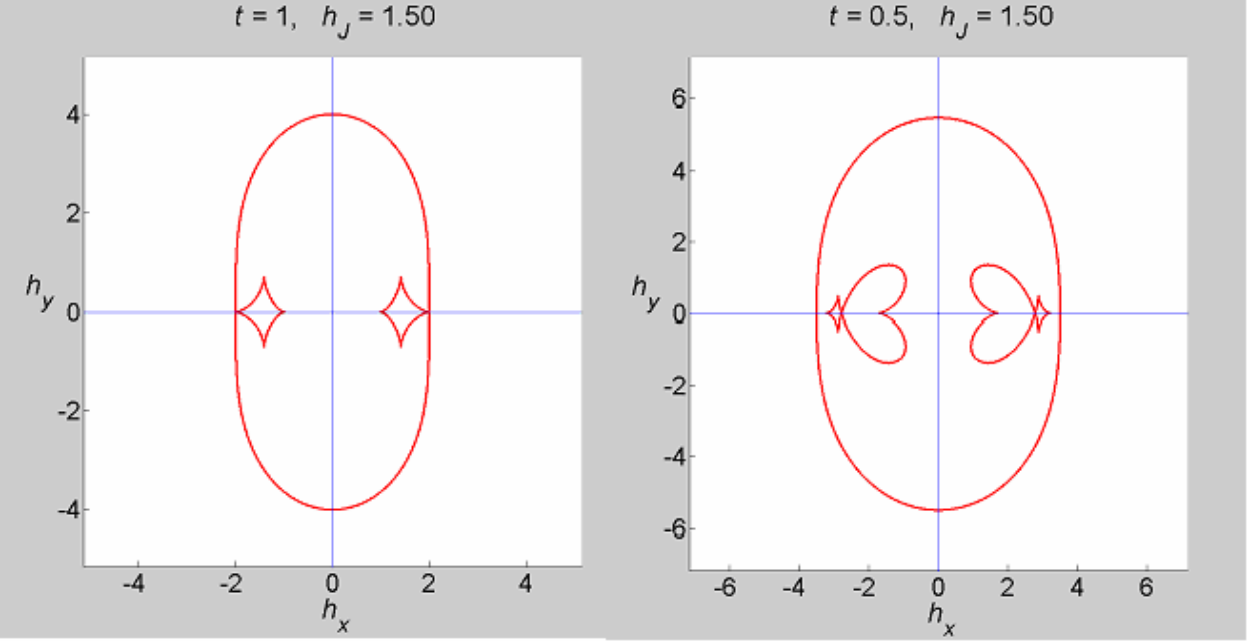

Figure 5.6. Critical curves for: t=1 and t=0.5 with $h_J = 1.5$.

The critical curve also depends on the coupling strength h_J between the two layers in SAF structure. As shown from Fig. 5.7, the critical curve evolves from simple astroid at zero coupling to a more complicated curve for larger coupling field values.

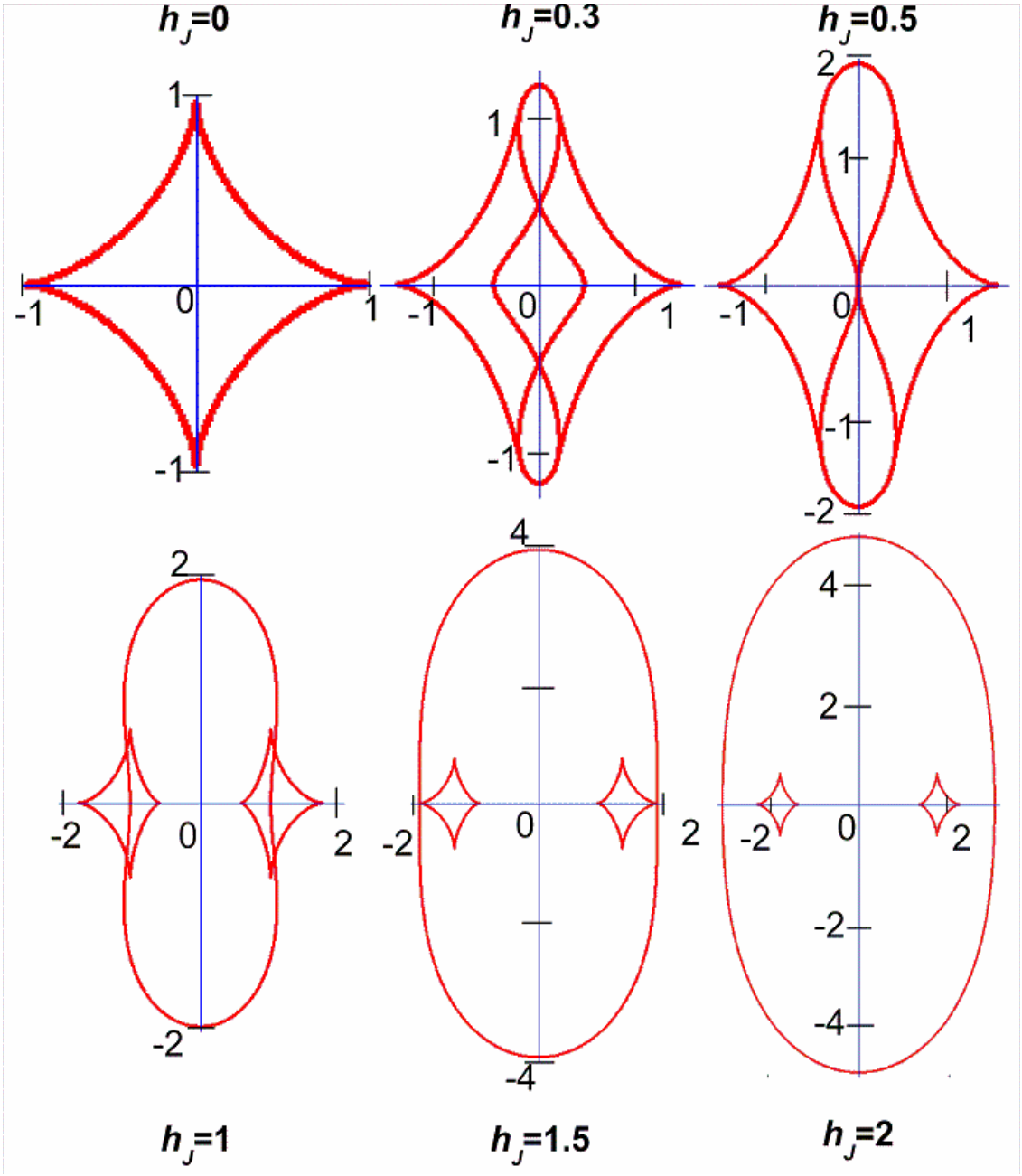

Figure 5.7. Critical curves for $m = k = t = 1$ evolving with increasing exchange-coupling field h_J from 0 to 2.

These critical curves play an important role in determining the conditions for obtaining the toggle-mode switching. Consequently, knowing the configuration of the SAF critical curve is of great importance in order to control its switching characteristics.

5.2.2 Critical curves and operating field margins

In a standard toggle MRAM, we apply the word field H_W and the digit field (or the bit field) H_D, sequentially, in the ±45° directions with respect to the easy axis. Based on the critical curves, we can specify the conditions for the field pulse sequence to obtain the "toggle-mode" switching and "direct-mode" switching which Savtchenko, et al. [23-25] defined. Figure 5.8 shows critical curves and the operating field margins for toggle mode (the area hatched by the inclined lines) and the direct write mode (the area hatched by vertical lines). The detail of this work was presented in the paper published by Fujiwara and his co-workers [23, 24].

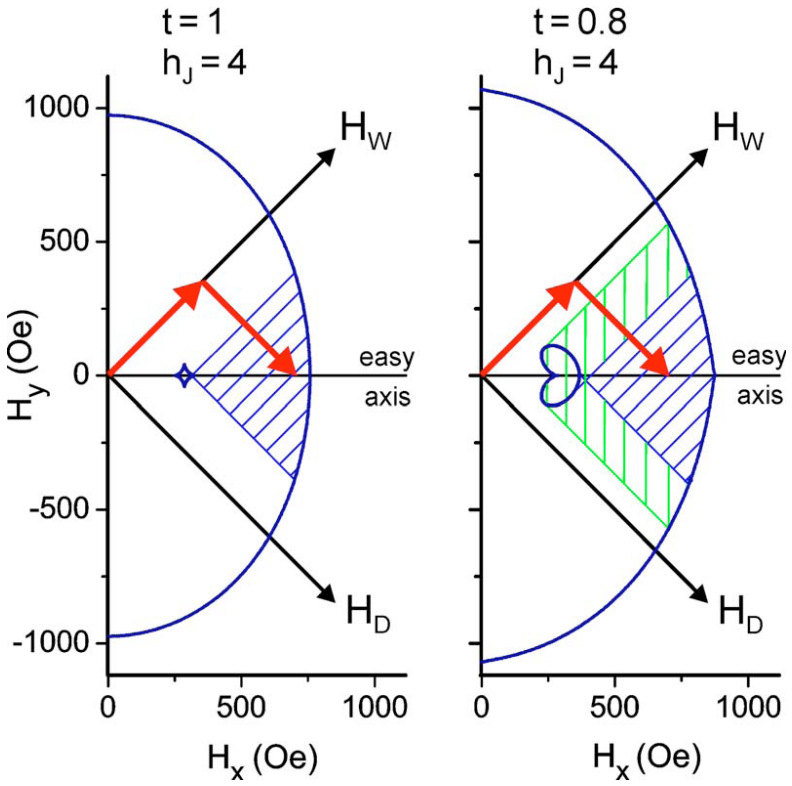

Figure 5.8. Critical field curves obtained by Fujiwara et al. [23, 24] for $h_J = 4$ and for $t = 1$ (left) and $t = 0.8$ (right), with the operating field margins for the toggle mode (the area hatched by the inclined lines) and the direct mode (the area hatched by vertical lines). The amplitude of the word and digit field showed in the figures is $H_W = H_D = 500$ Oe.

For toggle mode the state 1 is switched to a 0 state after field pulse sequence, and repeating the field pulse sequence the stored 0 state returns it to a 1 state. Toggle mode only results in magnetization switching without being able to choose the final state. Thus, to be able to write the memory element into the desired state, the initial state of MRAM must first be read and compared to the state to be written. For direct writing the state 1 is switched to a 0 state after field pulse sequence, but the state 0 is not switched. When using the direct write method there is no need to determine the initial state of the MRAM cell because the state is switched only if the state being written is different from the stored state.

5.3 Dynamic critical curve of SAF

The magnetization switching of SAF can be elegantly described using the concept of critical curve (CC) as presented in previous section. However, all these descriptions are restricted only to a quasistatic regime, where the magnetization dynamics and precessional effects are neglected. The devices using SAF structures require a high throughput and very short access time, and as a result the magnetization is forced by pulsed magnetic fields to switch at nanosecond and sub-nanosecond time scales for which the static CC (sCC) approach is not anymore adequate. For uncoupled magnetic systems it was shown that a pulsed magnetic field can provide a high-speed coherent switching [104] well below the static limit predicted by Stoner- Wohlfarth (SW) model [14]. Later [4] the dynamic CC of a SW particle was given. In this section a dynamic generalization of sCCs for coupled magnetic systems is presented, analyzing the magnetization switching of SAF elements subjected to pulsed magnetic fields. As in Ref. 4 for a SW

particle, the boundary between switching/nonswitching regions represents the natural generalization of sCC, namely the dynamic CC (dCC). Comparing sCCs, which are currently used for studying the switching in toggle MRAM, with dCCs it will be shown that a consistent switching can be achieved only under specific conditions that take into account the dynamics of the magnetic moments [105].

5.3.1 Model

The model is based on Landau-Lifshitz-Gilbert (LLG) equation (Eq. 1.40) assuming that the magnetization in each layer is uniform (single domain). For the switching process we only consider the soft SAF stack from a MRAM cell, and consider that the two ferromagnetic layers are identical except to the thickness. As ferromagnetic material, permalloy with saturation magnetization $4\pi M_s = 10.8$ kG was used. The magnetic layers are assumed to be in the shape of ellipsoids making the demagnetizing field uniform across the entire layer. The ellipsoid's principal axes are taken along x, y and z: long-axis $2a = 120$ nm along Ox and short-axis $2b = 100$ nm along Oy. The thickness of bottom layer (considered to be adjacent to the tunnel junction and determining the state of the cell memory) is $t_1 = 5\ nm$, leading to the demagnetizing fields: $H_{d,x} = N_x M_s = 318.8$ Oe, $H_{d,y} = N_y M_s = 417$ Oe, $H_{d,z} = N_z M_s = 10.06$ kOe, and to in-plane uniaxial shape anisotropy field $H_{sh,1} = \left(N_y - N_x\right) M_s = 98.2$ Oe, where N_x, N_y, and N_z are the corresponding demagnetizing factors. Hereby we assume two contributions to anisotropy: an easy plane and an easy axis (EA) that is directed in this plane. It must be noted that in a quasistatic regime the easy plane anisotropy does not count due to in-plane

arrangement. The thickness t_2 of top layer is varied so that $t = t_2 / t_1 \leq 1$; a thickness imbalance also means a shape anisotropy imbalance. The intrinsic magnetocrytalline anisotropy is neglected.

The effective fields consist of applied field, demagnetizing field, phenomenological anti-ferromagnetic exchange coupling mediated by the spacer layer, and magnetostatic coupling between the two layers. The last two couplings are described by $h_J = W_{ex} / \left(2K_{sh,1} S t_1\right)$ and $h_{mag} = W_{mag} / \left(2K_{sh,1} V_1\right)$, respectively, where W_{ex}, W_{mag} are the exchange and magnetostatic energy when both layers are aligned along the easy axis $S = \pi ab$ is the layer's area, and V_1 is first layer's volume. The magnetostatic interaction field was calculated using themethod presented in Ref. 66. All magnetic fields presented throughout the rest of this chapter are normalized by $H_{sh,1}$.

Because an instantaneous change of the applied field from zero to some value is not very realistic, sinusoidal time dependence for the field pulse rise and fall as described in the previous chapter (see Fig. 4.4) are assumed. The rise/fall time is a function of the pulse's amplitude, so that the field sweep rate v_H, defined as the ratio between the amplitude and pulse's rise/fall time, is constant. The field pulse width T_H is the amount of time the pulse takes to go from zero to high and back to zero again. The final state is taken after 5 ns from the termination of applied pulse.

5.3.2 Dynamic critical curves of symmetric and asymmetric SAF structures

In Fig. 5.9 we present sCCs for $t = 0.8$ and $t = 1$, respectively, obtained by making the determinant δ of the free energy's Hessian equal to zero [19]. Irreversible

discontinuous magnetization reversal occurs as the applied magnetic field crosses the interior curves in the way shown by thin arrows. For $t = 0.8$ [see Fig. 5.9(a)] the interior curve consists of a heartlike part (heart for short) and an astroid-like part, the height of the last being around 0.05, so that it appears almost like a point in the figure. The free energy has one minimum (one stable configuration) inside the hearts, while between them and the exterior curve the energy has two minima. For $t = 1$ [see Fig. 5.9(b)] the interior CC consists only of an astroid-like part, two pairs of degenerate minima existing inside it, one minimum outside the exterior CC (also called saturation CC because it is the locus of fields at which the two moments become parallel), and one pair of degenerate minima otherwise.

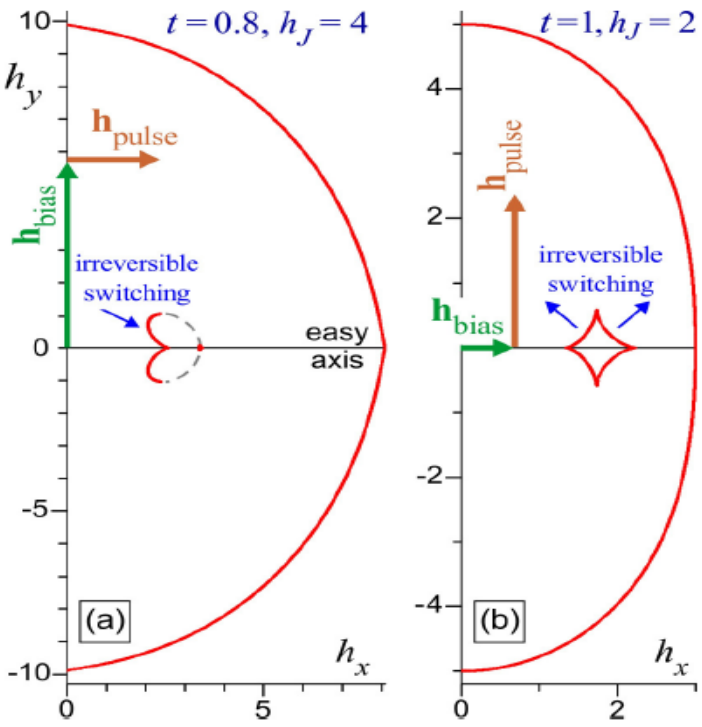

Figure 5.9. sCCs for an asymmetric SAF (a) and for a symmetric one (b). A strategy to point out CCs for an asymmetric SAF is to use a bias field perpendicular to EA and then a pulse field parallel to EA. For the symmetric case, a decreasing field is applied along EA, starting from positive saturation, and then a pulse field perpendicular to EA.

In a quasistatic regime, a discontinuous transition occurs when an increasing field starting from zero crosses the right side of the astroid-like part. Decreasing further the field back to zero, a discontinuous transition occurs when the field crosses the left side of the astroid, bringing the system back to the original state. Thus, a strategy to point out the CCs is to use both a bias and a pulse field (see Fig. 5.9), for $t = 0.8$ we have to start from $h_{bias} = 0$ and increase it perpendicular to EA, and for each h_{bias} value, field pulses with different amplitude are applied along EA (we denote with B_1 this field configuration). Comparing the system state before the pulse application to the state after completion of pulse, we identify the discontinuous transitions which take place, namely the left side of heart and the exterior CC. Because for $t = 1$ the B_1 configuration can not reveal the like CC, we decrease h_{bias} along EA starting from positive saturation, and then for each h_{bias} value, field pulses with different amplitudes are applied perpendicular to EA (B_2 configuration). This configuration can reveal the left sides of both astroid-like CCs, corresponding to $h_x > 0$ and $h_x < 0$, respectively.

The sCCs are restricted to the quasistatic regime and do not take into account the dynamics of the magnetization, i.e., the SAF is subject to a slowly varying field so that the system stays within one energy well and irreversible switches occur only when the state occupied by the system loses stability. If the pulse field has a rise time shorter than the relaxation time then the precessional term from LLG equation can carry the magnetization over a large range of motion before energy is dissipated (precessional regime). Also there is an out of plane component of magnetization.

In order to determine the parameter's values for reliable operation of a MRAM cell, we have studied the switching properties as a function of pulse's shape and length, damping, and magnetostatic coupling.

The switching behavior of an asymmetric SAF element as a function of the peak value of the pulse field and the strength of the bias field is presented in Fig. 5.10, together with sCCs. The damping coefficient $\alpha = 0.008$, typical for permalloy, was chosen [106].

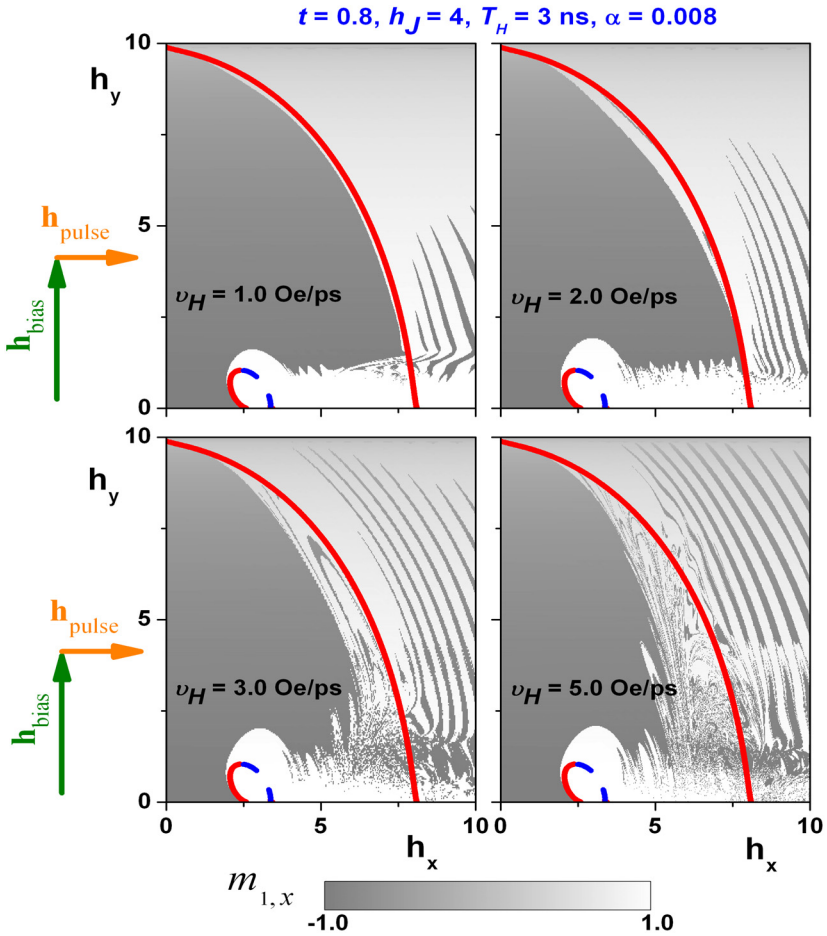

Figure 5.10. Switching diagrams of an asymmetric SAF at different values of sweep rates υ_H. The B_1 field configuration was used. Each point (h_x, h_y) is the co-ordinate of the total vector field $\mathbf{h}_{bias} + \mathbf{h}_{pulse}$ when $\mathbf{h}_{pulse}$ reached its peak value. Dark gray areas represent $m_{1,x} = -1$ (where $m_{1,x}$ is the $\mathbf{m}_1$'s projection on the x axis), white areas represent $m_{1,x} = 1$, and the intermediate values are represented with shades of gray. The bold lines are sCCs. The unrevealed right sides of CCs are presented by dotted blue curves.

One can see from Fig. 5.10 that the final state is sensitive to the sweep rate v_H. As v_H increases the nonswitching region corresponding to outermost dCC shrinks and an instability region, with switching/nonswitching fringes, grows up because a significant ringing of the magnetic moments still exists during the field pulse and the final state is determined by the positions of the moments at the end of the pulse. The region corresponding to interior dCC, where switches can occur, is enlarged compared to sCC, and what is important to observe is that only a digit or word field (applied at $\pm 45^0$ with respect to the easy axis) in toggle MRAM, can switch the magnetization.

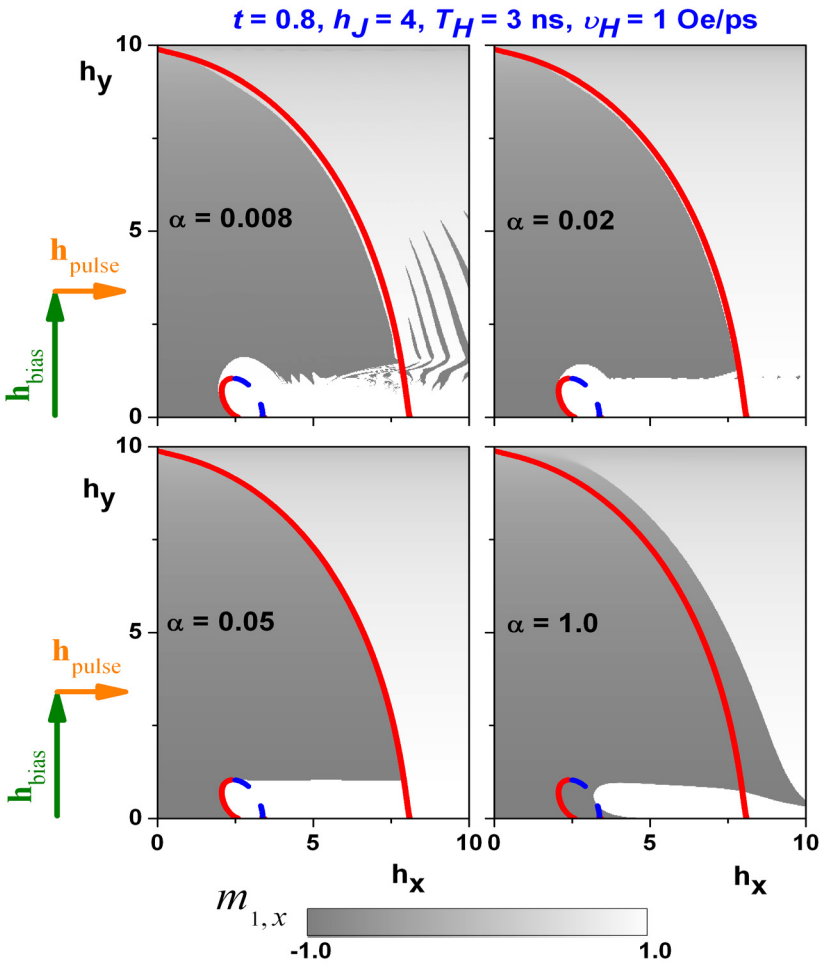

Figure 5.11. Switching diagrams of an asymmetric SAF at different values of damping parameter α.

Consequently, using sCCs instead of dCCs in SAF characterization can lead to inadvertent switching of half-selected memory cells. Also, we observe that irreversible switches appear when the field crosses the upper right part of the heart, in contrast with the static case.

In order to minimize dynamical effects, rare-earth dopants were used in Ref. 107 to increase α (α describing the energy dissipation and magnetization's relaxation into the magnetic field's direction) [107]. As α increases the instability fades away (see Fig. 5.11) the interior dCC shrinks towards sCC and the exterior dCC expands to sCC, at $\alpha = 0.05$ dCCs pretty much concur with sCCs.

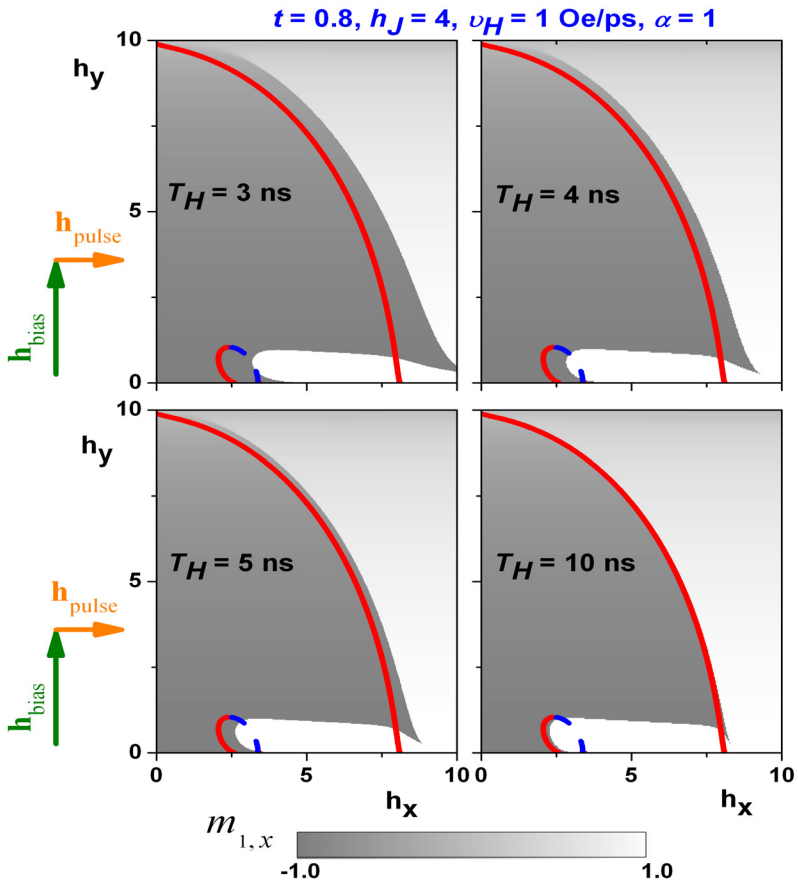

Figure 5.12. Switching diagrams of an asymmetric SAF at different values of pulse length T_H.

Further, for $\alpha > 0.05$ the magnetization can not follow the applied field and dCCs shift toward higher fields. Instead, using longer pulses dCCs move back toward sCCs as shown in Fig. 5.12.

Similarly, in the case of symmetric SAF, as v_H increases the nonswitching region corresponding to outermost dCC shrinks and an instability region grows up (see Fig. 5.13). The regions corresponding to interior CC, shrink a little bit, and are almost independent on v_H.

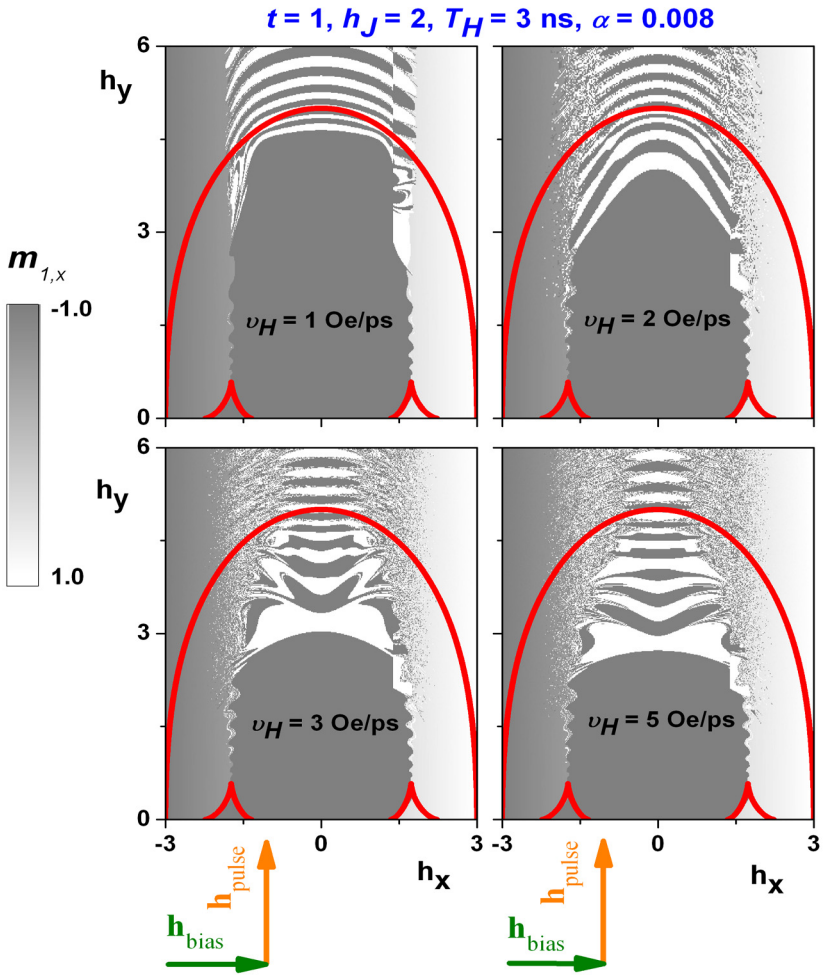

Figure 5.13. Switching diagrams of a symmetric SAF using B_2 configuration at different values of sweep rate υ_H.

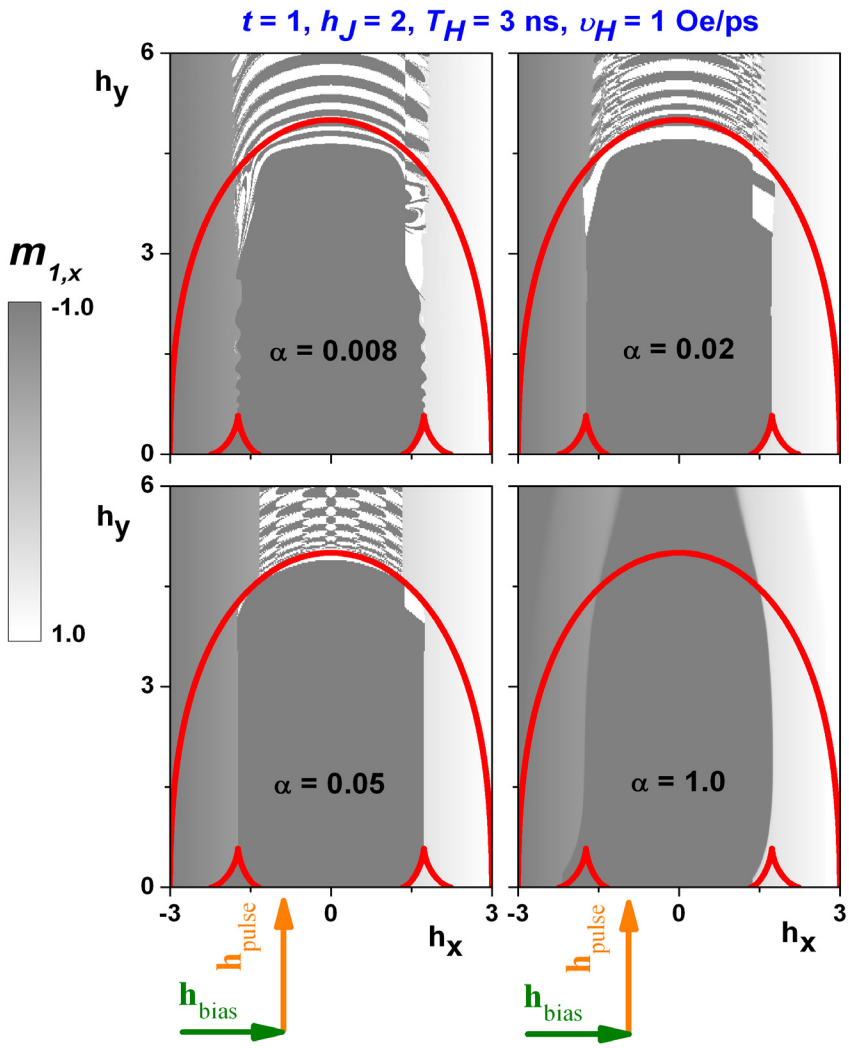

Figure 5.14. Switching diagrams of a symmetric SAF using B_2 configuration at different values of damping parameter α .

As α increases the instability fades away and the interior dCCs shift toward higher fields (see Fig. 5.14). However, B_2 configuration can not reveal the entire exterior dCC, and in Fig. 5.15 we combine this method with B_1 configuration: the system switches when the increasing field crosses the right branch of the interior CC and reverses back when the decreasing field crosses the left branch, so that the interior CC is not revealed, but the switch corresponding to the exterior CC can be detected.

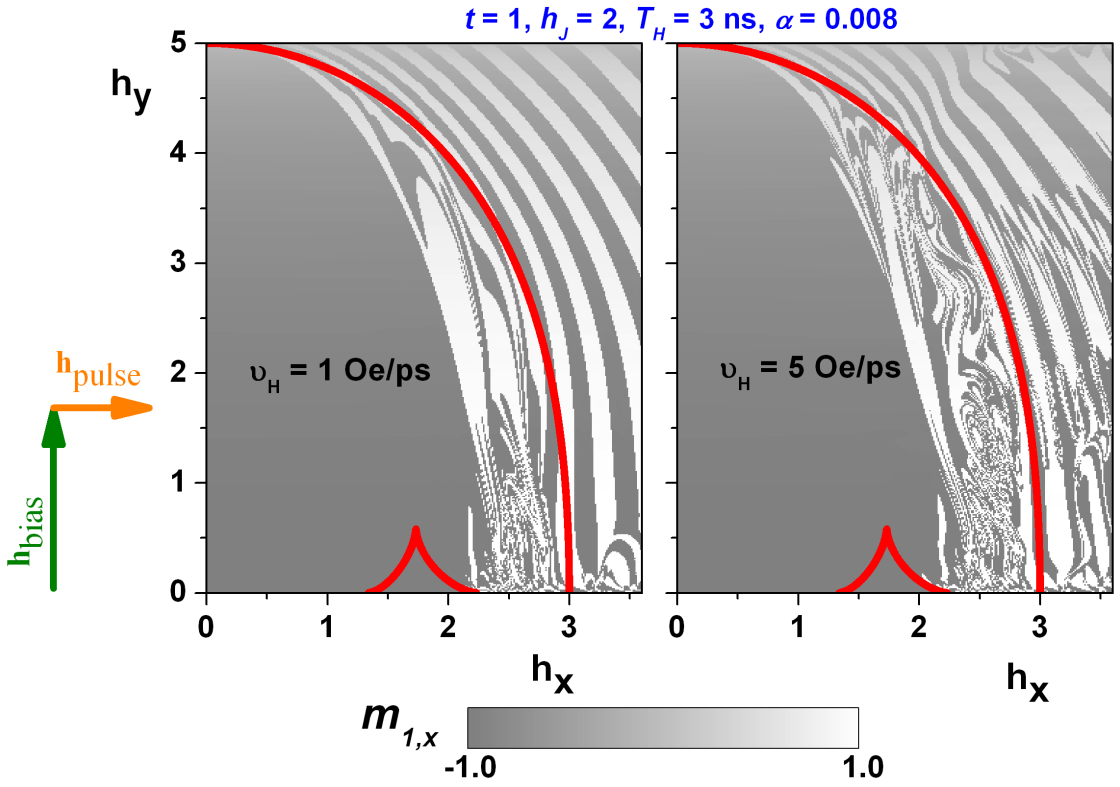

Figure 5.15. Switching diagrams of a symmetric SAF using B_1 configuration.

5.3.3 Magnetostatic coupling effects on dynamic critical curve

Until now we have neglected the magnetostatic coupling between the two layers, i.e., we have considered that the magnetostatic coupling is absorbed into the exchange constant h_J, both of them favoring an antiparallel alignment. However, due to the elliptical shape of the layers the magnetostatic fields have an asymmetry in the spatial dependence, whereas h_J has none. From Figs. 5.10 and 5.16 we can see the differences between exchange and magnetostatic coupling, both for sCCs and dCCs: the exterior sCC expands toward higher fields, while the interior CC shifts toward origin, increasing the possibility of undesirable switching of half-selected memory cells.

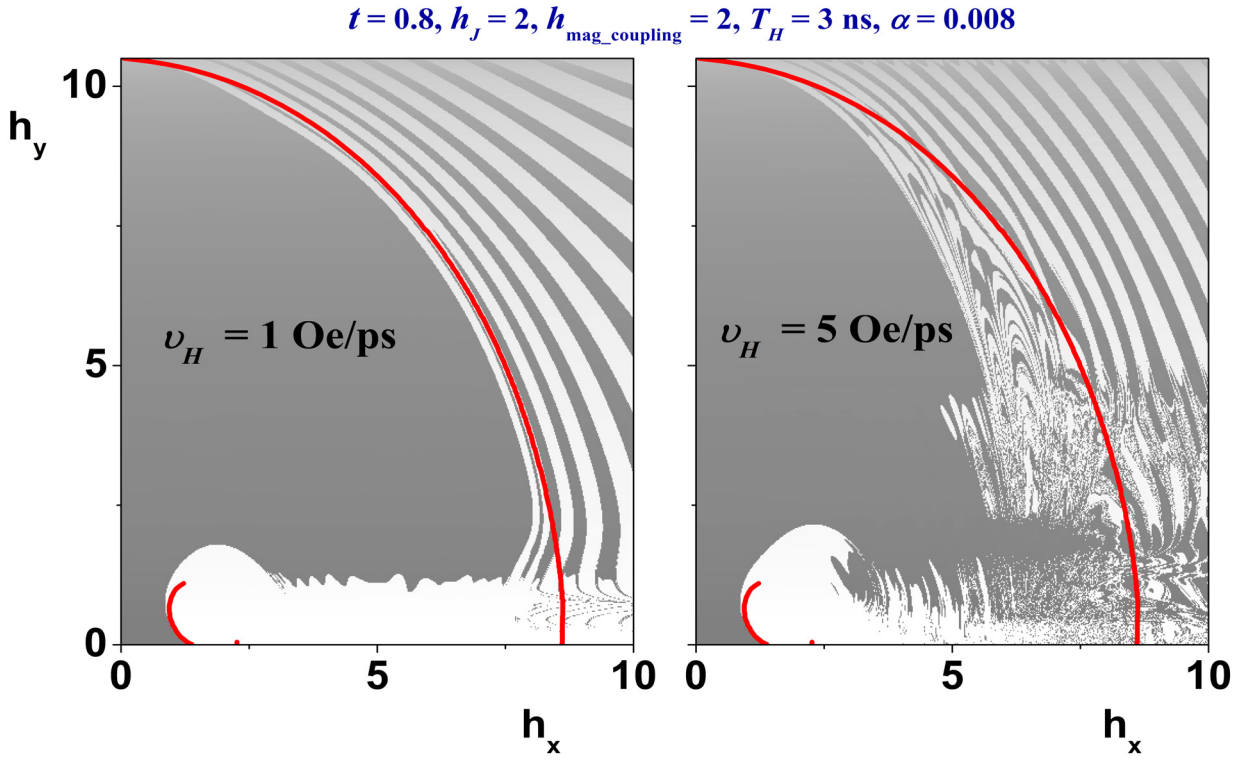

Figure 5.16. Switching diagrams of an asymmetric SAF taking into account both exchange and magnetostatic coupling.

5.4 Dynamic and temperature effects in toggle MRAM

In this section we expand the study on the dynamic switching of SAF in magnetic random access memory following the toggle mode mechanism. Based on dCCs discussed in the previous section, we will build up the toggle switching diagrams as originally proposed in the Ref. 108. Comparing the illustrative L-shaped critical switching curve presented in Fig. 5.4 in section 5.1.2, which is currently used for explaining the switching in toggle MRAM, with dynamic toggle switching diagrams it will be shown that a consistent switching can be achieved only under specific conditions that take into account the dynamics of the systems.

With memory area density increasing and the memory cell size further shrinking, the study of thermal fluctuations in toggle MRAM structures becomes extremely important in recording thermal stability. This section is motivated also by considerable interest in thermally assisted writing of MRAM, which might further increase memory density, while maintaining long data retention.

5.4.1 Dynamic toggle switching diagram

As mentioned previously, in toggle MRAM, the switching process is initiated by applying two orthogonally oriented, time delayed field pulses: word and digit fields $\mathbf{h}_{word}$ and $\mathbf{h}_{digit}$, in plane at $+45^0$ and -45^0 with respect to the easy axis of the element. The field pulses sequence is sketched in Fig. 5.17. The pulses with a width $T_W = T_D = T_H$ are delayed against each other with $\Delta T_{WD} = T_W / 2$ offset and ΔT_{WD} overlap.

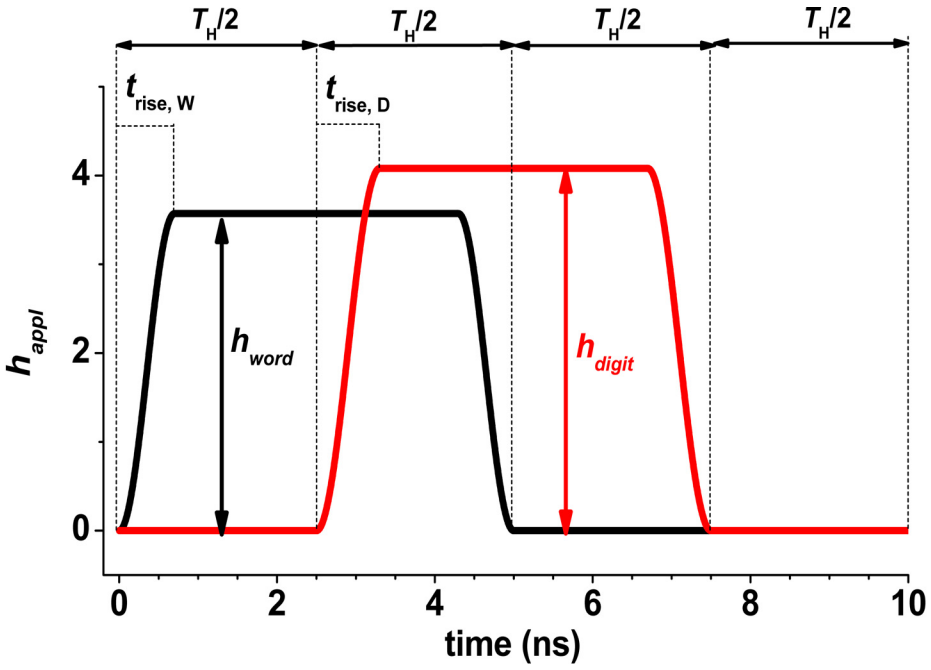

Figure 5.17. Time dependence of the applied field pulses. The field sweep rate is defined as $\upsilon_H = h_{word} / t_{rise,W} = h_{digit} / t_{rise,D}$ and it is constant.

The final state of the MRAM cell, which is determined by the orientations of both ferromagnetic layers with respect to each other instead of one as the top layer in the case of studying the dynamic critical curve of SAF, is taken at ΔT_{WD} after the termination of digit field pulse. The state "1" is defined as $\mathbf{m}_1 = -\hat{\mathbf{x}},\ \mathbf{m}_2 = \hat{\mathbf{x}}$ and the state "0" as $\mathbf{m}_1 = \hat{\mathbf{x}},\ \mathbf{m}_2 = -\hat{\mathbf{x}}$.

The toggle switching diagram showing the switching behavior of a symmetric and an asymmetric SAF element at $T = 0\ K$, as a function of the applied digit and word field pulse strengths for different values of the applied field sweep rate υ_H are presented in Figs. 5.18 and 5.19. The pulse's width is $T_H = 3\ ns$, and the antiferromagnetic coupling constant is $h_J = 4$. For a symmetric element, due to the symmetry, only nonswitching (black areas) or toggle mode (white areas) can be obtained. For an asymmetric element besides switching and toggle modes, the direct write mode is in effect (light-gray areas in Fig. 5.18). In addition, we have identified a different write mode that we called inverse write mode (color areas in Fig. 5.18) for which the state 0 is switched to a 1 state after field pulse sequence, but the state 1 is not switched. This mode is strongly affected by the dynamic switching of the magnetization [108].

From Fig. 5.18 and 5.19 we can see that the final state is sensitive to the sweep rate υ_H of the applied field pulses, and that the switching behavior shares similar features presented in the study of dynamic switching curve of SAF. The sCCs are rotated 45^0 with respect to the digit field.

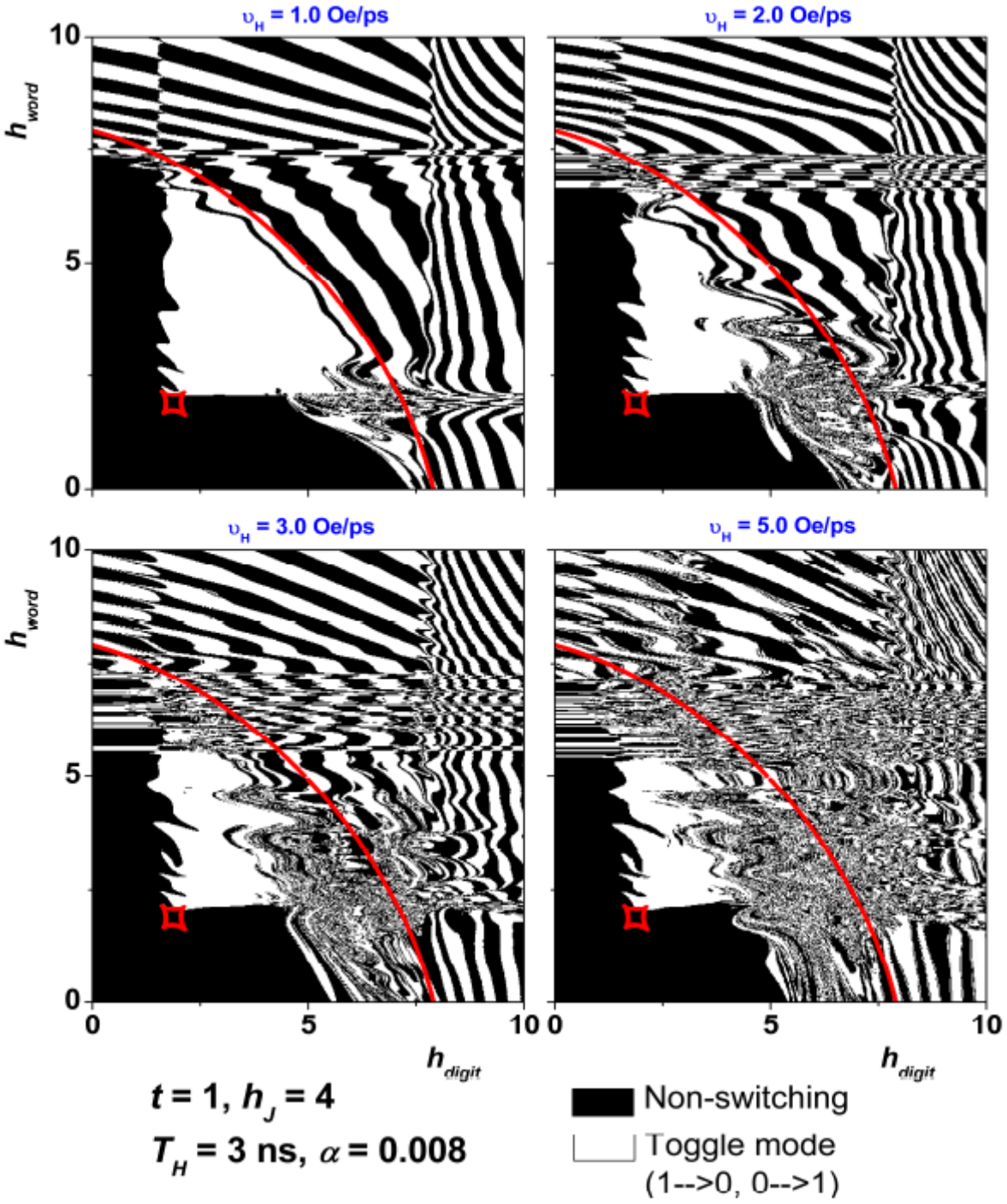

Figure 5.18. Toggle switching diagram of a symmetric SAF element, at $T = 0\ K$, as a function of the applied field pulse strengths for different values of the applied field sweep rate υ_H. The antiferromagnetic coupling constant $h_J = 4$ and the pulse width $T_H = 3\ ns$. Black areas represent nonswitching, and white areas toggle mode. The red lines are the sCCs.

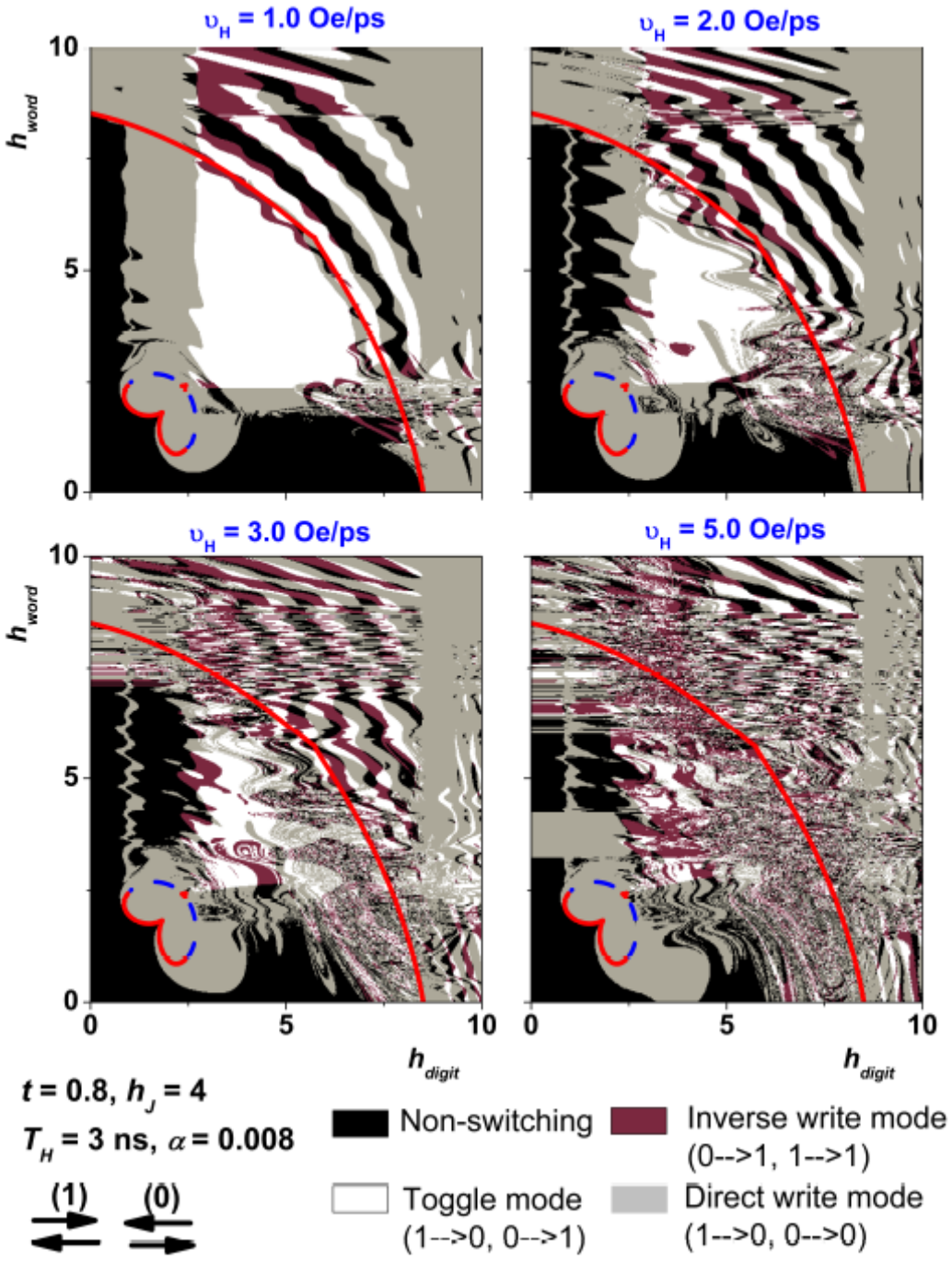

Figure 5.19. Toggle switching diagram of an asymmetric SAF element, at $T = 0\ K$, as a function of the applied field pulse strengths for different values of the applied field sweep rate υ_H. The antiferromagnetic coupling constant $h_J = 4$ and the pulse width $T_H = 3\ ns$. Black areas represent nonswitching, light-gray areas direct write, white areas toggle mode, and areas in color represent inverse write mode. The red lines are the left parts of sCCs. The unrevealed right parts of sCCs are indicated by dotted blue lines.

As we can see from Figs. 5.18 and 5.19 the boundary which delimits the toggle mode along $\mathbf{h}_{word}$ and $\mathbf{h}_{digit}$ axes is not smooth, and the switching and nonswitching areas alternate with increasing field amplitude. As the field sweep rate increases the extent of the instability region is also increasing. Compared to the results for $\upsilon_H = 0.5$ Oe/ps, we observe at $\upsilon_H = 4$ Oe/ps a strongly alternating behavior in the upper right part of the diagram for both cases symmetric and asymmetric elements. This alternating behavior has two causes: If the pulse's length is too short a significant ringing of the magnetization still exists during the field pulse and the final state is determined by the position of the magnetization at the end of the pulse. On the other hand, we have found that for low values of damping constant α, the basins of attraction of fixed points have a layerlike structure, similar with the case of a single Stoner-Wohlfarth particle. In order to minimize the first cause we have made simulations with longer field pulses see Fig. 5.20. The diagrams are zoomed in into the region inside the critical curve which is more important for investigating the switching of MRAM cell.

In addition we also take into account a uniaxial intrinsic anisotropy $H_{Ku} = 10$ Oe along the x-axis. The diagrams reflect a higher stability of the switching process along the $\mathbf{h}_{word}$ and $\mathbf{h}_{digit}$ axes but still show an alternating behavior in the upper right part. As we can see in Fig. 5.20 (b), the two magnetization vectors switch from a fixed point, followed by a few ringing periods. For a fast and reliable operation such ringing must be avoided as the damping time can take several nanoseconds.

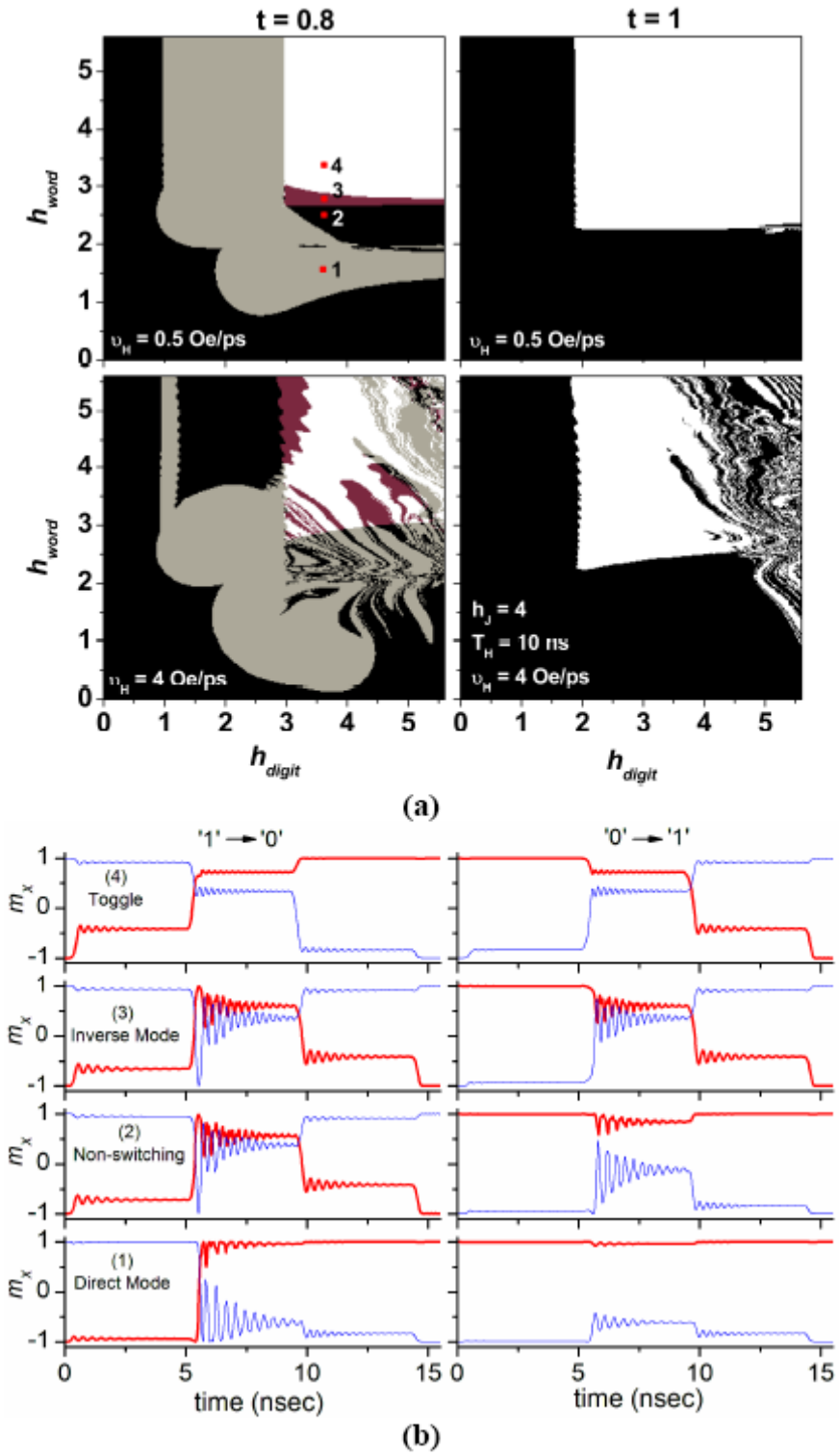

Figure 5.20. (a) Toggle switching diagram of an asymmetric (left) and symmetric (right) SAF element for $T = 0$ K, $h_J = 4$, $T_H = 10$ ns, and two values of the field sweep rate: $\upsilon_H = 0.5$ Oe/ps and $\upsilon_H = 4$ Oe/ps. (b) Time evolution of $m_{1,x}$ (red line) and $m_{2,x}$ (blue line) when the initial magnetization state is "1" (left) and "0" (right) at the positions indicated in the second switching diagram.

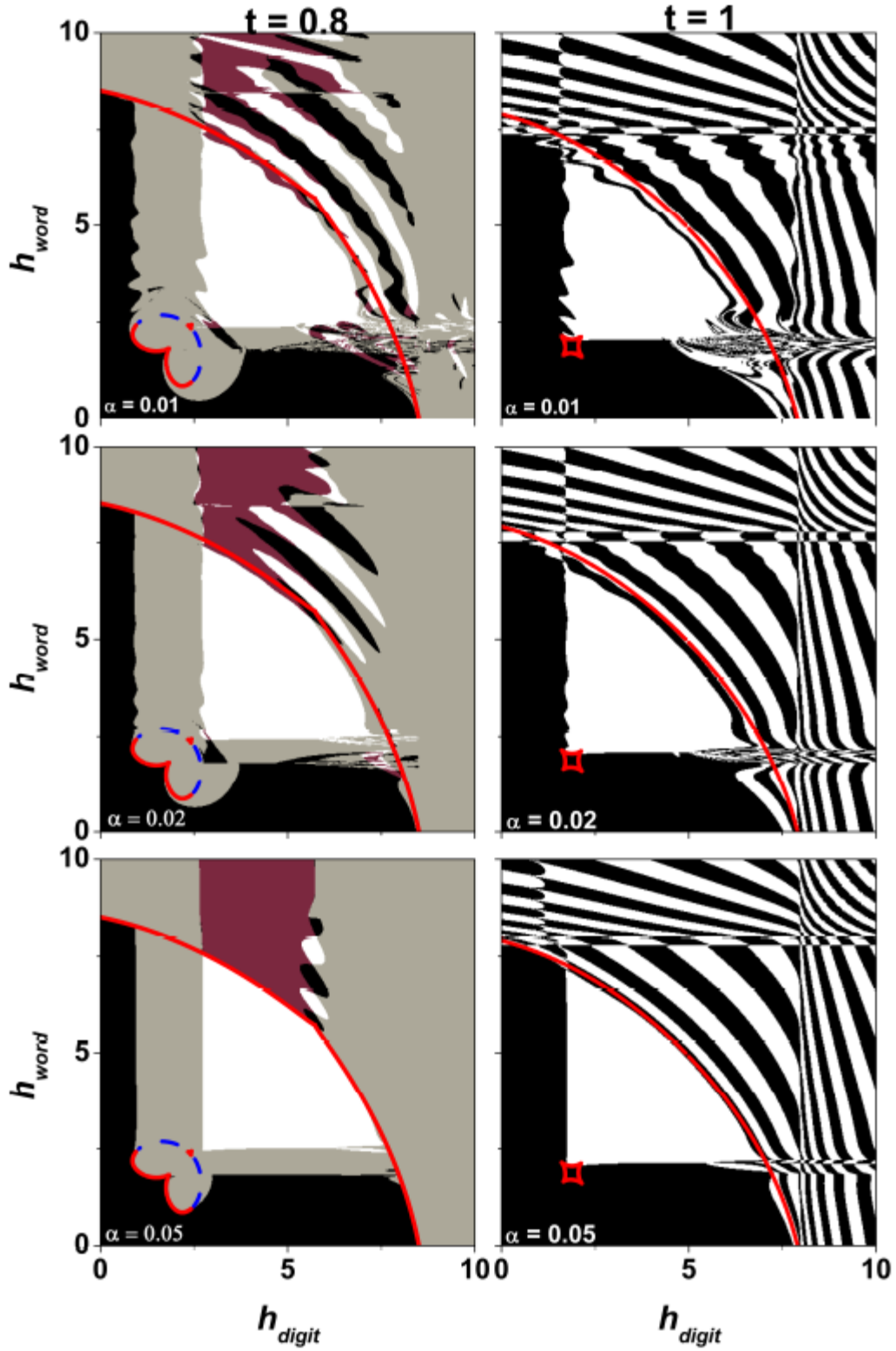

Figure 5.21. Toggle switching diagram of an asymmetric (left) and a symmetric (right) SAF element for $T = 0$ K , $h_J = 4$, $T_H = 3$ ns , $\upsilon_H = 4$ Oe/ps , and different values of the damping constant α .

The ringing can be avoided either by a precise control of a pulse amplitude/duration and MRAM cell parameters so that the system moves along a ballistic trajectory, or using a relatively slow rise time pulse.

In all the previous presented cases we observed that for an asymmetric element the direct write mode boundary is shifted toward the $\mathbf{h}_{digit}$ axis as the field sweep rate is increased, which reflects the instability of the switching process. Recent studies [94, 95] for ultrathin films show that, the damping constant α is enhanced when a nonmagnetic metal is deposited on the ferromagnetic film. Our simulations show that an increase of α diminishes the layer structure of the switching diagrams and gives rise to a clearer separation between the nonswitching/direct mode and toggle mode see Fig. 5.21. An increase of α increases the energy dissipation rate and consequently diminishes the ringing of the magnetization.

5.4.2 Thermal relaxation effect

As MRAM device sizes continue to shrink and operating frequencies continue to increase, high-frequency magnetic noise due to the thermal fluctuations may pose a fundamental limitation to MRAM performance. The magnetic moments effect random oscillations by thermal activation close to the bottom of the energy minima, but also fluctuations can allow the system to be thermally activated over finite energy barriers.

In the presence of thermal agitation it is supposed that the dissipative term in LLG equation describes only the statistical (ensemble) average of rapidly fluctuating random forces, and that for an individual particle a stochastic thermal field should be added.

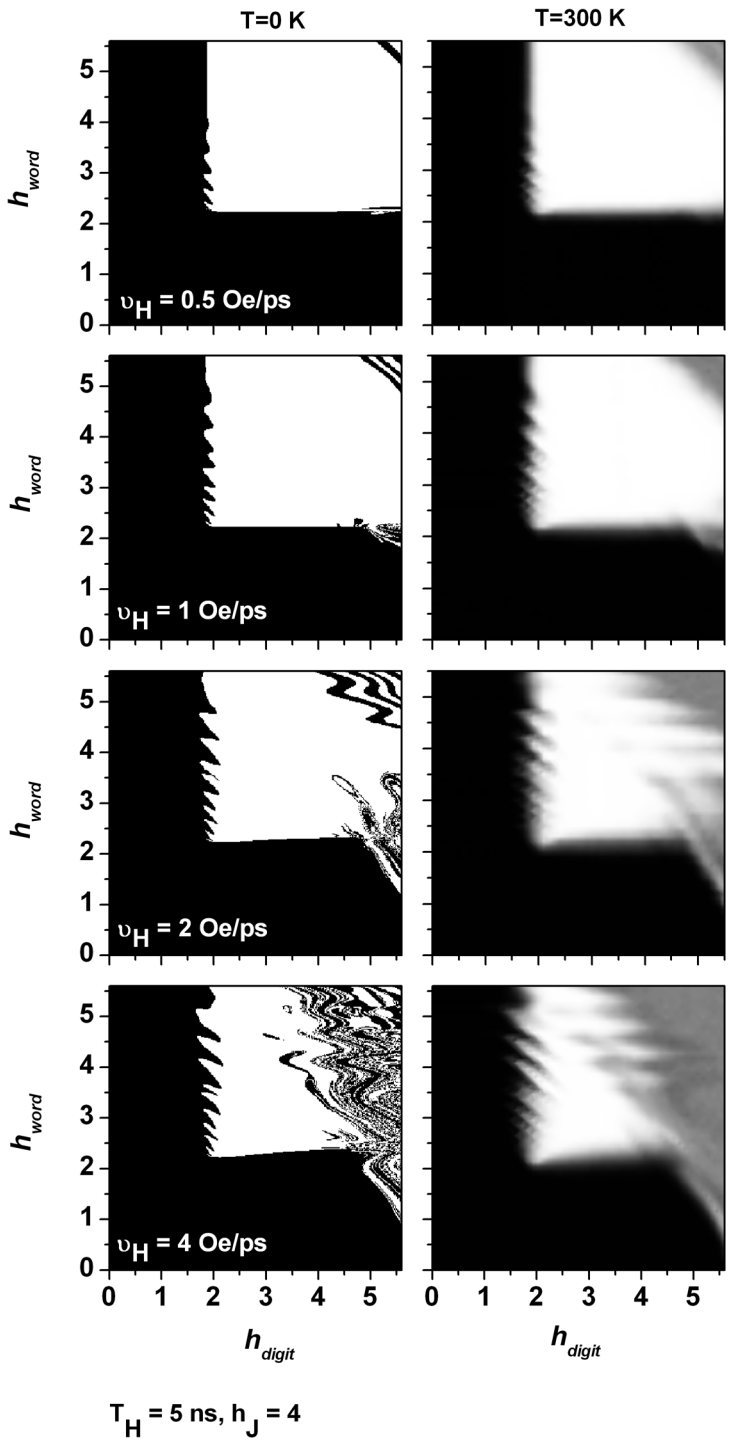

Figure 5.22. Probability of switching of a symmetric SAF element for $T = 300$ K, $h_J = 4$, $T_H = 5$ ns, and different values of the applied field sweep rate υ_H. Black areas represent nonswitching, i.e., switching probability $P = 0$, white areas $P = 1$, and the intermediate values of switching probability are represented with shades of gray.

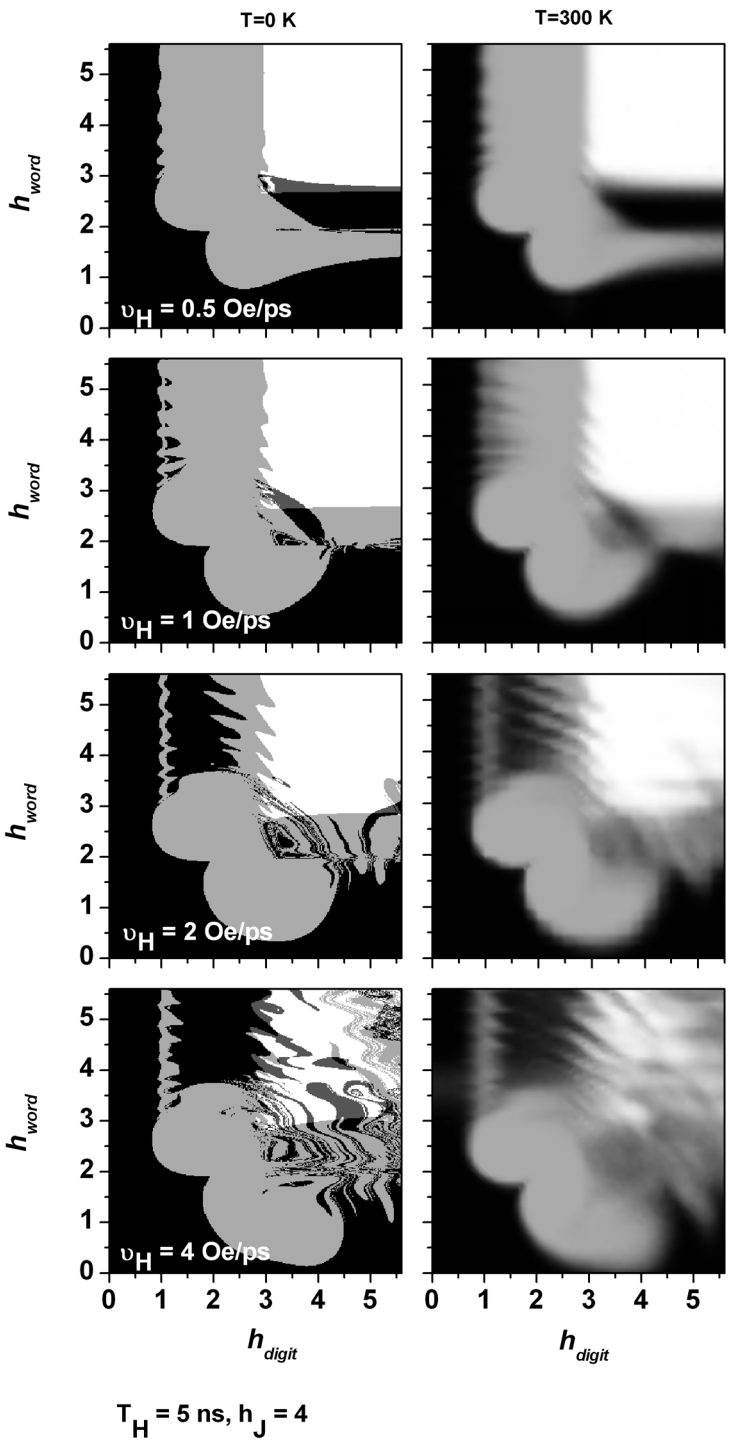

Figure 5.23. Probability of switching of an asymmetric SAF element for $T = 300$ K, $h_J = 4$, $T_H = 5$ ns, and different values of the applied field sweep rate υ_H. Black areas represent nonswitching, i.e., switching probability $P = 0$, white areas $P = 1$, and the intermediate values of switching probability are represented with shades of gray.

The stochastic field changes the deterministic motion of the magnetization into a random walk. The magnetic properties follow from an average over many numerical realizations of the dynamic process (discretized Brownian paths).

The probability of switching is plotted in a gray coded diagram as a function of the applied digit and word field pulse strengths in Figs. 5.22 and 5.23 for different values of the applied field sweep rate υ_H. Each simulated point from diagrams represents the statistic of 1024 repeatedly writing operations at certain h_{digit} and h_{word}. We can see that instead of a clear border between switching and nonswitching areas we have a transition region where the final state is sensitive to thermal fluctuations. This can be a consequence of the magnetization vector trajectories which do not lie in the layer planes and can provide a lower switching field, below the static limit, as we have shown previously.

5.5 Summary

In this chapter the role of the synthetic antiferromagnet (SAF) structure on magnetic random access memory (MRAM) has been presented. Its magnetization reversal has been extensively studied using both concepts of static and dynamic critical curves (sCC and sDC). Our new concept of dynamic critical curve, which is defined as the boundary between switching/nonswitching regions in the switching diagram of SAF elements subjected to a pulsed magnetic field, has been proposed. Comparing sCCs, which are currently used for studying the switching in toggle MRAM, with dCCs one can see that a consistent switching can be achieved only under specific conditions that take

into account the dynamics of the systems. We have also shown that using the sCCs instead of dCCs in characterization of a SAF can lead to inadvertent switching of half-selected memory cells.

Furthermore, in this chapter the switching properties of a MRAM cell in toggle mechanism have been investigated. We have shown that besides nonswitching, toggle, and direct mode as described based on sCC, an inverse write mode can be identified. In dealing with the problem of improving the writing time, one needs to pay careful attention to the parameters describing the pulse shape. As the applied field sweep rate υ_H rises, the switching diagrams increasingly have layerlike structures with alternating switching/nonswitching areas. The extent of the instability region is increasing with υ_H. This alternating behavior has two causes: the ringing of the magnetization during the field and the layerlike structure of basins of attraction of fixed points. A reliable switching is obtained only if the ringing is avoided either by a precise control of the pulse and MRAM cell parameters, so that the system moves along a ballistic trajectory, or using a relatively slow rise time pulse.

Finally, the thermal fluctuations affecting on the switching behavior of toggle MRAM have been demonstrated at the end of the chapter. We have pointed out that instead of a clear border between switching and nonswitching areas, the transition region is sensitive to thermal fluctuations.

Conclusion

The evolution of data storage technology has been impressive over the last fifty years. If the 20th century is well known as the *information technology era* with the huge development of electronic devices relying strictly on the transport of the electrical charge of electron, the 21st century will be known as *the century of spintronic devices*. As electronic devices become smaller, quantum properties of the wavelike nature of electrons are no longer negligible. Consequently we are approaching into a new era of spintronic devices where information is stored into spin as one of two possible orientations. Spintronic devices offer the possibility of enhanced functionality, higher speed and reduced power consumption. Spin lifetime is relatively long, on the order of nanoseconds. Magnetic storage based on novel technology can be nonvolatile. One of the most promising candidates for application as a nonvolatile spintronic memory device is magnetic random access memory (MRAM). MRAM uses magnetic storage elements instead of electric used in conventional RAM. Tunnel junctions are used to read the information stored in MRAM cells, typically a "0" for zero point magnetization state and "1" for antiparallel state. It has the potential to be fast, dense and cost efficient with low power consumption. The higher the information density on MRAM, the smaller the magnetic cell must be. The higher the writing speed of information on MRAM, the faster the manipulation (i.e. reversal) of the moments must become. Thus "smaller" and "faster"

represents the driving force for the advancement of MRAM and of the magnetic storage technology in general.

This thesis focuses on the speed of manipulating the magnetization in MRAM and on understanding the switching behavior of magnetic systems. As the technologic demand pushes for lower access time, the study of dynamics of the moments in a MRAM cell becomes indispensable. In this work we present the study on both static and dynamic aspects of magnetization reversal.

From static point of view, the magnetization switching can be elegantly described using the concept of critical curve (CC) or Stoner-Wohlfarth (SW) astroid which is defined as the locus of in-plane fields at which the irreversible magnetization reversal occurs, and developed initially for uncoupled magnetic systems. Based on the remarkable properties of CC, both the hysteresis loops and the corresponding transverse susceptibility curves can be obtained, providing a lot of useful information about micromagnetic and structure properties of magnetic materials. Currently there are a lot of experimental methods to measure the critical curve have been proposed. One of those methods, the one based on the detection of singularities of reversible susceptibility experimental curves as discussed in detail in this work, is a new, sensitive and simple method. As a proof, we used this method to determine the critical curves of different samples of Co/SiO_2 multi-layers.

Furthermore, as a demonstration to show how important role of the critical curve in investigating magnetic systems, the study of switching behavior of the magnetization in conventional magnetic random access memory (MRAM) following Stonner-Wohlfarth

reversal has been presented. The critical curve describes the boundary between switching and non-switching regions and gives the map of "full-select" and "half-select" switching fields.

The study of dynamic behavior of magnetization in MRAM cells subjected to a short magnetic field pulse is also addressed in this work, giving the so-called dynamic critical curve. We observed not only the time evolution and switching behavior of an isolated MRAM cell under different pulsed applied fields, but also its magnetization behavior when taking into account the dipolar interacting field created by its nearest neighbors in MRAM structure. One important conclusion was made is that, in dealing with the problem of improving the density of data storage medium, the dipolar interaction between neighboring magnetic elements needs to be taken into account.

Although development of MRAM is in its early stages of commercial production, there are still problems to be solved such as the half-select margin issue and activated errors, limit the usefulness of SW MRAM to small arrays and short lifetimes.

A new approach, the toggle mode, that effectively eliminates the half-select disturb phenomenon present in conventional MRAM has been proposed by Leonid Savtchenko. In "toggle mode" MRAM, so-called Toggle-MRAM, the cell is modified to contain a pinned SAF as the hard magnetic layer and a free SAF as the soft magnetic layer. Through the use of two coupled magnetic free layers instead of a single free layer as in conventional MRAM, the toggle MRAM bit state can be programmed via a "toggling" mode using the programming pulse sequence. The theory of simple uncoupled films of CC based on Stonner-Wohlfarth reversal is no longer applicable in the case of

coupled films as SAF. Consequently, new theories of CCs of SAF have been extensively studied. However, the CCs of SAF are restricted only on a quasistatic regime, where the dynamics and precessional effects are neglected. In this thesis we have proposed a new dynamic generalization of sCCs, analyzing the magnetization switching of SAF elements subjected to pulsed magnetic fields. Comparing with sCCS, which are currently used for studying the switching in toggle MRAM, dCCs give the consistent switching only under specific conditions that take into account the dynamics of the systems. Based on dCCs, we go further to build up the toggle switching diagrams of MRAM cell subjected to pulse sequence. We have shown that the dynamic switching diagrams still keep the ideal L-shaped critical switching curve except that the boundary between nonswitching/toggle mode regions is not smooth and the final state is sensitive to the pulse shape.

Besides the toggle switching scheme to improve the write process in MRAM, a newer technique for controlling the magnetization reversal based on the current-induced spin transfer torque introduced by Slonczewski and Berger has been proposed, constituting a new generation of MRAM, so-called spin torque MRAM (STT-RAM). It replaces the conventional method utilizing current induced magnetic field. The transfer of the spin angular momentum between two magnetic layers by the current flowing perpendicular to plane can reverse the magnetization of one of the magnetic layers. The novel technology utilizing the spin-transfer torque is expected to reduce the switching time of magnetization as well as to increase the recording density of MRAM.

This thesis provides the exploration of the dynamic switching triggered by spin angular momentum transfer in a pulsed current used in STT-RAM. We have shown that

in the switching diagrams the boundary between stable ultrafast switching and nonswitching regions is not smooth but it has a seashell spiral pattern (fringes), with switching and non-switching areas alternating with increasing current pulse amplitude and duration.

Furthermore, we have investigated the magnetization switching employing both the spin-transfer torque and the torque by a magnetic field. When the system undergoes the competitive torques of a spin-polarized current and an external field, the final direction of the magnetization is uniquely determined regardless of the initial direction. This gives the relaxing-precessional switching an advantage over the precessional switching. The precessional switching properties of magnetization are strongly enhanced by the presence of the spin-transfer torque current. Reversal processes become complex, but switching regions are enlarged.

With memory area density increasing and the memory cell size further shrinking, the study of the thermal fluctuations in MRAM structures becomes extremely important in recording thermal stability. This work is prompted also by a considerable interest in thermally assisted writing of MRAM, which might further increase memory density, while maintaining long data retention. Our results reveal that the thermal fluctuations affect the switching behavior.

In conclusion, this dissertation provides a theoretical analysis of magnetization dynamics in nanometer scale of different MRAM structures over nanosecond time scales. The results presented are of direct technological relevance for increasing the speed of data processing in MRAM. They offer valuable information for the design of magnetic

field pulse that guarantee precessional switching and are also filling many gaps existent in understanding ultrafast magnetization reversals in nano-scale magnetic systems.

References

[1] B. Hillebrands and K. Ounadjela, *Spin dynamics in confined magnetic structures I*. Berlin ; New York: Springer, 2002.

[2] B. Hillebrands and K. Ounadjela, *Spin dynamics in confined magnetic structures II*. Berlin ; New York: Springer, 2003.

[3] R. P. Cowburn, "The future of universal memory," *Materials Today, July/August 2003,* pp. 32-38, July/August 2003.

[4] M. Bauer, J. Fassbender, B. Hillebrands, and R. L. Stamps, "Switching behavior of a Stoner particle beyond the relaxation time limit," *Physical Review B,* vol. 61, pp. 3410-3416, Feb 1 2000.

[5] S. Kaka and S. E. Russek, "Precessional switching of submicrometer spin valves," *Applied Physics Letters,* vol. 80, pp. 2958-2960, Apr 22 2002.

[6] L. Berger, "Emission of spin waves by a magnetic multilayer traversed by a current," *Physical Review B,* vol. 54, pp. 9353-9358, Oct 1 1996.

[7] L. Berger, "Multilayer configuration for experiments of spin precession induced by a dc current," *Journal Of Applied Physics,* vol. 93, pp. 7693-7695, May 15 2003.

[8] J. C. Slonczewski, "Current-driven excitation of magnetic multilayers," *Journal Of Magnetism And Magnetic Materials,* vol. 159, pp. L1-L7, Jun 1996.

[9] J. C. Slonczewski, "Excitation of spin waves by an electric current," *Journal Of Magnetism And Magnetic Materials,* vol. 195, pp. L261-L268, May 1999.

[10] T. Gerrits, H. A. M. van den Berg, J. Hohlfeld, L. Bar, and T. Rasing, "Ultrafast precessional magnetization reversal by picosecond magnetic field pulse shaping," *Nature,* vol. 418, pp. 509-512, Aug 1 2002.

[11] I. Tudosa, C. Stamm, A. B. Kashuba, F. King, H. C. Siegmann, J. Stohr, G. Ju, B. Lu, and D. Weller, "The ultimate speed of magnetic switching in granular recording media," *Nature,* vol. 428, pp. 831-833, Apr 22 2004.

[12] J. C. Slonczewski, IBM Research Memorandum 003.111.224, 1956.

[13] A. Thiaville, "Extensions of the geometric solution of the two dimensional coherent magnetization rotation model," *Journal Of Magnetism And Magnetic Materials,* vol. 182, pp. 5-18, Feb 1998.

[14] E. C. Stoner and E. P. Wohlfarth, "A mechanism of magnetic hysteresis in heterogeneous alloys," *Philosophical Transactions of the Royal Society of London,* vol. A240, pp. 599-644, 1948.

[15] L. Savtchenko, B. N. Engel, N. D. Rizzo, M. F. Deherrera, and J. A. Janesky, "Method of writing to scalable magnetoresistance random access memory element " US Motorola, Inc. (Schaumburg, IL) 2003.

[16] J. C. Slonczewski, U. S., 1997.
[17] M. Hosomi, H. Yamagishi, H. Ymamoto, T. Bessho, K. Higo, and Y. Yamane, *International Electron Devices Meeting,* 2005.
[18] Y. Huai and P. P. Nguyen, U.S., 2005.
[19] H. Chang, "Analysis of static and quasidynamic behavior of magneostatically coupled thin magnetic films," *IBM Journal of Research and Development,* vol. 6, pp. 419-429, 1962.
[20] H. Chang, "Coupled Biaxial Films," *Journal of Applied Physics,* vol. 35, pp. 770-771, 1964.
[21] E. Goto, N. Hayashi, T. Miyashita, and K. Nakagawa, "Magnetization and Switching Characteristics of Composite Thin Magnetic Films," *Journal of Applied Physics,* vol. 36, pp. 2951-2958, September 1965.
[22] D. C. Worledge, "Spin flop switching for magnetic random access memory," *Applied Physics Letters,* vol. 84, pp. 4559-4561, May 31 2004.
[23] H. Fujiwara, S. Y. Wang, and M. Sun, "Magnetization Behavior of Synthetic Antiferromagnet and Toggle-Magnetoresistance Random Access Memory," *Transactions of the Magnetics Society of Japan,* vol. 4, pp. 121-129, 2004.
[24] H. Fujiwara, S. Y. Wang, and M. Sun, "Critical-field curves for switching toggle mode magnetoresistance random access memory devices," *Journal of Applied Physics,* vol. 97, p. 10P507, 2005.
[25] S. Y. Wang and H. Fujiwara, "Optimization of magnetic parameters for toggle magnetoresistance random access memory," *Journal Of Magnetism And Magnetic Materials,* vol. 286, pp. 27-30, Feb 1 2005.
[26] D. C. Worledge, "Single-domain model for toggle MRAM," *Ibm Journal of Research and Development,* vol. 50, pp. 69-79, Jan 2006.
[27] D. C. Worledge, P. L. Trouilloud, and W. J. Gallagher, "Theory for symmetric toggle magnetic random access memory," *Applied Physics Letters,* vol. 90, p. 3, May 2007.
[28] C. Radu, D. Cimpoesu, A. Stancu, and L. Spinu, "Measurement of the critical curve of a synthetic antiferromagnet," *Applied Physics Letters,* vol. 93, p. 022506, 2008.
[29] H. Fujiwara, "Evolution of magnetization configuration phase diagram with increasing exchange coupling in synthetic antiferromagnets," *Applied Physics Letters,* vol. 93, pp. 172502-3, 2008.
[30] S. Chikazumi and C. D. Graham, *Physics of ferromagnetism*, 2nd ed. Oxford, New York: Clarendon Press ; Oxford University Press, 1997.
[31] J. L. Dormann, D. Fiorani, and E. Tronc, "Magnetic relaxation in fine-particle systems," in *Advances In Chemical Physics, Vol 98*. vol. 98 New York: John Wiley & Sons Inc, 1997, pp. 283-494.
[32] G. Bertotti, *Hysteresis in magnetism : for physicists, materials scientists, and engineers*. San Diego: Academic Press, 1998.
[33] Y. Lu, P. L. Trouilloud, D. W. Abraham, R. Koch, J. Slonczewski, S. Brown, J. Bucchignano, E. O'Sullivan, R. A. Wanner, W. J. Gallagher, and S. S. P. Parkin,

"Observation of magnetic switching in submicron magnetic-tunnel junctions at low frequency," *Journal Of Applied Physics,* vol. 85, pp. 5267-5269, Apr 15 1999.
[34] W. Wernsdorfer, "Classical and quantum magnetization reversal studied in nanometer-sized particles and clusters," in *Advances in Chemical Physics, Vol 118*. vol. 118 New York: John Wiley & Sons Inc, 2001, pp. 99-190.
[35] L. Spinu, H. Pham, C. Radu, J. C. Denardin, I. Dumitru, M. Knobel, L. S. Dorneles, L. F. Schelp, and A. Stancu, "Probing two-dimensional magnetic switching in Co/SiO2 multilayers using reversible susceptibility experiments," *Applied Physics Letters,* vol. 86, pp. 012506/1-012506/3, 2005.
[36] A. Aharoni, E. H. Frei, S. Shtrikman, and D. Treves, "The Reversible Susceptibility Tensor of the Stoner-Wohlfarth Model," *Bulletin of the Research Council of Israel,* vol. 6A, pp. 215-238, April-July 1957.
[37] L. Néel, *Ann. Geophys.,* vol. 5, p. 99, 1949.
[38] W. F. Brown, "Thermal Fluctuations of a Single-Domain Particle," *Physical Review,* vol. 130, p. 1677, 1 June 1963.
[39] L. D. Landau and E. M. Lifshitz, "On the theory of the dispersion of magnetic permeability in ferromagnetic bodies," *Phys. Z. Sowjet.,* vol. 8, pp. 153-169, 1935.
[40] T. L. Gilbert, "A phenomenological theory of damping in ferromagnetic materials," *IEEE Transactions on Magnetics,* vol. 40, pp. 3443-3449, Nov 2004.
[41] W. T. Coffey, P. J. Cregg, and Y. P. Kalmykov, "On the theory of Debye and Néel relaxation of single domain ferromagnetic particles," in *Advances in Chemical Physics*. vol. 83, I. P. a. S. A. Rice, Ed. Wiley, New York, 1993, pp. 263-464.
[42] J. C. Mallinson, "On Damped Gyromagnetic Precession," *IEEE Transactions On Magnetics,* vol. 23, pp. 2003-2004, Jul 1987.
[43] R. Kikuchi, "On the minimum of magnetization reversal time," *Journal of Applied Physics,* vol. 27, p. 1352, 1956.
[44] P. R. Gillette and K. Oshima, "Magnetization Reversal by Rotation," *Journal of Applied Physics,* vol. 29, pp. 529-531, 1958.
[45] H. Risken, *The Fokker-Planck equation*, 2nd ed. Berlin: Springer, 1989.
[46] C. W. Gardiner, *Handbook of Stochastic Methods*, 2nd ed. New York: Springer, 1997.
[47] R. Kubo and N. Hashitsume, *Progress of Theoretical Physics Supplement,* vol. 46, p. 210.
[48] J. L. García-Palacios and F. J. Lázaro, "Langevin-dynamics study of the dynamical properties of small magnetic particles," *Physical Review B,* vol. 58, p. 14937, 1998.
[49] M. E. J., *Stochastic Calculus and Stochastic Models*. New York: Academic, 1974.
[50] W. Rumelin, "Numerical Treatment of Stochastic Differential-Equations," *Siam Journal on Numerical Analysis,* vol. 19, pp. 604-613, 1982.
[51] M. d'Aquino, C. Serpico, G. Coppola, I. D. Mayergoyz, and G. Bertotti, "Midpoint numerical technique for stochastic Landau-Lifshitz-Gilbert dynamics," *Journal Of Applied Physics,* vol. 99, p. 08B905, 2006.

[52] C. Serpico, I. D. Mayergoyz, and G. Bertotti, "Numerical technique for integration of the Landau-Lifshitz equation," *Journal Of Applied Physics,* vol. 89, pp. 6991-6993, Jun 1 2001.
[53] d. A. Massimiliano, S. Claudio, and M. Giovanni, "Geometrical integration of Landau-Lifshitz-Gilbert equation based on the mid-point rule." vol. 209: Academic Press Professional, Inc., 2005, pp. 730-753.
[54] N. Hayashi and K. Saito, *Japanese Journal of Applied Physics* vol. 35, pp. pp. 6065-6073, 1996.
[55] B. N. Engel, N. D. Rizzo, J. Janesky, J. M. Slaughter, R. Dave, M. DeHerrera, M. Durlam, and S. Tehrani, "The science and technology of magnetoresistive tunneling memory," *IEEE Transactions On Nanotechnology,* vol. 1, pp. 32-38, Mar 2002.
[56] T. M. Maffitt, J. K. DeBrosse, J. A. Gabric, E. T. Gow, M. C. Lamorey, J. S. Parenteau, D. R. Willmott, M. A. Wood, and W. J. Gallagher, "Design considerations for MRAM," *IBM Journal of Research and Development,* vol. 50, pp. 25-39, Jan 2006.
[57] C. R. Chang, "Micromagnetic Studies Of Coherent Rotation With Quartic Crystalline Anisotropy," *Journal of Applied Physics,* vol. 69, pp. 2431-2439, Feb 15 1991.
[58] L. Spinu, A. Stancu, C. J. O'Connor, and H. Srikanth, "Effect of the second-order anistropy constant on the transverse susceptibility of uniaxial ferromagnets," *Applied Physics Letters,* vol. 80, pp. 276-278, Jan 14 2002.
[59] L. Spinu, I. Dumitru, A. Stancu, and D. Cimpoesu, "Transverse susceptibility as the low-frequency limit of ferromagnetic resonance," *Journal Of Magnetism And Magnetic Materials,* vol. 296, pp. 1-8, Jan 1 2006.
[60] J. C. Denardin, M. Knobel, L. S. Dorneles, and L. F. Schelp, *Materials Science and Engineering,* vol. B 112, p. 120, 2004.
[61] L. Spinu, H. Srikanth, E. E. Carpenter, and C. J. O'Connor, "Dynamic radio-frequency transverse susceptibility in magnetic nanoparticle systems," *Journal Of Applied Physics,* vol. 87, pp. 5490-5492, May 1 2000.
[62] A. Anguelouch, B. D. Schrag, G. Xiao, Y. Lu, P. L. Trouilloud, R. A. Wanner, W. J. Gallagher, and S. S. P. Parkin, "Two-dimensional magnetic switching of micron-size films in magnetic tunnel junctions," *Applied Physics Letters,* vol. 76, pp. 622-624, Jan 31 2000.
[63] I. Beardsley, "Modeling the record process," *Magnetics, IEEE Transactions On Magnetics,* vol. 22, pp. 454-459, 1986.
[64] I. S. Jacobs and C. P. Bean, "An Approach to Elongated Fine-Particle Magnets," *Physical Review,* vol. 100, p. 1060, 1955.
[65] M. Tejedor, H. Rubio, L. Elbaile, and R. Iglesias, "External Fields Created By Uniformly Magnetized Ellipsoids And Spheroids," *IEEE Transactions On Magnetics,* vol. 31, pp. 830-836, Jan 1995.

[66] C. Xu, P. M. Hui, J. H. Zhou, and Z. Y. Li, "Biased switching in an interacting pair of magnetic particles," *Journal Of Applied Physics,* vol. 91, pp. 5957-5961, May 1 2002.
[67] G. Bertotti, I. D. Mayergoyz, C. Serpico, and M. d'Aquino, "Geometrical analysis of precessional switching and relaxation in uniformly magnetized bodies," *IEEE Transactions On Magnetics,* vol. 39, pp. 2501-2503, Sep 2003.
[68] H. N. Pham, I. Dumitru, A. Stancu, and L. Spinu, "Magnetization reversal in interacting magnetic systems," *Journal Of Applied Physics,* vol. 97, p. 10P106, May 15 2005.
[69] B. Mancoff, B. N. Engel, and N. D. Rizzo, U.S., 2006.
[70] E. B. Myers, D. C. Ralph, J. A. Katine, R. N. Louie, and R. A. Buhrman, "Current-induced switching of domains in magnetic multilayer devices," *Science,* vol. 285, pp. 867-870, Aug 6 1999.
[71] W. Weber, S. Riesen, and H. C. Siegmann, "Magnetization precession by hot spin injection," *Science,* vol. 291, pp. 1015-1018, Feb 2001.
[72] L. Berger, "Exchange Interaction Between Ferromagnetic Domain-Wall And Electric-Current In Very Thin Metallic-Films," *Journal Of Applied Physics,* vol. 55, pp. 1954-1956, 1984.
[73] C. Y. Hung and L. Berger, "Exchange forces between domain wall and electric current in permalloy films of variable thickness," *Journal of Applied Physics,* vol. 63, pp. 4276-4278, 1988.
[74] J. C. Slonczewski, "Conductance and exchange coupling of two ferromagnets separated by a tunneling barrier," *Physical Review B,* vol. 39, p. 6995, 1989.
[75] J. Z. Sun, "Spin-current interaction with a monodomain magnetic body: A model study," *Physical Review B,* vol. 62, p. 570, 2000.
[76] J. A. Katine, F. J. Albert, R. A. Buhrman, E. B. Myers, and D. C. Ralph, "Current-Driven Magnetization Reversal and Spin-Wave Excitations in Co /Cu /Co Pillars," *Physical Review Letters,* vol. 84, p. 3149, 2000.
[77] J. Z. Sun, "Spin angular momentum transfer in current-perpendicular nanomagnetic junctions," *Ibm Journal of Research and Development,* vol. 50, pp. 81-100, Jan 2006.
[78] H. Morise and S. Nakamura, "Stable magnetization states under a spin-polarized current and a magnetic field," *Physical Review B,* vol. 71, p. 014439, 2005.
[79] G. Bertotti, C. Serpico, I. D. Mayergoyz, A. Magni, M. d' Aquino, and R. Bonin, "Magnetization Switching and Microwave Oscillations in Nanomagnets Driven by Spin-Polarized Currents," *Physical Review Letters,* vol. 94, p. 127206, 2005.
[80] J. Miltat, G. Albuquerque, A. Thiaville, and C. Vouille, "Spin transfer into an inhomogeneous magnetization distribution," *Journal Of Applied Physics,* vol. 89, pp. 6982-6984, 2001.
[81] D. Berkov and N. Gorn, "Transition from the macrospin to chaotic behavior by a spin-torque driven magnetization precession of a square nanoelement," *Physical Review B,* vol. 71, p. 052403, 2005.

[82] D. V. Berkov and N. L. Gorn, "Magnetization precession due to a spin-polarized current in a thin nanoelement: Numerical simulation study," *Physical Review B,* vol. 72, p. 094401, 2005.
[83] Z. Li and S. Zhang, "Magnetization dynamics with a spin-transfer torque," *Physical Review B,* vol. 68, p. 024404, 2003.
[84] D. M. Apalkov and P. B. Visscher, "Spin-torque switching: Fokker-Planck rate calculation," *Physical Review B,* vol. 72, p. 180405, 2005.
[85] A. A. Tulapurkar, T. Devolder, K. Yagami, P. Crozat, C. Chappert, A. Fukushima, and Y. Suzuki, "Subnanosecond magnetization reversal in magnetic nanopillars by spin angular momentum transfer," *Applied Physics Letters,* vol. 85, pp. 5358-5360, 2004.
[86] T. Devolder, A. Tulapurkar, Y. Suzuki, C. Chappert, P. Crozat, and K. Yagami, "Temperature study of the spin-transfer switching speed from dc to 100 ps," *Journal of Applied Physics,* vol. 98, pp. 053904-8, 2005.
[87] T. Devolder, P. Crozat, J. V. Kim, C. Chappert, K. Ito, J. A. Katine, and M. J. Carey, "Magnetization switching by spin torque using subnanosecond current pulses assisted by hard axis magnetic fields," *Applied Physics Letters,* vol. 88, pp. 152502-3, 2006.
[88] T. Devolder, C. Chappert, J. A. Katine, M. J. Carey, and K. Ito, "Distribution of the magnetization reversal duration in subnanosecond spin-transfer switching," *Physical Review B,* vol. 75, pp. 064402-5, 2007.
[89] T. Devolder, C. Chappert, and K. Ito, "Subnanosecond spin-transfer switching: Comparing the benefits of free-layer or pinned-layer biasing," *Physical Review B,* vol. 75, pp. 224430-10, 2007.
[90] C. E. Patton, "Linewidth and Relaxation Processes for the Main Resonance in the Spin-Wave Spectra of Ni-Fe Alloy Films," *Journal of Applied Physics,* vol. 39, pp. 3060-3068, 1968.
[91] R. D. McMichael, M. D. Stiles, P. J. Chen, and J. W. F. Egelhoff, "Ferromagnetic resonance linewidth in thin films coupled to NiO," *Journal Of Applied Physics,* vol. 83, pp. 7037-7039, 1998.
[92] C. D. Stanciu, A. V. Kimel, F. Hansteen, A. Tsukamoto, A. Itoh, A. Kirilyuk, and T. Rasing, "Ultrafast spin dynamics across compensation points in ferrimagnetic GdFeCo: The role of angular momentum compensation," *Physical Review B,* vol. 73, pp. 220402-4, 2006.
[93] M. D. Stiles, W. M. Saslow, M. J. Donahue, and A. Zangwill, "Adiabatic domain wall motion and Landau-Lifshitz damping," *Physical Review B,* vol. 75, pp. 214423-6, 2007.
[94] R. Urban, G. Woltersdorf, and B. Heinrich, "Gilbert Damping in Single and Multilayer Ultrathin Films: Role of Interfaces in Nonlocal Spin Dynamics," *Physical Review Letters,* vol. 87, p. 217204, 2001.
[95] Y. Tserkovnyak, A. Brataas, and G. E. W. Bauer, "Enhanced Gilbert Damping in Thin Ferromagnetic Films," *Physical Review Letters,* vol. 88, p. 117601, 2002.

[96] P. M. Braganca, I. N. Krivorotov, O. Ozatay, A. G. F. Garcia, N. C. Emley, J. C. Sankey, D. C. Ralph, and R. A. Buhrman, "Reducing the critical current for short-pulse spin-transfer switching of nanomagnets," *Applied Physics Letters,* vol. 87, pp. 112507-3, 2005.

[97] D. Cimpoesu, H. Pham, A. Stancu, and L. Spinu, "Dynamic and temperature effects in spin-transfer switching," *Journal of Applied Physics,* vol. 104, pp. 113918-7, 2008.

[98] H. Pham, D. Cimpoesu, A. Stancu, and L. Spinu, "Switching behavior of a Stoner--Wohlfarth particle subjected to spin-torque effect," *Journal Of Applied Physics,* vol. 103, p. 07B105, 2008.

[99] N. C. Emley, F. J. Albert, E. M. Ryan, I. N. Krivorotov, D. C. Ralph, R. A. Buhrman, J. M. Daughton, and A. Jander, "Reduction of spin transfer by synthetic antiferromagnets," *Applied Physics Letters,* vol. 84, pp. 4257-4259, May 2004.

[100] S. Hernandez, M. Kapoor, and R. H. Victora, "Synthetic antiferromagnet for hard layer of exchange coupled composite media," *Applied Physics Letters,* vol. 90, p. 132505, Mar 26 2007.

[101] S. C. Byeon, A. Misra, and W. D. Doyle, "Synthetic antiferromagnetic soft underlayers for perpendicular recording media," *IEEE Transactions On Magnetics,* vol. 40, pp. 2386-2388, Jul 2004.

[102] A. Veloso and P. P. Freitas, "Spin valve sensors with synthetic free and pinned layers," *Journal of Applied Physics,* vol. 87, pp. 5744-5746, May 2000.

[103] M. A. Ruderman and C. Kittel, "Indirect Exchange Coupling of Nuclear Magnetic Moments by Conduction Electrons," *Physical Review,* vol. 96, p. 99, 1954.

[104] L. He, W. D. Doyle, and H. Fujiwara, "High-Speed Coherent Switching Below the Stoner-Wohlfarth Limit," *IEEE Transactions on Magnetics* vol. 30, pp. 4086-4088, 1994.

[105] H. Pham, D. Cimpoesu, A. Stancu, and L. Spinu, "Dynamic critical curve of a synthetic antiferromagnet," *Applied Physics Letters,* 2009 (accepted to publish).

[106] C. E. Patton, Z. Frait, and C. H. Wilts, "Frequency dependence of the parallel and perpendicular ferromagnetic resonance linewidth in Permalloy films, 2-36 GHz," *Journal of Applied Physics,* vol. 46, pp. 5002-5003, 1975.

[107] W. Bailey, P. Kabos, F. Mancoff, and S. Russek, "Control of magnetization dynamics in $Ni_{81}Fe_{19}$ thin films through the use of rare-earth dopants," *IEEE Transactions On Magnetics,* vol. 37, p. 830, 2001.

[108] D. Cimpoesu, A. Stancu, and L. Spinu, "Dynamic and temperature effects in toggle magnetic random access memory," *Journal of Applied Physics,* vol. 102, p. 013915, Jul 2007.

Appendices

A. Flowchart for solving LLG equation

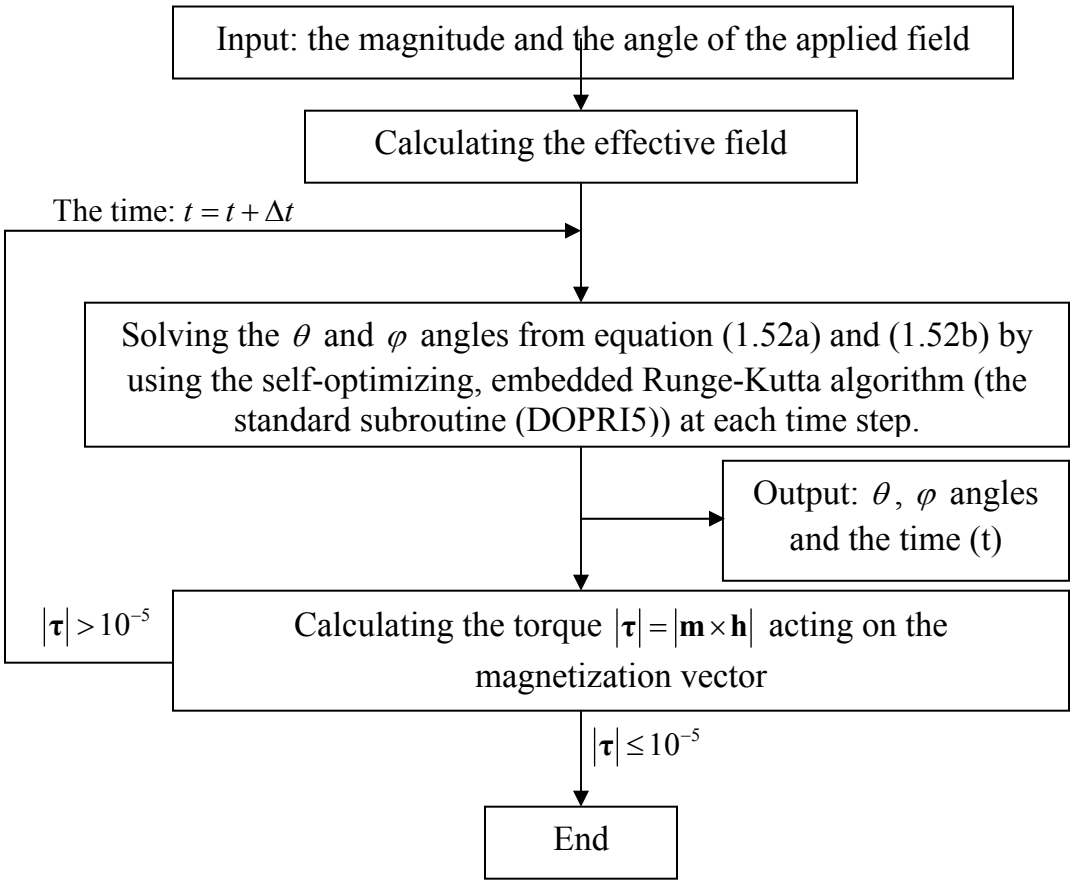

This flowchart shows how the LLG equation is solved. We calculated the magnitude of the torque acting on the magnetization vector via the formula $|\boldsymbol{\tau}| = |\mathbf{m} \times \mathbf{h}|$ for checking the stability of the magnetization vector. When the torque is very small, the magnetization vector will be stabilized and the program will end. Our code can run on PC.

B. External fields for uniformly magnetized ellipsoids

Remember that the equation of an ellipsoid is given by

$$\frac{x^2}{a^2+u}+\frac{y^2}{b^2+u}+\frac{z^2}{c^2+u}=1$$

where *a*, *b*, and *c* are the principle axes of the ellipsoid as shown in Fig. B.1. Here, the parameter *u* defines an ellipsoidal surface.

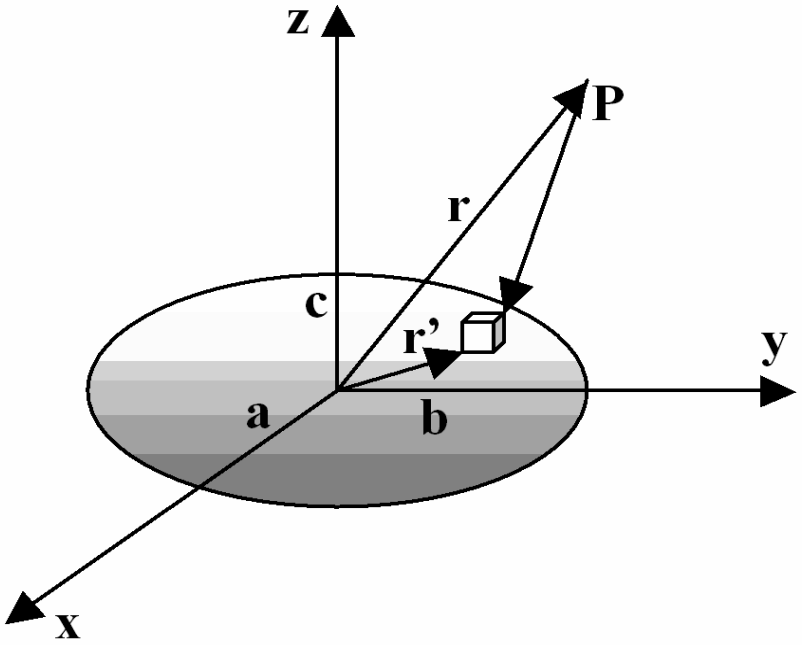

Figure B.1. An ellipsoidal particle with coordinate system.

From Ref. 38, the field at arbitrary point external **P** created by a uniformly magnetized ellipsoid can be calculated as follows:

$$\mathbf{H}_{dip} = -\frac{1}{2}abc \times$$

$$\begin{bmatrix} A_e - \dfrac{2x^2}{D\left(a^2+u\right)^2 E}, & -\dfrac{2xy}{D\left(b^2+u\right)\left(a^2+u\right)E}, & -\dfrac{2xz}{D\left(c^2+u\right)\left(a^2+u\right)E} \\ -\dfrac{2xy}{D\left(a^2+u\right)\left(b^2+u\right)E}, & B_e - \dfrac{2y^2}{D\left(b^2+u\right)^2 E}, & -\dfrac{2yz}{D\left(c^2+u\right)\left(b^2+u\right)E} \\ -\dfrac{2xz}{D\left(a^2+u\right)\left(c^2+u\right)E}, & -\dfrac{2zy}{D\left(b^2+u\right)\left(c^2+u\right)E}, & C_e - \dfrac{2z^2}{D\left(c^2+u\right)^2 E} \end{bmatrix} \times \begin{bmatrix} M_x \\ M_y \\ M_z \end{bmatrix}$$

where $D = D(u) = \sqrt{\left(a^2+u\right)\left(b^2+u\right)\left(c^2+u\right)}$ and $E = \dfrac{x^2}{\left(a^2+u\right)^2} + \dfrac{y^2}{\left(b^2+u\right)^2} + \dfrac{z^2}{\left(c^2+u\right)^2}$

with the coefficients are given by

$$A_e = \int_u^\infty \frac{d\lambda}{\left(a^2+\lambda\right)D(\lambda)};\ B_e = \int_u^\infty \frac{d\lambda}{\left(b^2+\lambda\right)D(\lambda)};\ \text{and}\ C_e = \int_u^\infty \frac{d\lambda}{\left(c^2+\lambda\right)D(\lambda)}$$

However these integrals turned out to be so complicated, thus for simplicity, we consider the case *a*=*b*=*c*.

Hence

$$D(u) = \left(x^2+y^2+z^2\right)^{3/2} = R^3;\ E = \frac{1}{R^2},\ \text{and}\ A_e = B_e = C_e = \frac{2}{3R}$$

where $R = \left(x^2+y^2+z^2\right)^{1/2}$, therefore,

$$\mathbf{H}_{dip} = \frac{abc}{R^3}\begin{bmatrix} \dfrac{x^2}{R^2} - \dfrac{1}{3}, & \dfrac{xy}{R^2}, & \dfrac{xz}{R^2} \\ \dfrac{xy}{R^2}, & \dfrac{y^2}{R^2} - \dfrac{1}{3}, & \dfrac{yz}{R^2} \\ \dfrac{xz}{R^2}, & \dfrac{zy}{R^2}, & \dfrac{z^2}{R^2} - \dfrac{1}{3} \end{bmatrix} \begin{bmatrix} M_x \\ M_y \\ M_z \end{bmatrix}.$$

List of Publications

[1] W. Bao, Y. Qiu, Q. Huang, M. A. Green, P. Zajdel, M. R. Fitzsimmons, M. Zhernenkov, S. Chang, M. Fang, B. Qian, E. K. Vehstedt, J. Yang, **H. Pham**, L. Spinu, and Z. Q. Mao, "Tunable (delta pi, delta pi)-Type Antiferromagnetic Order in alpha-Fe(Te,Se) Superconductors," *Physical Review Letters,* vol. 102, pp. 247001-4, 2009.

[2] T.J. Liu, X. Ke, B. Qian, J. Hu, D. Fobes, E. K. Vehstedt, **H. Pham**, J.H. Yang, M.H. Fang, L. Spinu, P. Schiffer, Y. Liu, Z.Q. Mao, "Charge carrier localization induced by excess Fe in the Fe_{1+y}(Te,Se) superconductor system", *Physical Review B*, 2009 (accepted to publish)

[3] B. Qian, P. Kumar, M. H. Fang, J. Hu, T. J. Liu, D. Fobes, **H. Pham**, X. S. Wu, L. Spinu, and Z. Q. Mao, "Ferromagnetism in iron-pnictide CuFeSb", submitted to *Journal of the American Chemical Society,* 2009.

[4] **H. Pham**, D. Cimpoesu, A. Stancu, and L. Spinu, "Dynamic critical switching curve of a synthetic antiferromagnet," *Applied Physics Letters,* 2009 (accepted to publish).

[5] M. H. Fang, **H. Pham**, B. Qian, T. J. Liu, E. K. Vehstedt, Y. Liu, L. Spinu, and Z. Q. Mao, "Superconductivity close to magnetic instability in Fe(Se[sub 1 - x]Te[sub x])[sub 0.82]," *Physical Review B (Condensed Matter and Materials Physics),* vol. 78, pp. 224503-5, 2008.

[6] D. Cimpoesu, **H. Pham**, A. Stancu, and L. Spinu, "Dynamic and temperature effects in spin-transfer switching," *Journal of Applied Physics,* vol. 104, pp. 113918-7, 2008.

[7] **H. Pham**, D. Cimpoesu, A. Stancu, and L. Spinu, "Switching behavior of a Stoner--Wohlfarth particle subjected to spin-torque effect," *Journal Of Applied Physics,* vol. 103, p. 07B105, 2008.

[8] J. W. Eslick, **H. Pham**, C. Radu, and A. Puri, "Quantum entanglement in an oscillating macroscopic mirror," *European Physical Journal D,* vol. 38, pp. 553-562, Jun 2006.

[9] **H. Pham**, I. Dumitru, A. Stancu, and L. Spinu, "Magnetization reversal in interacting magnetic systems," *Journal Of Applied Physics,* vol. 97, p. 10P106, May 15 2005.

[10] L. Spinu, **H. Pham**, C. Radu, J. C. Denardin, I. Dumitru, M. Knobel, L. S. Dorneles, L. F. Schelp, and A. Stancu, "Probing two-dimensional magnetic switching in Co/SiO2 multilayers using reversible susceptibility experiments," *Applied Physics Letters,* vol. 86, pp. 012506/1-012506/3, 2005.

[11] C. Bach, L. Dang, L. Nguyen, and **H. Pham**, "Application of disordered Ising Model for explanation of some properties of magnetic perovskites," in *the first Conference of Asian consortium for computational materials science held in Bangalore (India)*, 2001.

[12] **H. Pham**, C. Bach, P. K. Schelling, and T. Lanh, "Calculation of some properties of perovskite $BaTiO_3$ by self-consistent tight binding method," in *the fifth National Conference on physics, Hanoi*, 2001.

Vita

The author was born in Vietnam in 1980. He received his high school diploma in 1997 from Halong High School for talented students, and then enrolled at Hanoi University of Science in Hanoi, the capital of Vietnam. He completed his bachelor of science in Physics there in 2001. After that to further enhance his education, he applied to University of New Orleans and became a UNO graduate student starting in August 2003. In 2005 he received his Master of Science in Physics and continued Ph.D in engineering and applied science. He earned his Ph.D in 2009.